SCHOOL OF ENGINEERING

The University *of* Liverpool

The Energy-Absorbing Behaviour of Novel Aerospace Composite Structures

Thesis submitted in accordance with the requirements of the

University *of* Liverpool for the degree of

Doctor *of* Philosophy

By

Jin Zhou

March 2015

ACKNOWLEDGEMENTS

I would like to express my gratitude to my supervisor Dr Z.W. Guan and Professor W.J. Cantwell for their kind guidance, direction and advice throughout my PhD studies. I have extremely appreciated my supervisors who always support and advise on my work. I would like to acknowledge the work of my supervisors involved on the published papers.

I also would like to thank the staff in the School of Engineering who provided assistance on sample preparations and testing, especially Dr Robert S Birch, Mr Dave Atkinson and Mr Stephen Pennington.

Finally, I would like to especially appreciate my parents for their supports to my education.

LIST OF PUBLICATIONS

1. Zhou J., Hassan M.Z, Guan ZW and Cantwell W.J., The Low Velocity Impact Response of Foam-based Sandwich Panels. Composites Science and Technology. 2012; 72(14):1781-1790.
2. Zhou J., Guan Z.W., and Cantwell W.J., The Perforation Resistance of Sandwich Structures Subjected to Low Velocity Projectile Impact Loading. Aeronautical Journal. 2012;116:1247-1262.
3. Zhou J., Guan Z.W., and Cantwell W.J., The Impact Response of Graded Foam Sandwich Structures. Composite Structures. 2013; 97:370-377
4. Zhou J., Guan Z.W., Cantwell W.J. and Liao Y., The Energy-Absorbing Behaviour of Foam Cores Reinforced with Composite Rods. Composite Structures. 2014; 116: 346–356.
5. Zhou J., Guan Z.W., and Cantwell W.J., The Influence of Strain-rate on The Perforation Resistance of Fiber Metal Laminates. Composite Structures. 2015; 125:247–255.
6. Zhou J., Guan Z.W., and Cantwell W.J., Numerical Modelling of Impact Response of PVC Foam Based Sandwich Panels, Proceedings of the 20th UK Conference of the Association for Computational Mechanics in Engineering (ACME12), 2012; pp. 215-218
7. Zhou J., Hassan, M.Z., Guan Z.W. and Cantwell W.J. Modelling the Low Velocity Impact Response of Foam-based Sandwich Structures. Proceedings of 33rd International Technical Conference. SAMPE Europe; Paris Porte de Versailles 2012; pp 10.
8. Zhou J., Guan Z.W. and Cantwell, W.J., Modelling Graded Foam-Based Sandwich Structures Subjected to Projectile Impact, Proceedings of the International Conference on Computational Mechanics (CM13), Durham, UK, 2013; pp66
9. Zhou J., Guan Z.W., and Cantwell W.J., Numerical Modelling Graded Foam-Based Sandwich Structures Subjected to Impact, Proceedings of the 19th International Conference on Composite Materials (ICCM19), Montreal, Canada, 2013; pp6597-6605.
10. Zhou J., Cantwell W.J. and Guan Z.W., Numerical Modelling of Perforation Resistance of Foam-Based Sandwich Panels, Proceedings of the 19th International Conference on Composite Materials (ICCM19), Montreal, Canada, 2013; pp6568-6576.

11. Zhou J., Guan Z.W., and Cantwell W.J., The Compressive Damage of Fibre Rod Reinforced PVC Foam Cores for Energy Absorption Applications, Proceedings of the 1st IFSEEM International Forum on Special Equipment and Engineering Mechanics Nanjing, P. R. China, July 10-12, 2013; pp77-81

12. Guan, Z.W., Zhou J., and Cantwell W.J., Modelling Structural Behaviour of PVC Foam Sandwich Panels Reinforced by CFRP, Proceedings of the 19th International Conference on Composite Materials (ICCM19), Montreal, Canada 2013; pp7516-7523.

13. Guan, Z.W., Zhou J. and Cantwell W.J., Novel Sandwich Structures with High Energy Absorption, Proceedings of the 1st IFSEEM International Forum on Special Equipment and Engineering Mechanics, Nanjing, P. R. China. July 10-12, 2013; pp35-44

14. Zhou J., Guan Z.W. and Cantwell, W.J., Modelling Compressive Crush of Composite Tube Reinforced Foam Sandwiches. The 5th International Conference on Computational Methods, Cambridge, England, 28-30th July, 2014. ScienTech Publishing, Cambridge UK. 2014; Paper ID 151. (**Best Paper Award**)

15. Zhou J., Guan Z.W. and Cantwell, W.J., Numerical Modelling of Perforation Impact Damage of Fibre Metal Laminates. The 5th International Conference on Computational Methods, Cambridge, England, 28-30th July, 2014. ScienTech Publishing, Cambridge UK. 2014, Paper ID 152.

ABSTRACT

The aim of this research is to investigate the structural response of PVC foam based sandwich structures, composite reinforced foam cores and fibre metal laminates (FMLs) subjected to quasi-static and dynamic loading conditions. It also includes the investigation of the mechanical properties and energy-absorbing characteristics of the novel hybrid materials and structures for their potential use in aerospace and a wide range of engineering applications.

Firstly，a series of experimental tests have been undertaken to obtain the mechanical properties of all constituent materials and structural behavior of the composite structures, which are used to develop and validate numerical models. The material tests carried out include (1) tension properties of composite laminates and aluminium alloys, (2) compression of PVC foams, carbon and glass fibre rods and tubes, and fibre metal laminates in the edge wise and flat wise, (3) shear and bending of PVC foams, (4) Hopkinson Bar, (5) quasi-static and dynamic crushing of composite reinforced foams, and (6) projectile impact on fibre reinforced laminates, aluminium alloy panels, PVC foam based sandwich panels and fibre metal laminates. The corresponding failure modes are obtained to validate the numerical predictions. In addition, perforation energy and specific energy absorptions of various composite structures investigated are evaluated. Moreover, the rate-sensitivity of FMLs based on glass fibre reinforced epoxy and three aluminium alloys has been investigated though a series of quasi-static and impact perforation tests on multilayer configurations ranging from a simple 2/1 lay-up to a 5/4 stacking sequence. FMLs based on a combination of the composite and metal constituents exhibit a low degree of rate-sensitivity, with the impact perforation energy increasing slightly in passing from quasi-static to dynamic rates of loading.

Then, finite element (FE) models are developed using the commercial code Abaqus/Explicit to simulate the impact response of PVC foam sandwich structures. The agreement between the numerical predictions and the experimental results is very good across the range of the structures and configurations investigated. The FE models have produced accurate predictions of the impact load-displacement responses, the perforation energies and the failure characteristics recorded. The analyses are used to estimate the energy absorbed by the skins and

the core during the perforation process. The validated FE models are also used to investigate the effect of oblique loading and to study the impact response of sandwich panels on an aqueous environment and subjected to a pressure differential (equivalent to flying at an altitude of 10000 m). The modelling has been further undertaken on the low velocity impact response of the sandwich structures based on graded or composite reinforced PVC foam cores, with reasonably good correlation to the corresponding experimental results. Consequently, a series of finite element analyses have been conducted to investigate the influence of varying foam density, rod diameter, rod length and fibre type on the energy-absorbing characteristics of the reinforced foams. Perforation energies, impact resistance performance and unit cost of the structures have been evaluated.

Furthermore, the low velocity impact response of fibre metal laminates has been studied numerically. Here, the composite layer in FMLs is modelled using the modified 3D Hashin's failure criteria, which are implemented into the main programme through a user-defined subroutine, whilst aluminium alloys are modelled using Johnson-Cook plasticity and the corresponding damage criterion. A large number of simulations have been undertaken to cover FMLs with all stacking sequences and alloy types studied, which are compared with the experimental results in terms of the load-displacement trace and failure modes, with very good correlation. Similar modelling work has been carried out on the aluminium layer and composite layer individually. The energy to perforate the various FMLs is plotted and fitted on a single curve that can be used to predict the perforation energies of other configurations.

The dynamic characteristics of the composite structures through a series experimental tests and numerical predictions investigated in this project can be used in the design of lightweight composite structures for energy-absorbing applications.

CONTENTS

CHAPTER 1 INTRODUCTION

This chapter gives an overview of composite materials for energy absorption. It covers the background, history and development, advantages and disadvantages, applications, definition and classification of composite, fibre and resin types, overview of fibre reinforced lamina, sandwiches and fibre metal laminates investigated in this study.

1.1 Overview

1.1.1 Background

Composite materials have been extensively used in many military and civil applications due to their excellent strength and stiffness properties when compared to conventional materials. Composite materials have superior mechanical properties over metal materials, such as light-weight, resistance to corrosion, integral design and energy absorption capacity under impact/blast loading. For these reasons, composites are increasingly becoming competitive materials for use in the design and manufacture of primary structures in the aerospace industry. Their growing use has risen from their high specific stiffness and strength, and the ability to tailor and shape their structure in order to produce more aerodynamically efficient structural configurations. The super mechanical performance and advantage of composites provide a possibility to continue offer a critical demand on the next generation commercial and military aircraft as well as other aerospace applications.

The application of composites in commercial aircraft is an efficient way to reduce weight. With the rapid increase in fuel consumption and carbon emissions during the 21st century, the world is undergoing economic and climatic changes, which require a substantial improvement in the cost effectiveness, environmental influence of the most transport modes, including aircraft. The fuel efficiency and emissions reduction are more important on commercial aircraft in the highly competitive airline market. For instance, a commercial aircraft can save up to 360 gal (1360 l) of fuel per year if reducing one lb mass (0.453 kg) in 1980s (Kaw, 2006). The application of light-weight composites to replace conventional metal alloys is continuous ways to reduce the overall weight of the aircraft without sacrificing the performance of its components. The development of composite materials for aerospace applications will improve fuel efficiency to reduce carbon emissions and alleviate pressure on the environment. It is a significant step forward in the global fight against climate change. The increasing applications of composite materials will allow a continued growth in demand for air transportation.

1.1.2 History and development of composites

Natural composite materials are widely used, such as bamboo, leather and wood, which can go back to thousands of years ago. A composite bow was invented by Mongols before 1200 A.D. Straw bricks were used by Egyptians and Mesopotamian in 1300 B.C. More manmade composites exist in daily life, such as straw-bricks, concrete, tyres, plywood (glued laminated wood) and sport equipment. The modern composite was developed in the 20th century, when glass fibre reinforced resin composite was used in the 1930s. The applications of composites has significantly increased since 1970s, with development of new fibres, such as aramids, carbon, boron as well as hybrid systems made of composite and metal. The mechanical performance of composites to conventional materials was compared in a historical time line. The advantage of composites over the conventional materials was measured using specific strength, which is a ratio between the strength (σ) and the density (ρ) of a material. Figure 1.1 shows specific strength comparison between composites and fibres rate with other traditional materials in terms of (Kaw, 2006). The specific strength of composites is several times of that of steel and aluminium, which means the structures could be of less weight/mass to reduce material and energy consumption at the same strength requirement or the structure will be of a higher safety factor and stronger to replace a metal based structure. Composites have been the fast developed advanced materials in the 21st century.

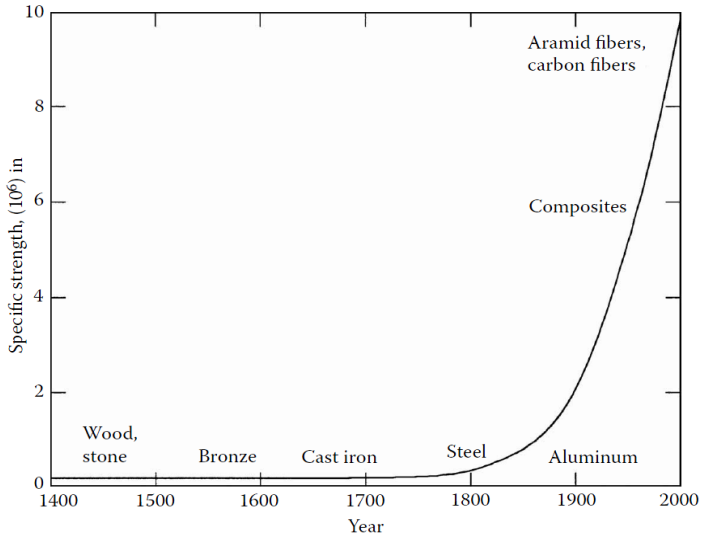

Fig. 1.1 Specific strength as a function of time of materials (Eager,1991).

Due to the excellent performance and advantages over conventional materials, composites are increasing their uses and applications on both military and commercial aircraft from 1970s. The composite was firstly applied in military aircraft as a pioneer use of advanced materials. The use of fibre-reinforced polymers has experienced a steady growth in the aircraft over the past 45 years. Figure 1.2 shows the percentage of composite components in military and commercial aircraft. In 1969, the boron fibre -reinforced epoxy was introduced to the militarily aircraft F-14 horizontal stabilizers. The fraction of carbon epoxy composites were increased by 2 to 4 percent by weight on fighter aircraft in the 1970s, such as the F-14, F-15, and F-111. Carbon fibre-reinforced epoxy has become the primary material in many wings, fuselages, and empennage components, with the production application of carbon fibres in the 1970s (Mallick, 2007). In the 1990s, this usage grew to 15 to 30 percent by weight, for example, in the A-6, AV-8, F/A-18, and F/A-22. However, in 1982, a vertical and short take-off and landing aircraft AV-8B, contains about 25% carbon fibre reinforced epoxy by weight and the F-22 fighter aircraft is made of 25% carbon fibre reinforced polymers by weight. In 1990s, the exterior surface of Stealth Bomber B-2 and Joint Strike Fighter F-35 is almost all made of carbon fibre reinforced polymers in order to implement the design features that minimize heat radiation and radar reflection. The superior performance and stealth characteristics of those aircraft are the benefit of the development and experienced applications of those lightweight and high-strength composite materials.

Composite materials have been used by commercial aircraft manufacturers in transport airplane components over decades. The composite content in each new aircraft has grown significantly, resulting in important weight savings since the introduction of prepregs in the 1970's. From the Boeing 737, 747 to 777 and the Airbus A310, A320, to A380, the weight ratio of composite has been increased from 5 % to more than 25% during the past 35 years. Started commercial service since 2011, the new large transport airplane Boeing 787 and Airbus A350 are made of over 50% of composites mostly as the major material of construction.

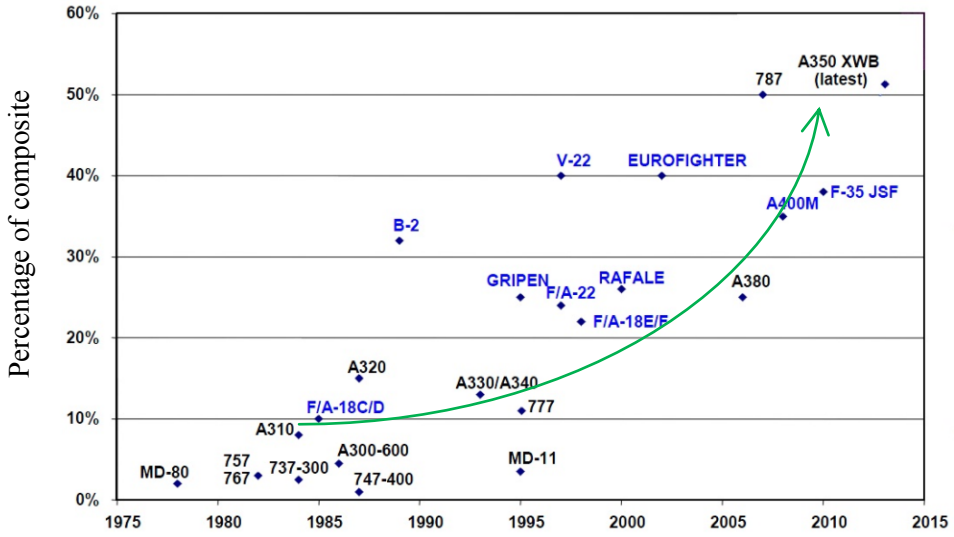

Fig. 1.2 Composite over time by percentage in military and commercial airplane (Mallick, 2007).

The total weight volume of the finished composite aerostructures was more than 21.3 million lb (9,662 metric tonnes) by 2013. The volume is expected to reach more than 30 million lb, delivered to the aerospace industry by 2015. Much of that growth was dominated by the continued ramp-up in production of the Airbus A350 XWB and the Boeing Co.'s 787. More widespread composites have being adopted by the aircraft manufactures include Boeing's 777X, Commercial Aircraft Corp. of China's C-919, Sukhoi Civil Aircraft's SuperJet NG and the Irkut MS-21 and Embraer's second-generation ERJ-170/190/195X models. Figure 1.3 shows the forecast percentage of demand for composites by weight. The dominant demand includes rotorcrafts, fixed-wing aircraft and related jet. Further, the largest demand on composite aerostructures is associated with regional commercial aircraft and jet engines. The commercial aerospace industry is the largest user of composites and advanced composites have become essential materials in all the aircraft construction.

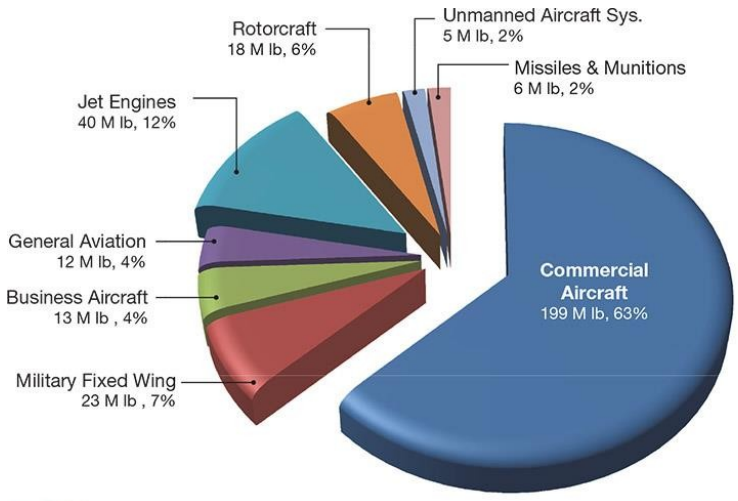

Fig. 1.3 Estimated market for aerospace composite structures (Red, 2014).

1.1.3 Definitions and classifications of composite

A composite is defined as a structural material, which consists of two or more separate constituents combined at a macroscopic level and are made from various combinations not soluble in each other, e.g. epoxy reinforced with carbon fibres and concrete reinforced with steel, etc. One constituent is called the reinforcing phase and the one in which it is embedded is called the matrix. The schedule of fibre reinforced matrix shown in Figure 1.4. Composites are also definied by Composite Materials Handbook, as combinations of materials differing in composition or form on a macroscale, i.e. "The constituents retain their identities in the composite; that is, they do not dissolve or otherwise merge completely into each other although they act in concert". The components normally exhibit an interface between one another and can be physically identified (Composite Materials Handbook, 2002).

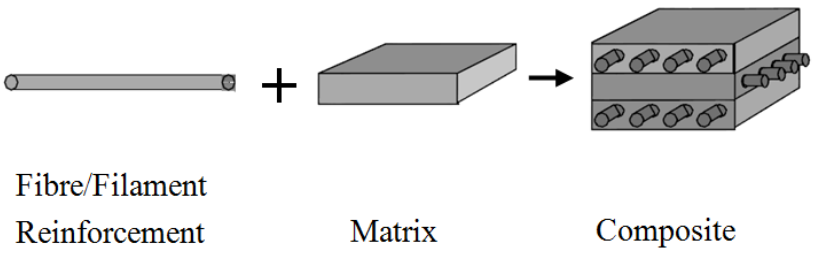

Fig. 1.4 The elements of a composite

Composites are classified by either the geometry of the reinforcement or by the type of matrix. For example, different geometry of reinforcement such as fibres, flake, particulate, and or different matrix such as polymer, metal, ceramic and carbon (Kaw, 2006).

Those factitious composites are classified into three main categories as (Matthews and Rawlings, 2008).

- Polymer Matrix Composites (PMC's),
- Metal Matrix Composites (MMC's) and
- Ceramic Matrix Composites (CMC's).

Polymer Matrix Composites (PMC's) consist of a polymer-based resin as the matrix reinforced by various discontinuous or continuous fibres (e.g. carbon, glass, aramid fibre). It is known as Fibre Reinforced Polymers/Plastics (FRP). The primary FRP composites used in industrial applications are the Glass Fibre Reinforced Polymers (GFRP) and Carbon Fibre Reinforced Polymers (CFRP). Continuous fibre composites are further classified by the types of fibre or polymer matrices, such as thermoplastic and thermosetting polymers. Laminas based on unidirectional or woven fibre are the fundamental units of continuous fibre matrix composite. Laminates are stacked in multilayer at various directions to make a multidirectional fibre reinforced laminate. Fibre reinforced laminate can be stacked with various foam core layer or metal layer to form a hybrid structures, such as PVC foam based sandwiches and aluminium based fibre metal laminates. The classifications of Fibre Reinforced Polymer based composites are shown in Figure 1.5 (Chai and Manikandan, 2014).

Metal Matrix Composites (MMC's) consist of fibres such as silicon carbide as reinforcement and a metal such as aluminium as the matrix, which are increasingly used in automotive industry. Ceramic Matrix Composites (CMC's) are made of a ceramic as the matrix and short fibres such as those fibres made from boron nitride and silicon carbide as reinforcement to be applied in a high temperature environment.

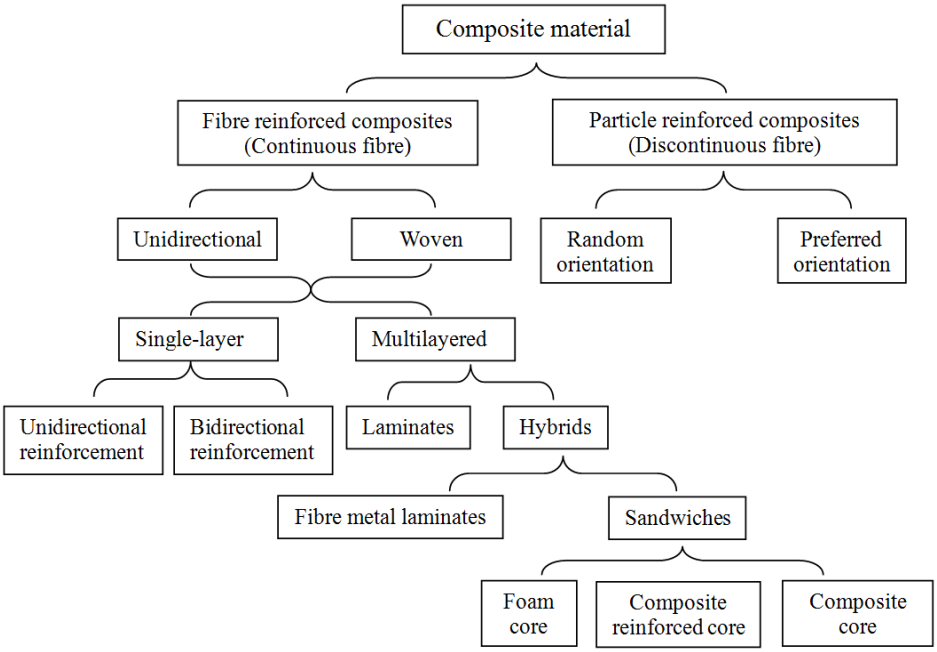

Fig. 1.5 Classification of composite (Chai and Manikandan, 2014)

In addition, nanocomposites are developed as a composite type, which consist of materials in nanometers scale (10^{-9} m). The constituents of composite less than 100 nm are usually classified as a nanocomposite. The material properties may be different from those of the most material at the nanoscale, which results in some properties of the composite material being better than it at the microscale. For example, nanocomposite films were applied as packaging applications for the military to improve properties such as elastic modulus and heat distortion.

1.1.4 Advantages and disadvantages

A composite material is composed of at least two elements working together to produce material properties that combine advanced properties of those elements. Since the fibre reinforced composite combines a reinforcing fibres and resin system, the properties of the resulting composite material are determined by the properties of both fibre and resin, as well as its volume fraction, fibres orientation and geometry. In general, most composites consist of a matrix material with good shear properties and low density (e.g. resin), and a reinforcement embedded in order to increase the stiffness and strength of the matrix, such as fibre or steel. The reinforcement fibres are embedded in matrix to carry load and the surrounding matrix is load transfer medium to keep fibres in the desired

orientation and location. The matrix also protects reinforcement to isolate environmental damages by high temperature and humidity. In this form, composite produces a combination of improved properties that cannot be achieved with either of the fibres and matrix acting individually although constituents retain their chemical and physical identities. Both the reinforcement fibre and resin matrix serve a number of functions to achieve useful advantages in a fibre reinforced composite material as below.

- Light weight
- High strength and stiffness to density ratio
- High fatigue and impact resistance
- Excellent fatigue resistance
- High energy absorption
- Good corrosion resistance
- Formable to complex shape
- Improve creep-life time
- Controlled low thermal expansion
- Lower manufacturing cost and reduction of maintenance costs
- Enhanced properties via tailorable properties (Anisotropic vs. isotropic)

Advanced composites are high performance composite materials that are traditionally used in the aerospace industry. The most common advanced composites are polymer matrix composites (PMCs), which is made of thin fibres (e.g., carbon, aramids, graphite, boron) and reinforced polymer matrix (e.g., epoxy, polyester, urethane). For instance, Kevlar/epoxy, carbon/epoxy and boron/aluminium composites are examples (Kaw, 2006). These materials have been widely used in industrial applications, due to high strength, low cost and simple manufacturing process.

The advantages of advanced composite out-performing the conventional materials are usually measured using specific modulus and specific strength. The former is a ratio between Young's modulus (E) and density (ρ), and the latter is a ratio of strength (σ) to density (ρ) of the material. Figure 1.6 shows comparison of the mechanical performance between composites and traditional light metals in terms of specific modulus and strength (EADS Deutschland GmbH, 2004; Kaw, 2006) The advanced composites serve several times of the specific modulus and strength over conventional

metals such as aluminium, steel and magnesium The additional advantages of high performance composites over the conventional materials include improved fatigue, impact and corrosion resistance.

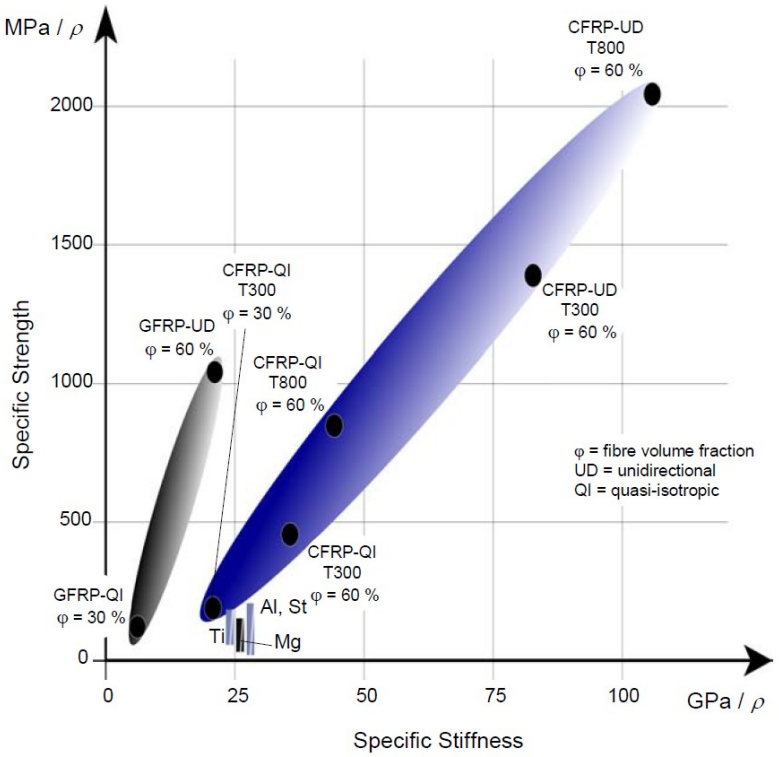

Fig. 1.6 Comparison of the mechanical performance of composites and light metals (EADS Deutschland GmbH Report, 2004)

Although there are the excellent characteristics offered by composite materials, several disadvantages still exist, e.g.

- High materials, fabrication and repair costs,
- Complex manufacturing processes including refrigerated transport and storage, limited shelf life of raw materials (thermoset matrix),
- Unique assembly process such as curing time, pressure and temperature request,
- Relatively brittle with low toughness due to weak matrix,
- Manufacturing defects such as delamination, voids, inclusions and porosity,
- Environmental degradation of matrix,
- Difficulty of recycling.

1.2 Fibre reinforced laminates

A fibre reinforced laminate is made of multi layers of the fibre-reinforced plastic (fibres and matrix) by stacking the unidirectional fibre or woven fibre layers and curing them into the desired thickness at certain temperature and pressure. Fibre-reinforced plastic (FRP) is a composite material made of a polymer matrix reinforced with fibres. It is also known as fibre-reinforced polymer. The fibre layers in various forms can be incorporated into a matrix either in random discontinuous lengths or continuous lengths, as shown in Figure 1.7.

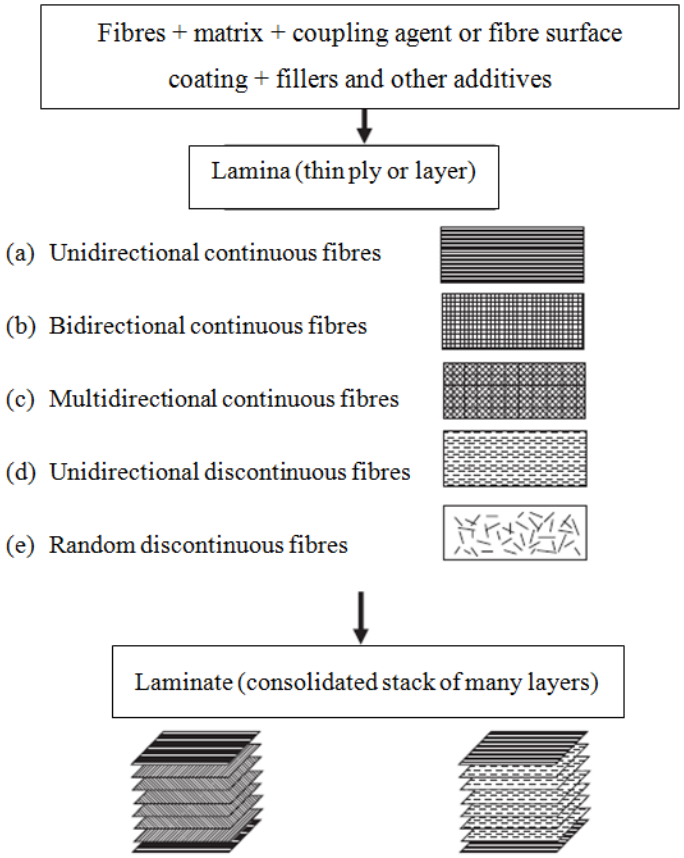

Fig. 1.7 Basic stacking construction of fibre reinforced laminate (Mallick, 2007)

The most common fibres in commercial applications are various types of carbon, glass, as well as aramid (known as Kevlar). A limited usage of other fibres includes polyester, polyethylene, boron, quartz, basalt, ceramics, silicon carbide and aluminium oxide. The various types of matrix could be classified based on chemical compositions and microstructural arrangements. The matrix materials could be a polymer, a ceramic or a metal . A polymer is most commonly used as the matrix, which can be epoxy, vinylester, polyester, thermosetting plastic, etc.

1.2.1 Fibre type

The role of the reinforcement in a composite is to increase the mechanical properties of the matrix system. The properties of composite are affected in different ways by different fibres used in composites. Figure 1.8 shows tensile properties and characteristics of common fibres.

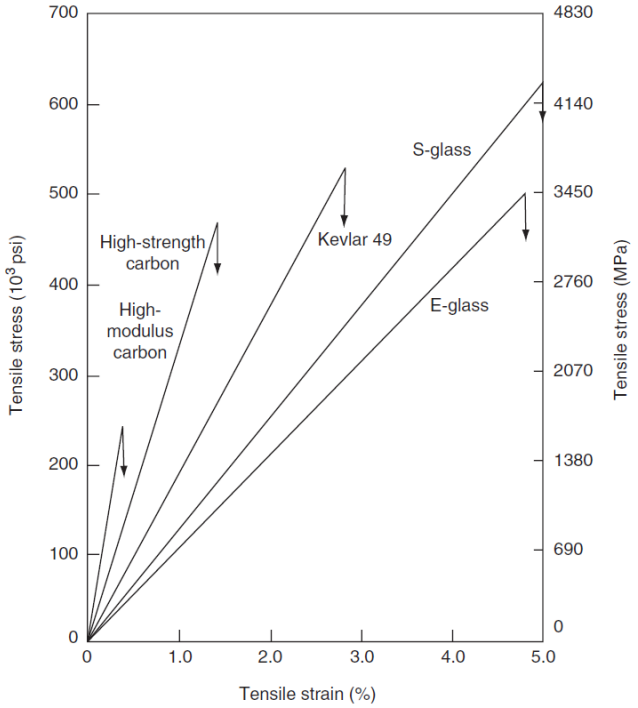

Fig. 1.8 Schematic of tensile stress-strain diagrams for various reinforcing fibres. (Mallick, 2007).

Glass

Glass is the most common fibre applied in polymer matrix composites. Liquid glass is formed by blending quarry products heating the mixture in a furnace at temperatures between 1200 to 1600 ºC to produce glass fibre filaments with 10 - 20 microns in diameter. The advantages of glass fibres are low cost, relatively high strength, heat resistant, insensitive to moisture and an electrical insulator. The types of glass fibre used for structural reinforcements include, C-glass, E-glass, D, S and R-glass.

C glass: (corrosion) resists corrosion in a chemical environment, such as storage tanks.

E glass: (electrical) high strength and high resistivity, electrical, decorations and structural applications.

D glass: (dielectric) applied for low dielectric constants applications, such as radomes.

S glass: (silica) high strength, modulus, fatigue and stability under extreme temperature and corrosive environment.

R glass: enhanced mechanical properties, used in structural applications such as construction.

Carbon

Carbon fibre is produced by the controlled carbonisation, graphitisation and oxidation of carbon-rich organic precursors in fibre form. Advantages are high strength and stiffness, creep and fatigue resistance. The disadvantages are cost, poor impact resistance, electrical conductor.

Aramid

Aramid fibre is a artificial organic polymer, formed by spinning a solid fibre from a liquid chemical blend (an aromatic polyamide called PPTA). The advantages are high specific tensile strength, impact and abrasion resistance and fatigue resistance. The disadvantages are poor in compression, attacked by UV and acids, and low temperature resistance.

Fabric types and constructions

A fabric is defined as a fabricated assembly of long fibres of glass, carbon or aramid , or these fibres combination, to produce a flat fibres sheet with one or more layers in polymeric composite terms. The four main fibre orientation categories are: unidirectional, 0/90°, multiaxial and other random. Woven fabrics are the most common type in form of plain, twill, basket, satin and mock leno.

1.2.2 Resin systems for composites

Polymers are classified into two types, ‘thermoplastic’ and ‘thermosetting’, according to the effect of heat on their properties. Thermoplastics, like metals, soften with heating and eventually melt, hardening again with cooling. The resins that are used in fibre reinforced composites are referred as ‘polymers’ in sometimes. An important common property of all polymers is that they are composed of long chain-like molecules consisting of many simple repeating units.

Thermosetting materials, known as ‘thermosets’, are formed from a chemical reaction in-situ, where the hardener and resin or catalyst and resin are mixed and then undergo a nonreversible chemical reaction to form a infusible, hard product. Once cured, thermosets will not thaw to liquid again even

heated. The comparison of properties between Thermoplastics and Thermoset are shown in Table 1-1.

Table 1-1 The properties comparison between thermoplastics and thermoset (Kaw, 2006)

Thermoplastics	Thermoset
Soften on heating and pressure, easy to repair	Decompose on heating
Higher fabrication temperature and viscosities	Lower fabrication temperature
Can be reprocessed	Cannot be reprocessed
High strains to failure	Low strains to failure
Short cure cycles	Long cure cycles
Not tacky and easy to handle	Tacky
Excellent solvent resistance	Fair solvent resistance
Indefinite shelf life	Definite shelf life

Originally, Advanced Thermoplastic Composites (ATC's) used amorphous resins such as polyethersulphone (PES) and polyetherimide (PEI) for the matrix. However, where the increased solvent resistance was required, semi-crystalline polymers such as polyphenylene sulphide (PPS) and polyether ether ketone (PEEK) may be employed. The continuous reinforcement may be made from aramid, carbon and/or R, E and S-glass. Carbon is the most popular material for fibre reinforced composite as one of advanced composites in higher temperature applications.

Fibre reinforced laminate was applied as pioneering use of high performance advanced composite in high performance military aircraft to reach the aircraft's complex flight characteristics and design requirements, which request high strength reinforcement and higher temperature resistance and absorption radar energy as well. For example, the most exterior composite and load-bearing structure used carbon fibre/epoxy in the fifth-generation, supersonic stealth aircraft F-35 Joint Strike Fighter, to ensure in-flight service temperatures and high strength as well. Carbon and carbon-graphite fibre-reinforced polymer extensively were used in the primary structure of B2 Spirit stealth bomber in order to reduce the weight penalty.

1.3 Sandwich structures

Composite sandwich structures are finding increasing use in a wide range of lightweight structures due to their excellent specific properties, particularly when subjected to flexural loading. Sandwich structures mainly consist of a lightweight internal core and two external thin face layers of fibre

reinforced material bonded together by adhesive or resin layers in order to minimize the total weight and maintain structural rigidity, as shown in Figure 1.9.

1.3.1 Skin materials

In a sandwich structure, the skins are usually thin and strong, used in these lightweight panels. The face skins are often of composite materials or metallic materials such as fibre reinforced polymers, aramid, carbon fibre reinforced composite, glass fibre reinforced composite, steel or aluminium sheet structure.

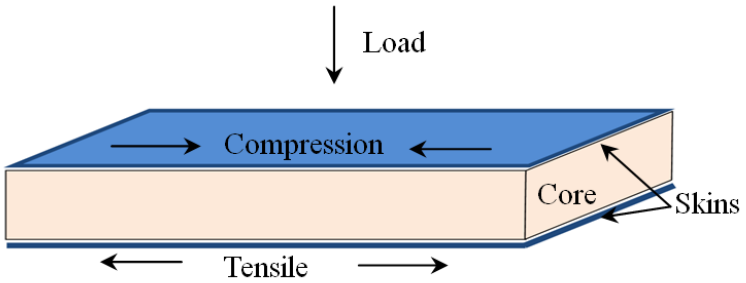

Fig. 1.9 Schematic of sandwich structures

1.3.2 Core materials

The relatively thick core is to keep the two face sheets apart at a desired distance and withstands the shear loads in the transverse direction, while the face skins carries the in-plain tensile and compressive stresses resulting from bending. The core should also take a stable compressive loading without premature failure to prevent the thin skins from failing in a buckling and wrinkling mode. The core materials are divided into several categories as honeycomb, foam, textile and corrugated cores. The core can be classified based on its material or structure, as PVC foam, aluminium foam, honeycomb cores, corrugated cores, truss or lattice cores.

Due to the excellent impact strength, energy absorption, light weight and thermal insulation, sandwiches structures have been used as primary components and second surfaces in aircraft, such as rotor blades, fuselage and wing components for rotor aircraft and helicopter, interior fittings, cockpit doors on commercial aircraft, used as hull, decks and interior fittings in ship and boat construction, used as collision protection, control stand, roof panels in transport containers, train and vehicles, used as rotor blades generator casings in wind energy plants as well.

1.4 Fibre metal laminates

Fibre metal laminates (FMLs) are hybrid structures of composite based on combinations of thin layers of metal alloys and fibre reinforced composite materials. The fibre metal laminates are stacked of metal layers by sandwiching fibre reinforced composite layers alternatively and curing under certain pressure and temperature. Figure 1.10 shows a 3/2 cofiguration of continuous glass fibre/ epoxy and aluminium based hybrid composite.

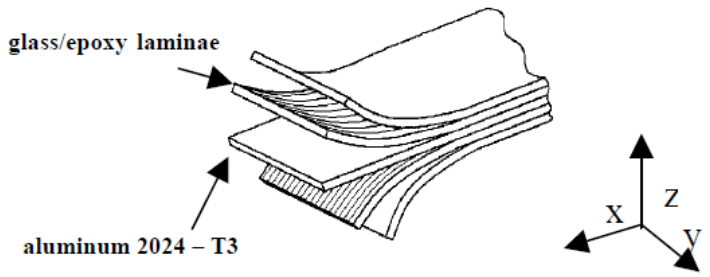

Fig. 1.10. Configuration of continuous glass fibre/epoxy hybrid composite. (Botelho et al, 2006).

The metals currently used in FMLs include aluminium, titanium or magnesium, and the fibre-reinforced layer is either a glass, carbon or Kevlar fibre reinforced composite. The classification of FML, based on constituent materials of metal and fibre reinforced plies (Vogelesang and Vlot, 2000).

A fibre metal laminates combines both the characteristics of two constituents materials to overcome the weaknesses of metallic and fibre reinforced plastic materials, such as low strength, corrosion, durability and fatigue resistance of metal, low impact resistance and bearing strength, reparability offered from fibre reinforced plastic. The combinations of multilayer FMLs offer considerable improvement in performance and several advantages as below (Vlot et al., 1993, 1999; Tamer et al. 2011)

- High specific stiffness, strength and lightweight
- Excellent fatigue characteristics
- Superior impact properties
- Corrosion resistance (protection of the metal components from corrosion)
- Blunt notch strength

- Better damage tolerance to fatigue crack growth,
- Reparability and low cost (Easy to repair)
- Formability
- Fire resistance,
- High fatigue resistance

Due to their advantages of the hybrid composite, FMLs are commonly used in aircraft in aerospace applications. A number of the traditional aluminium components have been substituted by extensive FML composites (Alderliesten and Benedictus, 2009). FMLs have been successfully introduced into a number of components on aircraft, such as upper fuselage of Airbus A380 and the bulk cargo floor of Boeing 777 based on GLARE, the cargo door of the Boeing C-1 and lower wing skin panels of the former Fokker 27 based on ARALL (Beumler, 2006).

1.5 Applications

1.5.1 Commercial airplane

Boeing started making use of composites on Boeing 767 in 1982, when less than 5% of structural weight was made of carbon/epoxy composites, which limited to the secondary structures such as landing gear doors, elevators, rudders, panels and floorings. About 10% structural weight of Boeing 777's was made of carbon fibre-reinforced epoxy, the composite components include most of the fuselage floor beams, engine cowlings, control surfaces and empennage (which include vertical stabilizer, horizontal stabilizer, rudder and elevator). The latest Boeing 787 Dreamliner is made of about 50% of the structural composites by weight. The airframe composite is made of carbon laminate and the secondary structures made of carbon sandwiches (which include elevator, rudder and engine cover). The schematic shown in Figure 1.12 consists of composites for Boeing 787 The majority of components using composite for Boeing 787 led a 20 fewer emissions and percent more fuel efficient than similarly sized airplanes.

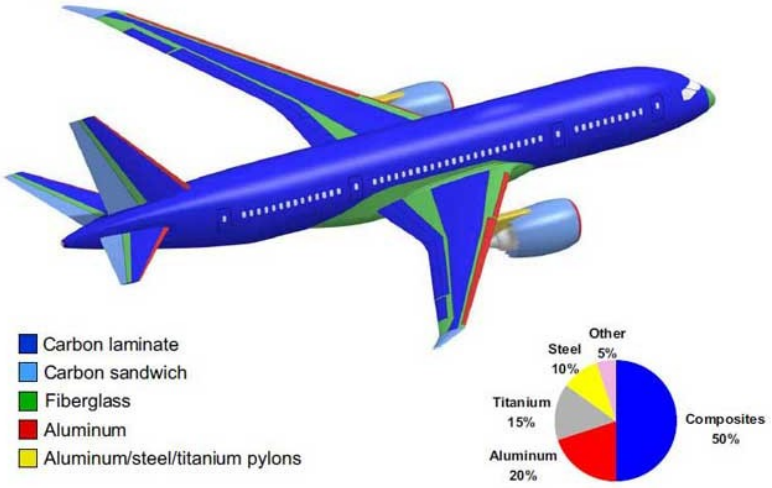

Fig. 1.11 Distribution of composite material on Boeing 787 (Soutis, 2005).

One of the largest aircraft Boeing 747-400 series was redesigned by increasing the wingspan and additional composite winglets to enhance fuel efficiency. The wing weight was reduced even after wingspan was increased as the results of increase using composite materials and special aluminium alloys. Airframe weight was reduced as well in a number of areas resulting from the use of composite materials such as honeycomb materials, carbon/epoxy and high strength aluminium alloys.

Airbus A310 was the first commercial airplane made from extensive composite components, which was introduced in 1987. Approximately 10% of the aircraft's weight was made of composites. The use of the composite vertical stabilizer made it about 400 kg lighter than the previously used aluminium vertical stabilizer (Soutis, 2005). Airbus A320 was introduced in 1988, which is the first aircraft in production with a tail section made of all composite including the tail cone, horizontal stabilizer and vertical stabilizer. Airbus has developed largely a derivative of its successful A330 twin-aisle aircraft since 1994, in which the weight of composite components increases to15 % of the total weigh. The world's largest passenger airplane A380 was introduced by Airbus in 2006. The composite components is A380 weighes about 25% of its weight and the major composite components is shown in Figure 1.13 schematically.

In 2013, the most recently launched all-new carbon fibre wing aircraft Airbus A350 XWB (Extra Wide-Body) is made of 52% reinforced plastic composites, which is a competitor to Boeing's B787 Dreamliner. The light-weight A350 XWB is able to offer 20% lower operating costs and fuel

efficiency improvements of up to 25% per seat. It is Airbus' response to airlines' priorities challenges of high fuel prices, increasing environmental concerns and rising passenger expectations for market demand of long range wide-body family with a medium capacity. It has been demonstrated that typical weight savings of 15-20% can be achieved by using the structural composite components in the above applications to instead of equivalent aluminium designs.

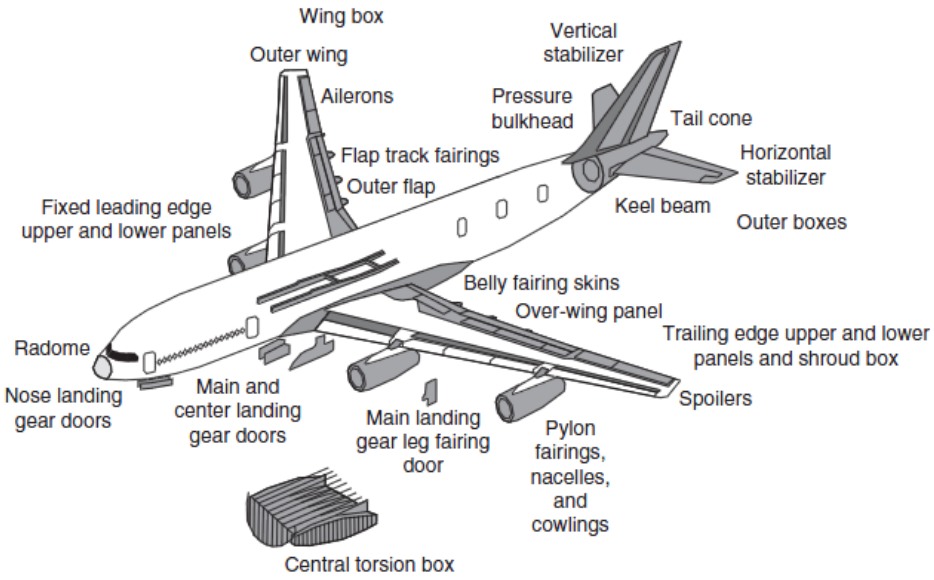

Fig. 1.12 Distribution of composite material on Airbus 380 (Mallick, 2007).

1.5.2 Military aircraft

Due to excellent performance of high strength, high temperature resistance and stealth requirements, high performance composites were largely applied in high performance stealth aircraft in military to reach its special design requirements and complex flight characteristics. The B-2 Spirit contains about 25% by weight of composite materials. The application of composite also contributes its distinctive aircraft construction and flying wing profile without fuselage or tail, which is a 33° angled leading edges of the wings and a double-W shaped trailing edge. The volume fraction of composite is considerable, which may exceed 60 percent due to majority of the airframe being made of the lower density but stronger composites. The applications of various composites and radar absorbing materials on exterior as well as higher-performing materials used for Hot Trailing Edge (HTE) skin to achieve minimizing the radar cross-section and additional reduction in its radar signature. A supersonic stealth aircraft, F-35 Joint Strike Fighter, is made of approximately 40

percent composites by weight, which uses the most of composite among any fighter aircraft up to date. The exterior composite components include the wings, fuselage, control surfaces, horizontal stabilizers, vertical stabilizers, flight-moveable doors as well as carbon fibre internal structural components to achieve super performance. Figure 1.13 shows the stealth bomber B2 and Fighter F-35. Automated fibre placement (AFP) technology was applied, to produce the wing and complex composite parts precisely. The exterior composites skin, exact outer shape, and assembly precision are guaranteed to ensure its low stealth requirements. Perhaps most crucially, a beneficial characteristic of this composite material is high strength, high temperature resistance and absorption of significant amounts of radar energy.

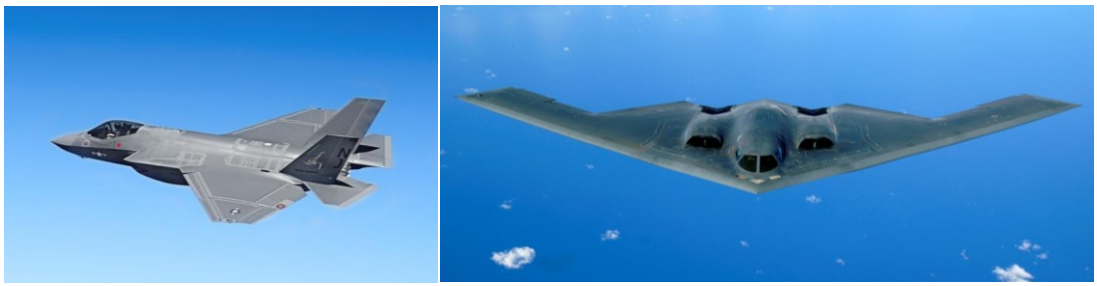

Fig. 1.13 The composite stealth bomber B2 and Fighter F-35

(Source: https://www.f35.com; http://en.wikipedia.org/wiki/Northrop_Grumman_B-2_Spirit)

1.5.3 Space and rotorcraft

In addition, composites are wildly applied in aerospace, such as space shuttles, solar panel of satellite, wind power, transportation, such as ship, boat, high speed train, and automotives. The environment in space request the materials are high specific strength and modulus, and dimensional stability during temperature changes in space. Payload bay door is sandwich laminate made of aluminium honeycomb core and of carbon fibre-reinforced epoxy face sheets, boron fibre-reinforced aluminium tubes used as the mid-fuselage truss structure of space shuttles, remote manipulator arm is made of ultrahigh-modulus carbon fibre-reinforced epoxy tube, Kevlar 49 fibre-reinforced epoxy used as pressure vessels. Fibre-reinforced polymers components are used in rotate craft and helicopters such as fairings, baggage doors, tail rotor spars, vertical fins and so on. Carbon or glass fibre-reinforced epoxy is used to make the rotor blades of helicopter in order to reduce weight and vibration characteristics of the blades.

1.5.4 Marine and automotive transportation

Due to excellent higher strength to weight ratio, composite components have been widely used in transportation vehicle, trains, ships and boats to reduce weight, improve fuel efficiency and maneuverability as well as the blade of wind power generation. Figure 1.14 shows the composite applications. Glass fibre-reinforced polymers have been used as the primary composite materials in high speed vehicle and trains. About 8% by weight of automobile parts are made of composites, including, doors, body panels and bumpers. Carbon fibre reinforced polymers also selected to be used in a few components in automobiles. Volume of composite applied on car bodies will allow to reduce but still to maintain the safety of vehicles.Almost 90% of boats and ships are constructed using either carbon and glass fibre-reinforced polyester or vinyl ester resin. Such as life boats, fishing boats, sail boats, yachts and dinghies. Carbon fibre-reinforced epoxy laminates and carbon fibre-reinforced epoxy skins with either foam core or honeycomb core based sandwich laminates have been used as the structures components such as the complete hull, deck, keel, boom, mast, and other structural.

Fig. 1.14 Applications of composite in transportation and wind power (Source: http://www.diabgroup.com; http://www.bmw.com; https://www.sunseeker.com/en).

1.6 Contribution of thesis and thesis outline

This thesis is combined with experimental and numerical studies aiming to investigate the both dynamic and quasi-static performance of three categories of composite structures for application in aerospace, automotive and marine industry. A wide range of the hybrid structures studied includes plain PVC foam panels, their associated sandwich panels, graded foam based sandwich structures, composite rod and tube reinforced foam structures and fibre metal laminates (FMLs).

The dynamic response of plain foam samples, their associated sandwich panels and FMLs was characterised by determining the energy required to perforate the panels in order to experimental and numerical investigate the impact perforation resistance of those structures. The FE models were also developed to investigate the effect of oblique loading on sandwich, impact response of sandwich panels on an aqueous support and the impact response of sandwich panels subjected to a differential pressure on interior and exterior surface which is equivalent to flying at an altitude of 10000 m. The impact response of sandwich structures has been studied to evaluate the perforation resistance due to influence of core combination, arrangement, foam type and density.

The energy-absorbing characteristics of polymer foams reinforced with either carbon or glass composite rods or tubes have been investigated for use in lightweight impact-resistant sandwich structures. The rate-sensitivity of those structures has also been evaluated. The increase of the volume fraction of composite and density of foam results in a significant increase in their compressive strength and energy absorption. The specific energy absorbing capacity has been summarized for use in the material design on core structures.

A series of quasi-static and impact perforation tests on a range of fibre metal laminates plates have been carried out which suggest that FMLs based on the glass fibre/epoxy and the various aluminium alloys are not particularly rate sensitive over the range of rates considered here. Both the maximum impact force and impact perforation energy are summarized based on stacking sequences of these material systems, regardless of the thickness of the hybrid material, its constituent materials or the applied strain rate. The energies to perforate the FMLs are plotted against that required to perforate the individual constituent materials, where it has been shown that all of the experimental data appear to fall on a straight curve that can subsequently be used for estimating the perforation energies of other configurations.

This thesis is divided into seven chapters, which is summarized below as follows:

Chapter 1 introduces an overview of composite materials and structures, their applications and highlighting the objectives of this research.

Chapter 2 presents a literature review on earlier and recently studies of experimental and numerical investigations on the PVC foam sandwiches, composite reinforced foams and fibre metal laminates.

Chapter 3 describes the specimen preparation and experimental procedure of both the quasi-static and dynamic tests on the composite structures. Here, the test procedures are related to tensile, shear, three point bending, quasi-static compression and Hopkinson bar tests, as well as impact perforation and crush tests.

Chapter 4 presents experimental results and the failure mechanisms of those structures. It also evaluates the corresponding perforation resistance and energy absorbing capacity. The detailed discussion cover impact perforation results on the plain foam panels, plain foam and graded foam based sandwich structures and fibre metal laminates. The discussion also include compression and dynamic crush results on the composite rod and tube reinforced foam structures as well as evaluation of the dynamic factor due to strain-rate effects.

Chapter 5 presents the development of the numerical modelling on the constituent materials of the composite structures investigated and the finite element method to simulate the response of those structures subject to various loading conditions. The constitutive models and damage criteria employed include elastic-plasticity and crushable foam criterion for PVC foam, Johnson-Cook plasticity and damage criterion for aluminium alloys; orthotropic elasticity and 2D Hashin's and 3D modified Hashin's criteria for fibre reinforced composites.

Chapter 6 presents the modelling results and validation against the experimental data and numerical predictions obtained from the validated FE models. The modelling results reproduced the quasi-static and dynamic responses of the composite structures tested including sandwiches, composite rod and tube reinforced foams, fibre metal laminates. A series of parametric studies are undertaken to cover extra data points and to predict loading conditions that are difficult to perform such as oblique impact.

Chapter 7 presents the conclusions of this study on those structures and summarises the overall findings and recommendations for future work.

CHAPTER 2 LITERATURE REVIEW

2.1 Introduction

This chapter presents an overview of literature review of the early and current research work on the composite structures, including sandwich structures, composite reinforced foam structures and fibre metal laminates (FMLs). Firstly, the historical development and background of sandwich and FMLs are reviewed. The classification of sandwich types, core categories, designation of aluminium alloys and FMLs were given. Subsequently, a review of potential hazards on composites in aerospace applications associated with impact and blast loading is addressed. Finally, investigations of low velocity impact response and perforation resistance on those structures are reviewed, including PVC foam based structures, graded foam based sandwiches and FMLs as well as the compressive crushing response of the composite reinforced foam structures.

2.2 Overview of composite structures

Due to their excellent specific properties, composite sandwich structures are increasingly finding their uses in a wide range of lightweight load-bearing engineering structures. Sandwich structures, such as those used in high-performance aerospace components, are typically based on thin composite skins bonded to a low density foam or honeycomb core. The skins are usually thin, often rendering these lightweight panels highly susceptible to damage by a hard projectile, such as that associated with runway debris or hail (Chai and Zhu, 2011; Heimbs, 2011)

The overall mechanical response of a sandwich structure is largely dependent on the properties of the skin, the stiffness and strength properties of the core, as well as the strength of the bond between skin and core. The need to strengthen the core and control its subsequent crushing characteristics is crucial to maximising energy absorption in sandwich structures. A number of approaches have been used to develop sandwich cores with a greater compression strength and superior energy absorption characteristics, including various types of cores with combinations of various layer types and density, reinforced by z-pinning, through-the-thickness stitching, composite rods, composite tubes. There are also many multilayer composite laminates structures are one of those laminates.

2.2.1 Background and classification of sandwich

Typically, sandwich structures, such as those used in high-performance aerospace components, are based on thin composite skins bonded to honeycomb core or low density foam. Ramadan et al. (2014) reviewed the historical development of sandwich structures and cores. A plywood based sandwich construction employed in a mosquito night bomber was the first application of sandwich construction back to World War II in England. Sandwiches consisting reinforced plastic faces and a low density core was a concept of sandwich construction in the United States during the same period. Marguerre (1944) conducted a first investigation on in-plane compressive loads on sandwich panels in Germany in 1944. A honeycomb core manufacturer Hexcel Corporation was established in the 1940s to make over 50% of the world's honeycomb core materials. There were a large number of investigations and publications in the later 20^{th} century.

Morris Kaufman (1969) reviewed the history of PVC foam development in a report for chemical and industrial production of Polyvinyl, Chloride. The first patent for PVC was filed in Britain in 1912 and Germany in 1913, and limiting its marketable applications until the early 1930s. The PVC was produced by more companies around the world and the volume was increased dramatically during the 1950's. The PVC foam was manufactured by combining PVC with polyurea at the molecular level in 1970s since than it has been widely applied and developed. Those core panels are widely used as a core material for variety of light-weight sandwich structures subjected to both static and dynamic loads to absorb impact energy. Today, PVC is one of top three most used plastic for industrial applications in the world.

2.2.2 Sandwich types

Since sandwich consists of two strong thin face skins to carry the in-plain tensile and compressive stresses, the cores are requested to take a stable compressive loading without premature failure and to prevent the skins from failing as well. The overall mechanical response of a sandwich structure is largely dependent on the properties of the skin, the stiffness and strength properties of the core, as well as the strength of the bond between skin and core. The need to strengthen the core and control its subsequent crushing characteristics is crucial to maximising energy absorption in sandwich structures (Chai and Zhu, 2011). The relatively thick core is to keep the two strong thin face sheets apart at a desired distance and withstand the shear loads in the transverse direction, while the face skins carries the in-plain tensile and compressive stresses resulting from bending. The face skins sheet can be composite materials such as fibre reinforced polymers, aramid, carbon fibre reinforced composite, glass fibre reinforced composite or metallic materials such as steel or aluminium. Core materials such as honeycomb, foam, textile and corrugated cores can be divided into several categories. Ramadan et al. (2014) summarized a number of investigations of sandwich structures based on various skin materials and foam core types over decades. The low velocity impact tests on sandwich structures with various skins and core materials as combinations are shown in Table 2-1.

Table 2-1 Categories of sandwiches structures subject to low velocity impact

Core types	Skins categories	References
PVC foam	PVC, Liner, PET, PEI, PU, PMI	Hassan et al., (2012)
RPU	Glass fabrics, carbon fabrics , carbon/Kevlar hybrid fabrics , Kevlar fabrics with vinyl ester resin	Xia and Wu (2010a, 2010b)
Closed cell PVC	Glass fibre/polyester	Lendze et al. (2008)
Polyurethane PU	Woven carbon/epoxy	Hosur et al. (2008)
Closed cell (PMI)	A bidirectional carbon/epoxy	Hosur et al. (2009)
Closed-cell PVC	Woven carbon fabric/epoxy laminates	Schubel et al. (2005, 2007)
PVC,PEI, PVC/PUR	A woven glass/phenolic resin	Cantwell et al. (2008)
Aluminium	UD glass reinforced polypropylene and woven glass reinforced polypropylene	Cantwell et al. (2008)

2.2.2.1 Skins

The face skins used for sandwich structures request a super strength to carry in-plain tensile and compressive stresses resulting from loading and to prevent face fracture or perforated by an exterior loading such as projectile impact. Table 2-1 also summarizes the face skins used for the foam based sandwiches. The composite fact skins such as carbon, aramid, and glass fibre reinforced composite has been used in those studies. Metallic materials such as steel or aluminium sheet even a hybrid skin face made from novel FML-reinforced skin were used to resistance high velocity impact perforation. Villanueva and Cantwell (2004) investigated impact resistance of novel FML-reinforced skin/aluminium foam core sandwich structures using a gas gun.

2.2.2.2 Core types

The core in sandwich structures is an importance constitute to carry stable compressive loading or perforation resistance and to prevent face skins fracture in a buckling mode. The core properties decide energy absorption capacity of sandwich structures. The core can be classified based on its

material or structure, such as PVC foam, aluminium foam, honeycomb, corrugated and truss cores. The categories of core material and structes for sandwiches are shown in Table 2-2 and typical cores types are shown in Figure 2.1. The classification of cellular materials for sandwich cores was classified hierarchically based on microstructures and configurations of cellular materials, summarized by Zhu et al. (2011).The density of the most used foam cores are in the range from 40 to 200 kg/m^3 and the density of those structure cores also varies from less than 30 kg/m^3 to more than 300kg/m^3. The thicknesses of core typically vary from 5 mm to 50 mm.

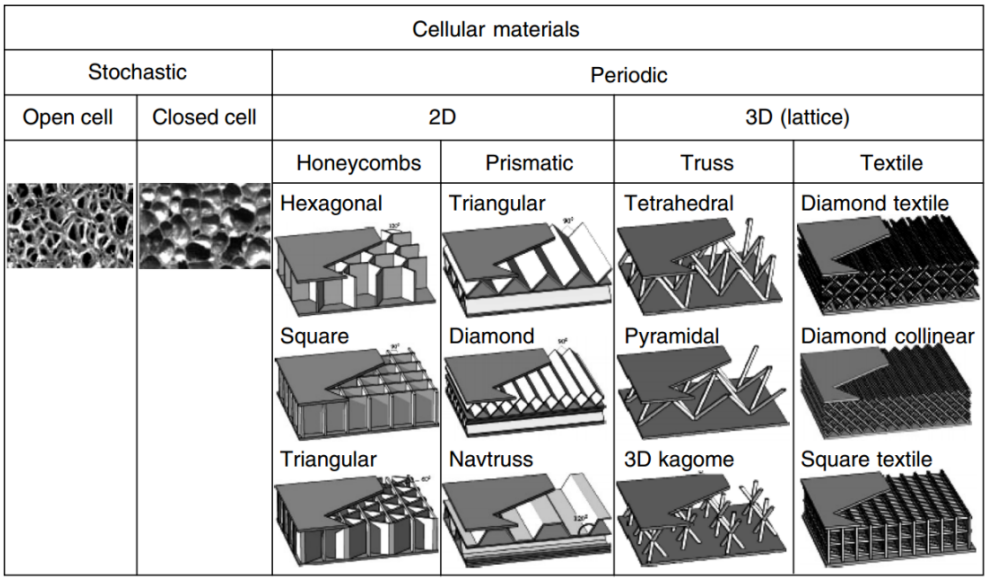

Fig. 2.1 Classification of cellular materials as cores for sandwich structures (Zhu et al., 2011).

Table 2-2 Categories of cores for sandwiches

Core types	Core material categories
PVC foam	PVC, Liner, PET, PEI, PU, PMI
Metal Foam	Open-call, closed-cell, aluminium, titanium and tantalum
Honeycombs	Hexagonal, square, trianglar
Natural fibre	Wood, balsa, bamboo
Fold	Paper fold, wood fold
Truss	Pyramidal, tetrahedral, , 3D kagome
Textile	Square textile, diamond collinear and diamond textile

2.2.2.3 Polymer foam cores

Foams are one of the most common core materials for sandwich structures. The core panels can be fabricated from various of synthetic polymers including polyvinyl chloride (PVC), polyethylene terephthalate (PET), polyetherimide (PEI), polymethacrylimide (PMI), polystyrene (PS), polyurethane (PU), polymethyl methacrylamide (acrylic) and styreneacrylonitrile (SAN). Due to the relatively low weight-specific mechanical properties and the mainly FST issues (fire, smoke, toxicity), only limited foams are used on aircraft structures in earlier years (Heimbs, 2012). However, the newly improved foam has no FST issues and more advantages have been considered in aircraft applications. Especially, recently developed reinforced foam core structures such as stitched foam core (Lascoup et al., 2010), z-pinning (Marasco *et al.*, 2006 a), and the composite reinforced foam core (Zhou et al, 2014) significantly improved crushing characteristics and higher energy absorption capacity, which led the foam core as potential use in lightweight aircraft.

AIREX® C70 is a closed cell, cross-linked polymer foam that combines high stiffness and strength to weight ratios with superior toughness. AIREX® R63 is a closed-cell, linear, thermoplastic polymer foam with extremely high damage tolerance. It is cold formable, dimensionally stable and is non-friable. AIREX® R82 is a thermoplastic rigid foam with excellent fire resistance, low smoke emissions and suitable to extremely hot or cold environments. AIREX® T92 is a thermoplastic structural rigid foam with closed cells and is suitable for lamination using all types of resins and processes Advantages of foam cores are listed as follows, (AIREX datasheet available from: http://www.airexag.ch).

- Excellent impact strength, high elongation
- High strength and stiffness to weight ratios
- High fatigue resistance
- Excellent energy absorption
- Low resin absorption
- Advantageous fire behavior, self-extinguishing
- Excellent sound absorption and thermal insulation
- Non biodegradable, non-decomposable
- Dimensionally stable

The major applications of the foam cores are:

- Aerospace (interior fittings, cockpit doors, insulating covers, radomes, low temperature tanks, helicopter rotor blades, fuselage and wing components for sporting aircraft explosion-proof freight containers
- Military (marine superstructures, antennas, communications equipment)
- Ship and boat construction (hull, bulkheads, decks, interior fittings, superstructures)
- Wind energy plants (generator casings, covers, rotor blades)
- Industrial components (containers, shelters, helmets tools, tanks, pipes, containers, covers)
- Rail and road vehicles, transport containers (roof panels, control stand, floor and ceiling components, doors, interior fittings, partition walls, side skirts, collision protection)

Hassan and Cantwell (2012) conducted a series of compression and impact tests on crosslinked PVC, a linear PVC and PET combined with thin glass fibre reinforced plastic skins based sandwich to evaluate the energy-absorbing, compression properties and strain-rate effect at quasi-static and impact rates of strain. The plastic collapse strength of the cores is highly rate-sensitive, which can be increased by up to one hundred percent in passing from quasi-static to dynamic rates of loading. A range of foam-based sandwich structures with multiple layer skins were investigated and shown that the perforation resistances out-perform the systems with monolithic skins and conventional GFRP/aluminium honeycomb sandwich structures.

2.2.2.4 Honeycomb

Honeycombs is used as a light weight sandwiched core structure based on series of cells, nested together to form structures similar in appearance to the cross-sectional slice of a beehive. A honeycomb offers 90 to 99 percent open space structure in its expanded form. Honeycomb structures can be produced from variety of different materials, such as aluminium, Nomex, or thermoplastics like polypropylene (Heimbs 2012). Hexagonal honeycomb structures are most widely used as sandwich core structures. Due to excellent mechanical performance and light weight, it has been used in numerous aircraft applications. One of the cases is that about 4000 m² of honeycomb was used in Airbus A380 in its structural design. Heimbs (2012) also reported specific energy absorption values of a number of aluminium honeycomb based core structures. A number of investigations were

conducted on honeycomb core based sandwiches. The experimental tests includes honeycomb core and woven glass vinylester skins based sandwiches by Mines et. al. (1998), aluminium honeycomb cores and glass/phenolic sandwich structures by Nettles and Hodge (1990) as well as a honeycomb core and carbon/epoxy and glass/epoxy facesheets based sandwiches by Park et al. (2008).

2.2.2.5 Foldcore

Folded cores are produced as three-dimensional cellular structures from a flat sheet of material by a folding process, such as in an origami-like manner. Folded cores offer a large design space for tailored properties, since various cores can be made of any of foldable materials (i.e. metal sheet, CFRP, CFRP laminates, papers, nature fibre sheet) and the geometry of unit cell can be designed according to the specific mechanical requirements.

Zuhri et al. (2014) investigated the compression properties of triangular and square honeycomb structures made of core materials based on co-mingled flax fibre reinforced polylactide (PLA) and polypropylene (PP) polymers. The strength and specific energy absorption characteristics of a range of triangular and square honeycomb structures were determined under quasi-static compression tests. It was shown that the energy-absorbing characteristics and compression strength of the square honeycomb cores out-performed the triangular counterparts and the PLA-based structures was associated relatively low failure strain due to poorer mechanical properties.

2.2.2.6 Balsa wood core

Balsa wood is a nature fibre reinforcement providing excellent stiffness to weight ratio, extremely high level of rigidity and excellent laminate adhesion properties. It is a renewable resource as a core material for sandwich. It is furthermore resistant to temperature changes, fire and chemicals after proper treatments. Besides being lightweight and environmentally compatible, the wood veneer based core panel offers the possibility to obtain its unique mechanical properties through the optimum alignment of various veneer layers and the integration of other materials. BALTEK® VBC is a structural core material based on balsa wood veneer. BANOVA® PLY is a lightweight plywood consisting of adhesively bonded balsa veneers. Both types of balsa wood are supplied by AIREX as renewable environmental friendly core materials.

Umer et al (2014) investigated energy-absorbing characteristics of a range of lightweight bamboo-reinforced foams as a natural environmentally friendly core material. Compression crushing tests on both individual bamboo tubes and tubes embedded in crosslinked PVC foams were carried out. It is noted that specific energy absorption of the bamboo tubes is increased significantly by means of wrapping procedure in order to reduce longitudinal splitting during compression. It also demonstrated bamboo tubes embedded higher density foams resulting in efficient support to the tubes and greater increases in SEA.

2.2.2.7 Other cellular structures

A number of other cellular structures for energy-absorption purposes have been used to develop innovative cellular structures in the aircraft applications, which are based on corrugated cores, metallic hollow spheres, metallic lattice core structures, natural fibre cores or selective laser melting (SLM) lattice cores.

Rejab and Cantwell (2012) investigated a range of triangular corrugation structures made from a glass fibre reinforced plastic (GFRP), a carbon fibre reinforced plastic (CFRP) and an aluminium alloy (AL) subjected to low velocity compression loading. The influence of unit cells, the thickness of the cell walls and the width in determining the mechanical behaviour and specific energy absorption of the sandwich structures was investigated. The dynamic test showed that dynamic strength enhancement factor increased for all the corrugation cores. It is also evident that both the specific strength and specific energy-absorbing characteristics of the structures are improved significantly using foam filling the composite corrugation systems. The increase in values of SEA for the foam filled GFRP and the CFRP systems were up to 160% and 105% respectively.

Alia et al. (2014) conducted a compression and blast test to investigate the energy-absorbing characteristics of polymer foams reinforced with small carbon fibre reinforced epoxy tubes. The influences of both foam density and tube arrangement on the crush behaviour of these lightweight core structures were established. It has been shown that specific energy absorption values of carbon tube reinforced out-perform the polymer honeycombs, aluminium honeycombs and metal foams.

Zupan et al. (2003) conducted uniaxial compression tests on aluminium egg-box panels to compare

the collapse strength and energy absorption. The tests showed that the performance of core structures was influenced by level of in-plane constraint and collapse failure in plastic buckling.

Smith et al (2013) carried out compressive tests on two truss lattice based on body-centred cubic (BCC) structures to investigate the yield strength and energy absorption of the lightweight lattice core structures. Experimental validation has shown that the improvement of potential SLM-built lattices achieved by reducing the unit cell aspect ratio.

Altenaiji et al. (2014) undertook a series of drop-weight impact tests on aluminium matrix syntactic foams made with different proportions of aluminium matrix and ceramic particles to investigate the energy-absorbing capability and effect of strain-rate on their compressive behaviour using drop weight impact. It has found Al7075-T with 250–500 μm ceramic microspheres is the best combination, which achieved the highest strength and the specific energy absorptions up to 55.3 kJ/kg at strain-rates 204 1/s. It has shown that the plateau stresses for those aluminium matrix syntactic foams increased by 20–30% from quasi-static to dynamic compression loading.

2.2.3 Energy-absorbing capacities of core structures

The performance of energy absorption capacity of lightweight sturcutces is usually evaluated using a specific energy absorption value in kJ/kg to compare the energy absorption to weight ratio. The absorbed energy is deterimined by the area under the load-displacement traces as a result of a compression or a tensile test of absorber material or structure. A typicl load-displacement trace of compression test on honeycomb core is shown in Figure 2.2 (Chai and Zhu, 2011)

The compressive stress of the core increases linearly up to the first peak stress before a resistance stress drops, consequently a constant plateau stress is associated to core crushing and a final state stress increases significant with core densification. The figure shows an ideal energy-absorbing core or structure to achieve a load-displacement trace associated with a constant plateau stress level to allow the maximum area under the curve.

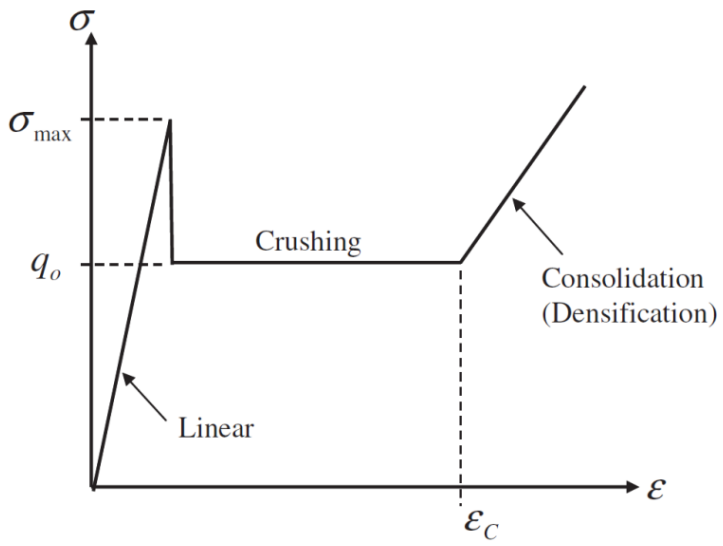

Fig. 2.2 Typical stress–strain relationship for bare honeycomb. (Chai and Zhu, 2011)

A number of experimental tests have been carried out to evaluate the specific energy absorption of sandwiches core. Based on the investigations of energy absorption capacity of those core structures mentioned, the energy-absorbing features are summarized in Table 2-3. Here, a widely range of core structures are compared with each other, which include aluminium foam core, honeycomb, foldcore, tube reinforced cores, corrugated-cores, truss and lattices structures. The specific energy absorption values of various types of core structures are compared here. The measured values of specific energy

absorption (SEA) on plain PVC foam range between 2-15 kJ/kg, however, composite tube embedded foam systems with an enhanced SEA value vary between 17.7 and 155 kJ/kg.

Table 2-3 Energy-absorbing capacity of core structures

Core types	Density (kg/m^3)	SEA (kJ/kg)	Reference
PVC, PET, Linear Foam	40-200	8-15	Hassan et al. (2012)
PMI foam, PVC foam	52–250	11–18	Heimbs (2012)
PI/PU/PE foam	69.2-104.2	2-9	Heimbs (2012)
Aluminium foam	n/a	12.3-28.5	Altenaiji et al. (2014)
Aluminium foam	270 -313	4.98- 5.5	Ochelski et al, (2012)
Aluminium matrix syntactic foam	1640	50.6	Tao and Zhao (2009)
Aluminium honeycomb	27–192	9–45	Heimbs (2012)
Nature fibre honeycomb	0.1-0.4	0.6-6.5	Zuhri et al.(2014)
Chiral CFRP honeycomb	n/a	96.5	Airoldi et al. (2012)
Polypropylene honeycomb	40	3.1	Alia et al. (2014)
Bamboo tube foam core	40-200	19-53	Umer et al, (2014)
CFRP tubes embedded PVC foam	40-280	21-155	Alia et al. (2014)
CFRP tubes embedded in PS foam	107.8	86	Heimbs (2012)
GFRP tubes supported by PS foam	n/a	17.7–32.6	Tarlochan et al. (2012)
Corrugated-cores	205-363	31.5-63.5	Ruzaimi and Cantwell (2013)
Carbon foldcore	103–114	4.5–22.5	Heimbs (2012)
Kevlar foldcore	48–113	2–7.5	Heimbs (2012)
Nomex	29–48	8–18	Heimbs (2012)
Lattice structure	3.5-13.9	0.6-6.4	Smith et al. (2011)
Composite pyramidal truss cores	20-35	0.75-8	Xiong et al. (2012)

2.2.4 Background and classification of FMLs

Fibre metal laminates (FMLs) are hybrid composite structures consisted of a number of thin sheets of metal alloys and composite plies of fibre reinforced polymeric materials. The first fibre metal laminate was introduced in 1978, known as ARALL (Aramid Reinforced Aluminium Laminate), using aluminium alloys and high strength aramid fibre bonded with adhesive layers in order to improve the fatigue behaviour at the National Aerospace Laboratory and at the Delft University of Technology in the Netherland (Villanueva and Cantwell, 2004). Four different types of standardized ARALL were introduced by the Alcoa Company in 1984. About 20% of weight saving was achieved by using ARALL instead of monolithic aluminium. The first application of ARALL was cargo doors in C17. The other major applications of fibre metal laminations in aviation industry were introduced by Straznicky et al. (2000). Following, the CARALL (Carbon Reinforced Aluminium Laminate) Laminates which consists carbon fibres was investigated. However, flight-simulation fatigue tests shown that lower fatigue resistance of CARALL due to limited failure strain of the carbon fibres. In 1990, another improved development was to introduce GLARE (Glass Laminate Aluminium Reinforced Epoxy) laminates, which consists of high strength glass fibre instead of aramid fibres with production operated commercially in 1992. Finally, a new concept of ARALL & GLARE fibre metal laminates, the Spliced Laminates, was launched by the Structural Laminates Company (SLC) in 1992 (Asundi and Choi, 1997). Tamer Sinmazcelik et al. (2011) reviewed investigations on historical development, advantages, disadvantages, production and applications of FMLs in aerospace applications.

Aluminium alloys have been used in primary structural materials and components as a mature application on both commercial and military aircraft over 80 years. Figure 2.3 shows the percentage of usage of aluminium and composites in several types of Boeing aircraft. Although the usage of composites is being increased from Boeing 747 to the latest Boeing 787, the volume fraction of aluminium over 70%, which still the most used material in the current operation aircraft Boeing 747, 757, 767 and 777 (Warren, 2004). Although composites show superior mechanical properties when compared to aluminium alloys, such as higher specific stiffness, specific strength, fatigue and corrosion resistance, their disadvantages (i.e. relatively low impact resistance, high certification and production costs, and complex manufacturing) make fibre metal laminates such as GLARE

(combines aluminium layers with glass fibre epoxy) are still alternative material systems for designers on current aircraft. They are widely used in aerospace industry, due to their excellent mechanical behaviour, easy design, sophisticated manufacturing processes, fault detection techniques and advantages of repair, recycling and joints (Dursun and Soutis, 2014).

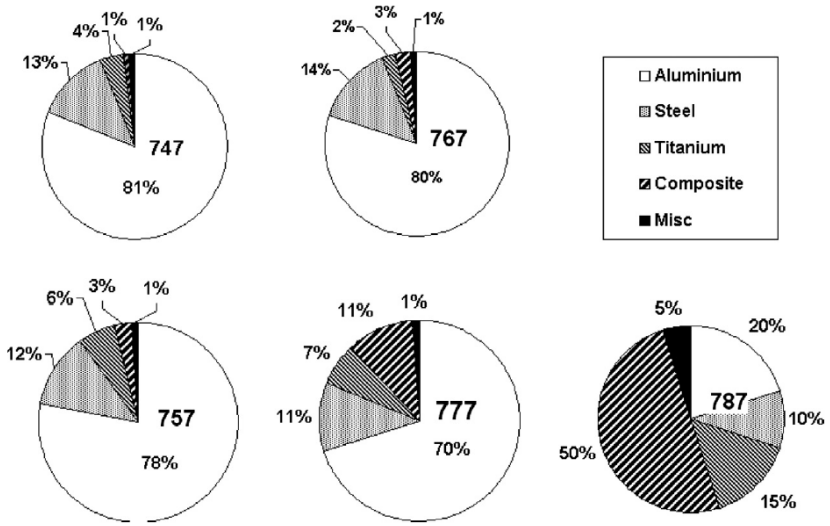

Fig. 2.3 Combination of materials used in Boeing Aircrafts (Warren, 2004).

2.2.5 Classification of FMLs

The metals currently used in FMLs include aluminium, titanium or magnesium, and the fibre-reinforced layer is either a glass or carbon or Kevlar fibre reinforced composite. The classification of FML is given in Figure 2.4, based on constituent materials of metal and fibre reinforced plies (Vogelesang and Vlot, 2000). Commercially available FMLs are GLARE, which is based on high strength glass fibres, ARALL on aramid fibres and CARALL on carbon fibres. It has been standardized in aircraft industry for high-performance, lightweight structures, i.e. the trades ARALL 1 is variant with aluminium 7075 layers and ARALL 2 uses aluminium 2024 layers (Botelho et al., 2006). The configurations and outperforming characteristics of commercially available GLARE and ARALL laminates were summarized by Chai and Manikandan (2014).

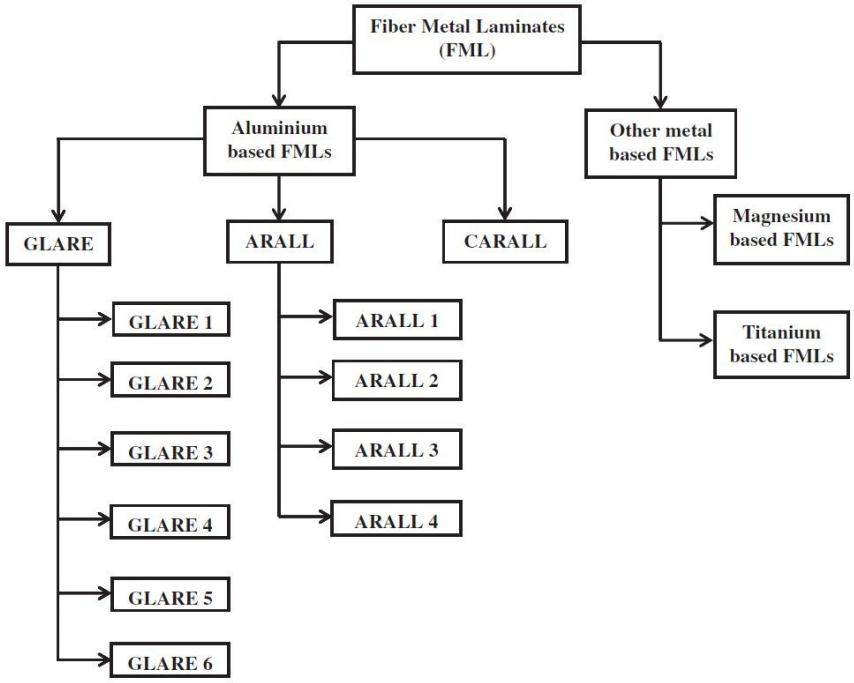

Fig. 2.4 Classification of FML based on metal plies (Chai and Manikandan, 2014)

2.2.6 Classification and temper designation of aluminium alloys

Aluminium alloys are classified depending on the fabrication process, chemical composition and the heat treatment. The classification groups alluminium alloys into different families to exhibit detailed mechanical and technological characteristics. The designation is established and shown in Table 2-4 (Mazzolani, 1985).

Table 2-4 Designation of aluminium alloys

Series designation	Major alloying elements
1XX.X	Aluminium (99.00% pure), can be work hardened.
2XX.X	Copper
3XX.X	Silicon, with additions of copper, magnesium
4XX.X	Silicon, also known as silumin.
5XX.X	Magnesium
6XX.X	Magnesium and silicon. easy to machine, are weldable unused series of numbers
7XX.X	Zinc, hardened to the highest strengths
8XX.X	Tin, other elements which are not covered

The type of designation is designated by a four digit number that may be preceded or followed by letters. The initial digit of 1 denotes that the aluminium content is greater than 99 percent. The initial digitals from 2 to 8 indicates the other alloys content of the main alloying element. The second digit denotes alloy modifications of an already existing alloy. In the first group, the third and fourth digits represent the percentage of aluminium above 99 percent. The figure represents the level of impurities. It is equal to 0 if the impurities are uncontrolled, and it can vary between 1 and 9 depends on the impurity content. In the other group, the second figure is equal to zero for the main alloy and varies between 1 and 9 for its modifications. The third and fourth digits are designated for different meanings to identify the specific alloy within each group. A suffix "A" denotes a national variation of the alloy, e.g. EN AW-6005A. The other content of alloy elements and heat conditions in each series are shown in Figure 2.5 graphically (Aluminium matter).

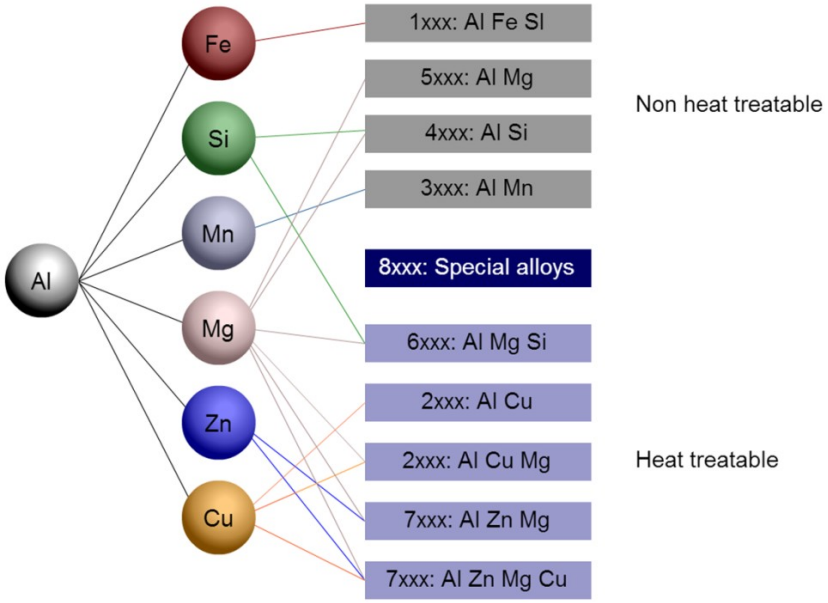

Fig. 2.5 Designation and major elements of aliminium alloy classification. (Source: http://aluminium.matter.org.uk)

The temper designation follows the cast or wrought designation number with a dash, a letter, and potentially a one to three digit number, e.g. 6061-O. The following definitions for the tempers are defined by the Aluminium Association. Table 2-5 shows the temper code and typical temper designation of aluminium alloys (Mazzolani, 1985).

Table 2-5 Heat treatment temper of aluminium alloys

Designation	Temper designation
- F	As fabricated
- O	Annealed state, the lowest strength, highest ductility
- H	Work-hardened state
- W	Solution heat treated only
- T	Heat treated to produce stable tempers
-T1	Cooled from hot working and naturally aged
-T2	Cooled from hot working, cold-worked, and naturally aged
-T3	Solution heat treated and cold worked
-T4	Solution heat treated and naturally aged
-T5	Cooled from hot working and artificially aged
-T6	Solution heat treated and artificially aged
-T651	Solution stress-relieved stretched and artificially aged.

Friction Stir Welding technology was introduced as an alternative way for joining techniques, after the invention of Friction Stir Welding (FSW) in 1991. The FSW joining technique led weldability of aluminium alloys coves all range of aluminium, including 2000 and 7000 series alloys being able to be welded. More types of joints such as lap joints and fillet joints can also be welded by FSW (Nandan et al, 2008). The advantages of joining techniques and weldability of various aluminium alloys also remain attractive for aluminium alloys used in the airframe construction and compete with composite. Research is continuously activated through the design and control of chemical compositions, and heat treatments in order to improve the static strength, fatigue, fracture toughness and corrosion resistance. High strength Al-Li and Al-Zn alloys, damage tolerant Al-Li and Al-Cu alloys are developed through the ratio control of chemical composition and effective heat treatments. For examples, a new generation of advanced Al-Cu-Li alloy 2050 was developed aiming to replace the 2000 series and 7000 series alloys (Kalyanam et al. 2009). A new generation of high strength thick plate alloy AA7040, AA7140 and AA7085 were developed as alternatives of 7050/7010. The high strength products improved damage tolerance by modifications in Zn/Mg/Cu ratios and solute

content. These products were selected for wing spar applications on the Airbus A380 (Chen et al. 2012).

2.3 Background and potential hazard on composite in aerospace applications

2.3.1 Background of potential hazard

A number of investigations have focused on the potential hazard resulting from an exterior or interior uncontained impact of an aircraft such as turbine engine failure. Heimbs (2011, 2012) reported the potential hazard of a aircraft from such impact, i.e. the blade off of an engine fan, rim release of a wheel rim fragment and tire rubber impact after wheel failure. The exterior impacts are usually from runway debris and stones, hail and ice, hydrodynamic ram and bird strike. Bird strike caused about 90% of all impact incidences apart from other damages by runway debris, hail or tire or wheel debris. The Federal Aviation Administration (FAA) reported that almost 90,000 bird strikes happened on commercial aircraft and over 243 aircraft were destroyed during 1990 to 2013 (Dolbeer et al., 2013; Meguid et al., 2008). Bird strike already causes a major structural damage as a serious threat of aircraft structures. A number of research reports investigated bird strike on all forward facing components on airplane, rotorcraft and helicopters, such as the forward fuselage skin, radome, window frame, the windshield, the leading edges of the wings and empennage and as well as engine fan blades and inlet of a aircrafts, as shown in Figure 2.6. The forward fuselage structure, windshield and rotor blades of helicopters are requested to resist impact by bird strike as well.

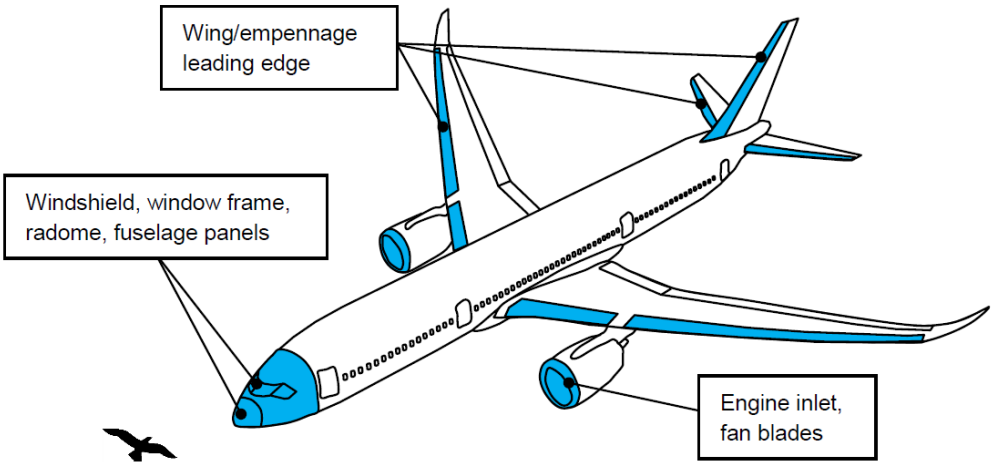

Fig. 2.6 Illustration of aircraft components exposed to the risk of bird strike (Heimbs, 2012)

Impact caused by the interior debris such rim release of a wheel rim fragment and tire rubber impact after wheel failure as well as the blade off of an engine fan blade was investigated.

Perez et al (2011) reported that hail impact velocity up to 300 m/s would lead to serious damage during flight. Impact resistance needs to be considered in structural design to against hail impact and prevents a serious damage on flying aircraft. The ice fragments released from a propeller of rotorcraft has the similar impact hazard as hail impact.

Heimbs (2012a, 2012b) reported that a debris impact from failed rubber tire is equal to a projectile mass of 2.45kg at velocity of 64 m/s, which may lead to an impact with a 5 kJ kinetic energy. The energy is partly absorbed by the rubber itself resulting of the hyperelastic behaviour of rubber with elastic deformation to store strain energy during the impact. However, the impact caused by a rim fragment of failure wheel may be significant amount of energies as the rigid aircraft wheels normally made from forged aluminium alloy (i.e. 2014-T6, 2040-T6 or 7050-T74). The wheel fragments are propelled with high energy over 8 kJ by assuming a wheel rim resulting from a mass of 1.68 kg at an impact velocity of 100 m/s due to wheel failure. The rim fracture occurs at weakest area of wheels flange due to high-cycle fatigue loading during take-off and landing, corrosion and braking.

Saucray (2011) investigated the hazard from blade-off of an engine fan and rotor engines. The impact energy of 180 kJ caused by a typical blade mass of 2.72 kg at a velocity of 366 m/s. In order to prevent or slow down the impact perforation and penetration, an engine containment typically consists of several energy-absorbing layers made of Kevlar or aluminium to avoid this hazard. The threats have been concerned due to the rotated blade mounted at the fuselage without any protective containment, which request a high capacity of energy-absorbing structures to protect the fuselage.

Due to the potential hazard in aircraft operations, the aviation authorities have concerned on the potential hazard resulting from outer parts of an aircraft or an uncontained turbine engine failure. Bird strike is a typical example has been evaluated by such regulations. For example, the certification criteria have required that aircraft should be able to continue safe flight and landing in situation of a medium birds impacting on gas turbine engines, the wing leading edges and the empennage leading edge at operational speed. Most of impact energy is absorbed by deformation of the structures, i.e. leading edge, in terms of composite material damage, core crushing and metal plasticity during impact. Therefore, the energy-absorbing capacity of components was requested to be evaluated by SEA value through specific impact or compressive crushing tests. The aviation

authorities, such as Federal Aviation Regulations (FAR), European Joint Aviation Regulations (JAR) and the Certification Specifications (CS) of the European Aviation Safety Agency (EASA) have required that all forward facing components of aircraft must to be proved at a certain certification approval level of bird strike resistance before in commercial operation (Heimbs, 2012).

2.3.2 Potential hazards associate with impact loading

Shochey et al. (1997) reported the hazards from aircraft turbine engine failure and aircraft fragments which jeopardize the aircraft to land safely due to failure of disrupt control or propulsion system. The investigation aims to enhance the survivability of commercial aircraft by protecting components of the aircraft to continue flight and landing safely in the event of uncontained turbine engine failure. Lee et al. (1997) reported an uncontained engine failure of rotating components in a turbine engine aircraft to be considered as a safety hazard to the aircraft itself. The investigation focused on lightweight materials to be considered for potential use in helicopter turbine engine rotor containment structures. The lightweight materials was identified and evaluated in the report, which could provide suitable containment and isolation from the failure hazard of small turbine engine rotor in worst case in order to minimum the hazard to the aircraft. Kermanidis et al (2005) reported that energy absorption is contributed mainly by structural deformation of the composite, metallic or hybrid leading edge during the bird impact on a leading edge of empennage or wing. A specified bird mass of 1.8-3.6 kg cause kinetic energies of 30 – 60 kJ at a strike velocity of approximately 180 m/s. Therefore, the EU project CRAHVI developed an absorber concept known as ‘tensor skin concept’ which is based on a unfolding and stretching of Dyneema plies and the structures are folded and embedded among carrying laminates. Hanssen et al (2006) investigated a cellular cores based structure using aluminium foam core as energy-absorbing cellular cores in order to improve sandwich panels as a lighter solution.

Olmi Franco and Nascimento (1999) developed a model to simulate the response of the rotor blade fragment impact on an airplane structure using the MSC/DYTRAN. The numerical model was developed to simulate the high velocity fragments impact in aircraft structures such as the fuselage region, in event of rotor engine failures. The model employs Johnson-cook constitutive law to take consider the effects of strain rate on aluminium and the simulation validated with experimental data.

Rouse et al Marshall (1997) presented a combined experimental and analytical investigation on composite sandwich fuselage side panel in order to reduce structural weight of a transport aircraft. The research indicates that the sandwich panel with two-frame and three-frame configurations has been evaluated with internal pressure loads and satisfied the desired requirements. The performance suggests that frame spacing of the sandwich structural can be greater than the usual width with minimum weight.

2.3.3 Potential hazards associate with blast loading

The potential hazard associated with blast loading including internal blast, such as explosive bombing by a terrorist attacks in a commercial aircraft or external blast by a explosive warhead or air pressure on military aircraft, were taken into consideration of structure degisn for aircraft. Heimbs (2012) reported the investigation progress that blast-mitigating structures were introduced to against blast loading on aircraft since first bombing threat in the 1950s. There is increasing concern relating to the possibility blast loading on aircraft structures with the increased risk of subversive activity. Hardening measures and protective linings were implemented into the main fuselage to perfect against explosive loading on blast-resistant sandwich panels (Zangani et al. 2010). Fleischer (1996) invegistated blast resistance of FMLs and indicated that aircraft luggage containers based on the fibre-metal laminate construction are capable of absorbing blast loading comparable to the loading responsible for destroying the Lockerbie plane. Wang et al (2009) invesitigated blast resistance of stepwise graded cores based sandwich composites. Mouritz (2001) investigated the blast resistance of stitched glass fibre reinforced vinylester laminates and showed that the reinforcement through thickness was an effective way to perfect against explosive blast loading. Franz et al, (2002) investigated the response of chopped strand mat (CSM) laminates to air blasts and observed that debonding, matrix cracking, and penetration were increased with increasing impulse. It was also shown that the threshold impulse of matrix cracking increased with increas of target areal density.

2.4 Review of impact response of composite structures

The investigation on the low velocity impact response of composite structures, including foam based sandwiches, graded foam based sandwiches, composite pins and tuber reinforced foam core and fibre metal laminates, are reviewed in this section.

2.4.1 Plain foam based sandwiches

Extensive experimental research has been undertaken to investigate the response of sandwich structures to localised impact loading and much of this work has been summarised in detailed reviews on the topic by Abrate (1997) and Chai and Zhu (2011). Mines *et al.* (1998) investigated the low velocity impact response of glass fibre/vinyl ester sandwich panels based on both aluminium honeycomb and Coremat cores. Their findings showed that the energy-absorbing capacity of the sandwich panels increased with the loading rate, this being due to strain rate effects in the core crush stress and the skin failure stress. Reyes and Cantwell (2004) conducted high velocity impact tests on sandwich panels based on fibre-metal laminate skins and an aluminium foam core and noted that the introduction of metal layers into the composite skins increased the specific perforation energy of the sandwich panels by over twenty percent. Zhou and Hill (2007) investigated the parameters affecting damage development and energy absorption in sandwich panels subjected to localised impact loading. They argued that changing the skin thickness not only changed the flexural rigidity of the panels, but also changed the mechanisms of load transfer between the upper and lower skins. This in turn influenced the development of damage within the structure.

A number of workers have attempted to model the impact response of sandwich structures using finite element methods. Lee *et al.* (1993) used a refined formulation of a composite sandwich panel to study the impact response of a sandwich plate. In their study, the face skins were modelled as two separate Mindlin plates, and the core was considered to offer both normal and shear stiffnesses. Good agreement was obtained between the predicted and measured impact responses. Yang and Qiao (2005) used a higher-order impact model to simulate the dynamic response of sandwich beams based on soft cores. They investigated the effects of impactor mass, initial velocity, core depth and core stiffness on the impact response of the beams and showed that varying the core depth had a significant influence of the impact response of the structure. Palazotto *et al*. (2000) used a

displacement-based, plate bending finite element analysis to model impact damage in sandwich plates based on a Nomex honecomb core. A comparison with low velocity impact and quasi-static indentation data highlighted the model's ability to predict important features in the behaviour of the sandwich panels. Atkay et al. (2008) used the finite element package PAM-CRASH to predict impact damage in sandwich panels based on both PEI foam and Nomex honeycomb cores and showed that the model was capable of reproducing the physical behaviour of the two types of structure. Zhou *et al.* (2012) investigated perforation failure in foam-based sandwich panels using the finite element analysis technique. The FE analysis accurately predicted the impact load-displacement responses and the perforation energies of both the plain foams and the sandwich panels.

Few attempts have been made to investigate the perforation behaviour of sandwich structures subjected to impact loading. Lin and Hoo (2005) developed an analytical model to predict the low velocity impact response of glass/epoxy-aluminium honeycomb panels. A three-stage perforation model was used that considered failure of the top composite skin, the honeycomb core and the lowermost composite skin. The perforation model was used to predicted the perforation velocity of the panel under low velocity impact conditions. Buitrago *et al.* (2010) used finite element techniques to model the process of impact perforation in sandwich panels based on carbon fibre/epoxy skins and an aluminium honeycomb core. They showed that most of the incident energy of the projectile was absorbed by the 2 mm thick composite skins, with the core absorbing between ten and twenty percent of the impact energy.

2.4.2 Graded foam based sandwiches

Although extensive research work has been undertaken to investigate the response of plain foam based sandwich structures, only a limited number of numerical studies have been undertaken to investigate the dynamic response of functionally-graded foam core based sandwich structures. Cui *et al.* (2009) proposed a functionally-graded foam model and investigated its energy-absorbing characteristics using the finite element method. It was shown that functionally-graded foams are superior in their energy-absorbing capability than plain foams and that convex gradients perform better than concave systems. It was found that the performance of such foams could be further improved if the density difference between each layer was increased. Other studies have investigated

functionally-graded foam sandwich beams subjected to various forms of dynamic loading (Gardber *et al*, 2012; Wang *et al*, 2009; Rahmani *et al*, 2010; Hohe *et al*, 2012).

Theoretical analyses and numerical modelling studies have also been undertaken on various functionally-graded sandwich structures subjected to static and dynamic loading. This includes continuously, piece-wise, layer-wise and exponentially functionally-graded cores. Etemadi *et al* (2009) developed a 3-D finite element model to simulate sandwich panels with functionally-graded cores subjected to low velocity impact loading. Using validated models, they studied the effect of varying the projectile velocity and kinetic energy, as well as the influence of beam dimensions on the impact behaviour and associated indentation and displacement histories. Avila (2007) developed a failure criterion to model piece-wise functionally-graded sandwich composites and successfully predicted the failure mechanisms that were obtained in the experimental data. The most impressive performance was exhibited by a beam configuration in which the highest density core was located directly below the upper face-sheet. Sburlati (2012) presented an elastic bending analysis for circular sandwich panels with exponentially-graded material cores. The solutions, associated sensitivity analyses, highlighted the advantages of graded cores in reducing interfacial stresses, thereby decreasing the likelihood of failure. An axisymmetric bending and stress analysis was also performed on circular functionally-graded sandwich plates subjected to transversely-distributed loads (Alipour and Shariyat, 2012). Comparisons with numerical results showed that even for thick sandwich plates with soft cores, the accuracy of the results was comparable to predictions offered by three dimensional elasticity theory. Icardi and Ferero (2009) attempted to optimise the performance of sandwich panels with functionally-graded core and faces. In their study, the distribution of properties through the thickness (core) and in-plane (face sheets) that minimise the interlaminar stresses at the interface with the core were determined. Although considerable work has been undertaken to study the impact and blast response of sandwich beams and panels, few experimental and numerical works have been made to investigate the perforation behaviour of graded foam core based sandwich structures subject to low velocity impact.

2.4.3 Z-pin and rod reinforced foam sandwiches

Due to relatively low specific energy absorption of foam core based sandwiches, it expects the foam core can be reinforced with composite in order to achieve a higher specific energy absorption. A concept has been developed to use foam cores reinforced with fibres, pins, rods or tubes to enhance and withstands the compression and shear loads in the transverse direction. Fibre-reinforced composite are being widely used in a broad range of load-bearing engineering applications, due to their excellent specific strength and stiffness properties, attractive fatigue properties and superior corrosion resistance. A newly developed sandwich concept is a sandwich or core reinforced with composite fibre, z-pinning, through-the-thickness stitching and the composite rods and tubes. The reinforced foam cores are significantly superior over the plain foams, which are be able to takes a stable compressive loading without premature failure to prevent the thin skins failing in a wrinkling and buckling mode, as well as to absorb a higher energy (Alia *et al,* 2014; Zhou *et al*, 2014). As composite rods are based on simple cylindrical rods widely available in markets, the rods reinforced sandwich structures offer a number of potential benefits, including a relative ease of fabrication of complex structures, superior energy-absorbing characteristics and a relatively low cost. As a concept of composite reinforced sandwiches, it is attractive to compare with the structures of z-pinning and stitching methods.

Extensive research has been undertaken to investigate the effect of z-pinning on the compression properties of composite materials. Mahfuz *et al.* (1999) investigated the low velocity impact response of sandwich structures based on foam cores reinforced with titanium pins. For the energy levels considered, they showed that reinforcing the foam with z-pins served to constrain the level of impact damage within the test samples. Zhang *et al.* (2003) investigated the effect of z-pinning on the low velocity impact resistance of composites and observed reductions in the level of damage of between 19 and 64%, depending on the impact energy level and laminate thickness. Childress and Freitas (1992) observed reductions of up to 50% in the level of damage sustained following hailstone impacts on z-pinned laminates. The authors showed that reduction in damage was associated with increased bridging traction forces, which in turn increased the delamination resistance of the composite. Research on z-pinned sandwich structures subjected to shock loading is relatively limited,

however, Z-directional pins were used to modify the core and improve overall response of sandwich structures under high strain rate impact loading (Vaidya, 2001). A large number of investigations and research progress on z-pins reinforced polymer composite laminates were reviewed by Mouritz (2007). The research work, including manufacturing, microstructure, mechanical properties, delamination resistance and damage tolerance of the z-pins reinforced composite structures, was summarized. Both the benefits and disadvantages were addressed.

A number of studies have been undertaken on stitched sandwich structures subjected to bending, shear and compressive loads. Raju and Tomblin (1999) investigated the energy absorption characteristics of sandwich panels containing through-thickness stitches, subjected to edgewise compression. The static crush tests showed that the average crush load increased with reducing stitch spacing, resulting in an increase in the total energy absorbed. The effect of stitch density and thread thickness on damage progression and failure in stitched composites subjected to out-of-plane loading were investigated by Tan *et al.* (2013). The impact resistance of foam-based sandwich structures can also be enhanced by through-thickness stitching. Novel stitch-bonded sandwich composite structures have been developed using a closed cell core and a woven broadcloth, and then subjected to increasing impact loads (Potluri, 2003). Lascoup *et al.* (2010) evaluated the low velocity impact resistance of sandwich structures based on a stitched foam core and glass fibre face-sheets. They found that the impact resistance of the sandwich structure was greatly improved by the presence of the stitches, with the global impact behaviour being influenced by the principal stitching parameters. Fan and Wu (2010) also studied the impact response of sandwich structures with through-thickness stitching. Compared to the unstitched samples, they showed that the maximum cracking width of the stitched samples decreased by 67% following a 25 Joule impact. Guan *et al*. (2014) modelled the blast resistance of sandwich panels based on three-dimensional woven S-glass/epoxy skins and a crosslinked PVC core using finite element techniques to investigate the effect of through-the-thickness stitching on the panels. The finite element model accurately predicted the failure modes and deformed shapes of the sandwich panels over the range of impulsive loading conditions.

There is limited work on investigating the energy absorption capability of foam cores with

embedded composite pins or rods. Cartie and Fleck (2003) investigated the effect of pin reinforcement on the through-thickness compressive strength of foam-cored sandwich panels. In their study, titanium and carbon fibre pins were inserted into a polymethacrylimide foam core in a sandwich panel, with carbon fibre face sheets, to enhance the through-thickness strength characteristics. It was shown that the foam core served to stabilise the pins against elastic buckling. In addition, the authors demonstrated that the core offered strength and energy absorption characteristics that exceeded the individual contributions from the foam and the unsupported pins. Marasco *et al.* (2006) measured the out-of-plane mechanical properties of two Z-pinned PMI foam sandwich panels, reinforced with carbon fibre pins. It was observed that out-of-plane shear failure occurred mainly at the core-face interface. Mouritz (2006) investigated the influence of volume fractions and pin sizes on the compressive behaviour of Z-pinned PMI core sandwich panels. It was found that the both modulus and strength of the sandwich structures increased with increasing pin volume fraction for a fixed pin diameter. Zhou *et al* (2014) investigated the progress failure of glass and carbon fibre rods subjected to compression. The specific energy absorption capability of 20 mm thick glass and carbon fibre rod reinforced PVC foams has been evaluated. Clearly, the energy absorption could be maximized if buckling failure of rods could be avoided by constraints of PVC foam. Furthermore, compressive tests were undertaken on glass and carbon fibre rods with nominal diameters of 2, 3 and 4 mm embedded in PVC foam with densities ranging from 40 to 200 kg/m^3. This investigation filled the gap of composite systems in millimeter scale between micro system in z-pinning diameter form 0.01 to 0.5 mm and macro system of tube diameter from 8 to 64 mm.

2.4.4 Tube reinforced foam sandwiches

2.4.4.1 Experimental test on tubes

Carbon or glass fibre reinforced tubes are currently finding increasing use in a wide range of high-performance engineering structures for energy-absorbing applications. An extra attractive feature of these lightweight materials is their ability to absorb significant energy under certain well-defined loading conditions. Extensive testing has shown that composites, when produced in a tubular form and loaded in compression, are capable of absorbing significant energy through a range

of failure mechanisms such as fibre fracture, matrix cracking, debonding and delamination (Farley and Jones, 1992). The impressive energy-absorbing capability has attracted the interest of many vehicle manufacturers, including Chrysler and Ford. Indeed, Jacob *et al*. (2002) calculated that only 0.66 kg of of a high performance thermoplastic matrix composite is required to absorb the energy of a medium-sized car travelling at 35 mph.

Specific energy absorption (SEA) capability measured in kJ/kg is most frequently used to evaluate the energy-absorbing capacity of a composite rod or tube. Published values for the SEA of widely-used composites such as carbon fibre rods and tubes reinforced foams, generally fall in the range 13–90 kJ/kg. SEA values can vary greatly, for example, from 20 kJ/kg for a pultruded glass fibre/epoxy (Jacob et al., 2002) to values well in excess of 100 kJ/kg for carbon fibre-based systems (Hamada,1996). The precise value depends on a number of parameters, e.g. the geometry of the composite, its fibre architecture, as well as the mechanical properties of the matrix phase. For example, Hamada *et al*. (1992) showed that the energy-absorbing capacity of a 55 mm diameter CFRP tube decreased by fifteen percent in passing from a unidirectional tube to one with its fibres oriented at +/-25°.

A number of researchers have studied the influence of specimen geometry on the energy-absorbing capability of composite tubes (Thornton *et al*., 1979). Thornton and Edwards (1982) investigated geometrical effects in the energy-absorbing response of tubes based on circular, square and rectangular cross-sections and showed that the former out-performed both their square and rectangular tubular counterparts. Farley *et al*. (1986) conducted tests on carbon and Kevlar fibre reinforced tubes, with ply orientations typical of those used in sub-floor beam structures and showed that the tube diameter to thickness ratio played a significant role in determining its subsequent strain energy-absorbing capacity. Similar trends were observed by Alia *et al*. (2014) following tests on circular composite tubes, with values increasing by over fifty percent as the D/t ratio is reduced from approximately 42 to 6. This evidence suggests that the use of very low values of D/t can lead to great enhancement on energy absorption in tubular structures. Following these initial tests on small diameter reinforcements, individual tubes were embedded in a polymer foam and crushed at quasi-static rates of strain. The energy-absorbing characteristics of polymer foams reinforced with small carbon fibre reinforced epoxy tubes were investigated and typical failure characteristics

associated with fibre fracture and matrix cracking and extensive splaying of theoe composite tubes were observed. Thornton and Edwards (1979, 1982) investigated geometrical effects in the energy-absorbing response of tubes based on various shape of cross-sections, while Farley (1986) conducted tests on different fibre based composites included carbon and Kevlar fibre reinforced tubes to examine the energy-absorbing capacity. Recently, Alia *et al.* (2014) investigated the influence of tube diameter on the specific energy absorption (SEA) characteristics of the chamfered CFRP tubes and the failure characteristics.

Several studies were undertaken to investigate the influence of strain-rate on the energy-absorbing capacity of composite reinforced foams (Alia *et al*., 2014; Zhou *et al,* 2014; Schmuesser and Wickliffe,1987). Although the carbon tube exhibits attractive SEA values under static compressive, the SEA values were lower at dynamic rates of loading. Alia *et al.* (2014) presented the resulting values of SEA comparison between the dynamic and quasi-static data, which indeed show a pronounced rate-sensitivity agreed with the reductions of SEA reported by Schmuesser and Wickliffe (1987). The reductions in energy absorption are up to 30% following dynamic tests on carbon, glass and Kevlar fibre tubes. The reductions for tube reinforced structures in SEA highlight the important enhancement of composite rods based structures at dynamic loading. In contrast, the dynamic enhancement effect of rods reinforced system investigated by Zhou *et al,* (2014) presented the enhancement using a dynamic enhancement factors (DEF) for the energy absorption and compression strength graphically. The energy absorption increased significantly up to 76% being recorded and strength enhancement at dynamic rates was double those measured at quasi-static rates. The dynamic enhancement factors show the advantage performance in both the energy absorption and strength of the composite rod reinforced foam over the tube reinforced foam.

2.4.4.2 FE modelling of tubes reinforced foam

Since experimental trials are usually time-consuming and costly, it is evident that modelling the crushing behavior to investigate the energy-absorbing characteristics using commercial finite element software would be great interest. Once these models are verified, they can be used to predict the response of rod and tube reinforced foams based on different configurations, loading and

boundary conditions to assist design practice. A number of numerical work has been carried out to model the response of composite tubes. Carla McGregora *et al*. (2010) developed a model to predict the damage propagation, failure mode and energy absorption in triaxially braided composite tubes under axial compression using LS-DYNA. The two-ply and four-ply square tubes were modeled to predict energy absorption of front rail structural components on vehicular under axial crushing. A micromechanical model was incorporated into the ABAQUS/Implicit through a user-defined subroutine by Beard and Chang (2002) to simulate the complete crushing process of plug-initiated triaxially braided composite tubes with promising initial results. Flesher (2006) developed a model and incorporated into ABAQUS/Explicit to model dynamic response of tube under crushing load. Another damage model on composite using LS-DYNA with a lower accuracy that the predicted SEA values of un-initiated tubes were 30-40% lower than the experimental results (Xiao *et al*., 2009). A developed model for composite tube was only able to capture the axial crushing features of plug-initiated braided composite tubes accurately (McGregor *et al.,* 2007), however the simulation results on tubes was not successfully on predicting failure modes due to model instability. There were also discrepancies between the predicted and observed failure modes.

It is a challenging task to develop a model that is able to capture both the energy absorption and failure mode. A few researchers have attempted to model crushing of composite tubes and to simulate a similar splaying mode of failure. Mamalis *et al*. (2006) developed a finite element modeling to simulate axial collapse of CFRP square tubes under static and dynamic load. The model introduced a third layer to model the resin layer into pulverized debris during axial crushing. The deletion of the failure elements in the middle layer resulted a lower energy absorption. Silcock *et al* (2006) developed a splaying mode of failure on glass/polyester tubes by using LS-DYNA. The model employed a spotweld approach and pre-defining a debris wedge to simulate a delamination, initiation and propagation of the splaying failure mode. Although the failure modes were simulated successful, the correlation between the measured and predicted load-displacement profiles was low. Pinho *et al*. (2004) developed a model to simulate the splaying mode of tube failure successfully using a decohesion element incorporated into ABAQUS. Both the delamination and the transverse tearing through thickness between the composite layer fronds were simulated. Both the load and failure modes was captured reasonably, however only a portion of the propagation during the crushing process was modeled. A number of commercial packages such as LS-DYNA and Abaqus,

were used to to simulate the response of composit tubes, however, the failure criteria of those numerical models for composite materials are usually using 2D elements, such as plane stress and continuum shell elements. Those existing failure criteria available in package do not consider the rate-dependent through composite thickness. Therefore, it is expect to develop a constitutive model with associated failure criteria suitable for simulating a composite material using 3D solid elements.

2.4.5 Fibre metal laminates

2.4.5.1 Experimental tests on FMLs

FMLs have attracted significant interest from the aerospace industry in recent years, finding extensive use on certain aircraft designs, such as the upper fuselage of the Airbus A380 aircraft (Elke Hombergsmeier, 2006). Research has shown that FMLs offer an outstanding fatigue resistance, with crack propagation in notched laminates being actively suppressed via a localised fibre bridging mechanism. A number of researchers have also shown that FMLs offer attractive properties when subjected to dynamic loading, such as that associated with localized impact loading (Vlot, 1993; Chai and Manikandan, 2014; Cantwell, 2000; Vogelesang and Vlot 2000). Vlot *et al*. (1998) conducted a series of low velocity impact tests on FMLs based and GLARE, comparing their response to that exhibited by a 2024-T3 aluminium alloy and a number of thermoplastic-matrix composites. Damage in the panels was evaluated by determining parameters such as the depth of the impact dent and the minimum crack energy. Initial damage in the GLARE panels often takes the form of cracking in the distal aluminium layer extending parallel to the local fibre direction. The resulting dent depths were slightly greater than those recorded on the plain aluminium alloys and significantly greater than those recorded on the fibre-reinforced thermoplastics.

Abdullah and Cantwell (2006) studied the impact behaviour of a glass fibre reinforced polypropylene FMLs. The results showed that the FML offered an impressive resistance when subjected to low and high velocity impact. They found that FMLs absorb more energy during plastic deformation in the aluminium and composite layers. Carrillo and Cantwell (2008) studied scaling effects in the impact response of FMLs based on a self-reinforced polypropylene. The laminates were scaled at both a ply level, where the laminate thickness was increased by scaling the

thicknesses of the metal layers and the number of woven plies in the centre of the FML, and a sublaminate level, where the thickness was increased by repeating the sublaminate block. It was demonstrated that both approaches could be employed to successfully scale the impact response of these hybrid materials, with the failure modes being similar in all four scale sizes.

Caprino *et al*. (2004) performed low-velocity impact tests on fibre metal laminates made of 2024-T3 sheets and S2-glass/epoxy prepreg layers. Various impact masses, velocities, and energies were applied in the tests to investigate the influence of these factors on the impact response. For comparison purposes, similar tests were also performed on monolithic 2024-T3 sheets with the equivalent thickness.

Wu *et al*. (2007) conducted impact tests on two types of GLARE in order to elucidate the mechanisms of damage propagation in these materials. It was observed that the specific energy for first cracking in GLARE laminate based on a 2/1 stacking sequence was ten percent higher than that associated with a 2024-T3 aluminium alloy. Cross-sections of impact-loaded FMLs highlighted damage between the distal aluminium ply and the adjacent composite. The authors suggested that delamination enables the GLARE FMLs to deform in a membrane stretching mode, thereby increasing energy absorption.

Vlot (1993) invegistigated the impact characteristics of GLARE, ARALL FMLs and monolithic aluminium at various strain-rates in terms of minimum cracking energy, damage resistance and tensile strength. Low and high velocity impact tests were conducted on monolithic aluminium, fibre metal laminates, and carbon thermoplastic composites and found that GLARE out-perform than other materials. Impact tensile tests were conducted to compare the tensile strength and relatively lower rate sinstensity of strength was obvioused. Vlot (1996) also conducted impact tests on an aluminium alloy and different types of FMLs and composites. There was a crack at the carbon and aramid fibres based FMLs and the energy absorption was lower than that of a glass fibre reinforced FML. A inspection on the tested specimens showed that the FMLs exhibited a similar indentation in size to those plain aluminium alloy. Vlot *et al*. (1999) conducted impact tests on GLARE and plain aluminium and showed that the FML exhibited an initial cracking energy. They also found that the impact damage resistance of these FMLs increased with increasing glass/epoxy content.

2.4.5.2 Modelling works on FMLs

A number of FE models have been developed to simulate the impact response of FMLs using numerical techniques. Lee *et al.* (2001) investigated the penetration and perforation behaviour of a 6061-T6 aluminium plate and a carbon fibre reinforced 6061-T6 aluminium metal-matrix composite plate subjected to projectile impact using an explicit finite element code, LS-DYNA3D. Perforation of the plate was found to occur for all the impact conditions studied. The deformation behaviour of the plate and projectile as well as the projectile post-perforation velocity and the deceleration of the projectile were strongly dependent on the plate properties and impact velocity. Guan *et al.* (2009) investigated the impact response of fibre metal laminates based on a woven polypropylene (PP) fibre reinforced composite and an aluminium alloy at velocities up to 150 m/s. Both the predicted failure modes and displacement of the FMLs were in a good agreement with the test data. Payenganeh *et al*. (2010) modelled the impact response of fibre metal laminates manufactured using a glass fibre reinforced polyester composite. The developed FE models were able to simulate the resistance force history, deflection, in-plane strains and stresses in FMLs subjected to low velocity impact loading. They demonstrated that the masses and velocities of the impactor and the stacking sequence were key parameters in determining the impact response of a fibre metal laminate. The results indicated that the positioning of the aluminium layes within the thickness of the laminate determines the subsequent response of the structure.

Fan et al. (2011) invesitigeated the low velocity impact response of 2024-O aluminium alloy sheets and a woven glass fibre reinforce plastic based FMLs ranging from the 2/1, 3/2 to 4/3 stacking sequences. The impact response was simulated using finite element (FE) models and showed good correlation. FE models were also developed to simulate the impact response and perforation threshold of the FMLs. The validated models were used to study the effect of projectile size, target size and striking location on the perforation behaviour of the FMLs. Seo *et al*. (2010) used finite element techniques to predict the dynamic response of GLARE-based FMLs and validated their predictions using the experimental data reported by Wu *et al.* (2007). They observed that agreement between the numerical predictions and experimental results were generally good for the different damage modes that were noted. When modeling the impact response of FMLs it is clearly important to employ appropriate material properties in the analysis.

As mentioned before, althouth a number of numerical models were developed to simulate the response of FMLs, there is a limitation on the existing commercial finite element codes to simulate the through-the-thickness 3D rate-dependent response of fibre reinforced composites. It is necessary to introduce user-defined constitutive models and failure criteria to capture the related dynamic features of the composite layers in FML panels. Limited numerical modeling was developed to investigate the structural response of composite using 3D solid elements. Recently, Thuc *et al* (2013) developed FE models, which were validated using experimental data from tests on FMLs based on a 2024-O aluminium alloy and a woven glass–fibre/polypropylene composite. The rate-dependent failure criteria for a unidirectional composite were used, which were based on the modified Hashin's 3D failure criteria (Thuc *et al*., 2013). The constitutive model and failure criteria were then implemented in ABAQUS/Explicit using the VUMAT subroutine. Based on the previous research (Thuc *et al*., 2013), a further parametric studies were carried out to investigate the influence of the properties of aluminium alloys on the blast resistance of FMLs for aerospace applications. A vectorized user material subroutine (VUMAT) was employed to define Hashin's 3D rate-dependant damage constitutive model of the GFPP (Thuc *et al*., 2014).

2.5 Summary

This chapter has given a review of relevant past and current research work on composite structures subjected to quasi-static and dynamic compression loading. A brief overview of historical background and classification of composite structures, including sandwich and FMLs, core types, and temper designation of aluminium alloys, are given. The background of investigations related to potential hazards on composite in aerospace applications was introduced. A number of reports and investigations for bird strike on aircraft structures were reported, associated with low velocity impact loading as well as potential hazard by a blast loading. Subsequently, research work was reviewed, which includes experimental and numerical methods to characterise and predict the response of impact and energy-absorbing capability of the related composite structures. Following this, a number of factors that affect the impact response of composite structures, including the loading rate, impactor diameter, geometry and material constituents of the composite structures were reviewed. Finally, this chapter also gives the review on the low velocity impact work for various composite structures investigated in the current research, including plain foam based sandwiches, graded foam based sandwiches, rod and tube reinforced foams and fibre metal laminates.

CHAPTER 3 EXPERIMENTAL PROCEDURES

3.1 Introduction

This chapter presents details of experimental work on specimen preparation, characterization of material properties and test methods. Initially, specimen fabrication includes PVC foam based sandwich structures, composite rod and tube reinforced foam cores and fibre metal laminates. The details of specimen geometry, configurations and manufacturing processes are given here. Subsequently, test methods on material characterization are described, which include the tensile, shear, three point bending, quasi-static compression and Hopkinson bar test to characterize the mechanical properties of PVC foam, composite rods and tube, composite reinforced foam, GFRP, aluminiums, and the strain rate effect under high strain rate. Following this, experimental procedures are presented to cover quasi-static compression, quasi-static perforation, drop hammer compression and low velocity projectile impact tests.

3.2 Preparation of specimen

3.2.1 Plain foam based sandwiches

The plain foam based sandwiches were manufactured by bonding plain PVC foam core with glass fibres reinforced plastic skins as per the schematic shown in Figure 3.1. All of the foam panels have a thickness of 20 mm. The thin composite skins were glued to the panel by using a two part epoxy adhesive under pressure at room temperature for twelve hours.

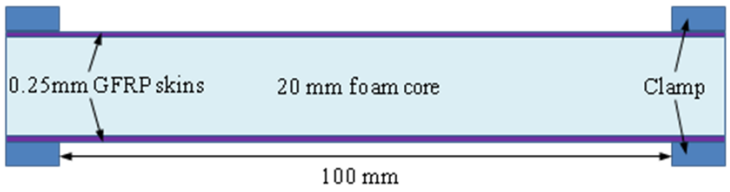

Fig. 3.1 Sketch of the configuration of sandwich panels.

Nine types of polymer foams with different densities were investigated in this study. Five of the foams were based on a crosslinked PVC (C60, 80, 100, 130 and 200), two on a linear PVC (L90 and L140) and two on a PET foam (PET105 and 135).

The two ply, 0.25 mm thick composite skins were based on woven E-glass fibres in a thermosetting epoxy resin matrix (Stesapreg EP 127-44-40 supplied by Gurit Ltd). The skins were per made by stacking GFRP plies and heated using a Meyer hot press machine, shown in Figure 3.2, following a procedure of heating to 125 ℃ under a pressure of 0.3 MPa for 60 minutes and then cooling to room temperature. The curing temperature history is shown in Figure 3.3 A digital thermocouple inserted between the prepreg plies to monitor the temperature during curing process.

Fig. 3.2 Meyer hot press used for manufacturing composite

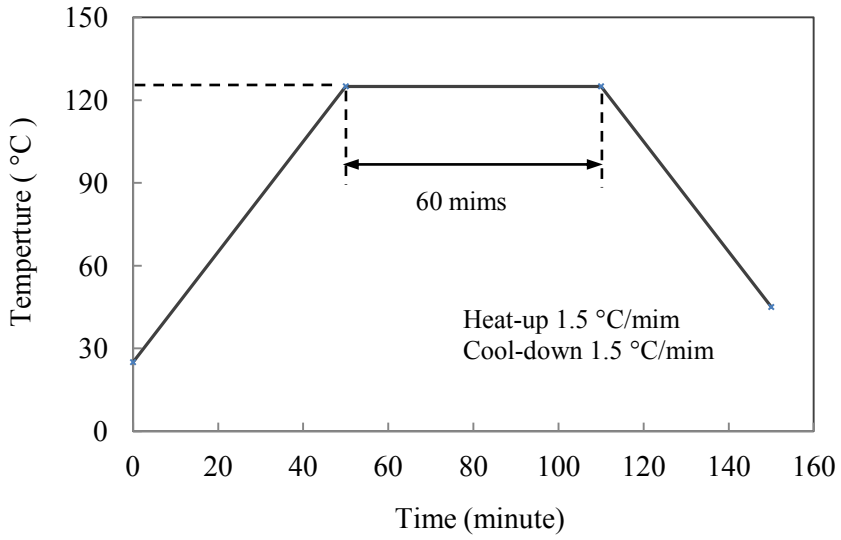

Fig. 3.3 Curing temperature history for GFRP and CFRP prepregs.

3.2.2 Graded foam based sandwiches

Graded foam based sandwich structures were made with carbon fibre reinforced plastic (CFRP) face sheets and graded/layered foam cores fabricated by bonding foams with different densities together. Core materials with varying through the thickness properties were manufactured by bonding three 10 mm thick foam panels together using a fast-drying contact adhesive. The carbon fibre skins were then bonded to the core, as shown schematically in Figure 3.4. A range of linear PVC, crosslinked PVC and PEI foams were bonded together to produce a three layer core. Table 3.1 summarises the properties of the nine different foams investigated in this study. Four of the foams were based on crosslinked PVC foams with densities between 60 and 200 kg/m^3. The three linear PVC foams have densities between 60 and 140 kg/m^3 and the two PEI foams offered densities of 60 and 80 kg/m^3. Table 3-1 also summarises the stacking sequences of the twelve configurations investigated here, in which the average core density varied from approximately 77 kg/m^3 to 113 kg/m^3. The average core density of specimen was based on three fabricated samples for each specimen. It should be noted that six of the twelve configurations were obtained by inverting the original stacking sequence, for example Core C2 was simply Core C1 turned upside down.

Prior to testing, the graded cores and carbon fibre reinforced plastic (CFRP) skins were bonded together using a two-part epoxy resin. The 0.35 mm thick skins were manufactured by stacking two woven CFRP plies (EP121 C15-53 from Gurit Ltd) and heated up to 125 °C using the Meyer hot press following the same curing temperature shown in Figure 3.3

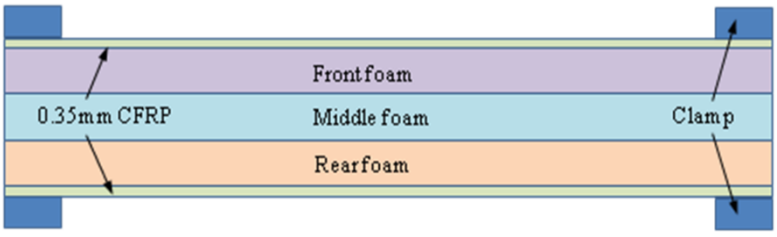

Fig. 3.4 Sketch of the stacking configuration of graded foam sandwich panels.

Table 3-1 Foam core configurations of the sandwiches investigated in this study.

Code	Configurations	Average density (kg/m^3)
C1	C100/P80/P60	80.0
C2	P60/P80/C100	80.0
C3	L80/C60/C200	113.3
C4	C200/C60/L80	113.3
C5	C80/L60/C100	76.7
C6	C100/L60/C80	76.7
C7	L60/P60/L140	86.7
C8	L140/P60/L60	86.7
C9	P80/P60/C200	113.3
C10	C200/P60/P80	113.3
C11	C60/L80/L140	93.3
C12	L140/L80/C60	93.3

3.2.3 Composite rod reinforced foam cores

The energy-absorbing characteristics of composite rods reinforced PVC foam cores for use in lightweight impact-resistant sandwich structures are introduced in this section. Crosslinked PVC foam cores with densities ranging from 40 to 200 kg/m^3, reinforced with carbon or glass composite rods with nominal diameters of 2, 3 and 4 mm have been fabricated. The crosslinked PVC polymer foams investigated in this study were supplied by Airex A.G, Switzerland and the composite rods supplied by EasyComposites, UK. The mechanical properties of the four foam materials, with nominal densities of 40, 80, 130 and 200 kg/m^3, were determined in an earlier study (Zaki, 2012) and details are given in Table 3-2. The PVC foam specimens were cut to a size of 50x50x20 (thickness) mm using a band saw. Nine holes were then drilled into the square foam samples as shown in Figure 3.5 (a). The diameters of the holes were exactly equal to those of the rods that were

inserted into them. The ends of rods were polished and levelled to ensure uniform loading when in contact with the loading platens. Plain foam samples prepared (i.e. without composite rods) having similar dimensions to those of their reinforced counterparts were prepared to carry out the same tests.

Carbon and glass fibre rods were inserted into the pre-drilled holes in the foam panels. A total of 24 material configurations were prepared, details of which are given in Table 3-2. Here, C200C3 corresponds to a 200 kg/m^3 crosslinked PVC foam reinforced with 3 mm carbon fibre (C) rods. Similarly C130G4 refers to a 130 kg/m^3 crosslinked PVC foam reinforced with 4 mm glass fibre (G) rods. Figure 3.5 (b) shows a typical carbon fibre rod reinforced foam sample.

Table 3-2 Summary of carbon fibre reinforced foam specimens

Specimen ID	C40 PVC	C80 PVC	C130 PVC	C200 PVC
2 mm carbon fibre rod	C40C2	C80C2	C130C2	C200C2
3 mm carbon fibre rod	C40C3	C80C3	C130C3	C200C3
4 mm carbon fibre rod	C40C4	C80C4	C130C4	C200C4
2 mm glass fibre rod	C40G2	C80G2	C130G2	C200G2
3 mm glass fibre rod	C40G3	C80G3	C130G3	C200G3
4 mm glass fibre rod	C40G4	C80G4	C130G4	C200G4

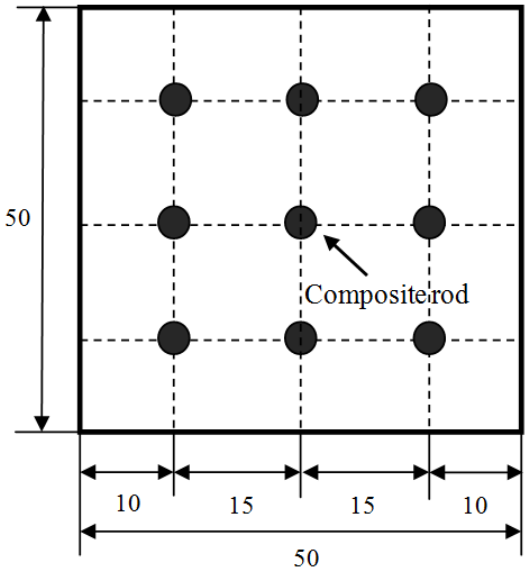

(a) Arrangement of the reinforcing rods,

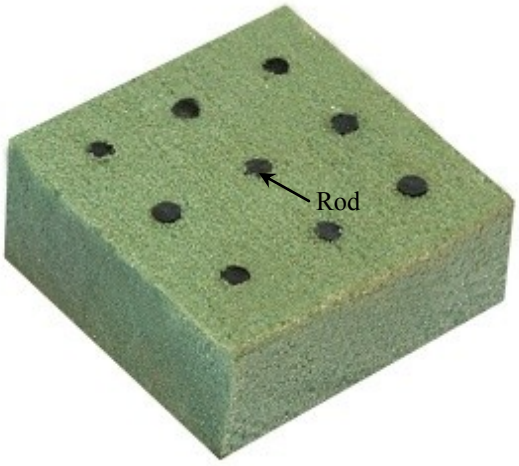

(b) A typical specimen based on 4 mm diameter carbon fibre rods.

Fig. 3.5 Composite rod reinforced PVC foam panel.

3.2.4 Composite tube reinforced core based sandwiches

Composite tube reinforced foams, with a similar structure of the rod reinforced core, were manufactured for use in lightweight energy-absorbing sandwich structures. The composite tube reinforce foam was developed to characterize the performance between rods and tube based

structures. The composite tubes with inner diameters of 8 to 12.5 mm were embedded in crosslinked PVC foam cores with densities ranging from 40 to 130 kg/m^3 as enhanced energy-absorbing structures. The composite tubes were supplied by Easycomposites, UK. It is manufactured using high modulus unidirectional pre-preg carbon fibre oriented to provide maximum strength in the longitudinal axis, also the use of pre-preg reinforcement oriented at 90° to ensures that the tube has good crush/burst strength around the section of the tube. This is a roll wrapped carbon fibre composite tube, which is manufactured from special high-modulus Toray T700 unidirectional pre-preg carbon fibre oriented at 0° (down the length of the tube) and unidirectional E-Glass oriented at 90° (rotated direction of the tube) by placing fibres in a [0,90,0,90,0] pattern. The overall strength of tube equal 50% CF at 0° and 50% CF at 90° direction. Table 3-3 summaries the details of tubes.

Table 3-3 Summary of carbon tubes used in this study

Samples Pictures					
Fibre type	Glass	Carbon	Carbon	Carbon	Carbon
Length (mm)	20	20	20	20	20
Inner dia. (mm)	8.5	8	10	12.5	14
Outer dia. (mm)	12.7	10	12.7	15.2	16.7
Thickness (mm)	2.1	1	1.35	1.35	1.35
D/t	4.05	8.0	7.41	9.26	10.37
Mass (g)	2.58	0.97	1.5	1.8	2

The crosslinked PVC polymer foams investigated were from Airex A.G. The mechanical properties of the four foam materials same as the foams used for rod reinforced foams, with nominal densities of 40, 80 and 130 kg/m^3. The PVC foam specimens were cut to a size of 100x100x20 (thickness) mm using a band saw. Nine holes were then drilled into the square foam samples as shown in Figure 3.6 (a). The diameters of the holes were exactly equal to those of the outer diameter of tubes that were inserted into them. The ends of tubes were polished and levelled to ensure uniform loading when in contact with the loading platens. Carbon fibre tubes with three inner diameters of 8, 10 and

12.5 and glass fibre rods with diameter of 8.5 mm were inserted into the pre-drilled holes in the foam panels. A total of 12 material configurations were prepared, details of which are given in Table 3-4. Here, C200C8 corresponds to a 200 kg/m^3 crosslinked PVC foam reinforced with a inner diameter of 8 mm carbon fibre (C) tubes. Similarly C130G8 refers to a 130 kg/m^3 crosslinked PVC foam reinforced with 8 mm glass fibre (G) tubes. Figure 3.6 (b) shows typical a carbon fibre rod reinforced foam sample.

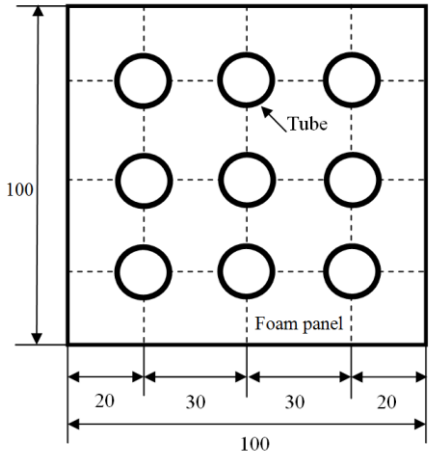

(a) Arrangement of the embedded reinforcing tubes,

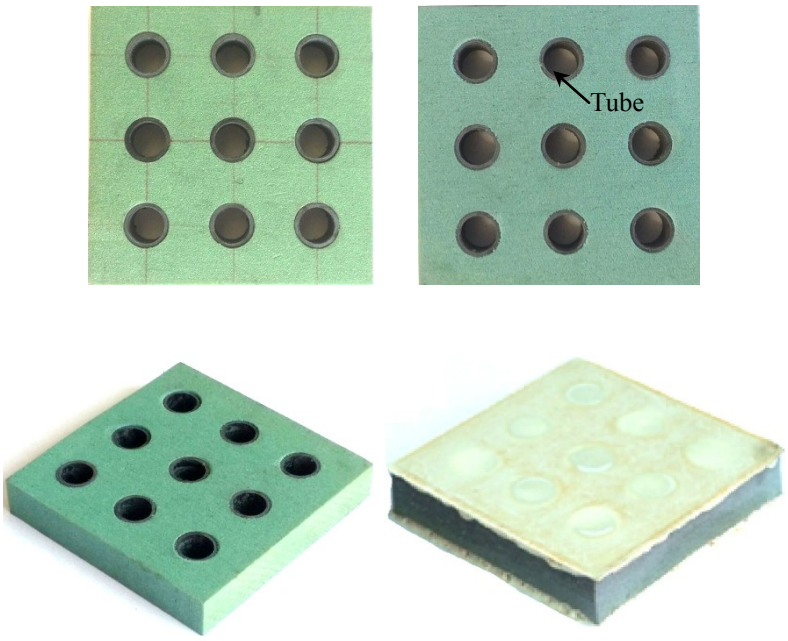

(b) A typical specimen based on 12.5 mm diameter carbon fibre tubes.

Fig. 3.6. A specimen of composite tube reinforced PVC foam panel

Table 3-4 Summary of composite tube reinforced foam panels based sandwiches

	C40	C80	C130
8 mm id carbon fibre tube	C40C8	C80C8	C130C8
10 mm id carbon fibre tube	C40C12	C80C10	C130C10
12.5 mm id carbon fibre tube	C40C12	C80C12	C130C12
8 mm id glass fibre tube	C40G8	C80G8	C130G8

3.2.5 Fibre metal laminates

Fibre metal laminates manufactured by stacking a series of multilayer configurations, ranging from a simple 2/1 lay-up to a nine ply 5/4 laminate. The FMLs studied in this investigation were based on a woven glass fibre resin plastic prepreg material (GFRP) supplied by Umeco Ltd (MTM56FRB-GF0100-40%RW) and three types of aluminium alloy, a 1 mm thick 7075-O alloy, a 0.5 mm thick 6061-O alloy and a 0.28 mm thick 6061-T6 alloy, supplied by Aircraft Materials Ltd. Table 3-5 summarises the various configurations investigated in this study, giving the thicknesses, areal densities and aluminium volume fractions in the FMLs.

Before manufacturing the laminates, the aluminium sheets were cleaned using an etching process. The FMLs were laminated by stacking the appropriate number of aluminium sheets and composite layers in a picture-frame mould. The manufacturing process for a 3/2 FML is shown schematically in Figure 3.7. The laminates were then placed in a Meyer press under a pressure of 0.4 MPa and heated to a temperature of 125 °C, at a rate of 1.5 °C/min. The curing temperature is shown in Figure 3.8. Following consolidation, the panels were cooled to a temperature below 60 °C, before removal from the press.

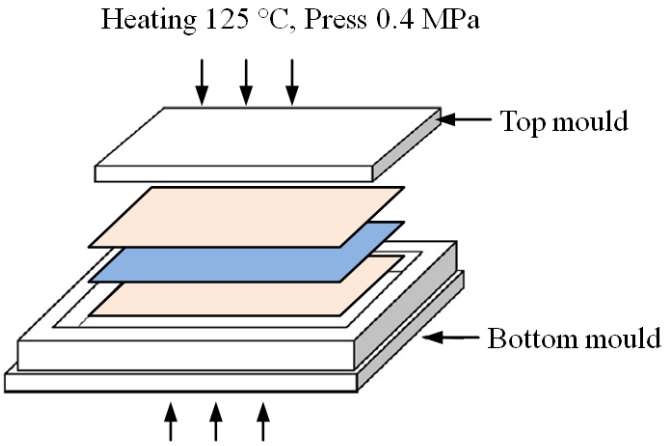

Fig. 3.7. Schematic of the stacking arrangement of a 2/1 FML in a picture frame mould.

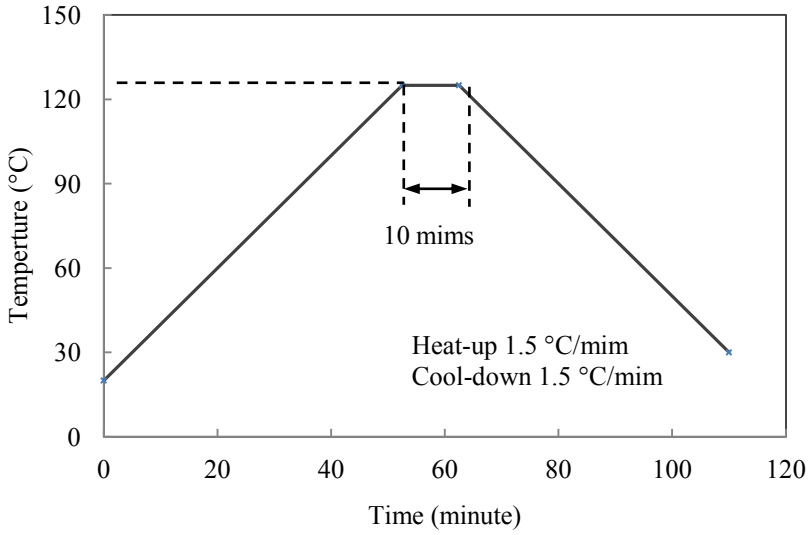

Fig. 3.8 Curing temperature of FMLs in hot press

Table 3-5 Geometry and characteristics of the FMLs

Stacking configuration	Thickness (mm)	Mass (g)	Areal density (kg/m^2)	Al Volume Fraction
1 mm thick Al7075-O + 5-plies of GRFP				
2/1 FML	2.95	75.28	7.528	0.678
3/2 FML	5.02	121.48	12.148	0.598
4/3 FML	6.90	170.37	17.037	0.580
5/4 FML	9.01	214.27	21.427	0.556
0.5 mm thick Al6061-O + 3-plies of GRFP				
2/1 FML	1.58	38.67	3.867	0.625
3/2 FML	2.61	63.7	6.37	0.577
4/3 FML	3.75	89.43	8.943	0.526
5/4 FML	4.84	117.66	11.766	0.515
0.28 mm thick Al6061-T6 + 3-plies of GRFP				
2/1 FML	1.05	27.16	2.716	0.533
3/2 FML	1.85	47.17	4.717	0.454
4/3 FML	2.75	67.04	6.704	0.407
5/4 FML	3.64	86.44	8.644	0.384
Constituent materials				
7075-O AL	1	28.36	2.836	1
6061-O AL	0.5	13.56	1.356	1
6061-T6 AL	0.28	7.48	0.748	1
3-PLY GRFP	0.55	12.5	1.25	0
5-PLY GRFP	1	20.6	2.06	0

3.3 Characterization of mechanical properties of materials

A series of compressive, tensile, shear, three point bending and perforation tests were conducted to characterize the material properties of those specimens.

3.3.1 Compression tests

Quasi-static compression tests on PVC foam cubes were carried out using the Instron 4505 universal testing machine, as shown in Figure 3.9. The specimens were placed between two stainless steel platens and subjected to loading at a crosshead displacement rate of 1 mm/min. The load-displacement traces were recorded to obtain the compression modulus and strength. The compressive tests were conducted according to BS ISO 844:1998 standard.

The compression tests on composite rods and tubes were carried out using the same testing machine. Prior to their insertion into the foams, individual carbon and glass fibre rods were subjected to axial compressive loading at a crosshead displacement rate of 1 mm/min. Load-displacement traces were recorded during the test and the compressive modulus and strength properties of the rods were determined. Three repeated tests were conducted on each type of rod.

Compression tests on the composite reinforced PVC foam panels were carried out using the aforementioned Instron 4505 universal testing machine. The panels were placed between two stainless steel platens and subjected to loading at a crosshead displacement rate of 1 mm/min. The load-displacement traces were recorded to obtain the compression strength and energy absorption characteristics of the reinforced foam panels. The compression tests on FMLs specimen were carried out using the same tester and procedure.

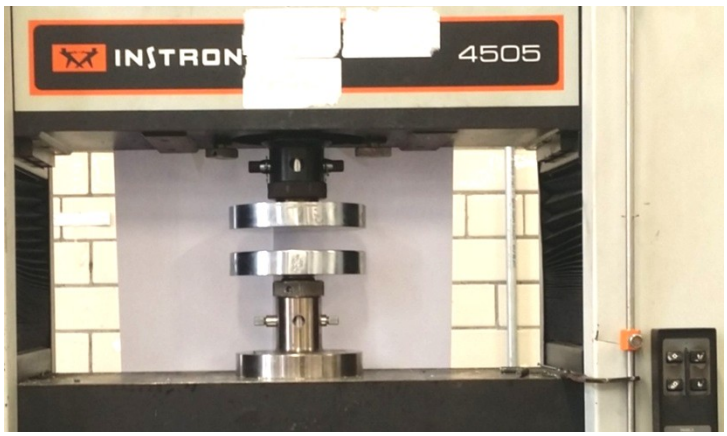

Fig. 3.9 Compression test using Instron 4505 universal test machine

3.3.2 Tensile tests

A series of quasi-static tensile tests were conducted on the GFRP and the three aluminiums alloys, using a screw-driven universal Instron 4204 testing machine, at a crosshead displacement rate of 1 mm/min, which is shown in Figure 3.10. A mechanical extensometer was attached to the specimen to measure strain.

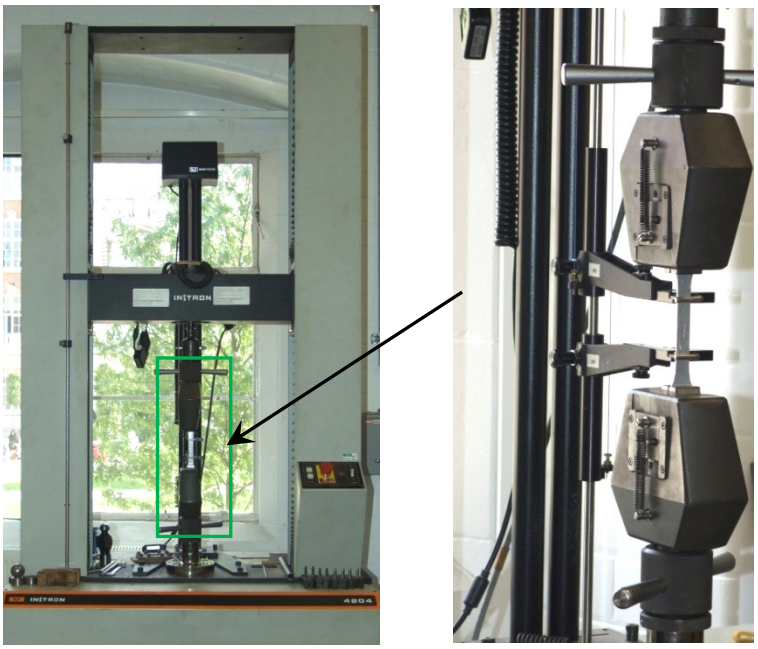

(a) Instron 4204 universal testing machine and mechanical extensometer

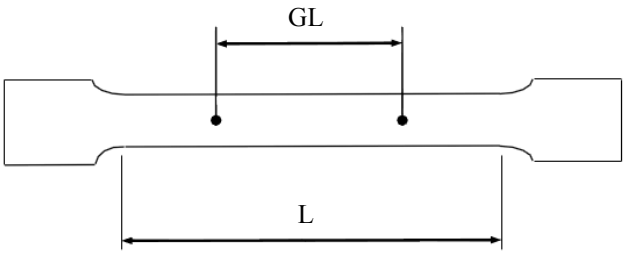

(b) Geometry of tensile specimen

Fig. 3.10 Tensile testing machine and tensile specimen

3.3.3 Fracture property of PVC foam (Single End Notch Bend Test)

The toughnesses of the materials were characterised in order to determine the work of fracture. Quasi-static single end notch bending test (SENB Model I opening) tests were conducted using an Instron 4045 universal testing machine and 5 kN load cell. The specimen were loaded in a fixture

under three point bending conditions shown in Figure 3.11 (a). The specimens were prepared as beams with dimensions of 120 x 30 x 20 mm and were introduced a notch length of 12 mm approximately in the middle of the sample. The test refers to the BS ISO 13586:2000 standard.

Shear tests (Mode II) on PVC foams were carried out in order to determine the shear strength and fracture energy. The tests were conducted using the shear geometry shown in Figure 3.11 (b). The sample was fixed at one end and loaded by a rigid transverse at 10 mm/min in a shearing mode. The load-displacement traces were recorded to obtain the shear modulus, strength and shear strength of PVC foam. The shear strength of the foam was determined from the maximum measured load and the area of the fractured ligament.

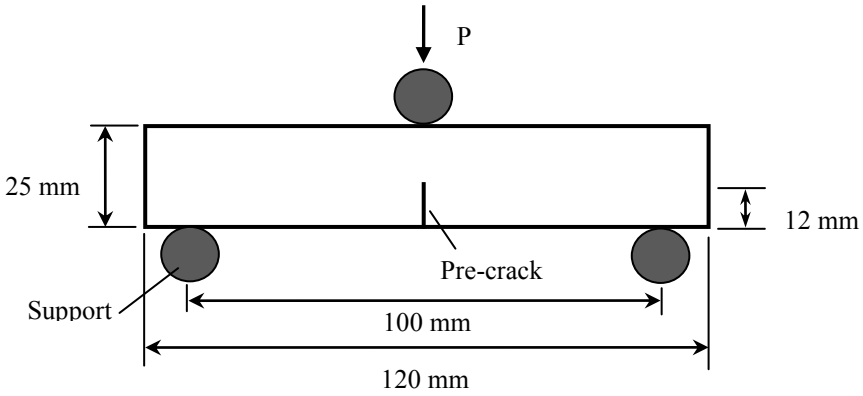

(a) Schematic of the SENB geometry

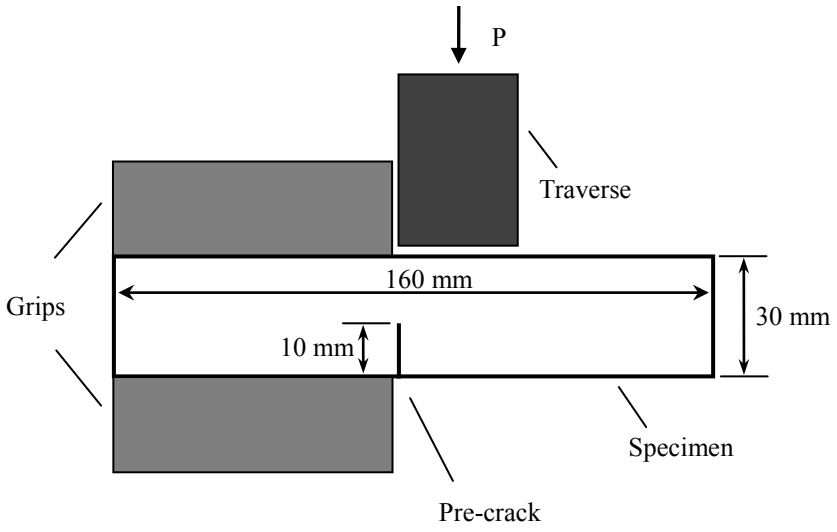

(b) Schematic of the Mode II test geometry

Fig. 3.11 Schematic of shear test on PVC foam

3.3.4 Three-point bending tests on composite rods

Three-point bending tests were carried out in order to determine the flexural modulus and strength of the composite rods. The tests were conducted using the fixture shown in Figure 3.12. Here, the length of the rods was 70 mm and the span between the supports was 50 mm. The crosshead displacement rate was also set to 1 mm/min. The load-displacement traces were recorded to obtain the flexural modulus and strength of composite rods.

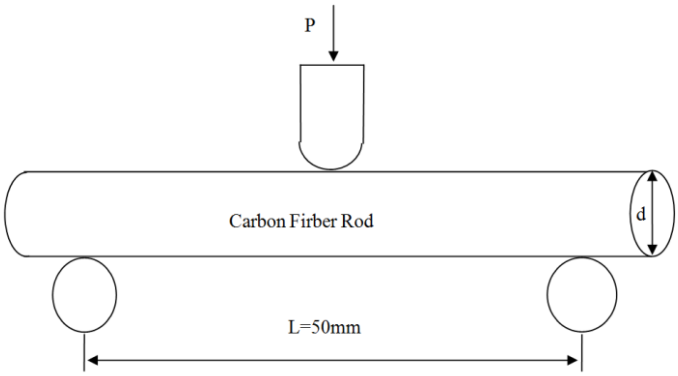

(a) Schematic of three points test

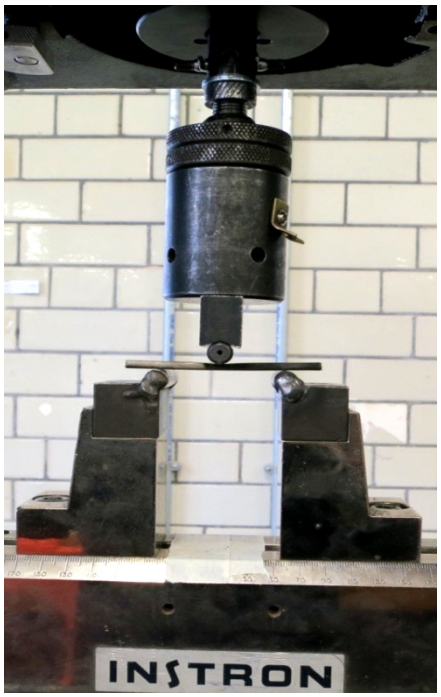

(b)Fixture of the three points bend test

Fig. 3.12 Three points bend test.

3.3.5 Quasi-static perforation tests

Quasi-static perforation tests were conducted on the FMLs and their constituent materials, using the square support shown in Figure 3.13 (b). Here, square plates, with dimensions of 100 x 100 mm, were clamped between two square-shaped steel fixtures with a 72 mm square central aperture. The clamps were then bolted to a steel block in preparation for testing. A hemi-spherical steel indenter, with a diameter of 12.7 mm, was used to load the samples centrally. The quasi-static tests were undertaken on an Instron 4505 universal testing machine at a crosshead displacement rate of 1 mm/min. The resulting load-displacement traces were recorded to determine the energy required to perforate the samples.

(a) Universal testing machine

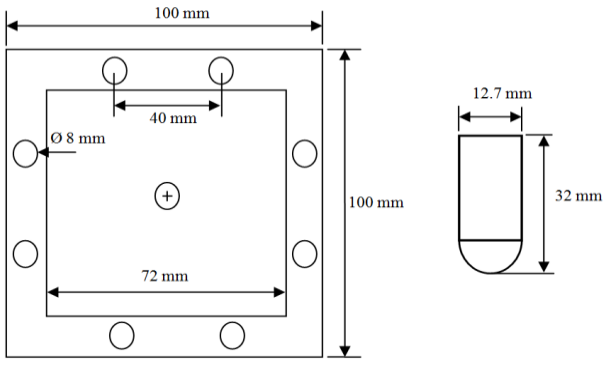

(b) The square fixture to clamp samples and the hemispherical projectile.

Fig. 3.13 Indentation Instron 4505 universal test machine

3.4 Experimental procedures of dynamic tests

Dynamic tests, including low velocity impact tests on sandwich structures and FMLs and impact crush on rod and tube reinforced foam panels, are described in this section.

3.4.1 Impact perforation of PVC foam core and sandwiches

Low velocity impact tests were conducted on both the plain foams as well as the sandwich structures using a drop-weight impact tower shown in Figure 3.14. The perforation resistance was investigated. Here, the 150 mm square panels (containing eight bolt holes along their edges) were placed on a 100 mm long steel cylinder fixed to a square steel base and clamped using a steel ring and ten bolts. Both the cylindrical support and the clamping ring had an internal diameter of 100 mm. The panels were impacted centrally by a carriage with a 10 mm diameter hemispherical head. The mass of the impactor was 5.56 kg and the release height of the impact carriage was varied between 0.2 and 1.4 metres. The impact force and displacement of the impactor were measured using a piezoelectric load cell and a high-speed video camera, respectively. The load-time traces were obtained by converting the recorded voltage-time traces using a 10 kN Kistler 9321A piezo-electric load cell during the impact tests. The movement of the projectile and specimen deformation during the impact event was recorded using a high speed camera positioned in front of the impact tower.

Tests were also conducted on sandwich panels placed on a water support. These tests were undertaken to simulate the effect on an internal impact on an immersed sandwich structure, such as a boat hull. Here, the circular ring support was filled with water and the panel was clamped as discussed previously. The schematic of sandwich supported on water is shown in Figure 3.15.

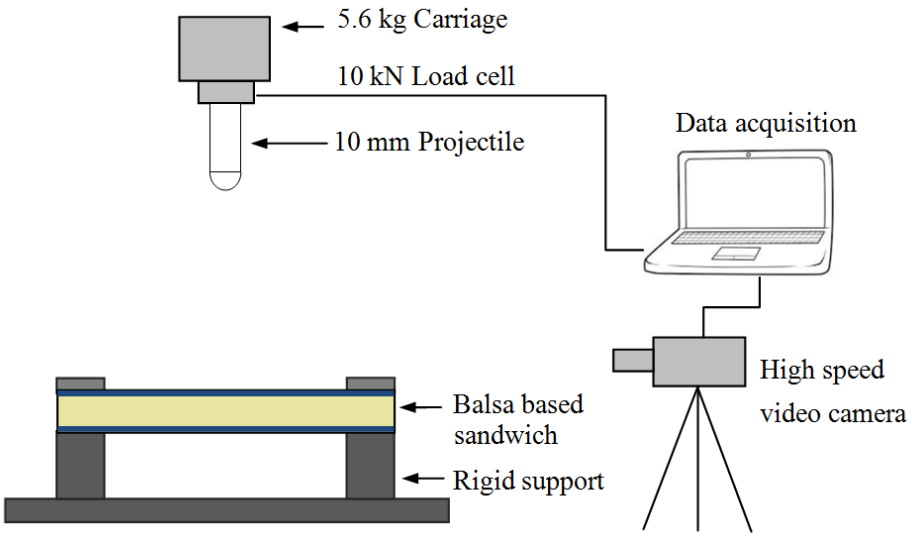

(a) Schematic of impact test

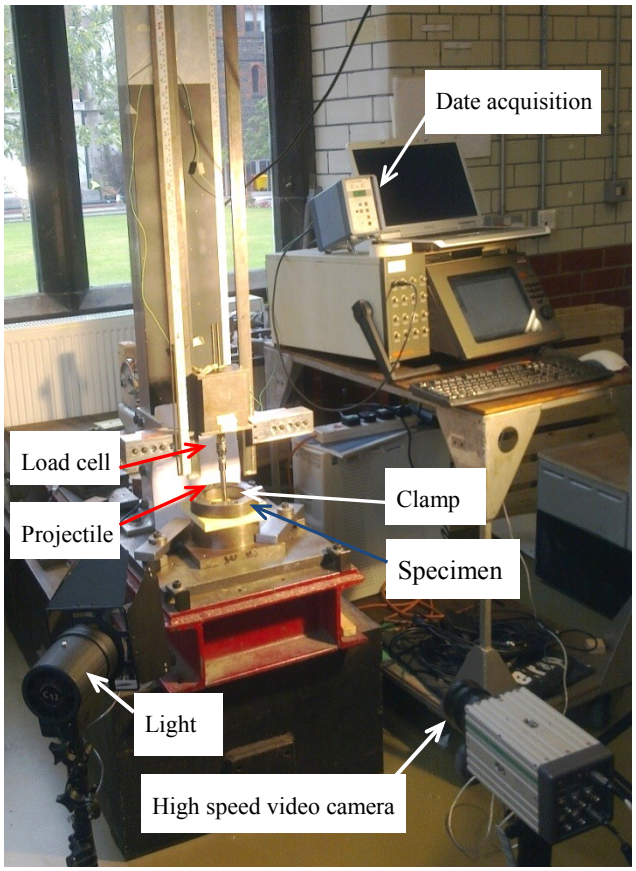

(b) Impact tower and test rig

Fig. 3.14 Low velocity test using impact tower

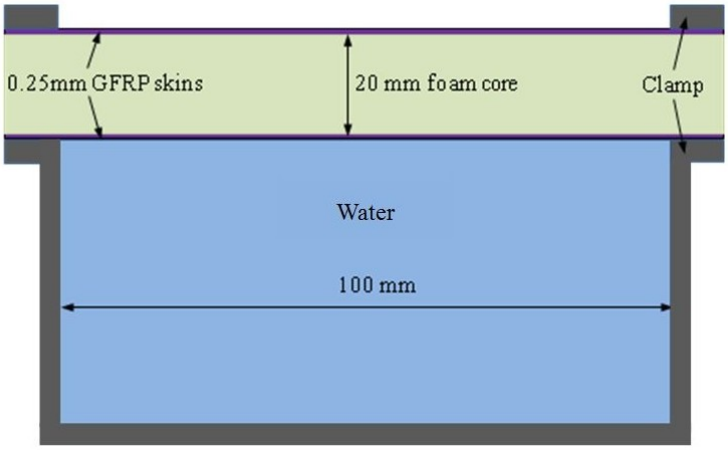

Fig. 3.15 Schematic of sandwich panel supported on water

3.4.2 Impact crush of composite rod and tube reinforced foam

The dynamic response of PVC foams reinforced with composite rods and tubes was investigated through a series of drop-weight impact crush tests. The impact crush was conducted on square panels using aforementioned drop-weight impact tower shown in Figure 3.16. The 50 x 50 x 20 mm specimens were placed on bottom rigid square platens with an edge diameter of 100 mm supported on a 100 kN load cell. The reinforced PVC specimens were crushed by top rigid platens with a carriage mass up to 40 kg. The release height of the impact carriage was increased up to a maximum of 1.4 meters. The displacement and impact force were recorded using a high-speed video camera and a piezoelectric load-cell, respectively.

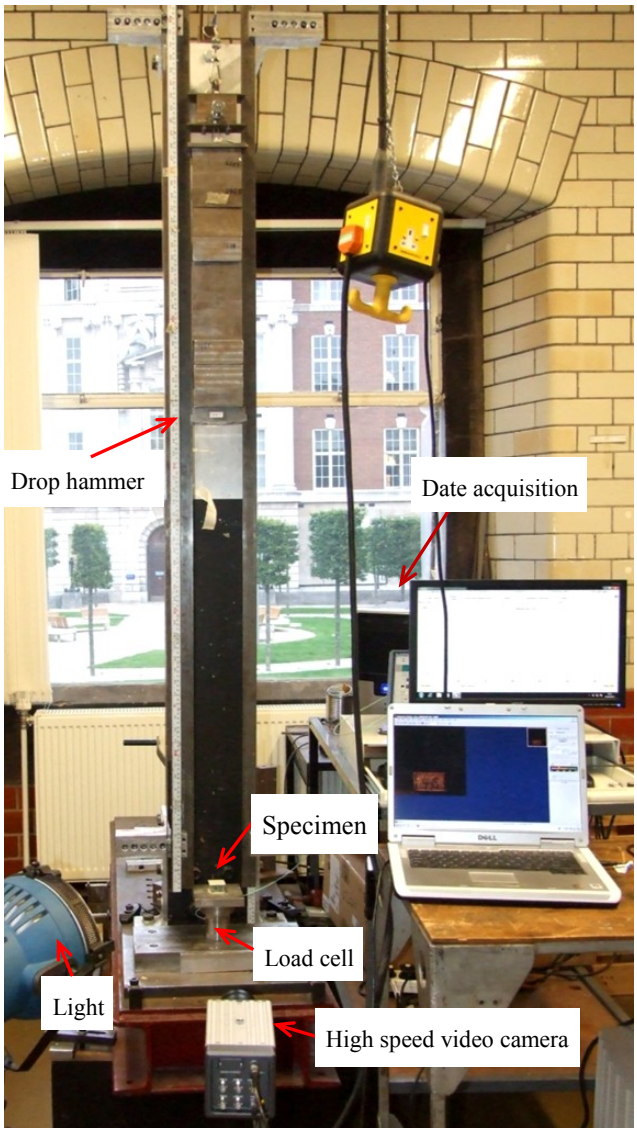

Fig. 3.16 Drop hammer impact tower test rig

3.4.3 Impact tests of FMLs

Low velocity impact tests were undertaken using the aforementioned drop-weight test rig, shown in Figure 3.17. Here, the 100 mm square plate FMLs specimens (containing eight bolt holes along their edges) were placed between two square-shaped steel fixtures with a 72 mm square central aperture and bolted to a steel block. The rig fixture is same as the quasi-static test shown in Figure 3.13(b). A hemi-spherical steel indenter, with a diameter of 12.7 mm, was used to load the samples centrally. The schematic of the fixture is shown in Figure 3.17. The mass of the impactor was 5.56 kg and the

release height of the impact carriage was varied up to 1.4 metres. During impact, the load was recorded using a load cell and the displacement using a high speed video camera. The absorbed energy was then used to calculate the specific perforation energy, by normalizing the measured energy by the areal density of the target.

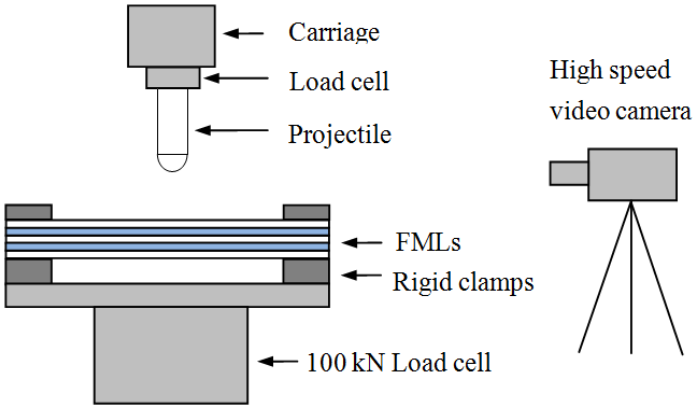

Fig. 3.17. Schematic of the test set-up for low velocity impact testing.

3.4.4 Split Hopkinson bar tests

Split Hopkinson bar tensile tests were undertaken to evaluate the strain-rate sensitivity of the GFRP and the three types of aluminium alloy using the rig shown schematically in Figure 3.18. The velocity of the input bar, and therefore the strain-rate in the test sample, was varied by adjusting the pressure in the main chamber of the gas gun. The geometry of the tensile test specimen is shown in Figure 3.18 (c). Specimens were cut in parallel and transverse to the rolling direction of the aluminium using a laser cutting device. In order to obtain an identifiable pulse signal and minimum signal noise, the gauge length varies between 8 and 12 mm and the width varies between 2 and 4 mm, dependent on the specimen thickness and strength.

The stress-strain relations obtained at different strain rates were used to obtain the parameters in the Cowper-Symonds constitutive equation, which is given as (Cowper, 1957):

$$\frac{\sigma_{dyn}}{\sigma_{stat}} = 1 + \left(\frac{\dot{\varepsilon}}{D}\right)^{\frac{1}{p}} \qquad \text{(Eq. 3.1)}$$

where $\dot{\varepsilon}$ is the strain rate and D and p are the Cowper-Symonds constants.

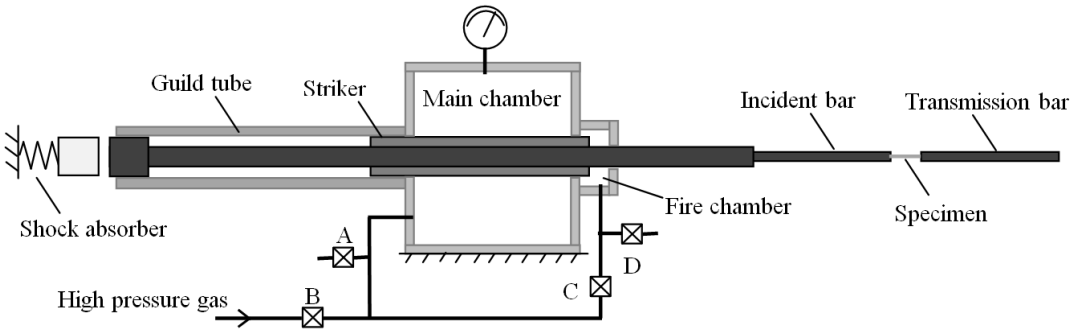

a. Split Hopkinson bar test rig.

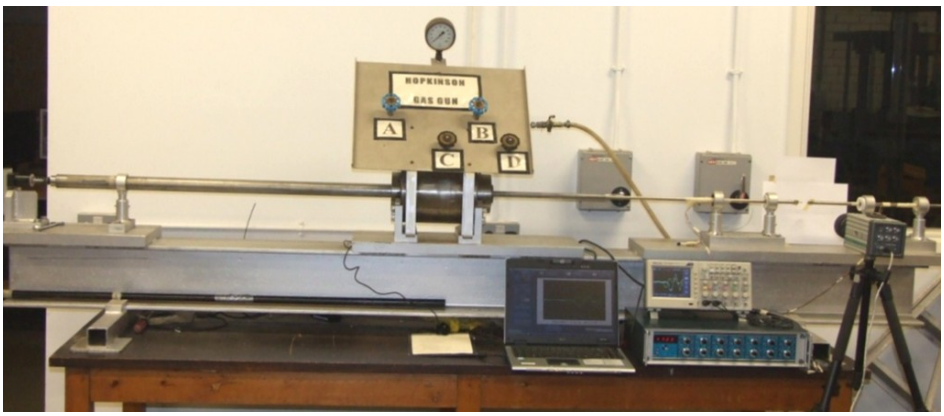

b. Photo of split Hopkinson bar test rig at University of Liverpool

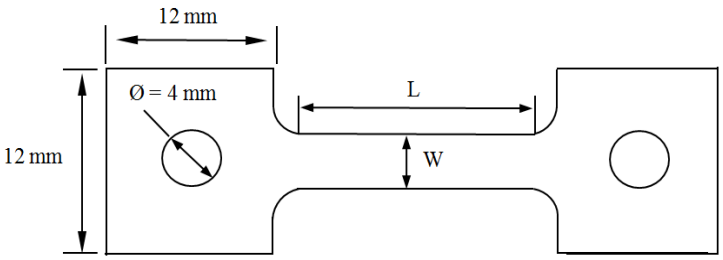

c. A tensile specimen for Hopkinson bar testing.

Fig. 3.18. Schematic of the test rig and tensile specimen for split Hopkinson bar testing.

3.4.5 Post-test procedures on samples

After testing, all the specimen panels were centrally sectioned through the perforated region, ground and then polished and photographed under an optical microscope to elucidate the failure mechanisms associated with the perforation process at both quasi-static and dynamic rates of the loading.

3.5 Summary

Details of experimental work relating to specimen fabrication, characterization of material properties, and experimental procedures for both the quasi-static and dynamic tests are presented. The specimens investigated include a plain foam core and graded foam core based sandwich structures, composite rod and tube reinforced foam core structures and aluminium based fibre metal laminates. The basic mechanical properties of the materials were characterized though compression tests on foam and composite reinforced foams, tensile test on glass fibre reinforced plastic and aluminium sheet, Single end notch bending test Mode I and shear test Mode II on PVC foam, three-point bending tests on composite rods and quasi-static perforation on fibre metal laminates. Dynamic tests conducted on the manufactured specimens included the low velocity impact on sandwiches and fibre metal laminates and compressive crush test on composite rod reinforced foam. All cross-sections of tested specimens have been processed to elucidate the failure mechanisms. The test results will be discussed in Chapter 4.

CHAPTER 4 EXPERIMENTAL RESULTS AND DISCUSSION

4.1 Introduction

This chapter presents experimental results on composite structures include foam based sandwiches, composite rod and tube reinforced foam and fibre metal laminates investigated in this research. Firstly, the material characterisation of constituent materials for composite structures has been evaluated to investigate the mechanical properties and strain-rate effects following both quasi-static and dynamic compressive loading. Impact test on plain foam panels and foam based sandwich structures, test of sandwich support on water have been presented here. Subsequently, results of compression tests and dynamic crush testing on rod and tube reinforced foam structures have been summarized to evaluate the energy absorption capability. Finally, tensile test on aluminium and GFRP have been undertaken following a range of strain rates in order to investigate strain-rate effects of the projectile impact on FMLs. Both quasi-static and dynamic perforation tests have been summarized and performance has been evaluated. The load-displacement traces and failure mechanisms of those tested specimens will be presented and the energies absorbed by the structures will be summarised and evaluated.

4.2 Impact response of PVC foam based sandwiches

4.2.1 Compression tests and mechanical characteristics of PVC foam

The mechanical properties of PVC foams have been characterized following compression tests described in Section 3.3.1. Figure 4.1 shows the typical stress-strain curves for the crosslinked PVC foam with increasing densities form 60 to 200 kg/m^3. The stress-strain traces show three distinct stages. The elastic stress following Hooke's law determined by the slope of this curve, when the compression strains less than yield strain of 5 %, before the stress reach its peak at a plastic collapse stress. The clear plateau stress continues as a relatively stable stress from the strain range of 6 % to 65 %. This stage offers a majority of the energy absorption capacity of foams. The final stage followed is the well-defined foam densification region, where the foam cell walls collapse and touch together which associated with the plateau stress increasing.

The obtained stress-strain curves also show the increasing of modulus and plateau stress with the

increase of foam densities. The value of the modulus of elasticity, the compression strength, the steady-state stress and the densification strain, were determined from the resulting stress-strain curves. The compression strength of the foams was determined from the initial peak in the stress-strain curve. The obtained traces will be used as material data to define the material constitutive relationship for FE models in the following Chapter 5.

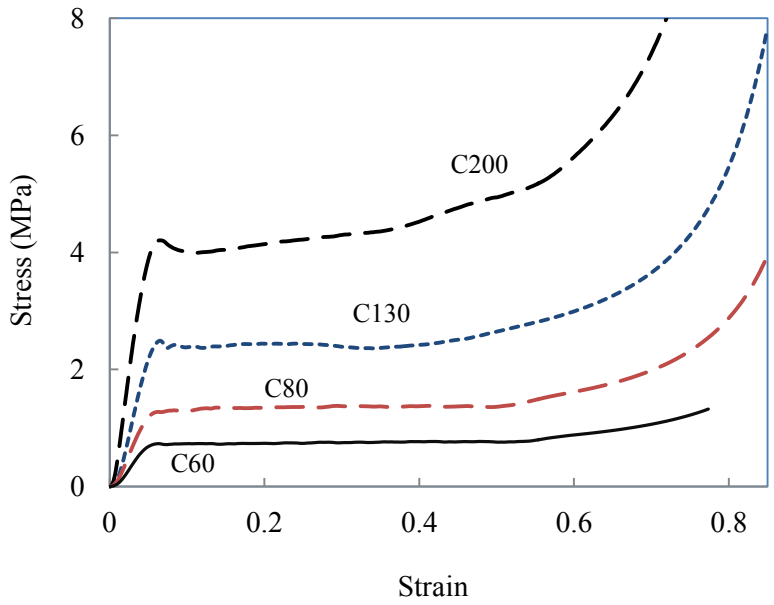

Fig. 4.1 Typical stress-strain traces on the crosslinked PVC following quasi-static compression tests.

The mechanical properties of the foam including crosslinked PVC, linear PVC, PET and PEI PVC have been obtained and evaluated (Hassan et al., 2012; Zhou et al., 2012). Table 4-1 summarises the properties of the thirteen different foams involved in composite structures of this investigation. Five of the foams were based on crosslinked PVC foams with densities between 40 and 200 kg/m^3. The three linear PVC foams offered densities between 60 and 140 kg/m^3. Two PET foams had densities of 105 and 135 kg/m^3 and the two PEI foams offered densities of 60 and 80 kg/m^3.

Table 4-1 Mechanical properties of the foams investigated in this research

Mechanical properties	C40	C60	C80	C100	C130	C200	L60	L90	L140	PET105	PET135	PEI 60	PEI 80
Density (kg/m^3)	40	60	80	100	130	200	30	90	140	105	135	60	80
Poisson's ratio	0.32	0.32	0.32	0.32	0.32	0.32	0.32	0.32	0.32	0.32	0.32	0.32	0.32
Compressive modulus (MPa)	37	69	97	125	160	280	30	56	110	90	140	46	62
Compressive strength (MPa)	0.45	0.9	1.3	1.9	2.6	4.8	0.38	0.9	1.6	1.4	2.4	0.7	1.1
Compressive fracture strain	0.68	0.7	0.7	0.7	0.7	0.7	0.7	0.7	0.7	0.7	0.7	0.7	0.7
Tensile modulus (MPa)	21	45	66	84	110	175	30	50	90	110	175	45	54
Tensile strength (MPa)	0.6	1.3	2	2.7	3.8	6	0.9	1.4	2.4	2.3	3.3	1.7	2.0
Shear modulus (MPa)	13	22	30	38	47	75	11	21	37	21	30	18	23
Shear strength (MPa)	0.45	0.8	1.2	1.6	2.3	3.5	0.5	1	1.85	0.9	1.3	0.8	1.1
Shear fracture strain	0.08	0.16	0.23	0.27	0.3	0.3	0.7	0.75	0.8	0.15	0.12	0.25	0.23
Work of fracture in tension (kJ/m^2)	0.16	0.26	0.44	0.62	0.76	1.33	2.38	6.06	12.1	2.3	2.5	0.87	15.8
Work of fracture in shear (kJ/m^2)	3.21	6.48	12.6	18.4	27.6	44.2	17.3	21.3	27.3	7.38	18.2	1.16	24.8

4.2.2 The effect of loading rate on the foam toughness

Dynamic compression tests have been undertaken using a drop-weight impact tower shown in Figure 3.6 to compare with quasi-static results in order to investigate the strain-rate effects in a range of foams subjected to compressive crushing loading. Figure 4.2 shows typical stress-strain traces for the C80 and C130 foams following dynamic crushing tests and quasi-static tests. Both traces exhibit similar trends with the force rising rapidly to a maximum value before dropping and becoming highly oscillatory. It is clear that all samples exhibit a clear plateau stress followed by well-defined densification region. As expected, both the modulus and strength of plain foams exhibit a pronounced dynamic enhancement, with the increases in strength and plateaus stress being approximately fifty percent for the 130 kg/m^3 foam. Figure 4.3 summarizes the strength of foams with density ranging between 40 to 200 kg/m^3 under both the dynamic quasi-static loading and indicates significant increases of strength with the increasing of foam density.

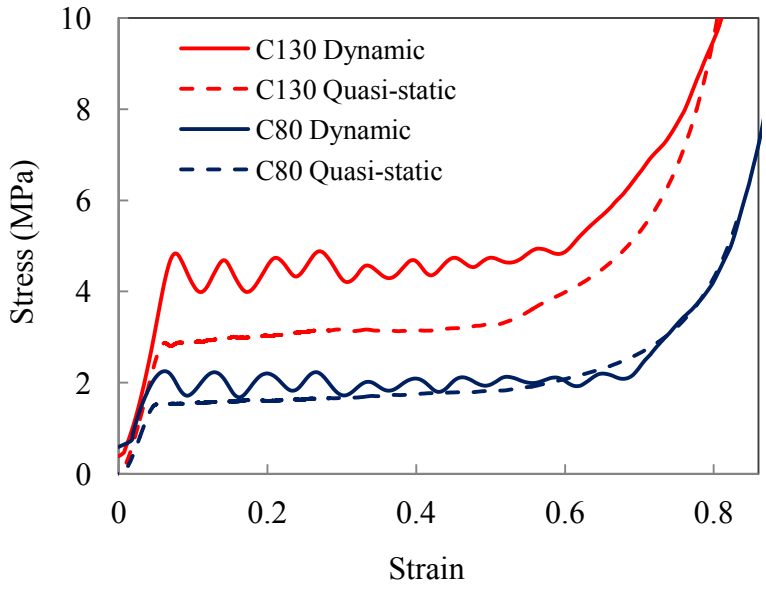

Fig. 4.2 Typical stress-strain traces following quasi-static and dynamic tests on the C80 and C130 crosslinked PVC

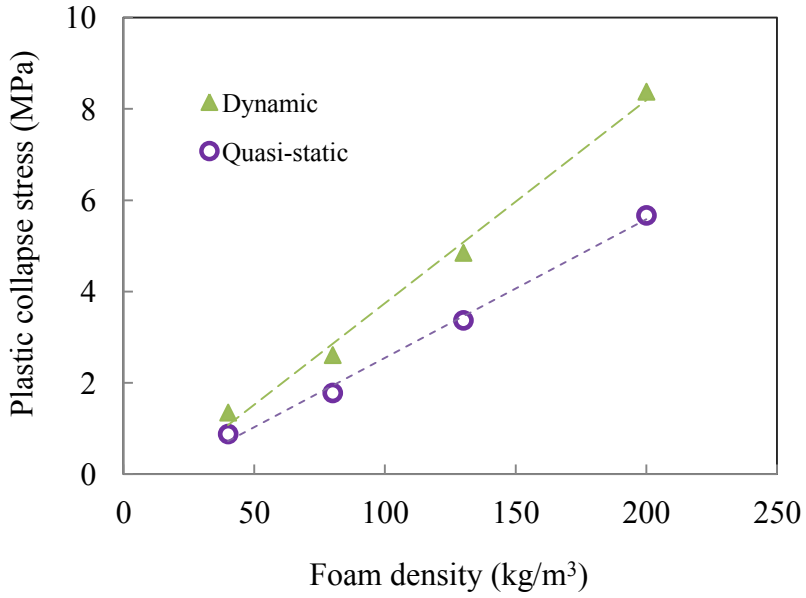

Fig. 4.3 The variation of plastic collapse stress with density for different loading rates at quasi-static and dynamic.

Both the energy required to crush the foam panels and specific energy absorption were determined from the area under the load-displacement trace. The resulting values of SEA are summarized in Figure 4.4. An examination of the figure indicates that the SEA values of dynamic load trend to plateau towards with increasing values, following a similar trend associated with the foam at quasi-static load. The maximum value of SEA in the figure is approximately 25.5 kJ/kg at dynamic rate, exhibits an significant increasing over the value maximum of 16.3kJ/kg at quasi-static rate. Both C80 and C130 foams exhibit increases in SEA with the latter being approximately fifty percent,

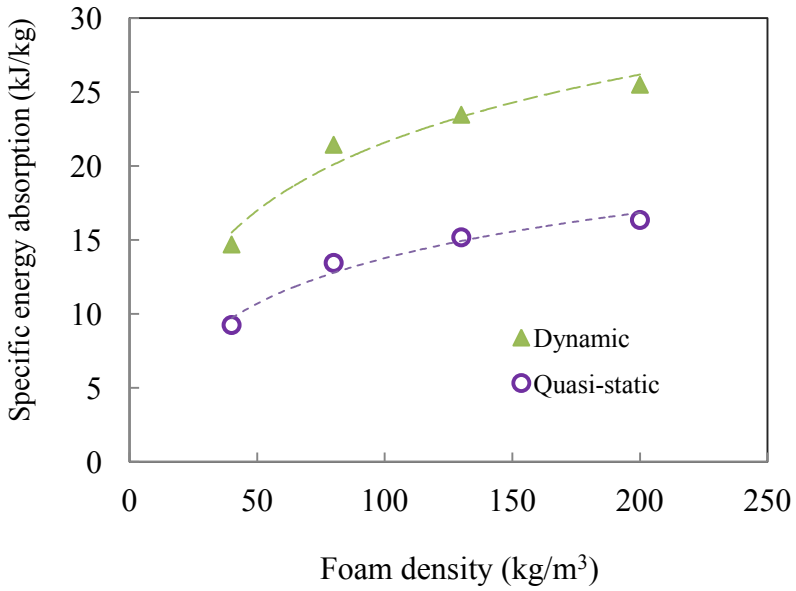

Fig. 4.4 The variation of SEA with density for different loading rates at quasi-static and dynamic strain rates.

4.2.3 The effect of ductile and shear properties on the toughness

The shear tests have been undertaken in order to evaluate the performance of perforation resistance on foams and define damage criterion of FE modeling in the following Chapter 5. The resulting values for work of fracture in tension and shear are presented in Table 4-2.

Table 4-2 Work of fracture values of foams and perforation energies of the sandwich structures

Foam	Work of fracture in tension (kJ/m^2)	Work of fracture in shear (kJ/m^2)	E_{perf} Core Experimental (J)	E_{perf} Sandwich Experimental (J)	Specific Perforation Energy E/ρ ($J \cdot m^3/kg$)
C60	0.26	6.48	3.93	10.69	0.178
C80	0.44	12.6	10.16	15.46	0.193
C100	0.62	18.4	8.76	18.34	0.183
C130	0.76	27.6	17.7	27.06	0.208
C200	1.33	44.2	32.92	55.85	0.279
L60	2.38	17.3	4.12	17.30	0.179
L90	6.06	21.2	5.33	20.07	0.223
L140	12.1	27.3	8.32	25.56	0.183
PET 105	2.3	7.38	9.57	9.12	0.087
PET 135	2.5	18.2	26.1	19.03	0.141
PEI 60	0.87	1.16	-	-	-
PEI 80	15.8	24.8	-	-	-

The toughness properties of the foams were characterised by determining the work of fracture from the energy under the load-displacement traces and the area of the fractured ligament following Mode I (opening) and Mode II (shear tests) tests. Figures 4.5 and 4.6 show load-displacement traces obtained following Mode I and Mode II tests on the foams. The former was obtained using the single edge notch bending geometry and the latter using a developed shear geometry described in Chapter 3.

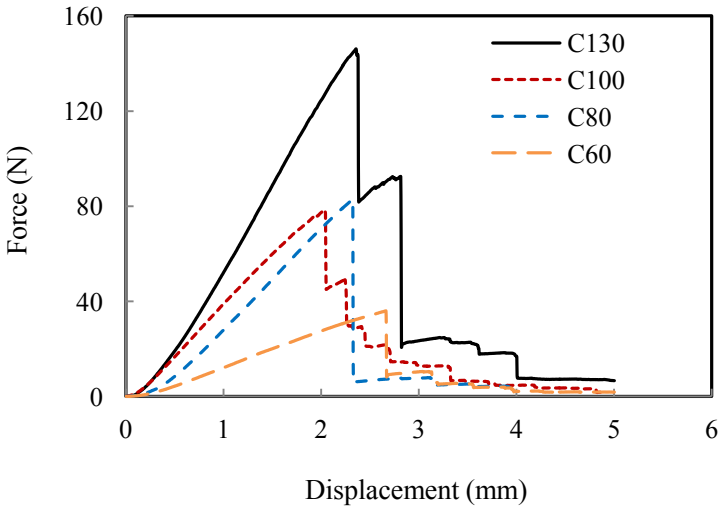

(a) Crosslinked foams,

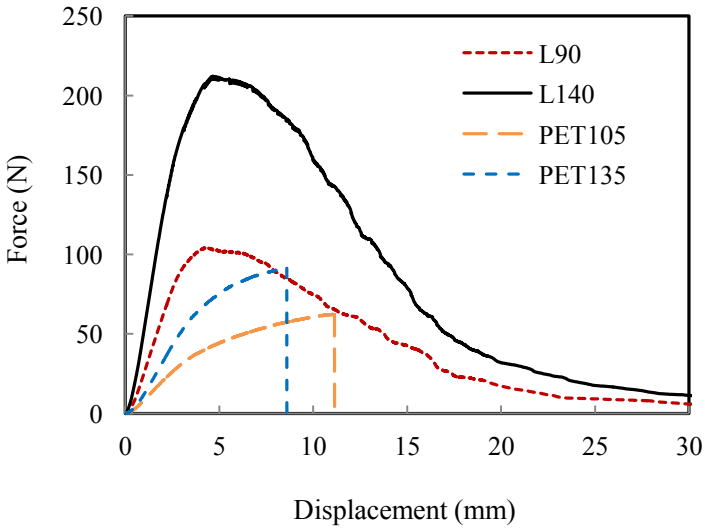

(b) Linear and PET foams,

Fig. 4.5 Force-displacement curves from the single edge notch bending tests for different foam cores.

An examination of Fig. 4.5 indicates that the crosslinked and PET foams fail in an unstable manner, whereas the linear PVC foam fails in a more ductile fashion involving gross plastic deformation in the cell walls. Failure in shear generally occurred in a stable fashion although some load drops were apparent in the crosslinked foams. Here, it is evident that the Mode I fracture properties of the linear PVC foams are significantly higher than those associated with its crosslinked counterpart. It is also evident that the Mode II work of fracture properties of the foams much higher than the Mode I values, with the difference being most pronounced in the crosslinked systems shown in Figure 4.6.

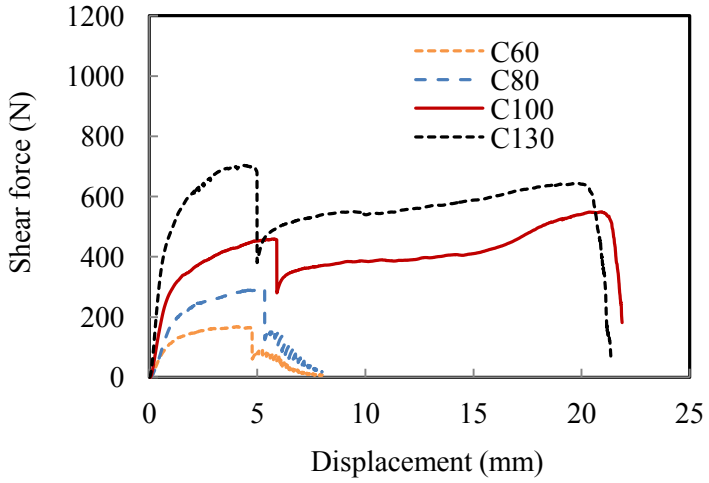

(a).Crosslinked foams,

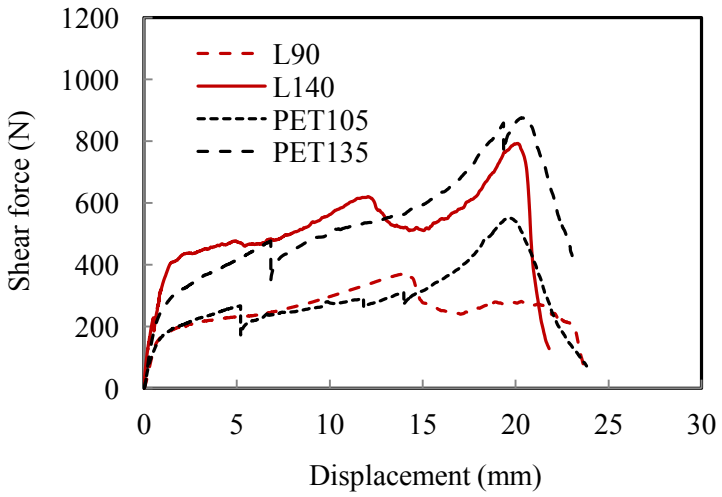

(b).Linear and PET foams,

Fig. 4.6 Force-displacement curves from the shear tests for different foam cores.

4.2.4 Impact response of plain PVC foam

Low velocity impact test has been carried out on PVC foam following the test procedures described in Section 3.4.1. Figure 4.7 (a) shows typical load-displacement traces following impact tests on three of the crosslinked PVC foams. All three experimental traces display similar trends. The initial portions of the load-displacement trace exhibit some oscillatory behaviour due to dynamic effects in the plate and ringing in the load cell, with its slope reflecting the elastic modulus of the foam. With increasing load, a knee is reached beyond which the slope of the traces decreases as the projectile starts to crush the foam and penetrate the top surface of the panel. Finally, the load drops sharply as the steel projectile perforates the target.

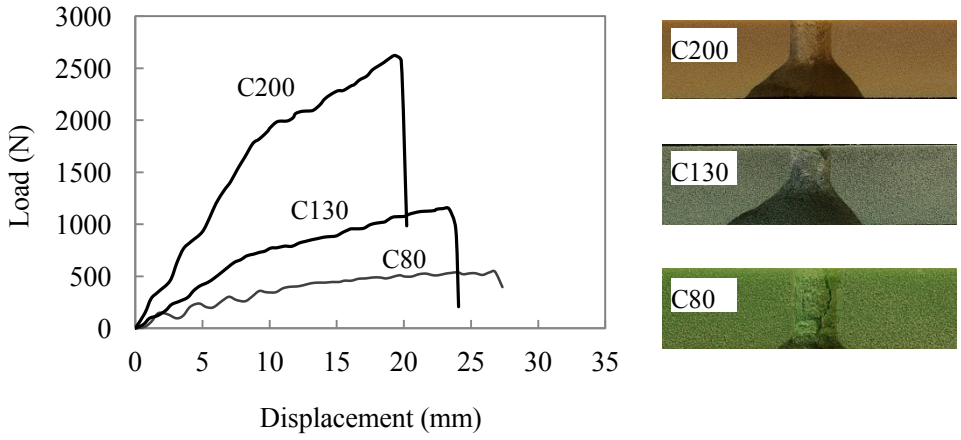

(a) load- displacement traces (b) Cross-sections

Fig. 4.7 Comparison of load-displacement traces and cross-sections of crossed-linked PVC foams.

Figure 4.7 (b) compares the experimental perforation zones for the three foam panels. The lowest density C80 foam (as well as the C60 and C100 foams) exhibited a cylindrically-shaped shear zone, similar in size to the diameter of the projectile. Perforation in the intermediate (130 kg/m^3) and high (200 kg/m^3) density foams resulted in a mixed mode of failure, with a cylindrical shear region in the upper half of the sample and a frustrum-shaped zone in the lower portion of the test panel. Similar distinctive conical-shaped fracture zones have been observed following impact on brittle glasses (Wilshaw, 1971), where it has been shown that locally-high tensile stresses under the indentor give rise to this low energy mode of fracture (Ball, 1996). The cross-sections suggest, therefore, that the 60, 80 and 100 kg/m^3 foams fail in the higher energy shearing mode, whereas the 120 and 200 kg/m^3 fail as a result of a lower energy, mixed tensile/shear mechanism. This evidence suggests the

perforation resistances of these foams are likely to be determined by the tensile and shear fracture properties of the foams. The fracture properties of these foams, subjected to these two modes of loading, have been investigated in a previous study (Hassan and Cantwell, 2012). In this earlier investigation, the work of fracture (W_f) values of these foams in tension and shear were measured using a recently-developed shear rig and the single edge notch bend (SENB) specimen geometry respectively. The resulting values are listed in Table 4-2 (Hassan and Cantwell, 2012). An examination of the data indicates that the shear values of W_f are significantly higher than their corresponding tensile values. This evidence suggests that those samples exhibiting a cone cracking mode of failure are not achieving their full potential in terms of their energy-absorbing capability.

Figure 4.8 (a) shows the load-displacement traces for the L140 and PET135 foam materials. Increasing the density from of the foam has a significant influence on the initial stiffness of the plate, the impact response with the maximum force and general shape of the load-displacement trace. Figure 4.8 (b) shows the resulting cross-sections for both foams, where it is clear that the liner L140 foam exhibits a mixed type of failure with the upper part of the plate failing in the higher energy shear mode whereas PET135 foam failure in a tensile mode at the lower region of the target. Failure in the PET system is less distinct, although there is some evidence of a transition region at the mid-plane of the sample.

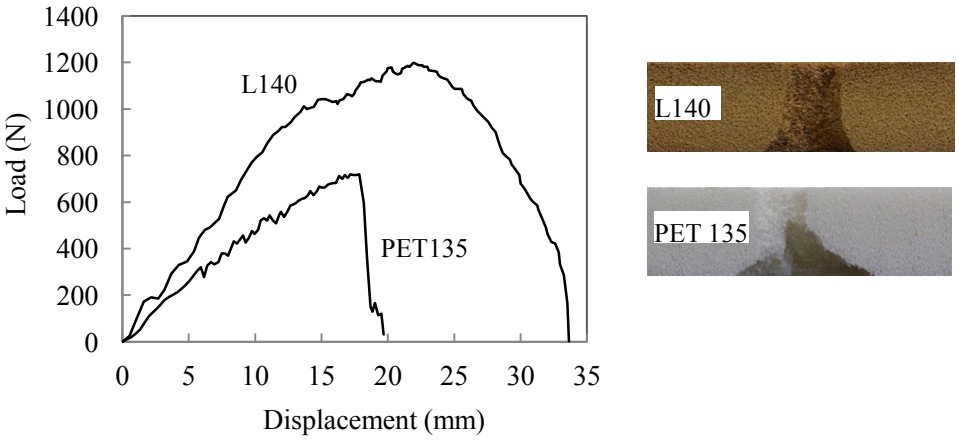

(a) load- displacement traces (b) Cross-sections

Fig. 4.8 Comparison of load-displacement traces and cross-sections of Liner PVC and PET foams.

Figure 4.9 presents a comparison of the measured perforation energies of nine plain core materials.

Once again, the energy required to perforate the foam panels were determined from the area under the load-displacement trace. The perforation energies of the three types of foam for the crosslinked PVC, linear PVC and PET foams are summarized here. It is evident that the linear PVC foams offer a superior perforation resistance to their crosslinked counterparts. Interestingly, an examination of the Mode II work of fracture data in Table 4-2 suggests that the higher density crosslinked foams would have out-performed their linear counterparts if failure had occurred in a pure shear mode rather than a mixed shear/tensile mode. Finally, it is evident that the PET foams offer the lowest perforation energies, with values approximately one half those offered by the crosslinked foams.

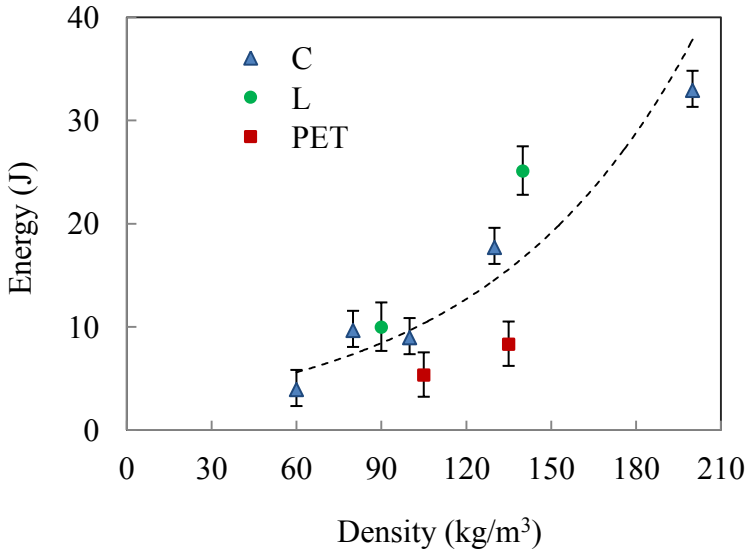

Fig. 4.9 Perforation energy versus density for the linear PVC, crosslinked PVC and PET PVC foam panels.

4.2.5 Impact response of plain foam based sandwiches

The sandwiches specimen descried in Section 3.3.1 have been tested following impact perforation descried in Section 3.4.1. Figure 4.10 presents typical load-displacement traces following low velocity impact on sandwich structures based on the three crossslinked foams presented in Figure 4.7. The lowest density foam exhibits a classic load-displacement trace (Wen et al., 1998) with pronounced peaks associated with fracture of the upper and lower skins and a relatively smooth plateau resulting from the projectile passing through the foam core. The trace for the 130 kg/m^3 foam exhibits an initial peak resulting from fracture of the top skin followed by a steadily increasing force up to final perforation. Here, a small final peak in the load is apparent as the projectile finally

fractures the lower surface skin. Finally, the highest density foam system offers a steadily increasing load-displacement curve in which failure of the composite skins is difficult to discern. A comparison of Figures 4.7(a) and 4.10 (a) suggests that the core plays an increasingly dominant role as the density of the foam is increased. Indeed, at higher densities, the load-displacement traces closely resemble those of the plan core panels. Interestingly, the failure processes were similar in all of the sandwich structures, with the projectile shearing a relatively clean hole through the target, Figure 4.10 (b). Given that there was little evidence of the distinct frustrum-shaped fracture zone observed in the higher density plain crosslinked cores, it is evident that the core in these sandwich structures is absorbing more energy than their plain foam counterparts.

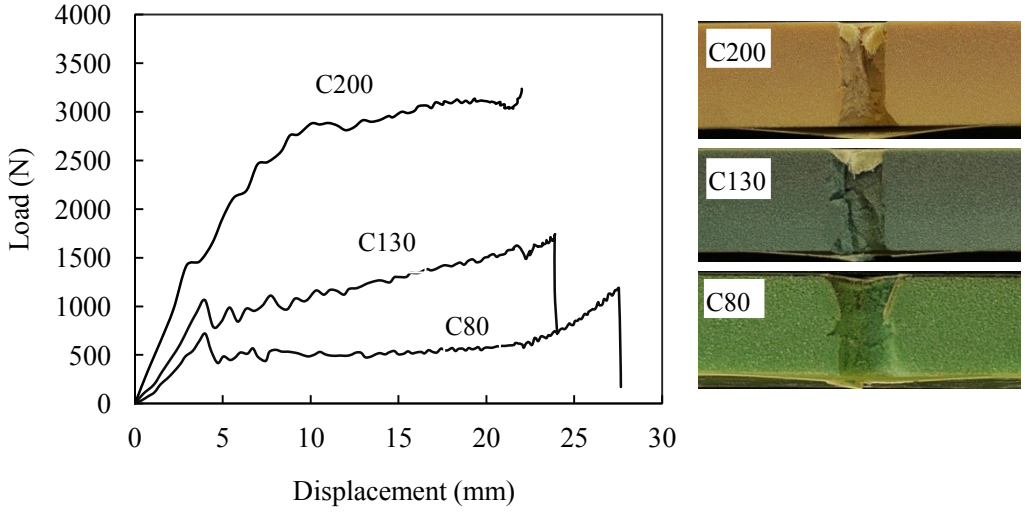

(a) load-displacement traces (b) cross-sections

Fig. 4.10 Comparison of load-displacement traces and cross-sections of sandwiches made with C70 foam cores.

Figure 4.11 (a) shows the load-displacement traces for the sandwich structures based on the 105 kg/m^3 PET and the 140 kg/m^3 linear PVC foams. The former exhibits two well-defined peaks resulting from fracture of the two skins as well as a region of constant force in which the projectile passes though the foam core. In contrast, the response of the higher density linear PVC foam is once again largely dominated by the fracture behaviour of the core material. The cross-section of the experimental PET-based system displays a frustrum-shaped fracture zone similar to that observed in the plain foam, Figure 4.11 (b) presents a distinct conical zone observed on both the higher density plain L140 and PET 135 cores.

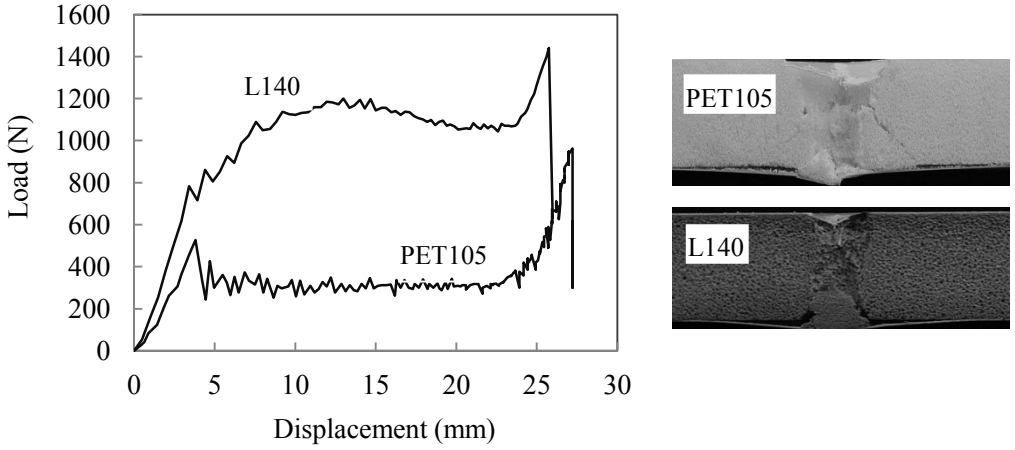

(a) load-displacement traces (b) cross-sections

Fig. 4.11 Comparison of load-displacement traces and cross-sections of sandwiches made with L140 and PET135 foams.

The energies required to perforate the sandwich structures are summarised in Figure 4.12. It is interesting to note that in certain cases, the addition of the composite skins has a important affect on the energy-absorbing capacity of the core. This is most pronounced in the highest density crosslinked PVC foam which exhibited a significant enhancement in impact resistance following the addition of skins. Here, a change in failure mode was observed, passing from a mixed tensile-shear in the plain foam to a pure shear mode in the sandwich. As shown in Table 4-2, the fracture energy associated with tensile failure is relatively low, and one would therefore expect a significant improvement in perforation resistance as the failure mode shifts to pure shear. From the figure it is also evident that the perforation resistance of the lowest density linear PVC foam is superior to that of its crosslinked counterpart, whereas the converse was true for higher density systems. Interestingly, the shear work of fracture values exhibit similar trends, the evidence suggests that the shear fracture properties of the linear and crosslinked foams cross at approximately 115 kg/m^3, a value similar to that observed in the perforation data in Figure 4.12. This evidence again supports the conclusion that the fracture properties of the foam strongly influence the perforation resistance of these thin-skinned sandwich structures. Finally, it is clear that the PET-based sandwich structures clearly offer the lowest perforation resistance reflecting the lower fracture properties of this foam.

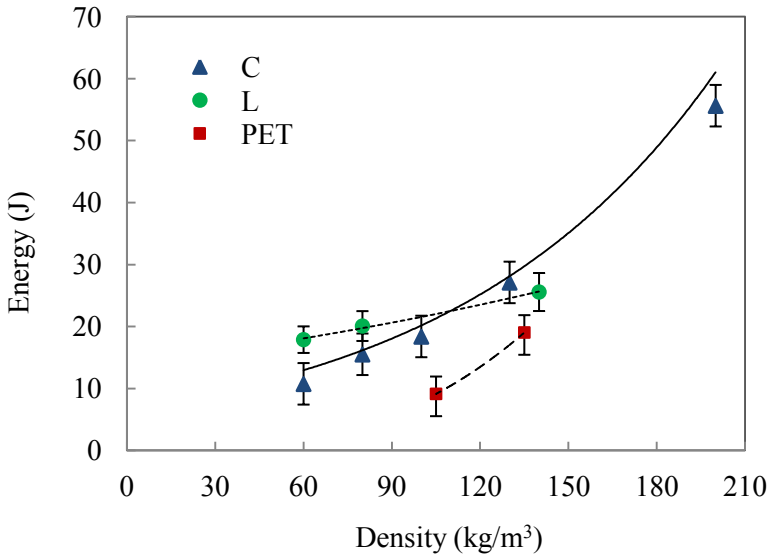

Fig. 4.12 Perforation energy versus density for the linear PVC, crosslinked PVC and PET-based sandwiches.

4.2.6 Impact response of sandwich panels supported on water

As a result of their superior specific properties and non-magnetic characteristics, sandwich structures are finding increasing use in the design of boats hulls and other primary marine structures. In order to investigate the influence of an aqueous environment on the dynamic response of a sandwich structure, a series of low velocity impact tests were undertaken on panels supported on a combined circular ring/water base, described in Section 3.4.1. Here, the ring support used for the earlier perforation tests was filled with water and panels were placed on the water base and clamped using a steel ring, shown in Figure 3.15, as before. Three types of sandwich structure were tested, these being based on the L140, the PET135 and the C130 foams. Figure 4.13 shows load-displacement traces for the L140 and PET135 based sandwich structures. An examination of the traces for the linear PVC sandwich structures (L140) in Figure 4.13 (a) indicates that the panels supported on the water foundation exhibit reasonably similar traces up to the point at which the projectile approaches the rear surface. Here, the force rises rapidly in the ‘wet’ system before dropping rapidly as the rear surface fractures. It is clear that the rear surface peak is much higher in the fully-supported wet panel than in its dry counterpart. Similar load-displacement traces obtained from the experimental test on the PET 13T based PVC sandwich structures shown in Figure 4.13 (b), indicates that the higher rear surface peak and lower resistance displacement. In addition, the wet panel exhibits

virtually no out of plane deflection, in contrast to the relatively flexible dry panel.

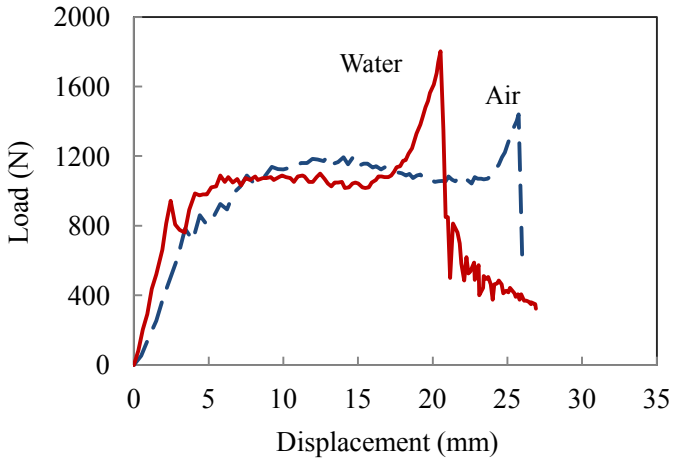

(a) L140 based sandwiches

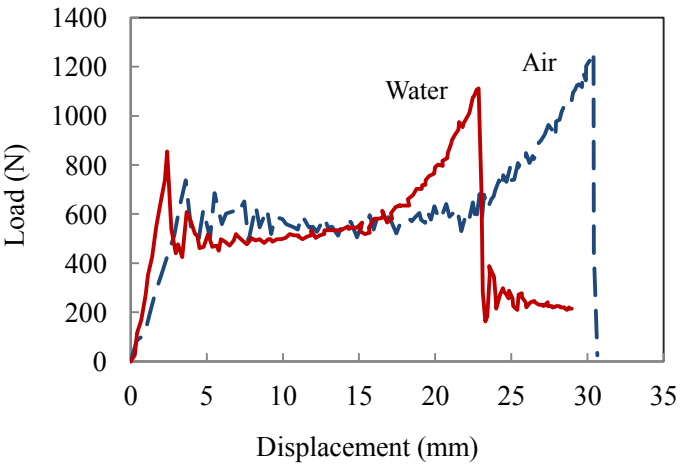

(b) PET135 based sandwiches

Fig. 4.13 Comparison of load-displacement traces of sandwiches made with PET135 and L140 foam cores between sandwiches supported on water and without support.

The measured perforation energies for the three wet sandwich structures are compared with their corresponding dry samples in Figure 4.14. From the figure, it is clear that the ‘wet’ panels offer a lower resistance to perforation than their dry counterparts. This reduction is largely associated with the inability of the former to deflect out-of-plane. This is demonstrated clearly in Figure 4.13, where the projectile displacement at the instant that the lower skin fails is similar to the initial thickness of the panel. It is interesting to note that the flexural response of the sandwich structures has been largely suppressed in an aqueous environment.

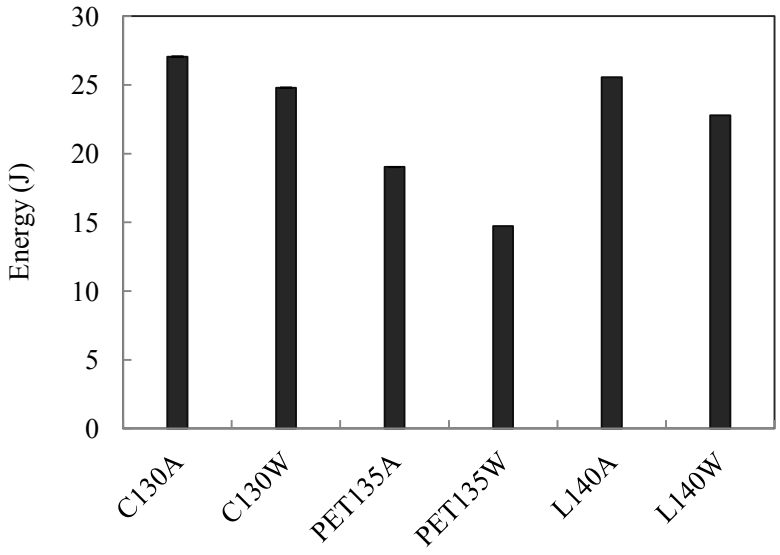

Fig. 4.14 Comparison of energy absorption of sandwiches made with C130, PET135 and L140 foam cores between sandwiches supported on water and without support.

4.3 Impact response of graded foam based sandwich panels

Low velocity impact tests have been undertaken on graded foam based sandwich structures. The layered foam core fabricated by bonding foams of different densities together, as description in Section 3.2.2, cover a range of linear PVC, crosslinked PVC and PEI foams together to produce a three layer core. Carbon fibre skins were then bonded to the core and the structures were loaded by a drop-weight impact carriage with a hemispherical head. Extensive testing on the twelve core configurations outlined in Table 3-3 in Chapter 3 has shown that the advantage of graded core over the plain core based sandwiches.The following section presents test results on load-displacement traces and failure modes. The energy absorption has been summarized and the performance comparison has been analyses in this section.

4.3.1 Low velocity impact tests of graded foam based sandwiches

Low velocity impact tests were conducted on the graded foam based sandwiches using a drop-weight impact tower, shown in Figure 3.14. Figure 4.15 (a) shows typical load-displacement traces for a sandwich panels based on the C100/P80/P60 and the equivalent inverted structure, i.e. the P60/P80/C100, foam combinations. An examination of the figure indicates that the force initially

increased up to approximately 500 Newtons at which point it reaches a plateau. The force then remains roughly constant as the projectile perforates the three foam materials, suggesting that the fracture properties of the three foams are similar. Finally, the force begins to increase rapidly as the projectile approaches the rear surface of the target. Here, it is likely that the lowermost foam is crushed between the steel impactor and the rear surface skin. Clearly, the peak force associated with fracture of the rear skin is significantly higher (by a factor of approximately three) than that needed to cause failure in the front skin. Finally, the force drops rapidly at a displacement of 36 mm as the projectile fully perforates the lower skin and passes through the composite. Figure 4.15(b) shows cross-sections of the fully perforated sandwich structures, where the presence of a distinct cylindrically-shaped shear zone is evident in both the test specimen and the model. An examination of the measured load-displacement traces for the equivalent inverted structure, i.e. the P60/P80/C100 core configuration also shown as dish line in the Figure 4.15(a) suggests that there are many similarities with its counterpart of the C100/P80/P60. Closer inspection highlights the presence of the three cores, with the plateau loads increasing from approximately 250 to 400 to 600 Newtons as the projectile passes through the three foams. The experimental trace also exhibits a more pronounced initial peak and a larger exit peak. The corresponding cross-sections are shown in Figure 4.15(b), where a cylindrically-shaped perforation zone is again present. Closer inspection of the lowermost foam highlights the presence of a frustrum-shaped zone similar to that observed following impact tests on plain foams (Zhou et. al., 2012). Cone-shaped fracture zones, such as this, are associated with a combined tensile/shear mode of failure, rather than the pure shear mode occuring during the earlier stages of the perforation process (Zhou et. al., 2012).

An similar configuration using two types of foam cores with low densities from 60 to 100 kg/m^3 and the corresponding cross-sections are shown are shown in Figure 4.15(c) and (d). i.e. the C80/L60/C100. Once again, the examination of the figure indicates that the resistance force remains roughly constant as the projectile perforates the three foam layers, suggesting that the fracture properties of the three foams are similar when foam density is in similar range. The cross-sections show a frustrum-shaped zone, which is similar to that observed in Figure 4.15(b).

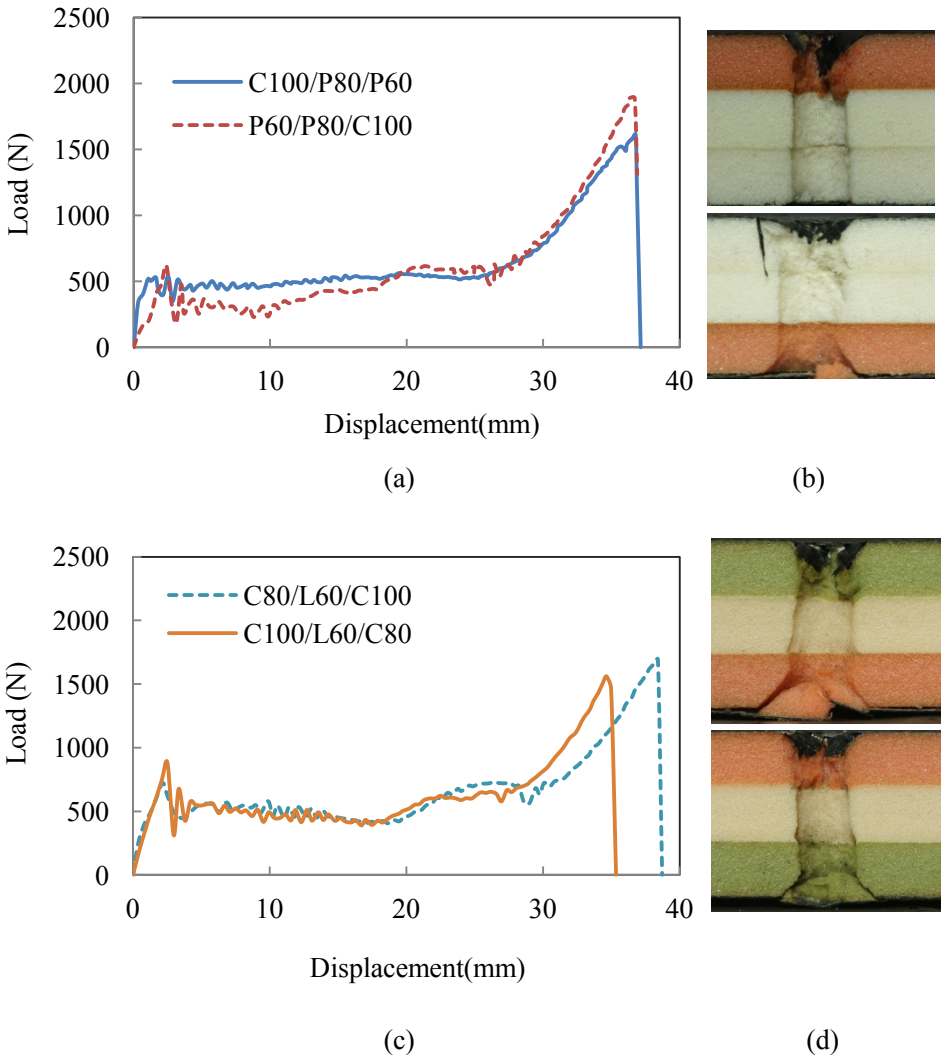

Fig. 4.15 Load-displacement traces and failed cross-sections for (a,b) the C100/P80/P60 and P60/P80/C100, (c d) for the C80/L60/C100 and C100/L60/C80 sandwich structure.

Figure 4.16(a) and (b) shows the experimental load-displacement traces for the L80/C60/C200 (dash line) and its inverted sandwich structure (solid line). The experimental trace exhibits a number of distinct regions as the projectile passes through the various components of the sandwich panel. The initial portion of the trace is linear up to approximately 850 Newtons, at which point the top surface skin fractures and the load drops. The force then oscillates around a value of approximately 750 Newtons, as the projectile passes through the tough L80 foam. The force then reduces as the impactor passes through the more brittle crosslinked foam (C60) before increasing rapidly as it encounters the C200 foam. The final stage of the load-displacement trace exhibits a region in which the force oscillates as the C200 foam is crushed and densifies under the constraint applied by the rear surface skin. Figure 4.16(b) shows that the perforation zone is again cylindrically-shaped, although a

small cone crack is in evidence at the exit surface. The load-displacement traces for the corresponding inverted sandwich structure are shown as dash line in Figure 4.16(a) as well. Here, the different fracture responses of the three foams are apparent, with the uppermost, high density C200 foam offering the greatest resistance to perforation and the more brittle C60 system exhibiting the lowest. It is also interesting to note that the force associated with fracturing the lowest skin is less than that apparent, due to the lower densification characteristics of the L80 foam. The resulting cross-section from the test, Figure 4.16(b), highlights the presence of a crack in the uppermost C200 foam that appears to have influenced the subsequent failure locus in the remainder of the structure. Load-displacement traces on configuration of the L140/L80/C60 and inverted core based sandwich structure are shown are shown in Figure 4.16(c). The failure mode in Figure 4.16(d) shows a delamination between foam layers.

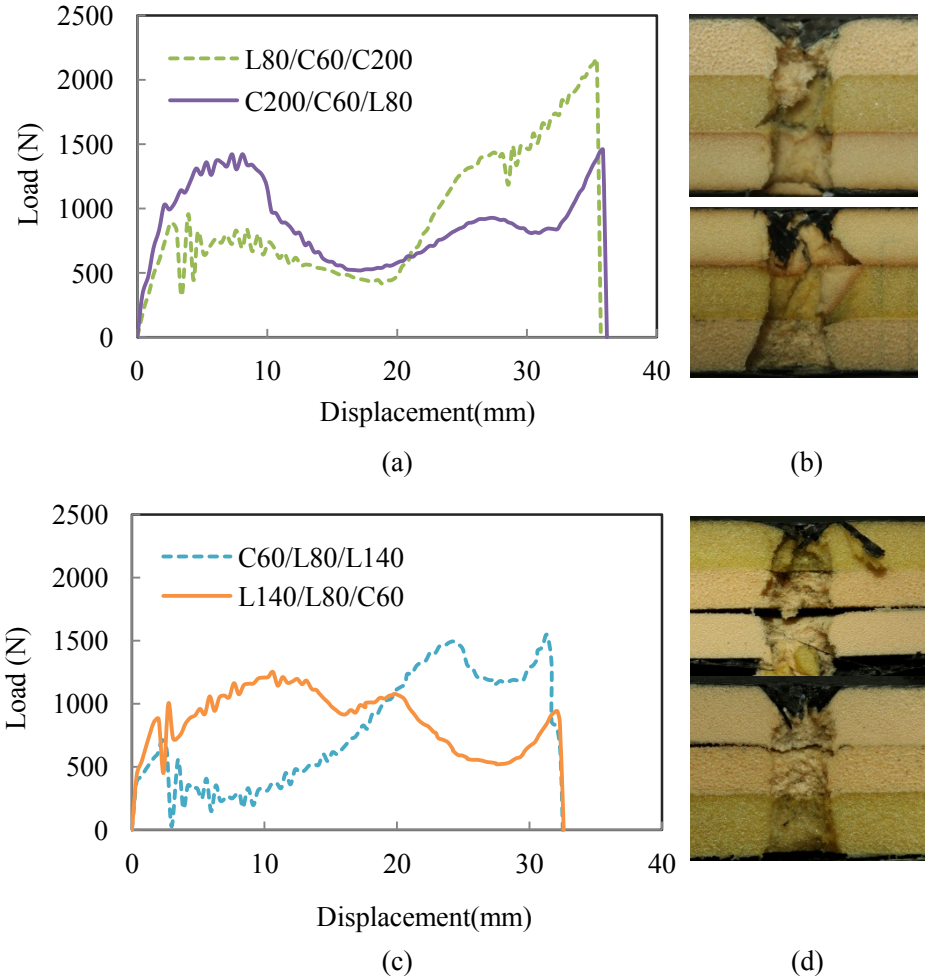

Fig. 4.16 Load-displacement traces and resulting cross-sections for (a, b) the L80/C60/C200 sandwich structure and its reverted structures, (c, d) for the L140/L80/C60 sandwich structure and its reverted structures.

Figure 4.17 (a) shows the force-displacement traces for the L60/P60/L140, C200/P60/P80 and their inverted sandwich structures. Clearly, there are similarities between this response and that sandwich with high density core layer at top shown as the solid lines in Figure 4.16 (a) and (c), with the perforation force increasing in three steps between the peaks associated with fracturing the upper and lower skins. The plateau force resulting from fracturing the tough high density L140 and C200 foam is significantly higher than that required to perforate its lower density L60 and P80 counterpart. A similar response on configuration of the inverted core based sandwich structure (P80/P60/C200 and P80/P60/C200) shown as the dash lines are shown in Figure 4.17(a) and (c). Finally, the resulting cross-section for both structures are shown in Figure 4.17 (b) and (d). It noted that the different core type of PEI foam was evaluated to compare with earlier configuration.

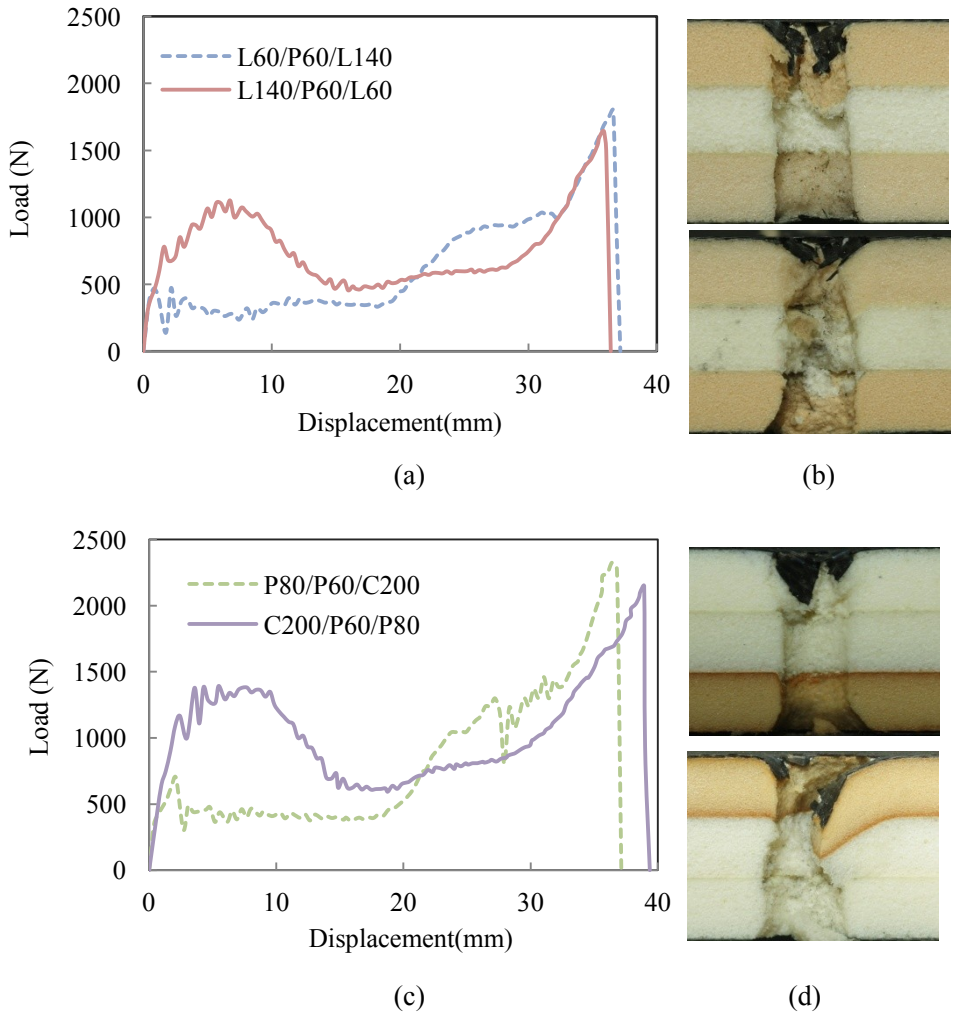

Fig. 4.17 Load-displacement traces and resulting cross-sections for (a, b) the L60/P60/L140 sandwich structure and (c, d) for the L140/P60/L60 sandwich structure.

4.3.2 Perforation energies of the sandwich panels

The energy required to perforate the sandwich structures was calculated by determining the area under the load-displacement traces. Figure 4.18(a) compares the perforation resistances of the twelve configurations investigated here. From the figure, it is clear that the perforation energy varies quite significantly, with the experimental values passing from 21.9 Joules for the C100/L60/C80 sandwich to 40.8 Joules for the C200/P60/P80 configuration. If the perforation energy of the layered target is assessed in terms of the average density of the core, the perforation resistance tends to increase with core density. Within each density grouping of structures, there are distinct variations that depend on the specific arrangement of the layers. This is most evident in Panels C9 (P80/P60/C200) and C10 (C200/P60/P80) in which the former has the high density C200 core at the top surface and latter at the rear surface. Placing the higher density, tougher foam uppermost resulted in a 30% increase in the perforation resistance. An examination of the cross-sections of Structure C9 highlighted the presence of a distinct cone-shaped crack in the lower C200 foam. This can be explained from the fact that this form of failure is associated with a mixed mode of loading (Mode I /Mode II) and also the fact that the Mode I work of fracture is much lower than its Mode II value. Clearly samples that fail in a mixed-mode of failure, such as panel C9, are therefore more likely to offer a lower resistance.

Given that the densities of the graded foam cores do vary quite significantly, the perforation energy of the various targets were normalised by the average core density to yield the specific perforation values and these are presented in Figure 4.18(b). When the data are normalised in this way, the previously-observed differences between the foams reduces, although the C200/P60/P80 system still offers the highest performance. The difference between the best-performing and the worst-performing configurations is reduced to 25%.

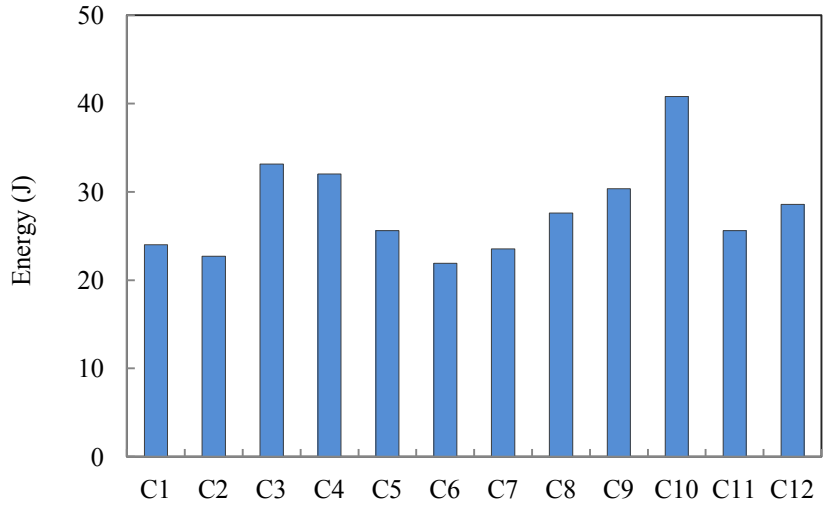

(a) Comparison of the experimental perforation energies.

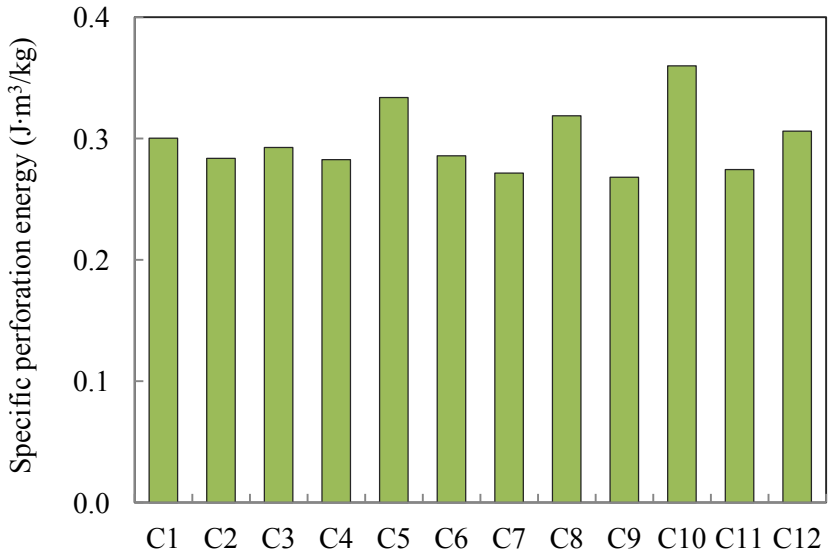

(b) Evaluation of energy absorption capacity normalised by the average core density to yield specific perforation values.

Fig. 4.18 Evaluation of perforation energies and energy absorption capacity of graded foam based sandwiches

Figure 4.19 shows a plot of the perforation energy versus average target density, highlighting the benefit of placing the highest density foam on the top surface. An examination of the figure indicates that those laminates in which the highest density foam is placed uppermost tend to out-perform equivalent systems in which the higher density foam is placed against the rear surface skin. The

figure also suggests that this enhancement tends to increase with increasing average foam density. Secondary benefits were also observed, such as placing the lowest density foam in the centre of the core and also placing a tough foam against the rear surface of the structure.

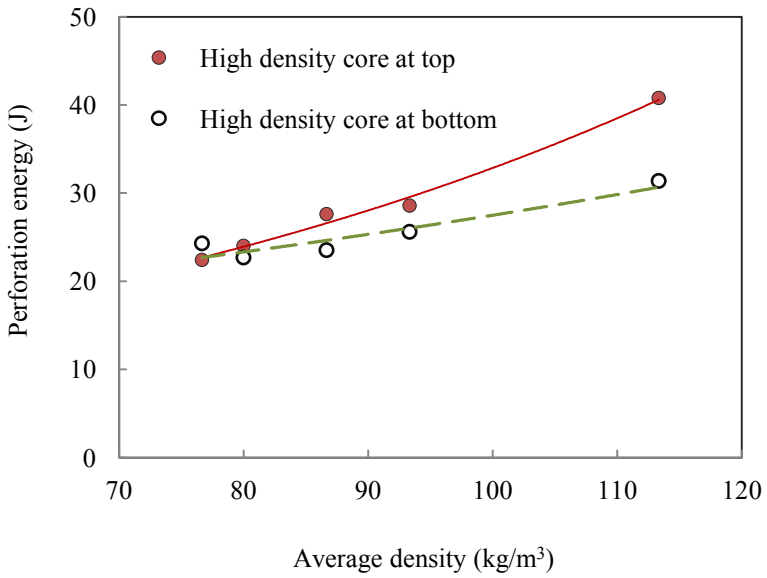

Fig. 4.19 Comparison of perforation energy against the average core density between different core layer arrangements.

Although performance is a key criterion in selecting a particular core for a given sandwich structure, cost is also an important parameter in the design process. Here, a cost factor was determined by normalising the cost of each foam by the cost of the most expensive foam tested here (this was the P80 foam) and then by multiplying this value by 100. The relative performance of each graded foam was then compared on a cost basis by dividing the perforation energy values by the cost factor, and these results are presented in Figure 4.20. An examination of the figure indicates that the perforation energy/cost ratio varies significantly across the range of structures considered. Of particular interest is Structure C5, based largely on low density foams. The performance of this sandwich structure out-performs Structures C1 and C2 by a factor of approximately four.

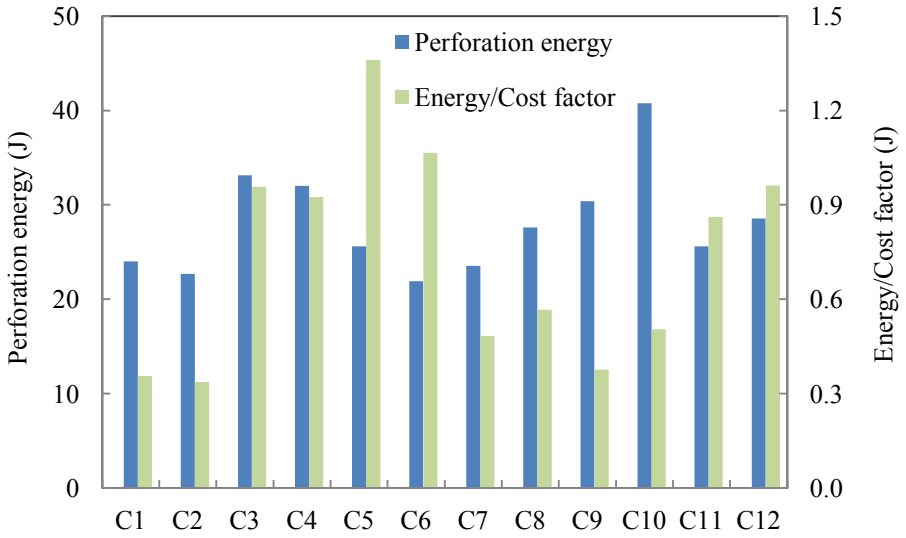

Fig. 4.20 Comparison of cost performance between graded foam based sandwiches.

4.4 Compression response of composite rod reinforced foam

Compressive tests have been undertaken on crosslinked PVC foam cores with densities ranging from 40 to 200 kg/m^3, reinforced with both carbon and glass composite rods with nominal diameters of 2, 3 and 4 mm on number of samples, described in Section 3.2.3. Drop-weight impact tests were conducted following the test procedures, described in Section 3.4.2 to investigate their dynamic performance and the results on their compressive strength and energy absorption are presented in the following sections.

4.4.1 Compressive tests of individual composite rods

Compressive tests have been conducted using the testing machine, described in Section 3.3.1. Figure 4.21(a) shows load-displacement traces following compressive tests on individual 4 mm diameter, 20 mm long carbon and glass fibre rods. An examination of the trace corresponding to the carbon fibre rod indicates that the force rises in a linear fashion up to approximately 2500 Newtons before dropping slightly and subsequently stabilizing at approximately 2300 Newtons. In contrast, the load-displacement trace for the GFRP rod drops sharply following the peak at 2100 Newtons to a much lower plateau value of 650 Newtons. It is worth noting that the Euler buckling loads for the 4 mm CFRP and GFRP rods are much higher than the plateau values in Figure 4.21 (a). Similar conclusions were drawn following the tests on the 2 and 3 mm diameter glass and carbon fibre rods, with failure occurring at loads significantly below those required to initiate buckling-type failure. Based on the energy under the load-displacement traces, it is evident that the carbon rods offer a much greater energy-absorbing capability than their glass fibre counterparts. This is highlighted by the difference in the specific energy absorption (SEA) values of the two types of composite, with the CFRP rods offering an average value of 59.5 kJ/kg, whereas the value for the glass-based system was only 19.6 kJ/kg. The resulting mechanical properties of the carbon and glass rods are summarised in Table 4-3.

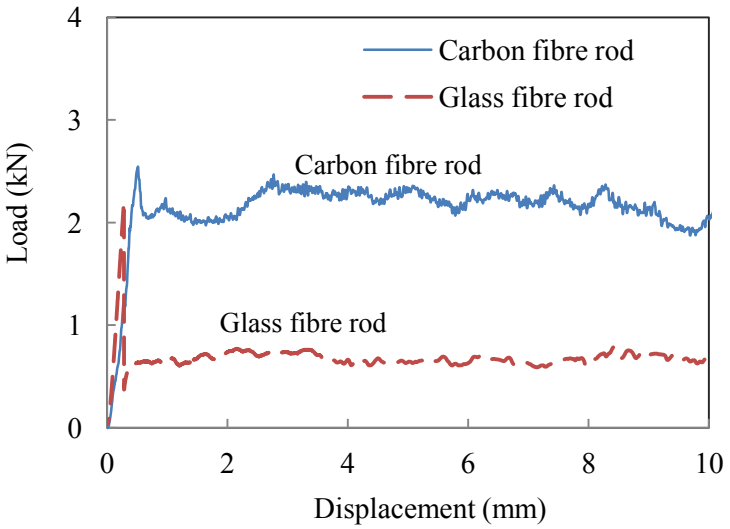

(a) Load-displacement traces

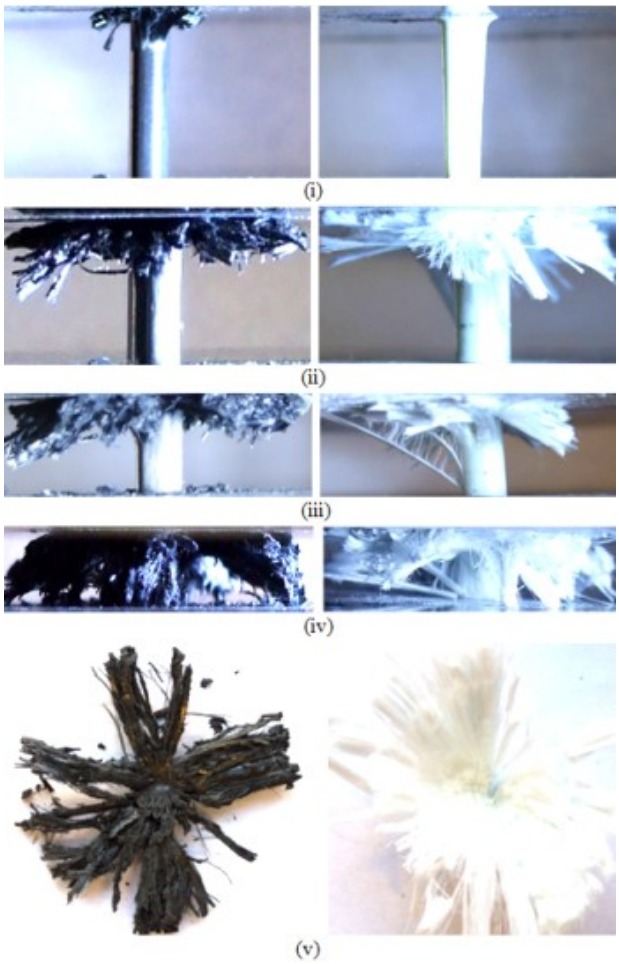

(b) Failure progress

Fig. 4.21 Compression load-displacement traces following tests on the carbon and glass fibre rods

Table 4-3 Mechanical properties of the carbon and glass fibre rods

	Carbon fibre rod	Glass fibre rod
Density (kg/m^3)	1986	2004
Tensile strength (MPa)	650	500
Compressive modulus (GPa)	8.1	14.3
Compressive strength (MPa)	202	167
Flexural modulus (GPa)	80	43
Flexural strength (MPa)	989	940
Weight fraction of fibre (%)	63.7	78.6

The failure modes in the individual carbon and glass fibre rods are shown in Figure 4.21(b). Failure in both rods initiated at the upper end of the sample. The carbon fibre rod exhibited a stable crushing process throughout the whole test, with the fibres splaying outwards during the crushing process. Similar failure modes have been observed during compression tests on carbon fibre reinforced epoxy tubes (Jacob and Fellers, 2012), where SEA values as high as 110 kJ/kg have been recorded. In contrast, the GFRP rods failed as a result of extensive longitudinal splitting immediately after the peak in the load-displacement trace. This longitudinal failure process is evident in certain micrographs, e.g. Fig. 4.21(b) iii, where long strands of composite have split away from the side of the rod.

4.4.2 Compressive tests on the reinforced foam samples

Figure 4.22 shows typical stress-strain traces for the carbon and glass fibre reinforced foams. The stress was determined from by the load divided by nominal area of specimen. All of the traces exhibit similar trends with there being little difference between the mechanical responses of the glass and carbon fibre reinforced foams. The stress-strain curves exhibit three distinct regions, these being a linear elastic region, a region of progressive crushing where the force remains roughly constant or drops slightly, and a final region of core densification, associated with a rapid rise in the measured force. An examination of the traces indicates that the onset of densification occurs at an earlier stage as the foam density increases.

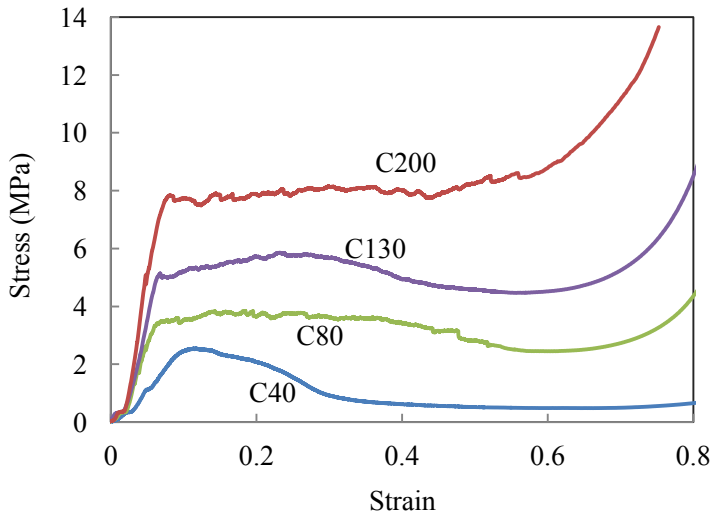

(a) 2 mm carbon fibre rods (Volume fraction of rods = 1.1 %),

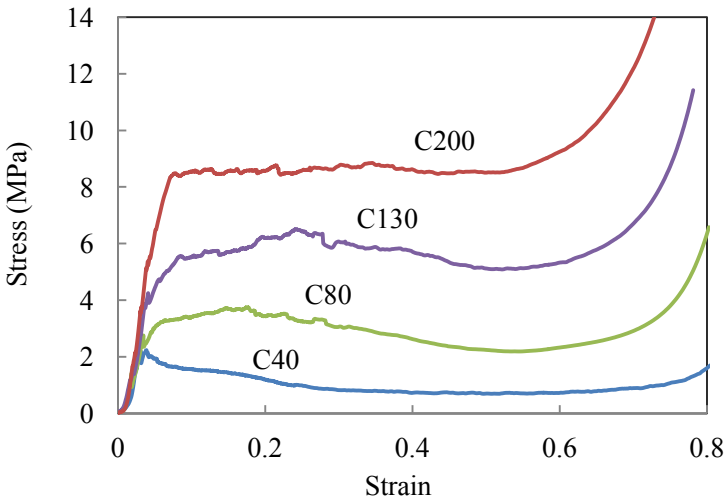

(b) 3 mm glass fibre rods (Volume fraction of rods = 2.5 %).

Fig. 4.22 Comparison of stress-strain traces of the reinforced foam panels with densities of 40, 80, 130, and 200 kg/m^3.

Figures 4.23(a) and (b) summarise the variation of the compression strength of the foams with both foam density and rod diameter. Also included in the figures are the values corresponding to nine free-standing individual rods. The latter were calculated based on the data from the compression tests on the individual rods. From the figure, it is evident that the compression strength of the reinforced foams increases in a linear fashion with foam density for a given rod diameter. It is interesting to note that the slopes of the traces for all of the reinforced samples are similar to that of the plain foams. Further, the values for the unsupported rods appear to sit on similar trendlines to those of the embedded rods. An examination of the figures indicates that there is a significant

improvement in the compressive performance in passing from a 3 mm diameter reinforcement to a 4 mm diameter rod. This enhancement in compression resistance is likely to be associated in a change in failure mode, for example from a mixed buckling-compression mode to one that is entirely compressive.

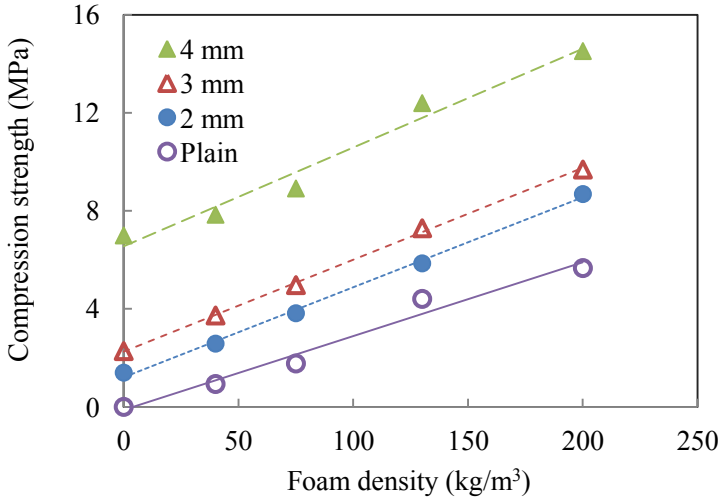

(a) Carbon fibre

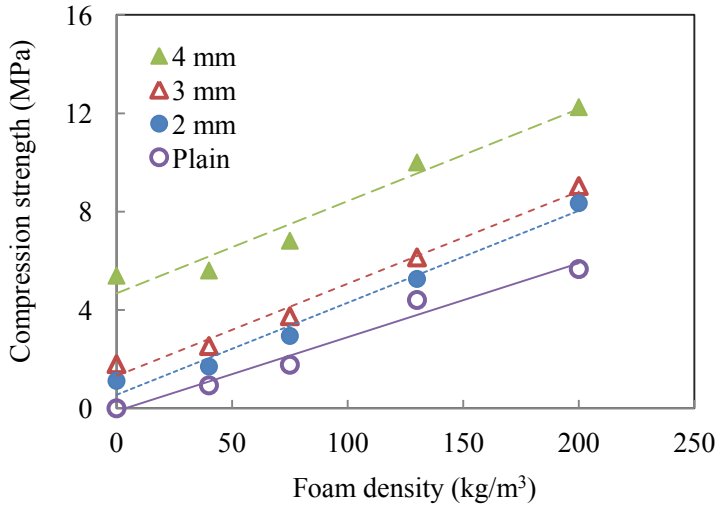

(b) Glass fibre

Fig. 4.23. Variation of the peak stress with foam density (a) carbon fibre reinforced PVC foam (b) glass fibre reinforced PVC foam.

Figure 4.24 shows photographic images of a number of compression specimens following testing at quasi-static rates of strain. Given that the edge length of each block is 50 mm, it is clear that 4 mm diameter glass and carbon rods have been extensively crushed. An examination of the 4 mm

diameter rods in the 80 kg/m^3 foam suggests that they have all experienced similar levels of crush, with the final fibre diameters being similar. This is not the case for the corresponding carbon fibre rods where the centremost fibre exhibits a significantly greater degree of crush. Increasing the foam density to 200 kg/m^3 serves to constrain the fibres to a greater degree, ensuring that the crush front remains roughly circular.

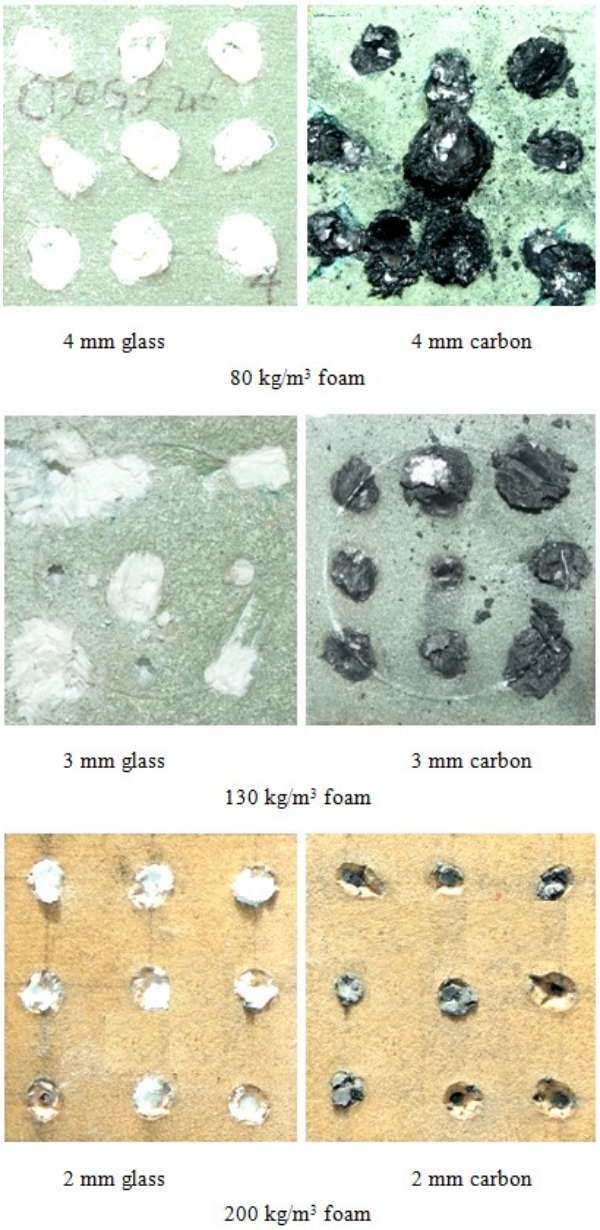

Fig. 4.24 Photo of deformed samples based on different foam densities and different rod diameters.

4.4.3 Energy absorption capacity

The energy required to crush the carbon and glass fibre rod reinforced foam structures were again determined from the area under the load-displacement trace. Figure 4.25 shows the resulting variation of energy absorbed as a function of foam density and rod diameter for the carbon and glass fibre reinforced systems.

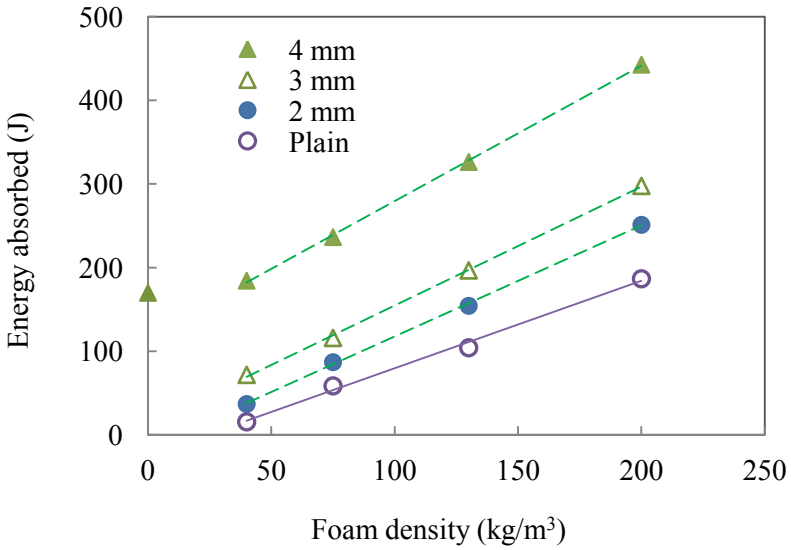

(a) Carbon fibre rods,

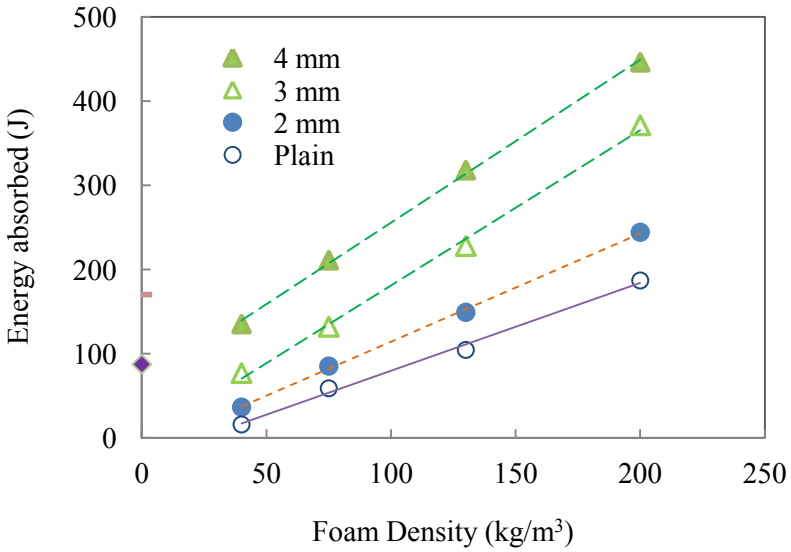

(b) Glass fibre rods,

Fig. 4.25 The influence of rod diameter and foam density on the energy absorbing characteristics of the carbon fibre reinforced foams.

For a given rod diameter, the absorbed energy increases with foam density in a linear fashion. It is interesting to note that the slopes of the trendlines for the different rod diameters are again similar to

that of the plain foam, supporting the view that the energy-absorbing characteristics of these reinforced foams can be estimated from the properties of their constituent materials, i.e. the composite rods and the foam shown in Figure 4.25(a). As before, there appears to be a significant increase in performance in passing from the 3 mm to the 4 mm diameter rods, which may be due to the fact that a number of the 2 and 3 mm diameter rods tilted over during testing. Similar trends to those observed in Figure 4.25(b) were observed in the data for the GFRP glass fibre rod reinforced foams.

Figure 4.26 shows the variation in the values of SEA for the glass-reinforced systems as a function of core density. Introducing the reinforcements into foam clearly enhance the energy-absorbing characteristic of the foam. For example, the SEA of the lowest density foam is increased by 130 % following the incorporative of 4 mm diameter GFRP rods, the corresponding percentage increase for the highest density foam is approximately 80 %. An examination of the figure indicates that the SEA values trend to plateau towards a constant value with increasing values, following the trends associated with the plain foam. The maximum value of SEA in the figure is approximately 29.7 kJ/kg. Similar trends were served in the SEA data for the carbon-based cores, with values being similar for the majority of reinforced foam panels. The exception to this relates to the lowest density foam reinforced with 4 mm diameter CFRP rods, where it was noted that the SEA values were largely insensitive to variations in foam density.

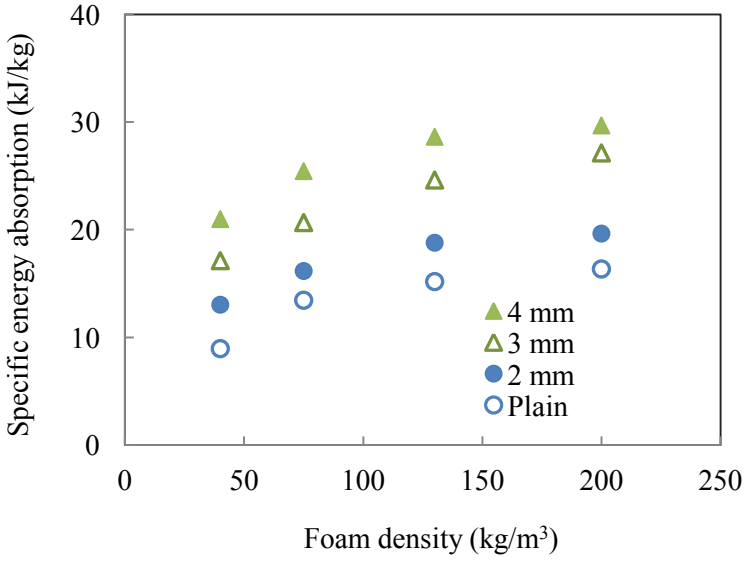

Fig. 4.26 The influence of the diameter of the glass rods and foam density on SEA.

4.4.4 The influence of volume fraction of composite rods

In next stage of this research investigation, the influence of varying the volume fraction of composite rods on the energy absorption capacity of the PVC foam panels was investigated. Here, rods between one and seventeen CFRP and GFRP rods, with a diameter of 4 mm, were inserted into the C130 foam and loaded in compression at a rate of 1 mm/min. Typical stress-strain curves following tests on a number of CFRP-reinforced samples are shown in Figure 4.27. From the figure, it is evident that the crushing resistance increases with increasing volume fraction of rods. The majority of the traces exhibit an initial drop in stress following peak load, similar to that observed during the tests on the plain rods, Figure 4.21(a). All of the traces associated with tests on foams with a higher volume fraction of rods exhibit a drop in stress at strains above 25%, before a subsequent increase as densification occurs. Similar trends to those apparent in Figure 4.27 were observed in the stress-strain traces associated with tests on the GFRP rods.

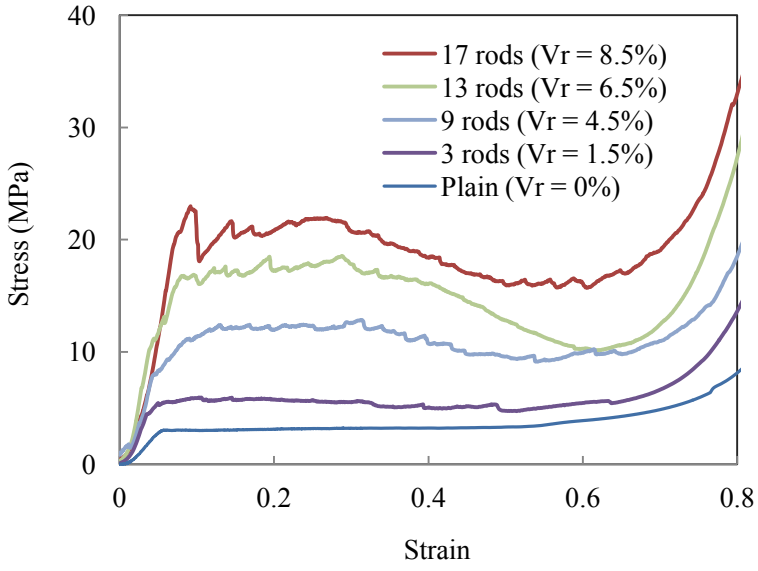

Fig. 4.27 Comparison of the stress-strain curves for the C130 foam reinforced with increasing numbers of 4 mm carbon fibre rods.

A subsequent examination of the failed composite rods indicated that the CFRP rods were reduced to debris rather than the much coarser strands observed following the tests on the plain pins shown in Figure 4.21(b). Interestingly, the GFRP rods were reduced to a much finer white powder, indicating that the presence of the supporting foam served to suppress the relatively low energy splitting failure

mode in the individual rods. An examination of the failed samples suggested that there was little interaction between individual rods when their separation was greater than approximately 15 mm. In contrast, when the rods were more closely packed (typically in samples with more than ten rods), there was evidence of interaction between the individual reinforcements.

Figure 4.28 shows the variation of the compression strength of the reinforced foams with volume fraction of composite rods. Clearly, the compressive strength, of both types of reinforced foam increases rapidly with increasing volume fraction of composite reinforcement. The trends appear to be linear, suggesting that the data follow a rule of mixtures relationship of the form:

$$\sigma = \sigma_r V_r + \sigma_f V_f \qquad \text{(Eq. 4.1)}$$

where V is the volume fraction and the subscripts r and f refer to the composite rods and foam respectively. The solid lines in Figure 4.28 represent the predictions of such a rule of mixtures model, from where it is clear that this simple approach predicts the data with reasonable success.

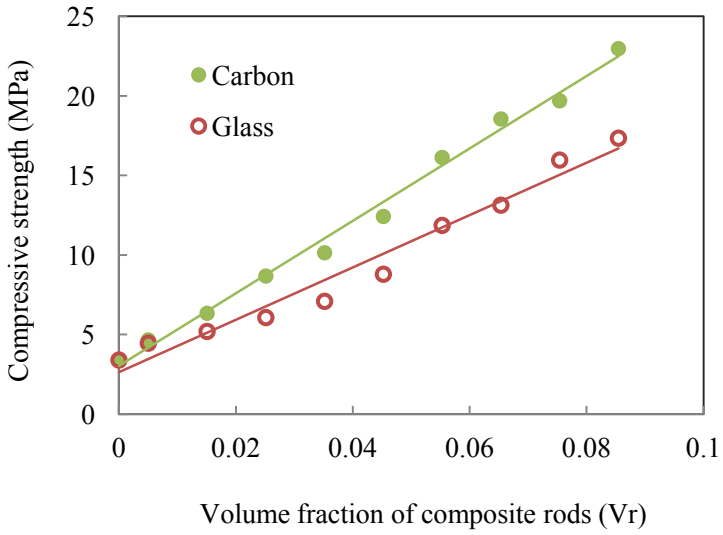

Fig. 4.28 The influence of volume fraction of glass and carbon fibre rods on the compressive strength of the C130 foam.

Figure 4.29 shows the variation of the energy absorbed by these reinforced blocks as a function of the volume fraction of composite rods. The trends for both the carbon fibre and glass fibre rod reinforced foam panels are again highly linear over the range of volume fractions considered. Once more, this evidence suggests that a simple rule of mixtures of the following form can be applied to the data:

$$E = E_r V_r + E_f V_f \qquad \text{(Eq. 4.2)}$$

Extrapolating the data for the carbon fibre rods to a value of $V_r = 1$, (i.e. a hypothetical solid CFRP block) yields a total energy of 6615 Joules and a value for the SEA of 67.7 kJ/kg. This value is reasonably close to that determined following the tests on the individual rods (59.5 kJ/kg). Similarly, extrapolating the data for the glass fibre/PVC hybrids to $V_r = 1$ yields an SEA for the plain GFRP composite of 51.5 kJ/kg. This is clearly much higher than the value determined from the tests on the unsupported rods (19.6 kJ/kg). However, given that the tests on the individual rods failed in a low energy splitting mode and the embedded rods failed as a result of localised crushing, it is likely that this higher value of SEA reflects this latter mode of failure.

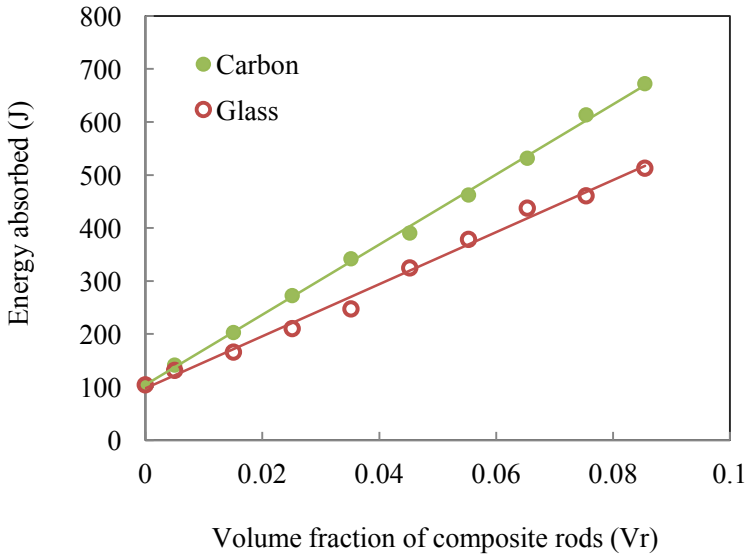

Fig. 4.29 Comparison of the energy absorption of 4 mm carbon and glass fibre rod reinforced C130 foam with increasing number of rods.

The specific energy absorbing characteristics of the reinforced foams were subsequently calculated and these values are shown as a function of the overall density of the system (i.e. including the contribution of the rods) in Figure 4.30. As the volume fraction of composite reinforcement increases from 0 to 0.085, the carbon-based foams exhibit an almost fourfold increase in SEA. Similarly, the SEA of glass-based foams increases by approximately three hundred percent over the same range of volume fractions.

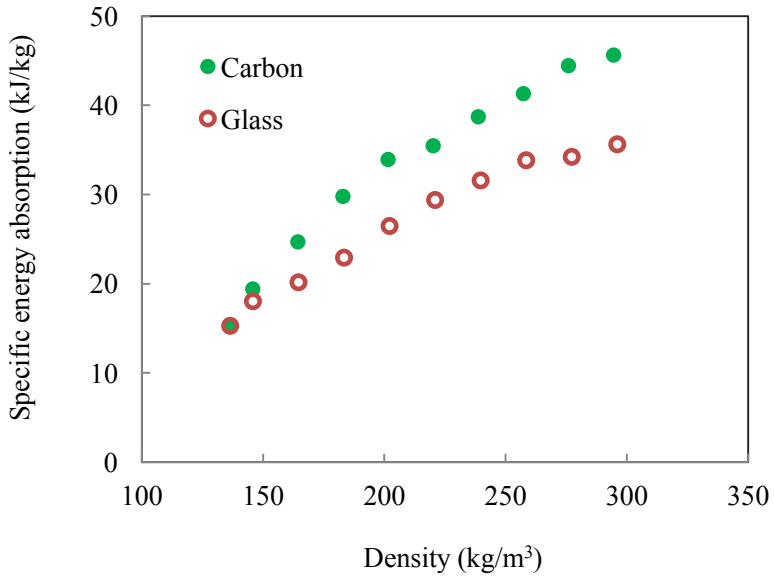

Fig. 4.30 Variation of the SEA with panel density for C130 foams reinforce with carbon and glass rods.

4.4.5 Drop hammer compression test of rod reinforced foams

The dynamic response of the rod-reinforced foams was investigated through a limited number of tests on glass and carbon reinforced 80 and 130 kg/m^3 foams. Figure 4.31 shows typical stress-strain traces following impact tests on the carbon fibre reinforced 130 kg/m^3 foam. Also included in the figure is the corresponding curve for the unreinforced foam. All four traces exhibit similar trends with the force rising rapidly to a maximum value before dropping and becoming highly oscillatory. This dynamic behaviour is likely to be related to ringing effects in the load cell. It should be noted that no attempt was made to filter the load signal following the impact test. In spite of such dynamic effects, it is clear that all four samples exhibit a clear plateau stress followed by well-defined densification region.

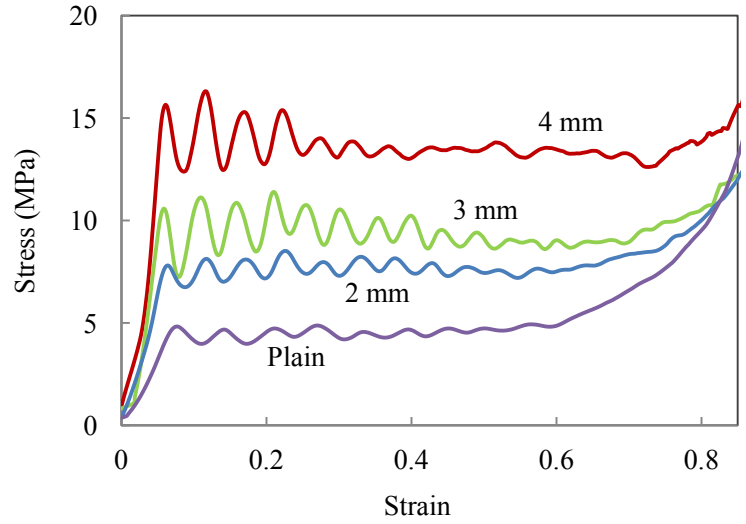

(a) Carbon rods,

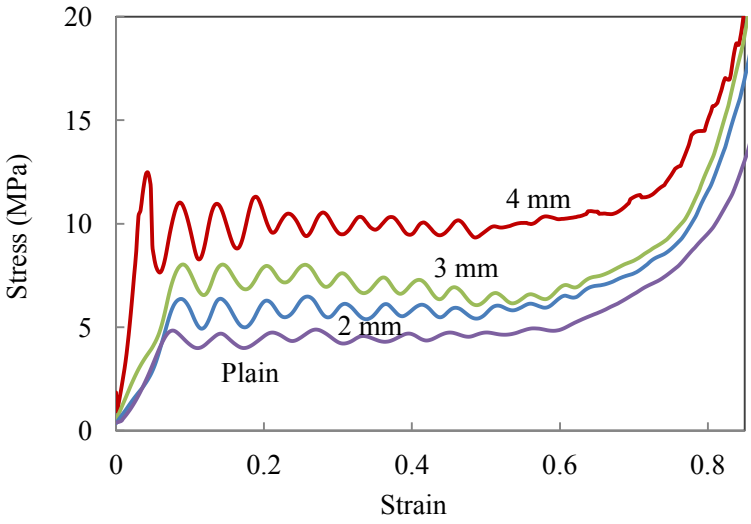

(b) Glass rods,

Fig. 4.31 Typical stress-strain traces following dynamic compression tests on the carbon reinforced C130 foam panels. The diameters of the nine rods are given on the figure.

As before, the compression strength of the reinforced foams was determined from the initial peak in the stress-strain curve and both the energy and SEA were determined from the area under the load-displacement trace. The resulting values of these key parameters are summarised in Table 4-4 and compressive strength and specific energy absorbing shown graphically in Figure 4.32 and Figure 4.33. Also included in the table, and presented graphically in Figure 4.34 are the dynamic enhancement factors (DEF) for the compression strength and energy (SEA). Once again, increasing the volume fraction of composite rods in the foam serves to increase the compression strength of the reinforced foams as well as the overall amount of energy absorbed by the samples. As expected, both

types of plain foams exhibit increases in strength and energy absorption, with the latter being approximately fifty percent. Rather surprisingly the strength of the two carbon fibre reinforced foams increased significantly at dynamic rates, with the 80 kg/m^3 systems offering strengths that were double those measured at quasi-static rates.

Similarly, the energy absorbed by the carbon-based systems exhibited a pronounced dynamic enhancement, with values of DEF between 1.44 and 1.76 being recorded. A subsequent examination of the failed samples indicated that the carbon fibres had been reduced to finer debris that were observed at very low rates of strain. The strength of the glass fibre-reinforced foams also increased with increasing strain rate, with the most significant increases being observed in the 80 kg/m^3 foam systems. For example, the dynamic compression strength of the 80 kg/m^3 foam reinforced with 4mm diameter rods was 92% higher than its quasi-static value. The equivalent increase for the higher density foam was 44%. In contrast, DEF values for energy decreased rapidly as diameter of the rods was increased. For example, the DEF for the 2 mm CFRP rods embedded in the 130 kg/m^3 foam was 28%, whereas that for the 2 mm rods was only 2%. An examination of the failed samples indicated that the failure modes were similar at both quasi-static and dynamic loading rates, i.e. the glass fibre rods were reduced to fine debris. The reasons for this determination in performance with increasing rod diameter are not clear and may be due to the relatively volume fraction of matrix in the rods.

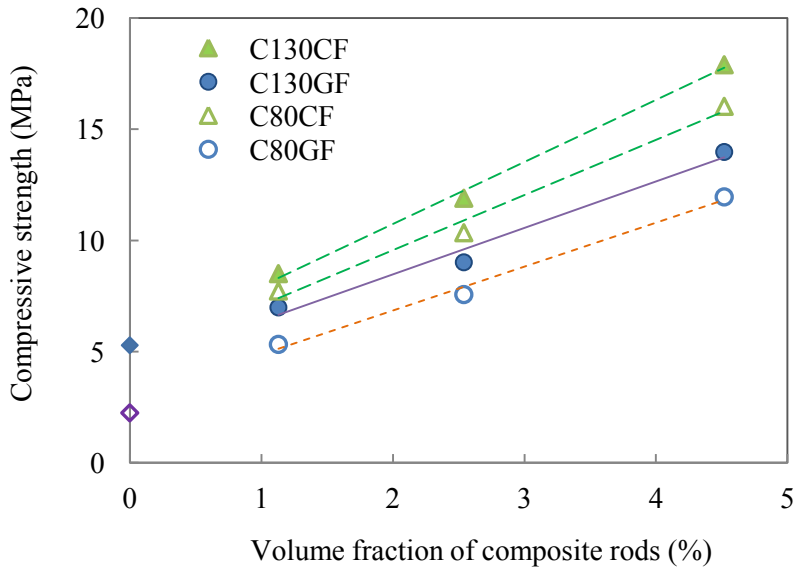

Fig. 4.32 The influence of pin diameter and foam density on the compressive strength of the reinforced foams subject to impact.

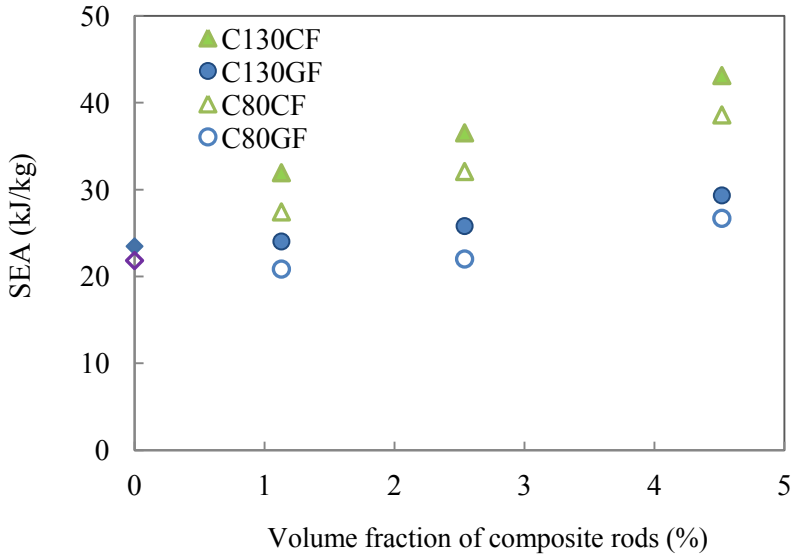

Fig. 4.33 The influence of pin diameter and foam density on the specific energy absorbing comparison of the reinforced foams subject to impact.

Finally, in terms of SEA, the 130 kg/m^3 foam reinforced with 4 mm diameter carbon rods proved to be the most attractive option, offering a value of approximately 43 kJ/kg. This value is approximately 60% higher than that measured at quasi-static rates. It is likely that this value could be increased further by increasing the volume fraction of composite in the foams.

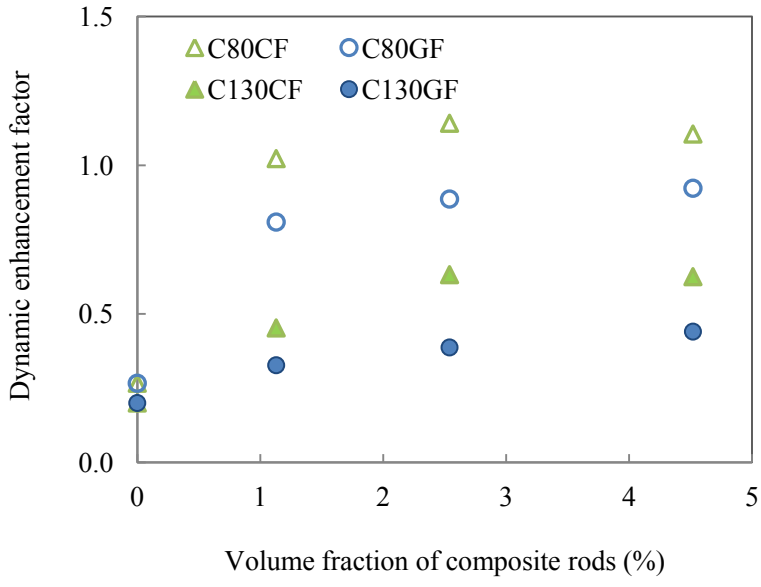

Fig. 4.34 The influence of composite type and volume fraction of rods on the dynamic enhancement factor.

Table 4-4 Summary of the compression strengths and energy absorption properties of the reinforced foams

					Quasi-static			Dynamic		Dynamic Enhancement Factor	
	Specimen ID	Rod diameter (mm)	Volume fraction (%)	Foam density (kg/m^3)	Compression strength (MPa)	Energy (J)	SEA (kJ/kg)	Compression strength (MPa)	Energy (J)	SEA (kJ/kg)	Strength	SEA
Carbon	C80 plain	0	0	80	1.78	58.8	14.04	2.25	85.8	21.44	0.26	0.53
	C80C2	2	1.13	80	3.82	87.1	17.40	7.73	137.4	27.43	2.02	1.58
	C80C3	3	2.54	80	4.83	116.1	18.27	10.35	204.0	32.08	2.14	1.76
	C80C4	4	4.52	80	7.62	221.7	26.89	16.03	318.2	38.59	2.1	1.44
	C130 plain	0	0	130	4.41	104.4	15.19	5.29	161.3	23.47	1.2	1.55
	C130C2	2	1.13	130	5.86	154.5	19.51	8.51	253.0	31.94	1.45	1.64
	C130C3	3	2.54	130	7.29	206.9	22.34	11.9	337.0	36.53	1.63	1.63
	C130C4	4	4.52	130	11.4	298.5	27.03	17.9	476.3	43.12	1.57	1.60
Glass	C80 plain	0	0	80	1.78	58.8	14.04	2.25	85.8	21.83	1.27	1.53
	C80G2	2	1.13	80	2.95	85.2	16.97	5.33	104.6	20.85	1.81	1.23
	C80G3	3	2.54	80	3.75	126.9	19.89	7.07	140.4	22.01	1.89	1.11
	C80G4	4	4.52	80	6.22	210.8	25.45	11.96	221.2	26.69	1.92	1.05
	C130 plain	0	0	130	4.41	104.4	15.19	5.29	161.3	23.47	1.2	1.55
	C130G2	2	1.13	130	5.27	149.0	18.79	6.99	190.6	24.03	1.33	1.28
	C130G3	3	2.54	130	6.14	217.8	23.62	8.52	238.6	25.8	1.39	1.09
	C130G4	4	4.52	130	9.71	317.8	28.64	13.98	325.5	29.33	1.44	1.02

4.5 Compressive response composite tube reinforced foams

The energy-absorbing characteristics and crashworthiness properties of PVC foam reinforced by composite tube have been investigated to compare the performance of structures with a similar configuration to the rod reinforced foams described in Section 4.4. The PVC foam density from 40 to 130 kg/m^3 reinforced by carbon tubes with diameters ranging between 8 to 12.5 mm have been tested in compression at both the quasi-static and dynamic rates. The specimen preparation was described in Section 3.2.4. The test procedures were presented in Section 3.3.1 and Section 3.4.2. A range of circular T700 carbon fibre reinforced epoxy tubes have been used to investigate the effect of tube diameter to thickness (D/t) ratio on the influence of SEA characteristics. The results of testing on the individual composite tubes, the tube reinforced foam, and 9 tube reinforced foam panels with GFRP skins are summarised in this section.

4.5.1 Quasi-static tests on composite tubes

4.5.1.1 Quasi-static tests on individual composite tubes

Figure 4.35 shows a comparison of typical load-displacement traces of individual carbon tube with an inner diameter of 8, 10, and 12.5 mm under compressive loading (D/t values between 7.4 and 10.3). An examination of the load-displacement trace corresponding to the 12.5 mm carbon fibre tube indicates that the force rises up to approximately 1230 Newtons before it drops slightly and it subsequently stabilized at approximately 1100 Newtons. In contrast, the trace for the 8 mm tube increases with a relatively low stiffness in a linear fashion up to the peak at 690 Newtons following a relative lower plateau value of 460 Newtons. Based on the energy under the load-displacement traces and mainly the plateau force, it is worth noting that the 12.5 mm carbon rods offer more than doubled energy-absorbing capability than the 8 mm tube. All three traces exhibit similar characteristics, with an approximately constant forces as a stable manner of failure during crushing process corresponding to displacement from 2 mm to 16 mm before the force is dropped at the final stage of collapse failure. The resistance increases in nonlinear manner with tube diameter from 8 mm (D/t ratio =8), 10 mm (D/t ratio =7.4), to 12.5 mm (D/t ratio =9.3).

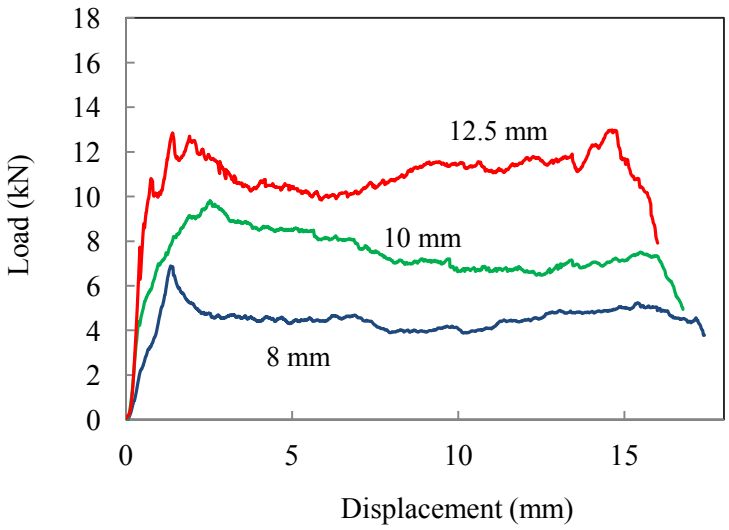

Fig. 4.35 Typical load-displacement traces following crush tests on individual tubes with different diameters (values of D/t)

The compressive tests on individual unidirectional glass fibre composite tubes were conducted to characterize their crush behaviour and compare the energy-absorbing capability with the wrapped carbon tubes described above. Figure 4.36 shows a comparison of typical load-displacement traces between the glass composite tube and wrapped carbon tubes (D/t ratio = 4.05). An examination of the trace corresponding to the glass fibre tube indicates that the force rises in a linear fashion up to approximately 17.2 kN before dropping sharply to a much lower plateau value of 3.7 kN, which is less than 25% of the first peak load. In contract, the stabilizing plateau value of the wrapped carbon fibre tube is over 90% of the strength following the peak. It is suggested that the wrapped carbon fibre tube exhibited a stable crushing process throughout the whole test, whereas the unidirectional one was through in a unstable crushing process during compressive loading without any constraint. Based on the energy under the load-displacement traces, the SEA value of carbon tubes is up to 89.8 kJ/kg, whilst the value for the glass-based system was only 31.1 kJ/kg. It is evident that the wrapped carbon tubes offer a much greater energy-absorbing capability than the unidirectional glass fibre counterparts.

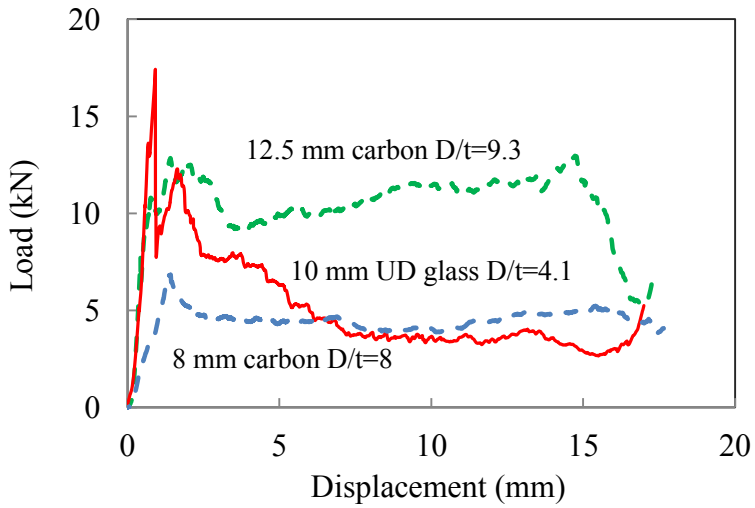

Fig. 4.36 Comparison of load-displacement traces following crush tests on individual glass and carbon tube (Solid line is unidirectional glass fibre tube, and dash lines are wrapped carbon tubes.)

The resulting mechanical properties of the carbon and glass fibre tubes are summarised in Table 4-5.

Table 4-5 Summary of carbon tubes used in this study

Samples Pictures					
Fibre type	Glass	Carbon	Carbon	Carbon	Carbon
Mass (g)	2.58	0.97	1.5	1.8	2
Energy (J)	79.9	65.7	111.3	161.7	181
SEA (kJ/kg)	31.0	67.8	74.2	89.8	89.5

Figure 4.37 shows a comparison of typical failure process of the carbon and glass tubes. An examination of the failure tubes highlights that crushing of the carbon tube leads to the upper part of the cylinder splaying outwards against the moving platen, generating a large amount of fine composite fragments during the test. The fractured debris and dust suggests that a significant amount of energy has been absorbed during the progress its failure. In contrast, the glass fibre based tube failed as a result of extensive longitudinal splitting in an unstable mode with delamination immediately at initial stage of crushing, following composite fracturing vertically in an interlaminar mode along its interlayer and cyclic annular. It was observed that the wrapped carbon tubes fracture into a multiplicity of debris, whereas the unidirection glass tubes failed in a lower energy delamination mode resulting in larger residues. Given that the fracture energy associated with delamination-type failure of glass tube is significantly lower than that associated with fibre fracture

of wrapped carbon tube, this qualitative evidence suggests that the unidirection glass tubes is less effective as energy absorbers. The different failure mechanisms are corresponding to the layers structure of the roll wrapped carbon tube and the unidirectional tube. This highlights the super performance of roll wrapped carbon fibre tube over the unidirection glass tubes.

Disp.	Carbon fibre tube	Glass fibre tube
1 mm		
5 mm	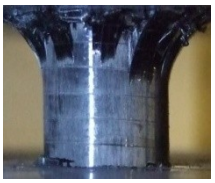	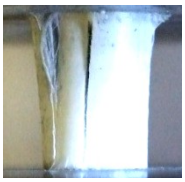
10 mm	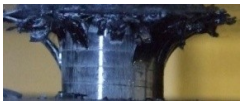	
15mm	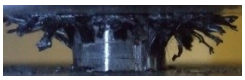	
18 mm		
Top view	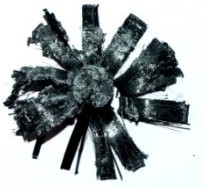	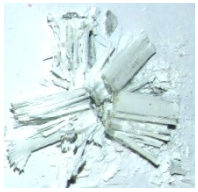

Fig. 4.37 Crushing failure process of carbon and glass fibre tubes under quasi-static compressive tests.

4.5.1.2 Compression tests on tube reinforced foam

The enhancement effect of the tube embedded in PVC foam was investigated initially. Figure 4.38 shows a comparison of the load-displacement traces following quasi-static tests on the 12.5 mm plain tube, the tube embedded C130 foam, and the equivalent unreinforced plain foam specimen. The load-displacement traces indicates that the stabilised crushing load for the tube reinforced foam system is approximately 23.9 kN. In contrast, the individual tube is 10.28 kN and plain C130 foam is 2.7 kN only. It highlights that the reinforced foam structure provides a crushing resistance that is significantly higher than the sum of individual components. The traces also indicates that the tube contributes most to the absorption, however the PVC foam serves to constrain the splaying process, resulting in higher levels of crushing within the embedded tube effective as greater energy absorbers. The cross-sections of tube reinforced foam in the following section also support that the composite tube embedded in foam had been fractured into even finer particles. This evidence clearly supports the suggestion that embedded tube in foam panel can modify the failure process and greatly enhance the crush performance of the tubes.

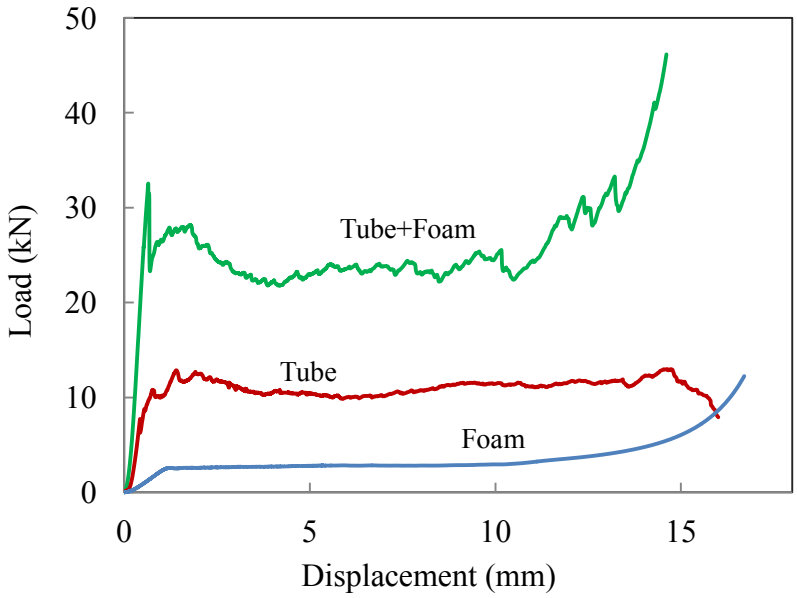

Fig. 4.38 Comparison of load-displacement traces of between C130 plain foam, individual carbon tube in a inner diameter of 12.5 mm and the tube embedded in the foam under compression load.

The resistance strength of tube reinforced foam was evaluated by comparison of stress-stain curve with the rod reinforced foam discussed in earlier section. The individual tube was embedded in a

square panel as a unite cell following compressive tests to evaluate the comparison strength and crushing resistance. A series of PVC foam panels with densities of 40, 80 and 130 kg/m^3 were embedded with CFRP tubes in three diameters, i.e. 8, 10 and 12.5 mm. Figure 4.39 shows load-displacement traces obtained from the corresponding experimental results of the 8 and 12.5 mm embedded in 130 kg/m^3 PVC foam panel. The test results of a plain PVC foam panel without any CFRP tube are also shown in the same figure to highlight the enhancement of carbon tube. Clearly, the force increases significantly up to a average plateau load of 11.3, 18.5 and 23.7 kN for the 8, 10 and 12.5 mm tube reinforced foam panel respectively. It noted that the plateau load of 12.5 mm reinforced foam panel is 8 times of the plain form panel without embedded tube. It also indicates that the resistance force with diameter of embedded tube enhanced from 11.3 kN of the 8 mm tube to 23.7 kN for the 12.5 mm tube reinforced foam.

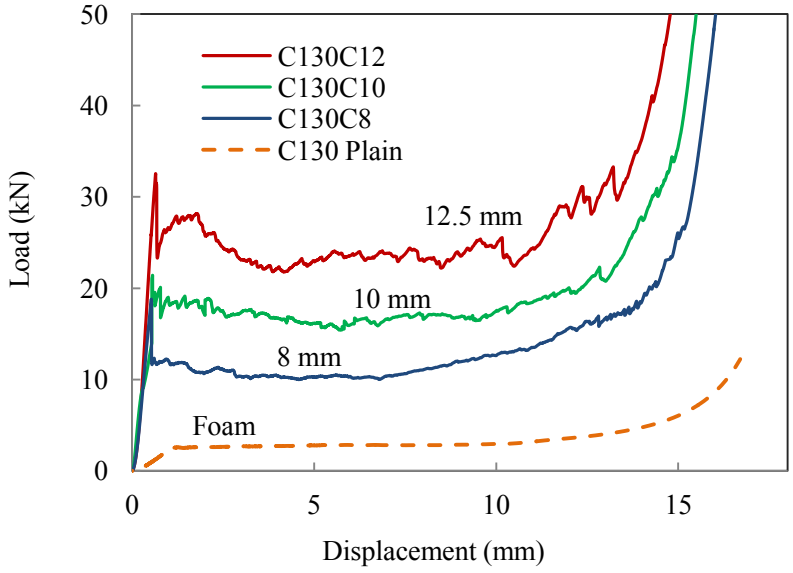

Fig. 4.39 Compressive tests on 8, 10 and 12.5 mm carbon fibre tube embedded in C130 foam panels under compressive tests.

It worth to note that the tube reinforced foam has super strength in contrast with the stress-stain curve of the rod reinforced C130 foam presented in Figure 4.23. The values of crushing strength for tube reinforced foams are of the range from 10.4 to 21.7 MPa, which is far over of the strength values of 5.9 and 12.4 MPa for the 3 mm and 4 mm rod reinforced foams. It is clear that the strength of the tube reinforced foam systems out-performs the rod reinforced foams.

Compressive tests on individual unidirectional glass tubes embedded in PVC foam density from 40 to 130 kg/m^3 were conducted to characterize the influence on crushing process of unidirectional glass tube constrained by PVC foam with increasing densities. Figure 4.40 shows the load-displacement traces for the glass fibre tube reinforced foams. Those curves exhibit similar features with carbon tube reinforced foam, in which the distinctive regions include a linear elastic one, a region of progressive crushing after a sharp drop of the load and a final region of the core densification. The comparison on the three traces indicates that the plateau value is increasing from 9.4 to 17.9 kN with the density increase of PVC foam, which is 2 times and 4 times of the plateau value on the trace of individual glass tube shown in Figure 4.36. The PVC foam greatly improve the crush its resistance of unidirectional glass tube. The improvement in the stabilized plateau value is approximately 16.48 kN for the glass tube embedded in C130 foam, which is 4 times the plateau value for the individual glass tube (3.7kN). An examination of those traces shown in Figure 4.39 and Figure 4.40 indicates that the enhancement on unidirectional glass tubes is significant higher than that of carbon tubes, as the failure process on unidirectional glass tubes is greatly modified by the constraint of PVC foam.

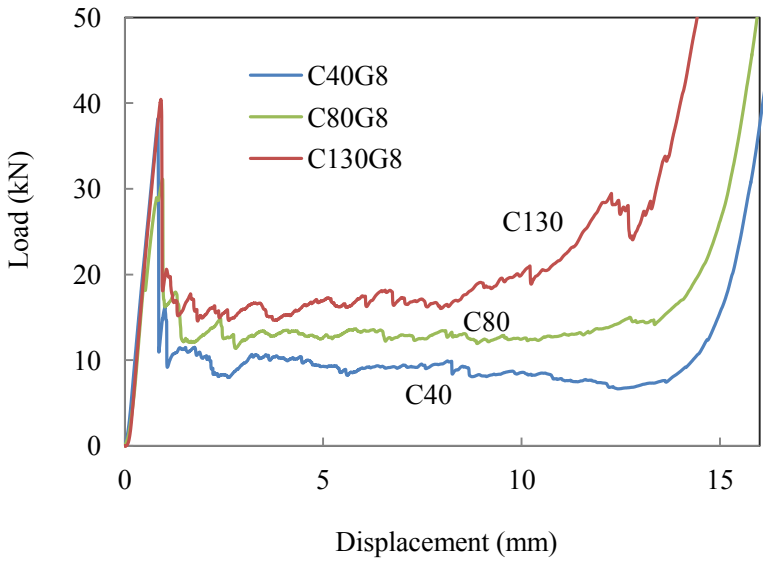

Fig. 4.40 Compressive tests on glass fibre tube embedded in C40m C80 and C130 foam panels.

4.5.2 Tests on tube reinforced foam based sandwiches

The next stage of this investigation focused on studying the influence of increasing the foam density and tube diameter on the energy-absorbing response of these tube reinforced foam sandwiches.

Figure 4.41 shows load-displacement traces for the carbon fibre tube reinforced C130 and C80 foams. All of the traces exhibit similar trends with the responses of the tube reinforced foams. The plateau values increase from 89 to 160 kN for the C80 foam panels and 119 to 188 kN for the C130 foams with the increase of tube diameters. The comparison of the traces suggests that the increasing of energy absorption is related to the increasing of foam density and tube diameter.

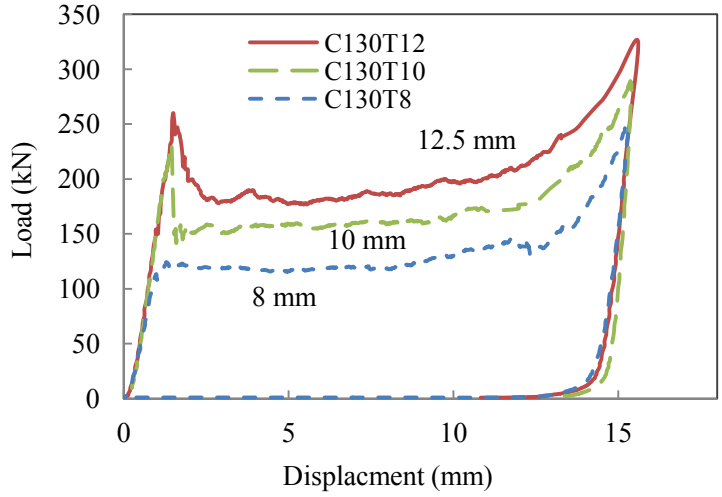

(a) C130

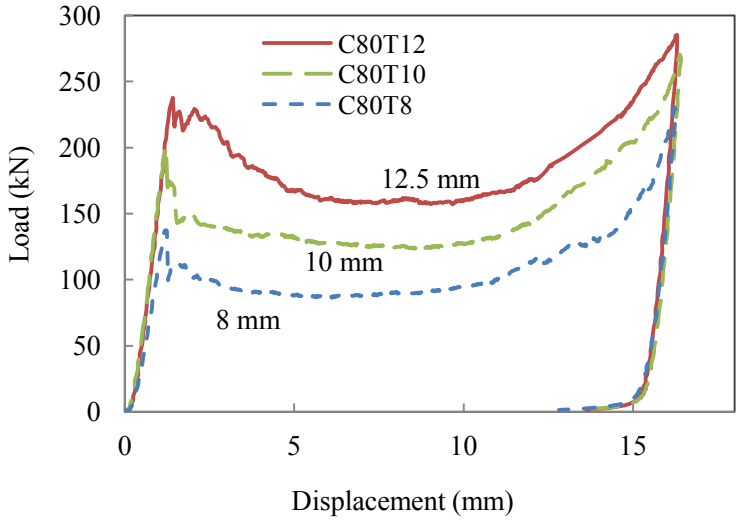

(b) C80

Fig. 4.41. Load-displacement traces following tests on the 9 tube reinforced sandwich structures (Comparison of load-displacement traces of C130 and C80 foam reinforced by 8, 10, and 12.5 mm

carbon fibre tube following compression load. 9 tubes embedded in 100x100 mm square sandwich panel with C130 PVC foam and 0.8 mm GRFP skins)

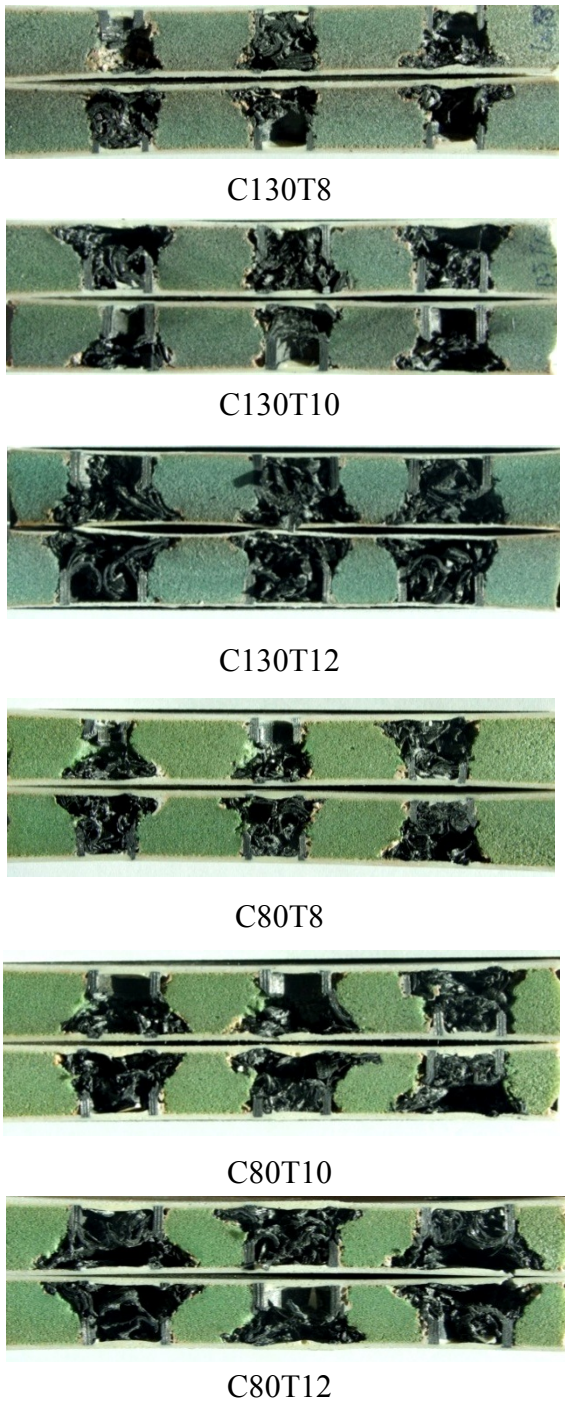

Fig. 4.42. Comparison of failure modes of carbon tubes reinforced foam based sandwiches under static compressive test.

Figure 4.42 shows photographic images of cross-sections on a number of compression specimens following tests at a quasi-static rate of strain. Given that the edge length of square panel is 100 mm, it is evident that the carbon tubes have been extensively crushed with a large amount of fragments between the panel skins. An examination of cross-sections of failed tubes highlights the triggered end of the cylinder splaying both inwards and outwards of tube during crushing process. It is clear that there were more significant amount fragments and fine particles generated due to the constraint and interaction between PVC foam and skins during the test. This interaction contributed a higher plateau value of the resistance during a stable crushing process, which offers a higher energy absorption.

The energy required to crush the composite tube reinforced foam structures was determined from the area under the load-displacement trace. The resulting variation of energy absorbed as a function of foam density and tube diameter for the composite reinforced foam structures are shown in Figure 4.43. It is noted that the absorbed energy increases with tube diameter for a given foam density. It also shows that the absorbed energy increases with foam density in a linear fashion for a given tube diameter. It is interesting to note that the slopes of the trendlines for the carbon tube with different diameters are similar. However, the slops of the trendline for the glass tube is significant higher than the slopes for carbon tubes. It highlights that the failure process on unidirectional glass tubes is greatly modified by the constraint of PVC foam with the increasing of foam density. All slopes of the trendlines for composite tube reinforced foam are above the plain foam. Once again, similar to the rod reinforced system it supports the view that the energy-absorbing characteristics of these reinforced foams can be estimated from the properties of their constituent materials, i.e. the composite tube and the foam. As before, there appears to be a significant increase in performance in passing from the 8 mm to the 12.5 mm diameter tubs and the increase in energy absorption with increase of foam density form 40 to 130 kg/m^3. It is also interesting to note that the significant enhancement on the glass tube embedded in a higher density foam is over the carbon tube counterpart, which offers a higher energy absorption. i.e. the glass tube embedded in C130 foam offers higher energy absorption although the individual tube offers a quite lower energy absorption than the wrapped carbon tube. There is an evidence to support the suggestion that the performance of glass tube embedded high density foam may be better than its carbon tubes counterpart. The significant enhancement of the glass fibre tube is

contributed to the constraints offered by foam. A higher crushing resistance and energy absorption were contributed by 100 % fibre of the unidirectional glass to against the load in longitudinal direction of tube, whereas there is only 60% of carbon fibre in longitudinal direction for the roll wrapped multiple layers carbon tube. The rest of 40 % woven fibre around a mandrel direction is same function as foam, offering less contribution against the compression loading. Another benefit maybe due to the lower D/t ratio value of 4.1 on the glass tube compare to the values of carbon tubes from 7.4 to 9.3.

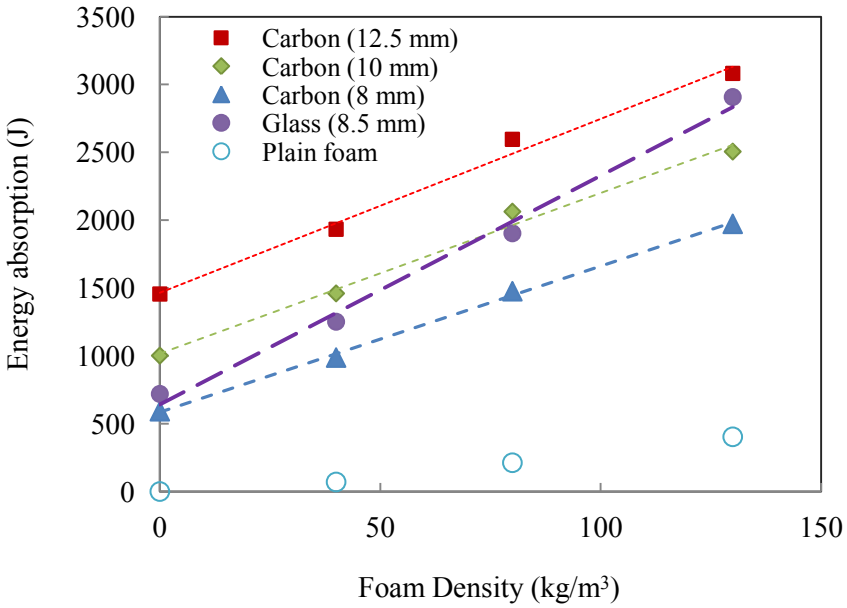

Fig. 4.43 The influence of rod diameter and foam density on the energy absorbing characteristics of the composite tube reinforced foams.

The variation in the values of SEA for the tube reinforced systems as a function of core density is shown in Figure 4.44. Introducing the reinforcements into foam significantly enhances the energy-absorbing characteristics of the foam and the enhancement is two times of rod reinforced system. For example, the SEA of the lowest density foam and rod reinforced systems is increased from 8.9 to 20.9 kJ/kg following the incorporative of GFRP rods, the corresponding increase for the highest density foam system is approximately from 15.8 to 29.6 kJ/kg. However, the SEA value for the carbon tube reinforced systems is increased from 61.1 to 87.7 kJ/kg and the glass tube systems passing form 41.3 to 62.9 kJ/kg. The resulting values of the compression strength, energy-absorbing and SEA results are summarised in Table 4-6 at end of this section. An examination of the Figure 4.44 indicates that the SEA values of the tube systems trend to plateau towards a approximately

value between 60 to 90 kJ/kg. It was noted that C80 foam reinforced with 12.5 mm diameter CFRP tubes offers a maximum value of SEA approximately 87.7 kJ/kg in the figure. It was also noted that the SEA values for the carbon tube reinforced foam were largely insensitive to variations in foam density. However, the SEA data of glass tube reinforced system show uptrend in foam density. The SEA values for the unidirectional glass fibre tubes are sensitive to variations in foam density and increasing largely with the increasing densities. It is expected that the SEA value for glass tube embedded in C200 foam will over perform the counterpart of carbon tube reinforced foams.

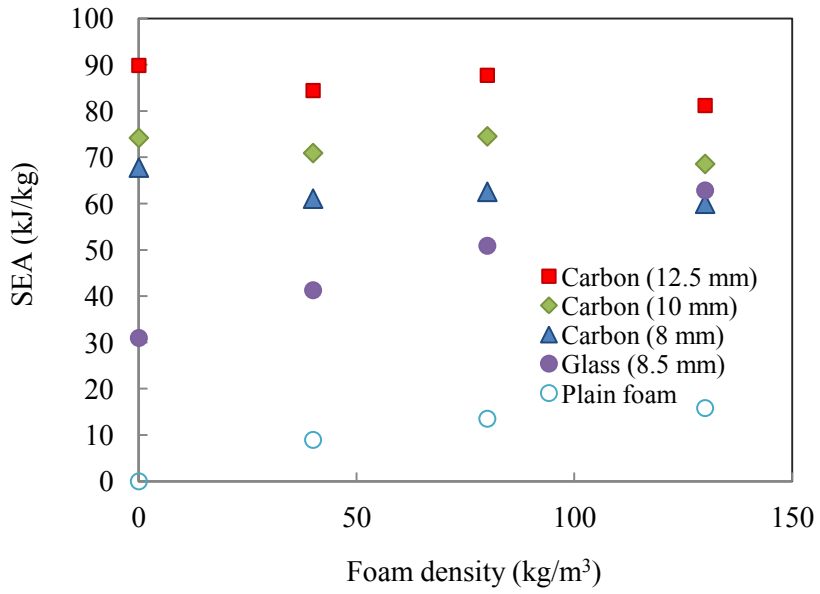

Fig. 4.44 The influence of rod diameter and foam density on the specific energy absorbing of the composite tube reinforced foams.

For a structure design, assume a structure is requested to have the energy absorption over 2000 J, the C80C12, C130C10, C130C12 and C130G8.5 will be candidates. However, the C80C12.5 will be the lightest structure due to the higher SEA and C130G8.5 will be heaviest due to lower SEA. Considering to the cost and performance issue, the C130G8.5 will be a priority option, due to the lower cost with satisfactory energy absorption request, although the SEA is lower due to a higher weight of glass tube.

4.5.2.1 Test on tube filled with balsa wood

The influence of tubes filled with a balsa wood rod on the compression response of these tube reinforced foam sandwich counterparts was investigated. The specimens were based on the same 100x100 mm foam panels embedded with 9 tubes, filled in a balsa wood rod with the same diameter of the inner diameter of the tube. The fibre direction of nature wood is same as the longitudinal direction of tube which is in the vertical direction to the face skins. The GFRP skins were bonded on the tube reinforced foam panels.

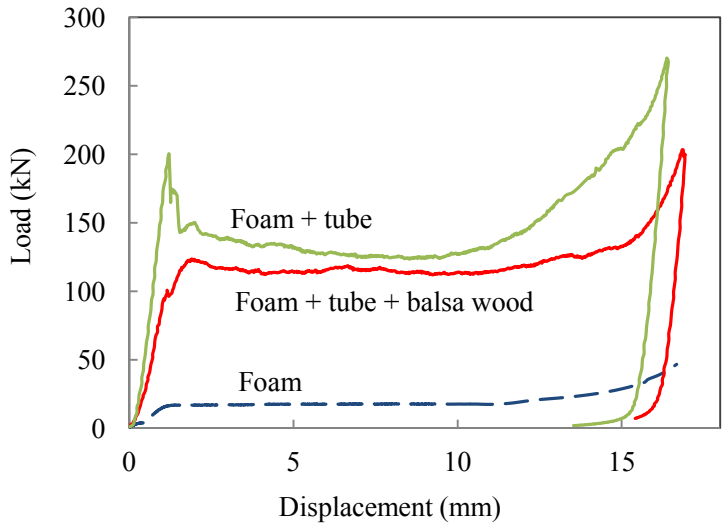

(a) C80 foam

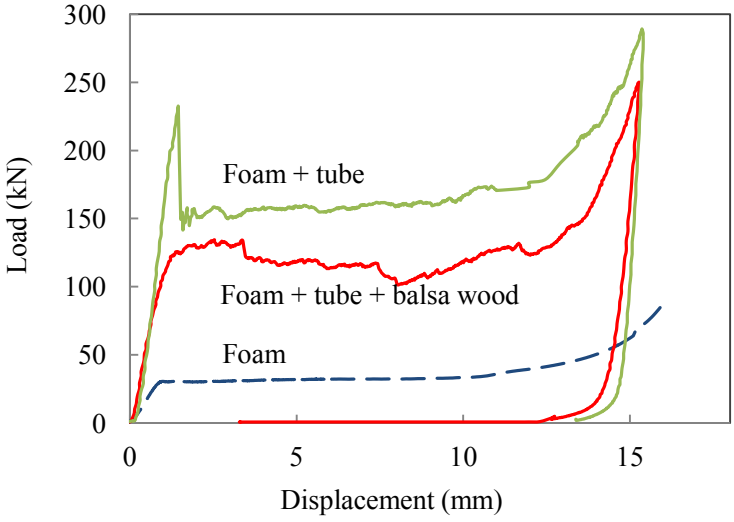

(b) C130 foam

Fig. 4.45 Comparison of load-displacement traces of 10 mm carbon fibre tube and tube filled with balsa wood reinforced C130 sandwich under compression test.

Figure 4.45 shows the comparison of load-displacement traces between the foam embedded with carbon tubes filled with balsa wood and its empty tube counterpart sandwich following quasi-static compression tests. The load-displacement trace of the former gives a lower resistance than the original traces without filling in any balsa wood filled in. The reason for this is due to the lateral expansion of the balsa wood under compression which further contributes to the damage of the carbon fibre tube. It obviously suggests that tube filled with balsa wood lead to low performance and absorbing less energy.

4.5.3 Drop hammer compression tests on tube reinforced foam sandwiches

The final stage of this investigation focused on studying the dynamic response of the glass and carbon tube reinforced foams with densities of 40, 80 and 130 kg/m^3. The stress-strain traces of the carbon fibre tube reinforced 130 kg/m^3 foams are shown in Figure 4.46. The corresponding curve for the plain foam is also included in the figure. All traces of tube reinforced foam exhibit similar trends with the force rising rapidly to a maximum value before a significant drop following highly oscillatory response. In contrast to the stress-strain traces of the rod reinforced foams (see Fig. 4.31) with the minimal drop on the plateau stress, the plateau value of the tube reinforced foams drops to below 50 % of the dynamic compressive strength. An examination of the traces between the quasi-static loading (Figure 4.39) and the dynamic loading (Figure 4.46) indicates that the plateau values of tube reinforced C130 form at dynamic loading is approximately 20-30% less than the its values at quasi-static loading, whereas the compressive strength is approximately 90-120 % higher than the values at quasi-static loading.

In spite of such dropping of the plateau values under dynamic loading, it is clear that all four samples exhibit a clear plateau stress, followed by well-defined densification region. This dynamic behaviour is similar to the test results on rod reinforced foams (Fig. 4.31), which is related to the ringing effects of the load cell.

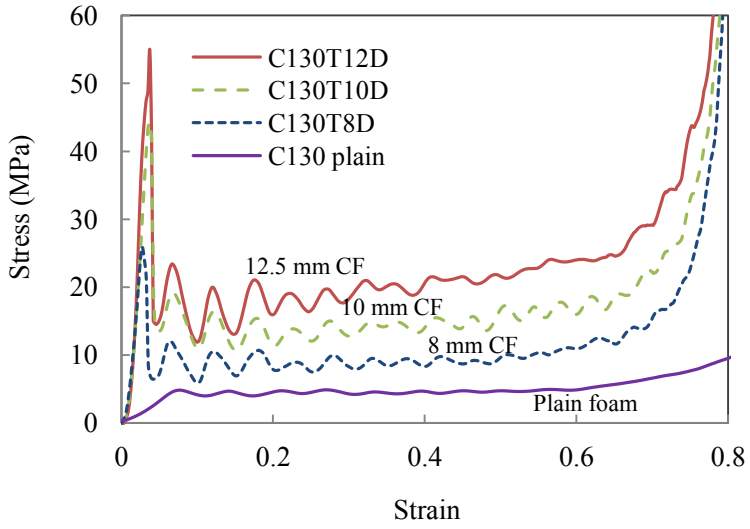

Fig. 4.46 Stress-strain curve of C130 foam reinforced by 8, 10, and 12 mm carbon fibre tube subjected to dynamic loading.

An examination of stress-strain traces on the carbon tube reinforced C80 foams, shown in Figure 4.47, indicates a similar response to the C130 systems (Figure 4.46). Both the tube reinforced C80 and C130 foams show an increase on the peak and plateau stresses with increasing the tube diameter from 8 to 12.3 mm. Here, the initial peak stresses are very similar between the two tube reinforced foam systems, which suggests that the impact resistance is primarily contributed by the embedded carbon fibre tubes.

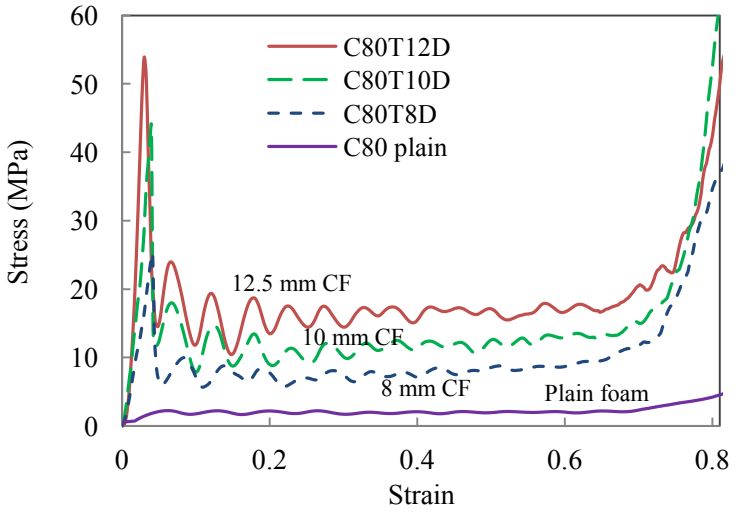

Fig. 4.47 Stress-strain curve of C80 foam reinforced by 8, 10, and 12 mm carbon fibre tube subject to dynamic loading.

Figure 4.48 shows the comparison of the stress-strain traces on glass tube reinforced foams with three densities form 40 to 130 kg/m^3. The traces also exhibit the similar features with the carbon tube reinforced foams. However, the difference between the traces is relatively small before the crush strain is above 20%, which suggests the dominant behavior of the glass tube.

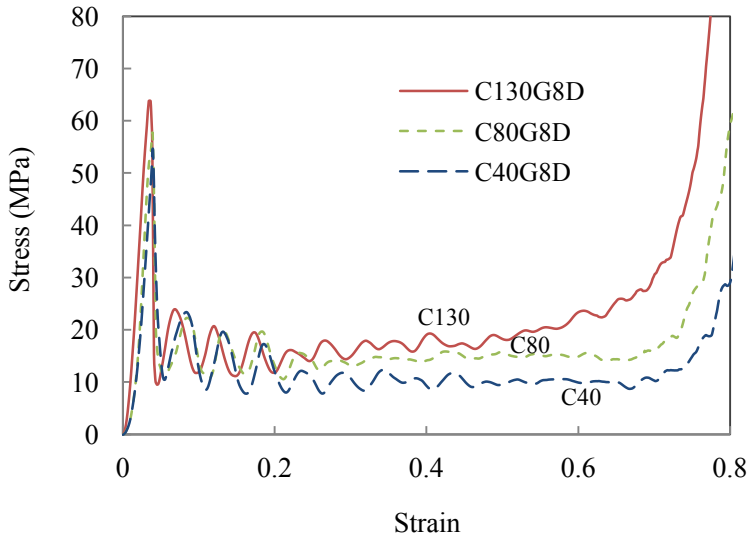

Fig. 4.48 Stress-strain curve of 8.5 mm glass fibre tube embedded in C40, C80 and C130 foam panels subject to dynamic loading.

Figure 4.49 shows photographic images of a number of specimens following compressive tests at both quasi-static and dynamic rates of strain. It is clear that there are some little different features between foam densities, tube type, skin thickness and load conditions. It is clearly seen the influence of foam densities, i.e. the higher foam density offers the higher constraint to the tubes embedded, which also contributes to remaining a rough circular cross-section in the foam density of 130 kg/m^3. The tube constrained in the high density foam was crushed into fine debris and dust, instead of fractured fragments in the low density foam, which suggests a significant amount of energy was absorbed during the crushing process for the former. Comparing the cross-sections of the quasi-static and dynamic sample, the carbon and glass tubes reinforced foam have been extensively crushed following dynamic loading. The both the carbon and unidirectional glass tube exhibits crushing in a relatively unstable fashion under dynamic load.

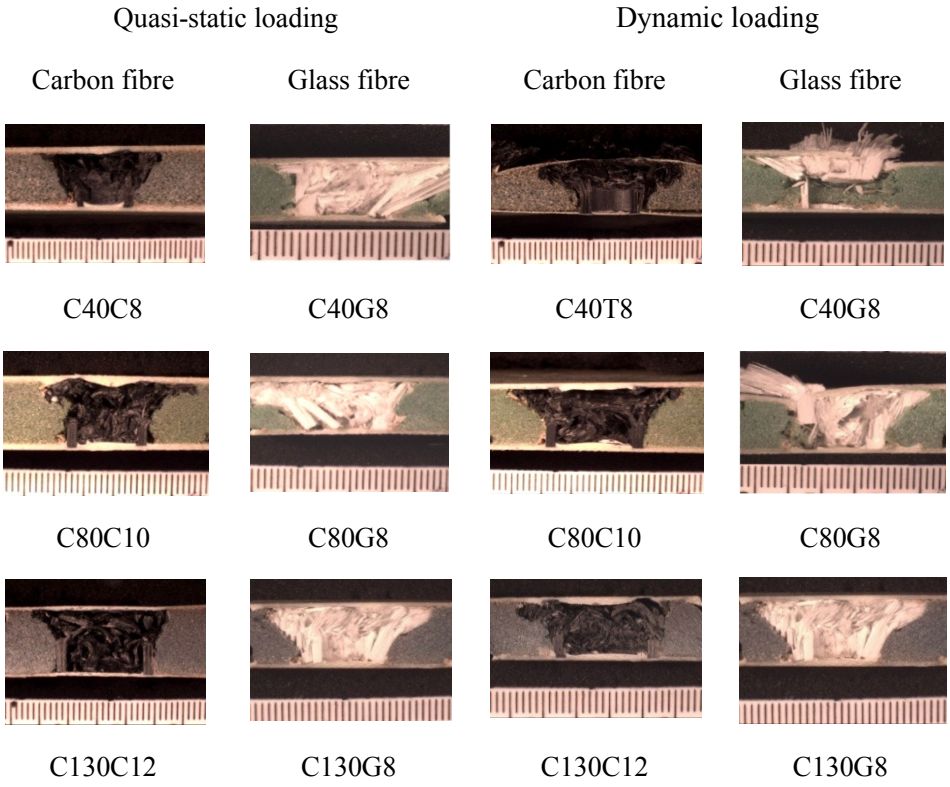

Fig. 4.49 shows photographic images of comparison between a number of carbon and glass specimens following compression testing at quasi-static rates of strain.

In comparison to the influence of the tube type between the roll wrapped carbon tube and unidirectional glass tube, the latter is more relied on the constraint of foam with higher density. An examination of the roll wrapped carbon tubes in the foams with three densities suggests that they all experienced the similar level of crush, with the fine fragments. This is not the case for the corresponding unidirectional glass fibre tubes, which experience a significantly greater degree of crush associated with the high density foam C130 and a brittle crush when the tube was embedded in the low density foam C40.

Regarding to the influence of loading rate, there is hardly any difference on the crushed pattern for the high density foam sandwich. However, in the low density cases, both the 0.2 (1-ply) and 0.4 mm (2-ply) GFRP skins were perforated by glass fibre tube and however, only the 0.2 mm GFRP skins was fractured by carbon tubes. It suggests that the 0.6 mm thick GFRP skin is recommended to the tube reinforced foams.

The energy-absorbing capability of the tube reinforced foams subjected to quasi-static and dynamic loading was also investigated. Similar to the rod reinforced foam, the compression strength of the tube reinforced foams was determined from the initial peak in the stress-strain curve and both the energy absorption and SEA were determined from the area under the load-displacement trace. The resulting values of these key parameters are summarised in Table 4-6. Only the selected tube reinforced foam structures based on C80 and C130 are shown graphically in Figure 4.50 to Figure 4.52.

Figures 4.50 summarizes the variation of the compression strength of the tube reinforced foams with foam density and tube diameter. The solid points are corresponding to the quasi-static tests and hollow ones to the dynamic results. From the figure, it is evident that the compression strength of the tube reinforced foams increases in a linear fashion with foam density for a given tube diameter. It is important to note that the slopes of the traces for all of the reinforced systems are similar to that of the plain foams. It is interesting to note that the dynamic compression strengths are significantly higher than that of its quasi-static value. The ratio of dynamic to quasi-static values on compression strengths are between 1.97 and 2.4 for the tube reinforced C80 and C130 foams.

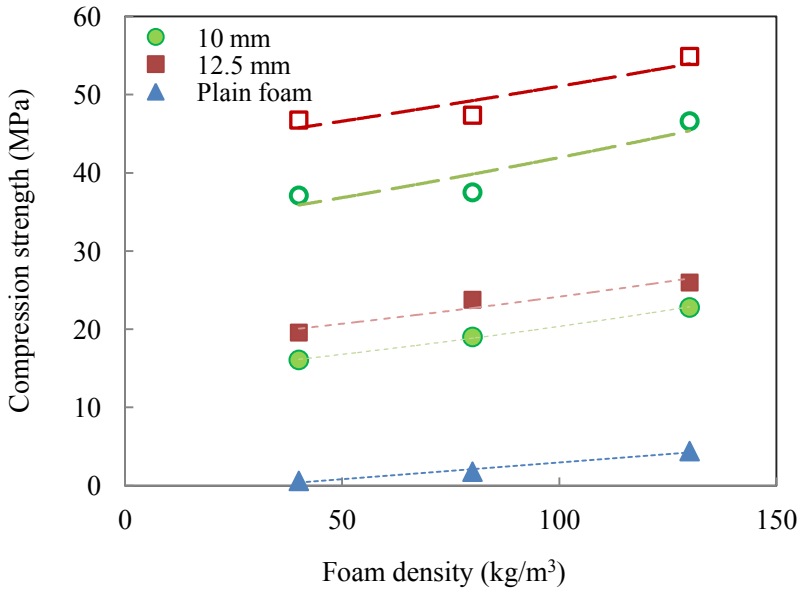

Fig. 4.50. The variation of the peak stress with foam density and the diameter of the carbon tubes at different loading rate. (Solid points are corresponding to quasi-static and hollow points to dynamic loading rates)

Figure 4.51 shows the variation of the specific energy absorption of the tube reinforced foams with foam density and tube diameter. Same as before, the specific energy absorbing values for the quasi-static tests are shown in solid points and that for the dynamic tests in hollow points. It is clear that introducing the tube reinforcements into foam efficiently enhance the energy-absorbing characteristic of the foam. i.e. the SEA values for the 10 and 12.5 mm carbon tube reinforcement system are around 74 and 87 kJ/kg approximately for quasi-static tests. An examination of the figure indicates that the SEA values for dynamic tests (hollow points) are lower than the corresponding quasi-static results (solid points) and the trend is decreasing to approximately 75% for its quasi-static values. It is also clear that the energy absorption values at dynamic rate are lower than the data at quasi-static rate, which suggests a distinct rate-sensitivity. This trend agrees with the investigations on carbon tubes at dynamic loading reported by Alia et al (2014). The reductions in SEA values due to the change in failure mechanisms at dynamic rates of loading. This also agrees with earlier finding on sizeable reductions in SEA at dynamic rates of loading observed by Schmuesser and Wickliffe (1987).

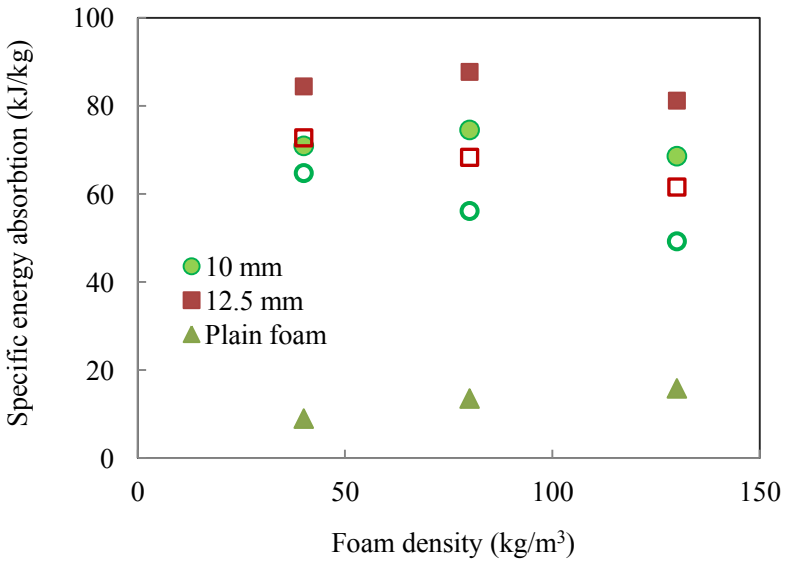

Fig. 4.51 The variation of the specific energy absorption of carbon tubes at the influence of the foam density at quasi-static and dynamic rates. (Solid points is corresponding to quasi-static and hollow points to dynamic rate)

The ratio of dynamic value to its quasi-static one as a dynamic enhancement factors (DEF) for the compression strength and energy (SEA) are also included in the Table 4-6, and presented graphically in Figure 4.52. Same with the rod reinforced systems, increasing the volume fraction of composite

tubes in the foam serves to slightly increase the compression strength of the tube reinforced foams as well as the overall amount of energy absorbed by the samples. However, the tube reinforced foams at dynamic rate exhibit increases in the compression strength being approximately 85% to 140%, whereas the energy absorption is decrease being approximately 10% to 37 %. In contract with the rods reinforced foam systems, the tube reinforced foams exhibits significantly higher energy absorbing capacity with high SEA values over the rod reinforced systems, whereas the carbon rod reinforced foam shows the advantage on dynamic rate. As expected, the possible flexible design and configuration on composite rod and tube as a combination offer advantages of both rod and tube for reinforcement of foam in applications of sandwich structures.

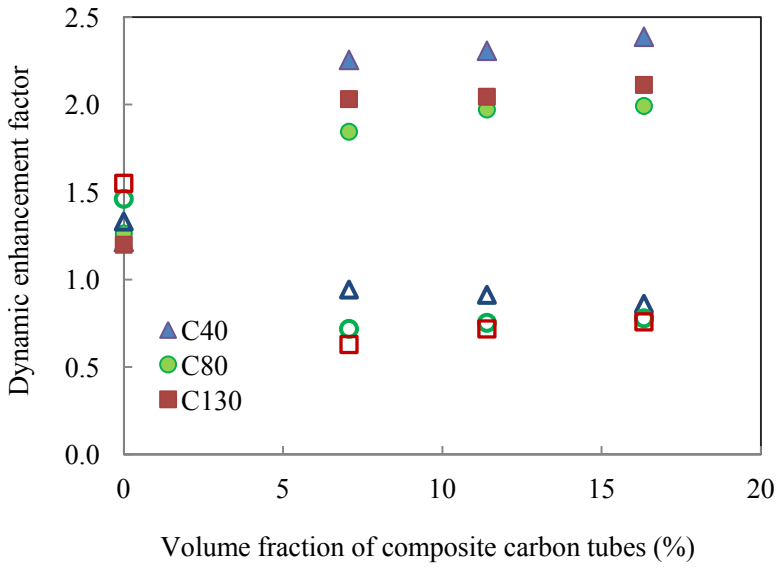

Fig. 4.52 The influence of composite tube and volume fraction of tubes on the dynamic enhancement factor. (Solid points is corresponding to compression strength and hollow points to and SEA)

Figure 4.53 shows the variation in the values of SEA for the composite reinforced systems as a function of composite volume fraction. The SEA values are based on the rod and tube systems subject to quasi-static and dynamic load. The volume fraction of composite increases with the diameter of composite rods and tubes embedded in foams. Increasing the volume fraction of composite in the foam serves to increase the SEA of the reinforced foams. The measured values of SEA vary between 16.9 and 43.2 kJ/kg for rod reinforced foam systems. The tube reinforced foam systems have SEA values in the range from 37.7 to 87.7 kJ/kg. As expected, both rod and tube reinforced foams exhibit increases in energy absorption and SEA values, with the tube system being approximately doubled over the rod system. Once again, it has been shown that the carbon rod based

systems exhibited a pronounced dynamic enhancement as summarized in Fig 4.34, whereas the tube system shows a disadvantage at a high strain-rate. However, the tube system still out-performs the rod system at both loading rates. The combined SEA charts for tube and rod reinforced foams in Figure 4.53 provides design options may be made to obtain SEA values between 16.9 and 87.7 kJ/kg on either composite rod or tube reinforced systems. The reinforced core structures can be selected as desired ones for sandwich structures.

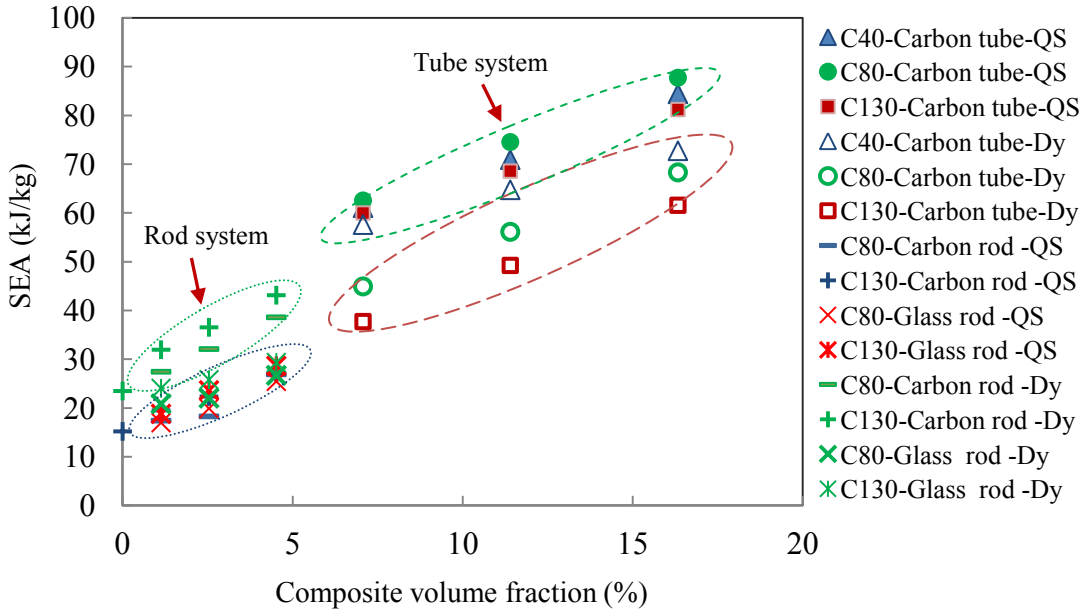

Fig. 4.53 The influence of the composite volume fraction on the specific energy absorbing characteristics.

Figure 4.54 summarizes the comparison of energy absorption capacity between composite reinforced foams and other core structures. Here, a widely range of core structures are compared with, which include rod and tube reinforced cores, corrugated-cores, aluminium foam core, honeycomb, foldcore, truss and lattices structures. The measured values of SEA on PVC foam, composite rod and tube systems in this study vary between 8.9 and 87.7 kJ/kg, shown as green bars in Figure 5.45. In the comparison, a large variation of SEA values obtained following investigations on composite and aluminium corrugated-core (approximately 31.5 and 62.5 kJ/kg) reported by Ruzaimi (2013), bamboo tube reinforced foam core (19 and 53 kJ/kg) tested by Umer et al (2014), carbon and Kevlar fold core (2-22.5 kJ/kg), aluminium honeycomb core (9 and 45 kJ/kg) reported by Heimbs (2012), aluminium syntactic foam (approximately 12.3 and 28.5 kJ/kg) tested by Altenaiji (2014), nature

fibre honeycomb (0.6 and 6.5 kJ/kg) reported by Zuhri (2014), pyramidal truss cores (0.75 and 8 kJ/kg), pyramidal truss cores (0.75 and 8 kJ/kg) reported by Xiong (2012) and lattice core (approximately 0.6 and 6.4 kJ/kg) tested by McKown(2008) and Smith (2011). Here, the carbon tube reinforced systems is out-perform to all the other structures compared, which is followed by the corrugated core structures. The carbon rod reinforced foam out-performs than the aluminium foam. It is also shown that the nature fibre honeycomb and lattice structure core are similar to have the lowest SEA value.

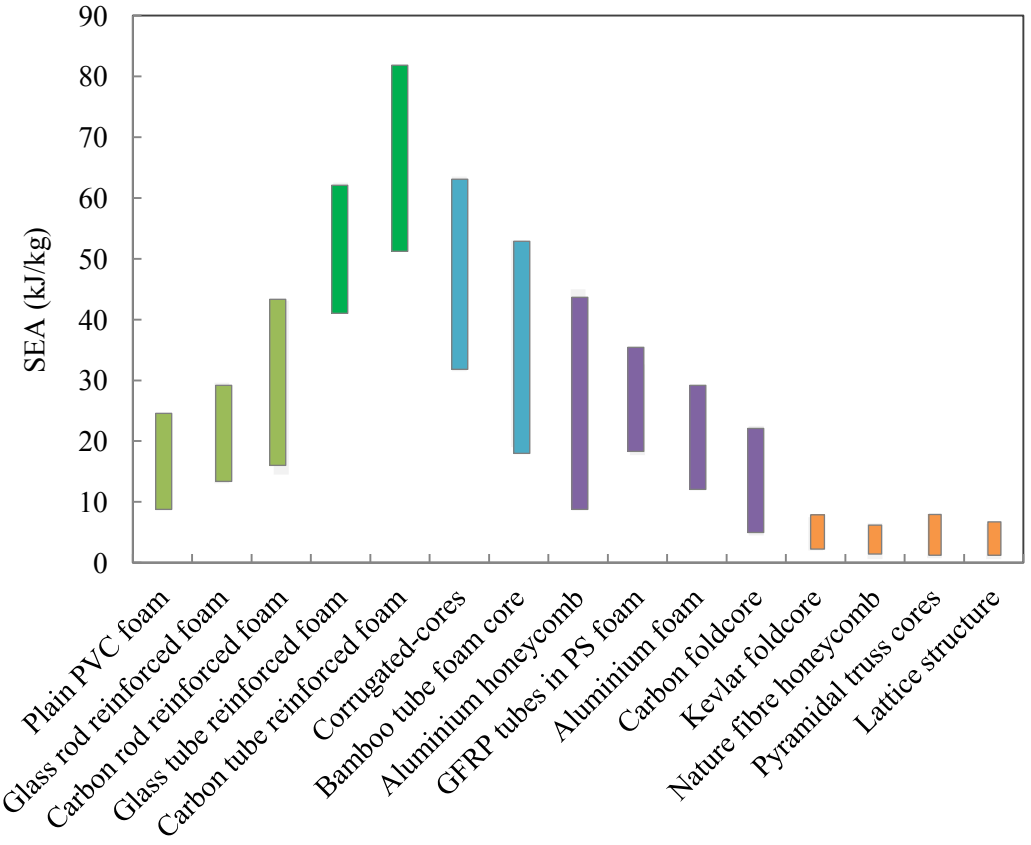

Fig. 4.54 The comparison on the specific energy absorbing characteristics between various core structures.

Table 4-6 Summary of the compression strengths and energy absorption properties of the tube reinforced foams based sandwiches

	Specimen details					Quasi-static			Dynamic			Dynamic Factor	
Specimen ID	Inner Dia. (mm)	Outer Dia. (mm)	Volume (%)	D/t Ratio	Mass (g)	Strength (MPa)	Energy (J)	SEA (kJ/kg)	Strength (MPa)	Energy (J)	SEA (kJ/kg)	Strength DEF	SEA DEF
C40 plain	0	0	0.0	0.0	0.9	0.60	7.80	8.96	0.73	10.38	7.93	1.22	1.33
C40C8	8	10	7.1	8.0	1.8	10.76	109.69	61.07	24.28	103.44	57.59	2.26	0.94
C40C10	10	12.7	11.4	7.4	2.3	16.07	162.23	70.92	37.10	148.08	64.73	2.31	0.91
C40C12	12.5	15.2	16.3	9.3	2.5	19.57	214.74	84.42	46.75	185.03	72.74	2.39	0.86
C40G8	8.5	12.7	11.4	4.1	3.4	22.70	139.03	41.29	54.44	165.91	51.94	2.40	1.19
C80 plain	0	0	0.0	0.0	1.7	1.78	23.56	13.52	2.25	34.40	9.31	1.26	1.46
C80C8	8	10	7.1	8.0	2.6	11.65	164.02	62.55	21.50	117.80	44.93	1.85	0.72
C80C10	10	12.7	11.4	7.4	3.1	19.01	229.20	74.53	37.50	172.57	56.12	1.97	0.75
C80C12	12.5	15.2	16.3	9.3	3.3	23.77	288.37	87.72	47.37	224.56	68.31	1.99	0.78
C80G8	8.5	12.7	11.4	4.1	4.2	33.40	211.45	50.89	57.38	220.29	53.02	1.72	1.04
C130 plain	0	0	0.0	0.0	2.8	4.41	44.80	15.82	5.29	69.44	10.07	1.20	1.55
C130C8	8	10	7.1	8.0	3.7	12.75	219.21	59.98	25.91	137.84	37.72	2.03	0.63
C130C10	10	12.7	11.4	7.4	4.1	22.78	278.35	68.57	46.60	199.85	49.23	2.05	0.72
C130C12	12.5	15.2	16.3	9.3	4.2	25.97	342.38	81.19	54.88	259.63	61.57	2.11	0.76
C130G8	8.5	12.7	11.4	4.1	5.1	44.30	323.04	62.85	63.80	230.56	44.86	1.44	0.71

4.6 Perforation resistance of the Fibre Metal Laminates

Rate-sensitivity effects in the perforation resistance of a range of fibre metal laminates (FMLs) made of three different aluminium alloys and a glass fibre reinforced epoxy resin have been investigated though a series of quasi-static and impact perforation tests on square plates. The specimen preparation for FMLs was described in Section 3.2.5. The perforation tests at both quasi-static and dynamic rates were presented in Section 3.3.5 and 3.4.1. Initial attention focused on assessing the rate-sensitivity of the constituent materials, i.e. the woven glass fibre reinforced epoxy and the three aluminium alloys though quasi-static tensile tests and split Hopkinson bar tensile tests was described in Section 3.3.2 and Section 3.4.4 respectively. This was followed by compressive tests in both the layer and edge directions using the test rig described in Section 3.3.1, in order to assess the compression resistance and bonding strength effects on the perforation resistance of FMLs. Finally, a series of perforation tests was undertaken on multilayer configurations ranging from a simple 2/1 lay-up to a 5/4 stacking sequence following quasi-static and dynamic rates of loading. Experimental results were evaluated in this section.

4.6.1 Tensile tests on constituent materials of FMLs

Figure 4.55 shows stress-strain curves following tensile testing on the three aluminium alloys. Clearly, all three alloys exhibit very different mechanical properties. The 6061-O offers a relatively low tensile strength, but a high failure strain. In contrast, the 6061-T6 alloy, offers a tensile strength that is approximately three times higher than that of its 6061-O counterpart, associated with a strain to failure that is roughly one third of the more ductile alloy. The 7075-O alloy exhibits properties that lie between those two materials. The mechanical properties of three alloys are summarized in Table 4-7. The glass fibre/epoxy exhibited a relatively linear stress-strain trace up to failure at an average stress of 438 MPa and a strain of 3.1%.

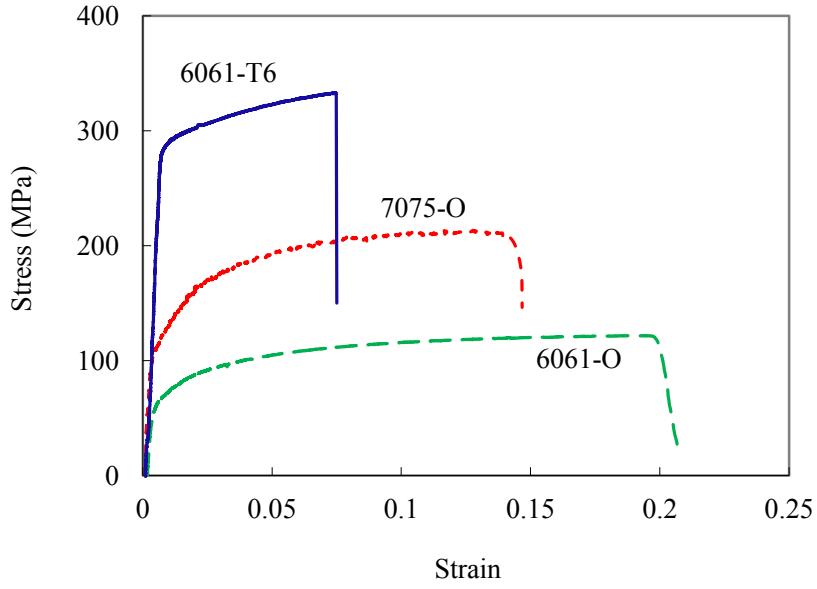

Fig. 4.55 Stress-strain curves following tensile tests on the 6061-O, 6061-T6 and 7075-O aluminium specimens,

Table 4-7 Tensile properties of the constituent materials used in FMLs

Specimen/Material	Thickness (mm)	Yield Strength (MPa)	Tensile Strength (MPa)	Elongation at break (%)
7075-OAl	1	111	213	13.5
6061-O Al	0.5	54.5	122	20.6
6061-T6 Al	0.28	275	332	7.5
GRFP	1	-	438	3.1

The strain-rate sensitivity of the GFRP and the three types of aluminium alloys were evaluated using Hopkinson bar tensile test rig. A typical data acquisition was conducted by recording the voltage signals measured in the incident bar and transmitted bar of the Hopkinson bar apparatus. Figure 4.56 shows typical pulses of incident, reflected and transmitted signals that were obtained from tensile Hopkinson bar apparatus at the University of Liverpool. The strain-rate in the test sample, which was determined by the velocity of the input bar, was varied by adjusting the pressure in the main chamber of the gas gun.

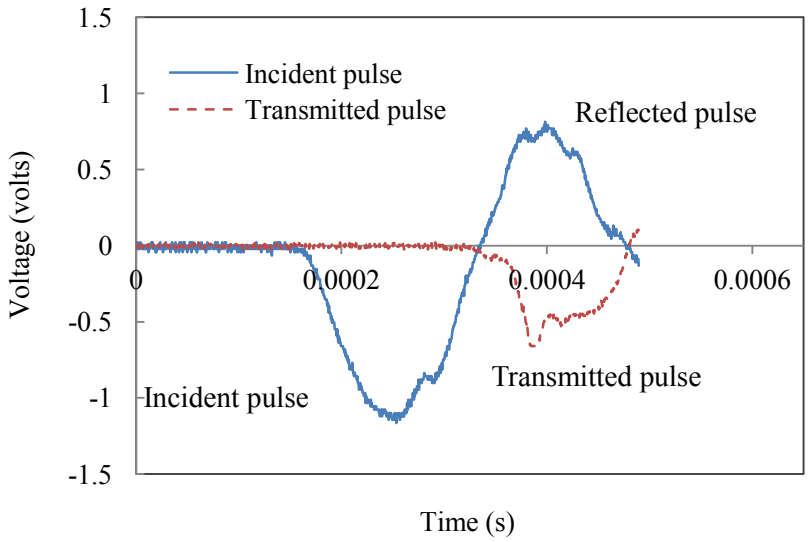

Fig. 4.56 Typical voltage pulses acquired from strain gauge on the incident and transmitted bars.

A series of Hopkinson bar tensile tests was conducted at various strain rates. Figure 4.57 shows the variation of tensile strength with strain-rate for the four materials investigated in this study. From the figure, it is clear that all four materials exhibit a relatively low degree of rate-sensitivity. The average dynamic tensile strength for the 6061-O, 6061-T6, 7075-O and GFRP are 146.1, 413.3, 259.1 and 480.9 MPa respectively at the highest rate of 970 s^{-1}. The tensile strength was increased slightly from the load rate at quasi-static rate of 0.0167 s^{-1} to dynamic rate of 970 s^{-1}.

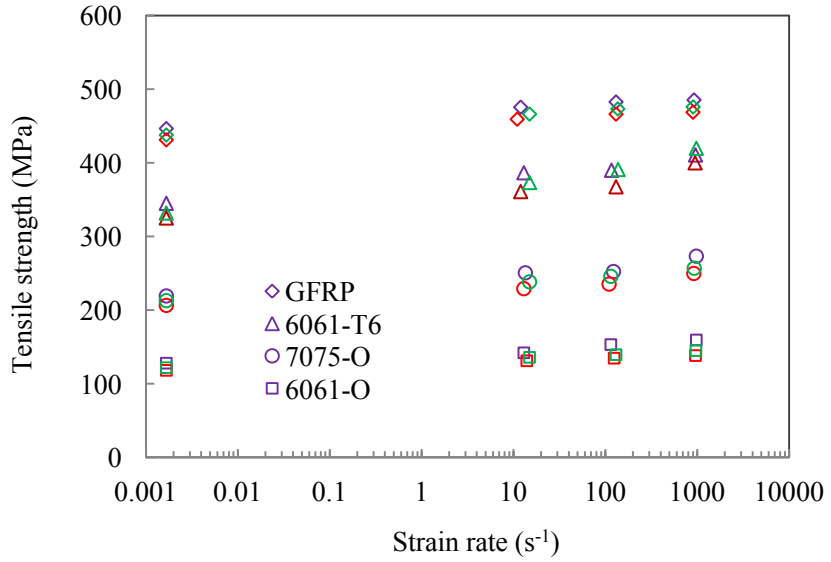

Fig. 4.57 The variation of tensile strength with strain rate for the constituent materials.

The Cowper-Symonds relationship, given in Equation 4-1, was applied to the data in Figure 4.57,

and the resulting values for the Cowper-Symonds constants D and p are given in Table 4-8.

$$\frac{\sigma_{dyn}}{\sigma_{stat}} = 1 + \left(\frac{\dot{\varepsilon}}{D}\right)^{\frac{1}{p}} \qquad \text{(Eq. 4.3)}$$

Table 4-8. Summary of the Cowper-Symonds coefficients for the four materials investigated in this study.

Material	$\dot{\varepsilon}$ range (s^{-1})	D (s^{-1})	p	R^2
7075-O	0.0017 - 950/s	422426.41	4.2403	0.9822
6061-O	0.0017 - 950/s	624835.69	4.3263	0.9813
6061-T6	0.0017 - 970/s	183603.42	4.0517	0.9989
GRFP	0.0017 - 950/s	74512671	5.3323	0.9785

Figure 4.58 shows the percentage of increases in tensile strength over the range of strain-rates from quasi-static to dynamic rate of 970 s^{-1}. The average increases in tensile strength over the range of strain-rates for the 6061-O, 6061-T6, 7075-O and GFRP are 19.7, 24.5, 21.6 and 9.8 % respectively. The increases of tensile strength for the three aluminium alloys are similar with a percentage of 11 % at lower loading rate. It is interesting to note that the rate-sensitivities of the three alloys are similar and greater than that of the composite.

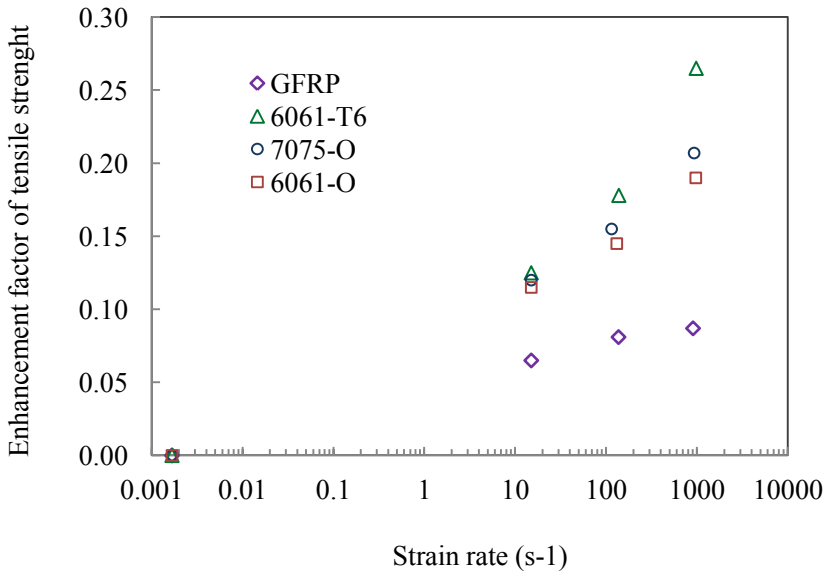

Fig. 4.58 Enhancement factor of tensile strength at strain rate of 0.00167/s, 15/s, 120/s and 950/s

4.6.2 Compressive tests on the FMLs

Compressive tests were carried out in both the layer and edge directions in order to assess the compression resistance and bonding strength effects on the perforation resistance of FMLs. Compressive tests were undertaken in attempted to investigate the influence of compression strengths on the damage initiation threshold.

Figure 4.59 shows a comparison of the stress-strain curves for 6061-O, 6061-T6, 7075-O based FMLs following quasi-static compressive tests on both the inter-laminar direction and the edge direction. In the Figure 4.59 (a), the curves show the higher compression strength of 592 MPa for 6061-T6 based FMLs, followed by 349MPa and 322 MPa for the 7075-O and 6061-O, which is corresponding to the order of tensile strength of the three aluminium alloys. The highest compression modulus is 7075-O based FMLs, followed by the 6061-T6 and 6061-O. The stress-strain curves for compressive tests in edge direction (Fig. 4.59 b) show that the both the highest strength and modules for the 6061-T6 over the relative lower value on 6061-O and 7075-O. Both the strength and modulus were influenced mainly by the thickness of aluminium layer and GFRP, which determined by the bonding strength of resin between layers. The comparison of strengths in both directions are shown in Tables 4-9 and 4-10.

Table 4-9 Compression test on aluminium FMLs specimen

FMLs Configuration	Thickness (mm)	Compression Strength (MPa)	Elongation at break (%)
7075-O 5/4 (5-ply) FMLs	9 mm	364.6	10
6061-O 5/4 (3-ply) FMLs	4.8 mm	332.6	13
6061-T6 5/4 (3-ply) FMLs	3.6 mm	591.2	22.4

Table 4-10 Edge compression test on aluminium FMLs specimen

FMLs Configuration	Thickness (mm)	Compression Strength (MPa)	Elongation at break (%)
7075-O 5/4 (5-ply) FMLs	9 mm	132.3	3.5
6061-O 5/4 (3-ply) FMLs	4.8 mm	152.1	2.8
6061-T6 5/4 (3-ply) FMLs	3.6 mm	302.3	3.9

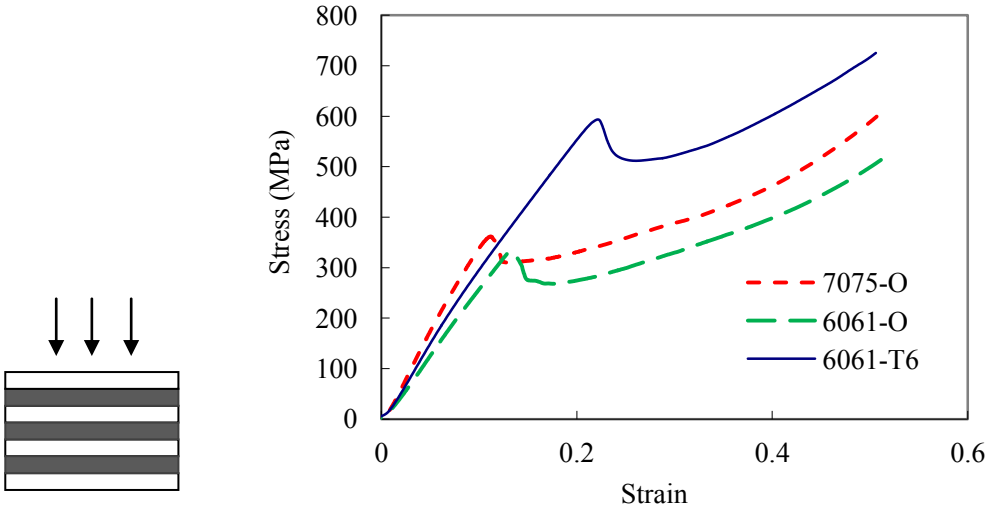

(a) Inter-laminar direction

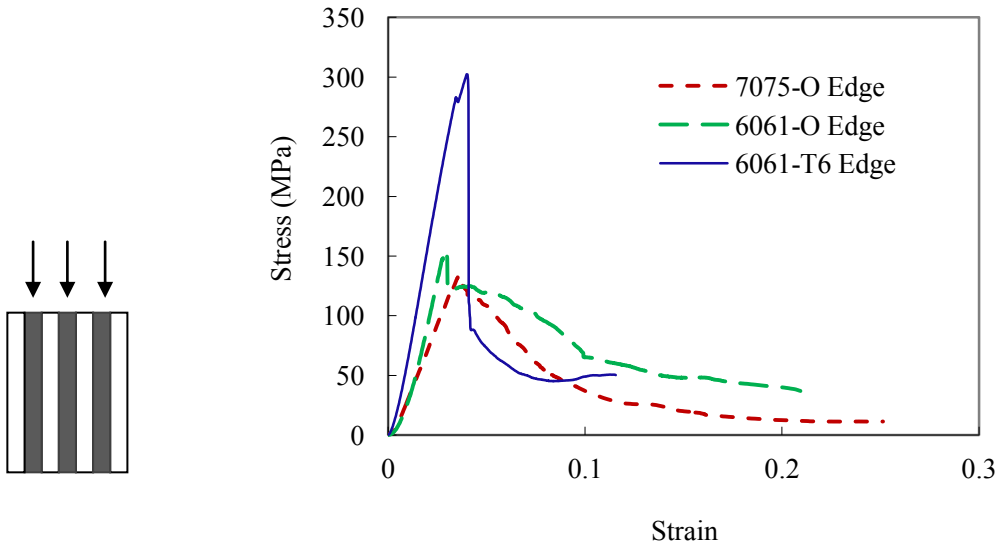

(b) Edge direction

Fig. 4.59 Comparison of stress-strain curve for edge compression tests on 6061-O, 6061-T6 and 7075-O aluminium based FMLs specimens with 4/3 stacking sequence.

4.6.3 Perforation tests on individual layers

Prior to conducting perforation test on the FMLs, a series of tests were undertaken on plain CFRP and plain aluminium alloy samples. Figure 4.60 shows the force-displacement traces following quasi-static tests. It is noted that the peak resistance increasing with the thickness of CFRP layers and the 1 mm 7075-O aluminium shows higher peak load up to 2.6 kN, over the 0.5 mm 6061-O and 0.28 mm 6061-T6 plates. The traces also show that the 7075-O and 6061-O have a maximum

displacement around 8.35 mm at peak load, whereas the 6061-T6 only 4.1 mm. In all cases, the energy required to perforate the samples were calculated based on the area under the force-displacement traces of these various materials. Both the peak load and maximum displacement determine the perforation resistance and energy absorption.

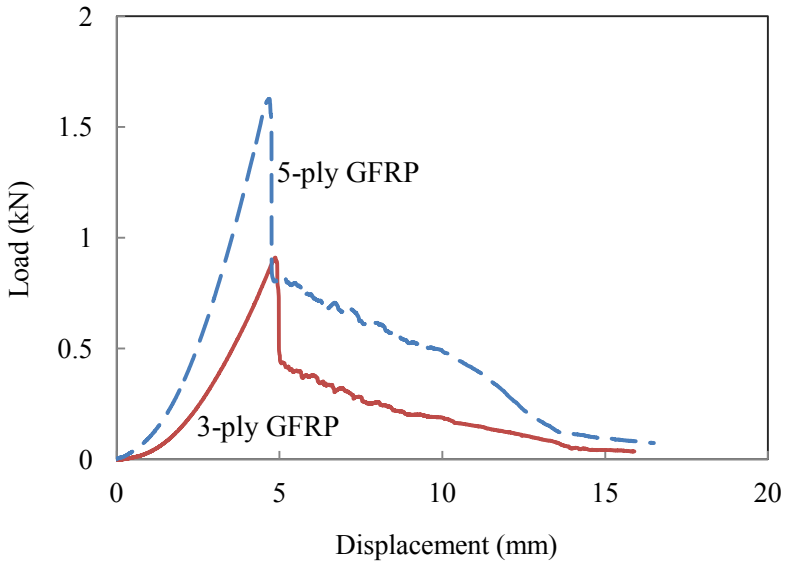

(a) Load-displacement traces of glass fibre layers

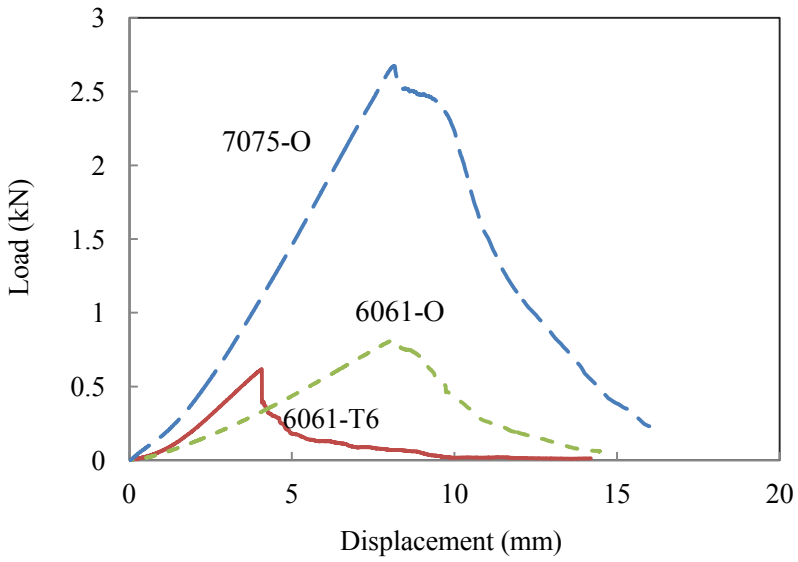

(a) Load-displacement traces of aluminium plate

Fig. 4.60 Comparison of load-displacement traces of static test on individual layer of 7075-O, 6061-O and 6061-T6 aluminium

4.6.4 Quasi-static perforation tests

Figure 4.61 shows typical force-displacement traces following quasi-static indentation on FMLs based on the 6061-T6, 6061-O and 7075-O alloys. The trace for the 2/1 6061-T6 alloy, shown in Figure 4.61(a), exhibits some stiffening during the initial loading region, due to membrane effects in this relatively thin laminate. The sample starts to fracture under the indentor, before a tensile crack appears on the lower surface and the force starts to reduce. The force gradually drops to zero as the projectile perforation the target. Similar trends are apparent in the thicker laminates, with the maximum force increasing rapidly as the overall laminate thickness increases. It is believed that the small load drop in the thickest laminate is associated with yielding in the top surface aluminium layer under the point of application of the impact force. Traces corresponding to the tests on the thicker 6061-O and 7075-O alloy are shown in Figure 4.60 (b) and (c). Here, the maximum forces are clearly much higher than those in Figure 4.61(a), due to the increased thickness of the FMLs.

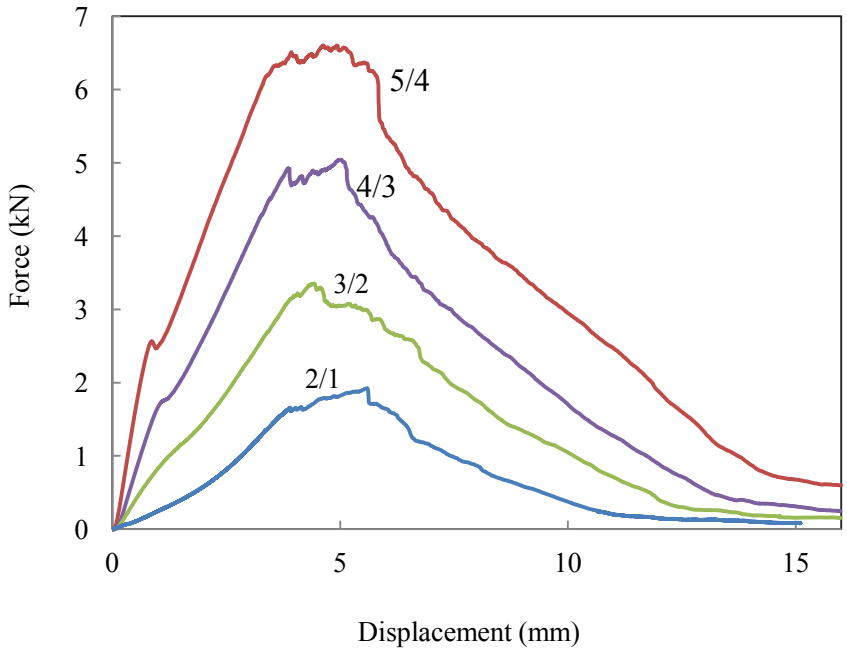

(a) 6061-T6 aluminium alloy,

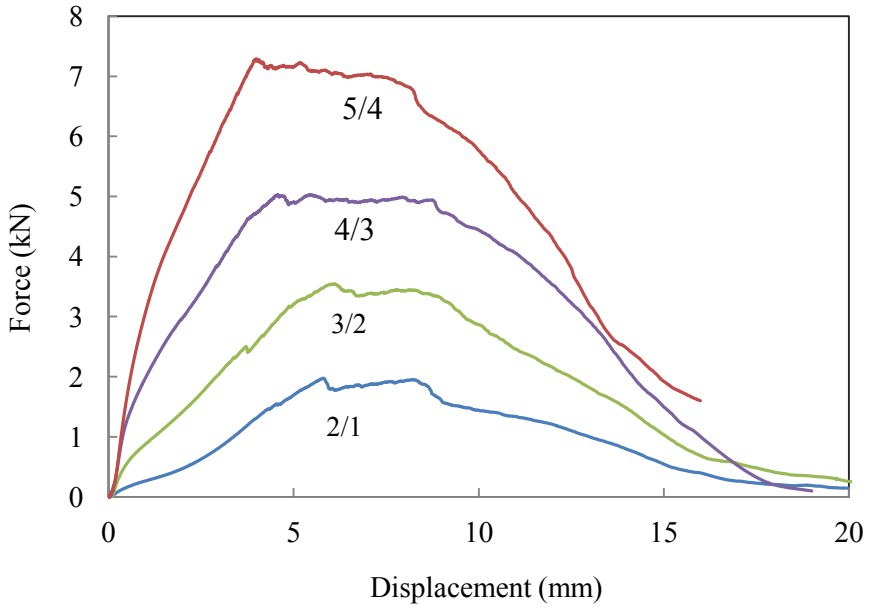

(b) 6061-O aluminium alloy,

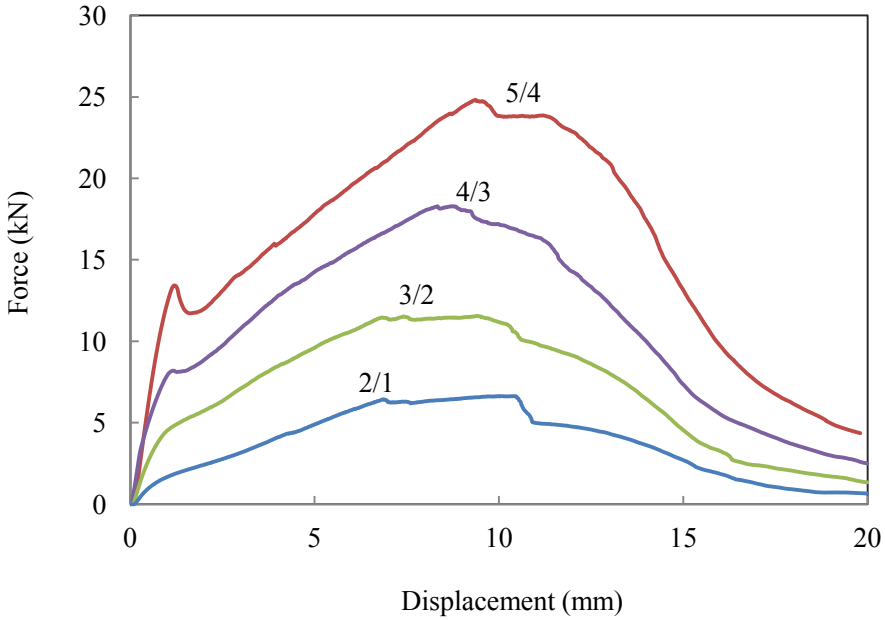

(c) 7075-O aluminium alloy

Fig. 4.61 Load-displacement traces following quasi-static perforation tests on FMLs based on the 6061-T6 and 7075-O aluminium alloy.

The areas under the various load-displacement traces were determined and used to establish the energy absorbed by the test samples during the perforation process. Figure 4.62 shows the variation of absorbed energy with plate thickness for the three material systems and the four stacking configurations. From the figure, it is clear that the energy required to perforate the laminates

increases with thickness. The evidence suggests that the increase in energy is roughly linear with thickness, with the two 6061 alloys exhibiting a similar performance. In contrast, the 7075 system appears to offer a superior performance for a given target thickness.

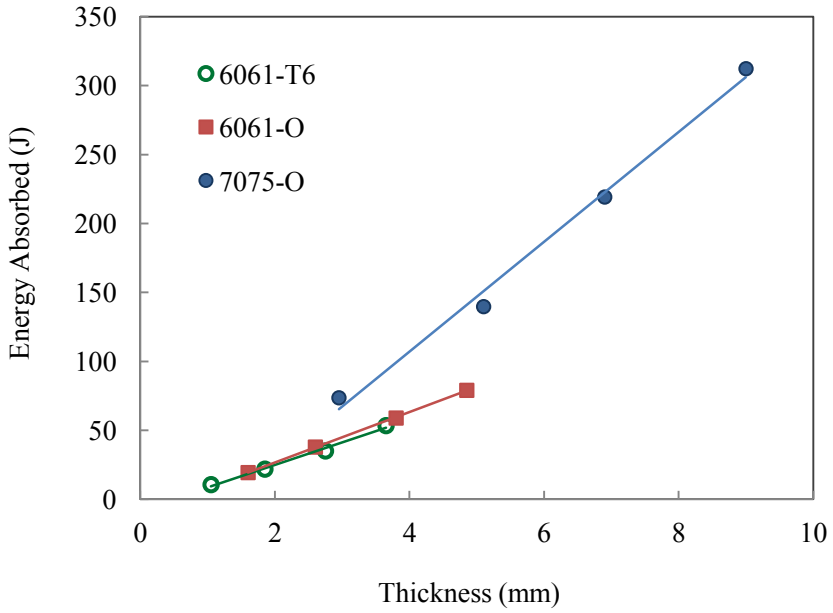

Fig. 4.62 The variation of the energy absorbed during quasi-static perforation as a function of plate thickness.

Figure 4.63 shows cross-sections of the twelve FML configurations investigated in this study. In all cases, the perforation process involves local plastic deformation of the aluminium alloy, as well as fracture of the composite plies close to the point of impact. Failure in the test samples involved tensile fracture on the lower surface of the sample, leading to a cross-shaped fracture pattern. These cracks tended to propagate upwards through the thickness of the laminate, enabling the projectile to finally push through the plate, leading to the formation of a hole, as shown in the front and rear surface photographs in Figure 4.64. Close examination of Figure 4.63 suggests that there is a higher level of adhesion in the two 6061 alloys than in the 7075 system. Other than this observation, there are no significant differences between the various stacking configurations. It is worth noting that similar failure patterns have been observed following high velocity impact tests on FML plates.

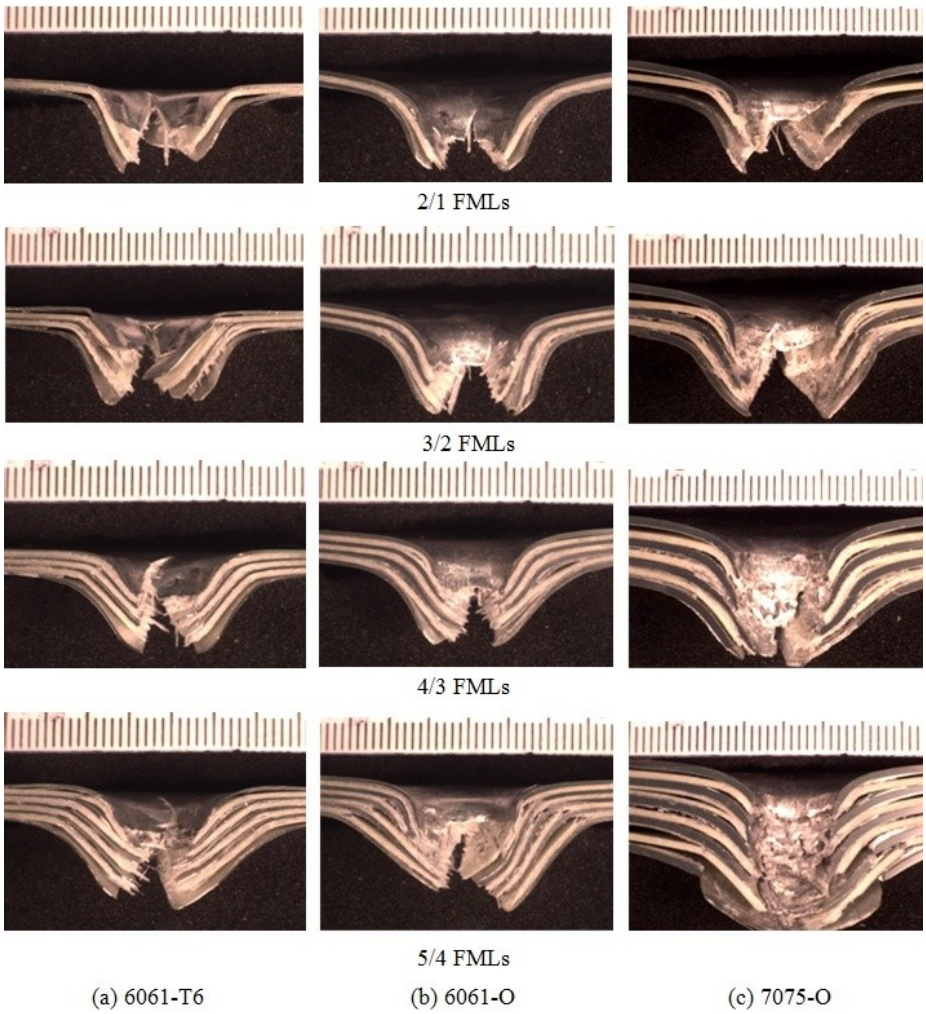

Fig. 4.63 Comparison of cross-sections following quasi-static perforation tests on FMLs based on the 6061-T6, 6061-O and 7075-O aluminium alloys.

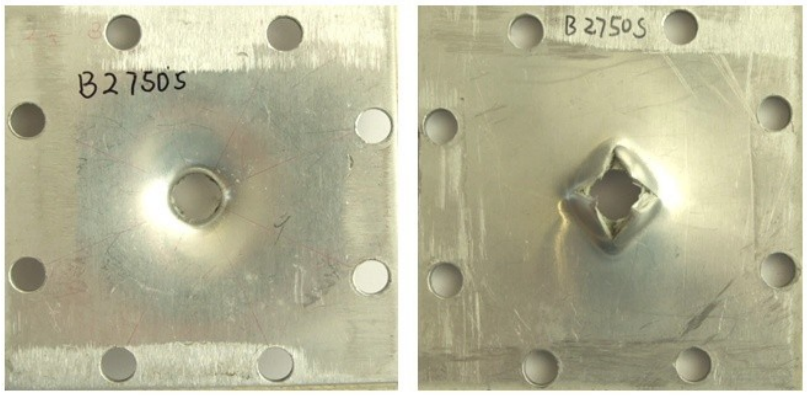

(a) 3/2 FMLs

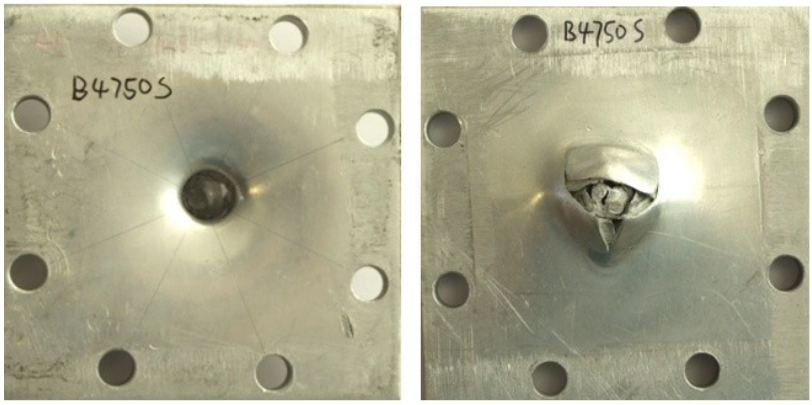

(b) 5/4 FMLs

Fig. 4.64 Photographs of the front and rear surfaces of FMLs based on the 7075-O FML following quasi-static perforation testing (a) a 3/2 configuration and (b) a 5/4 configuration.

Figure 4.65 summarizes the SEA values of the various FMLs investigated here. From the figure, it is clear that the 7075-O based laminates offer the highest levels of specific energy absorption, with values being approximately double those measured on the 6061 laminates. This enhanced performance may not be due to the specific properties of the aluminium alloy, but may be due to the fact that the aluminium layers are very thick in these systems. It is interesting to note that the 6061-O laminates outperform their T6 counterparts, although this may also be due to the increased thickness of the metal layers. An examination of the figure indicates that the value of SEA increases in passing from a 2/1 to a 3/2 to a 4/3 FML etc. Vlot et al. (1998) conducted quasi-static perforation tests on a range of carbon, glass and Kevlar fibre FMLs and his data when normalized by areal density, gave values for the SEA of GLARE between 4.95 and 5.7 Jm^2/kg.

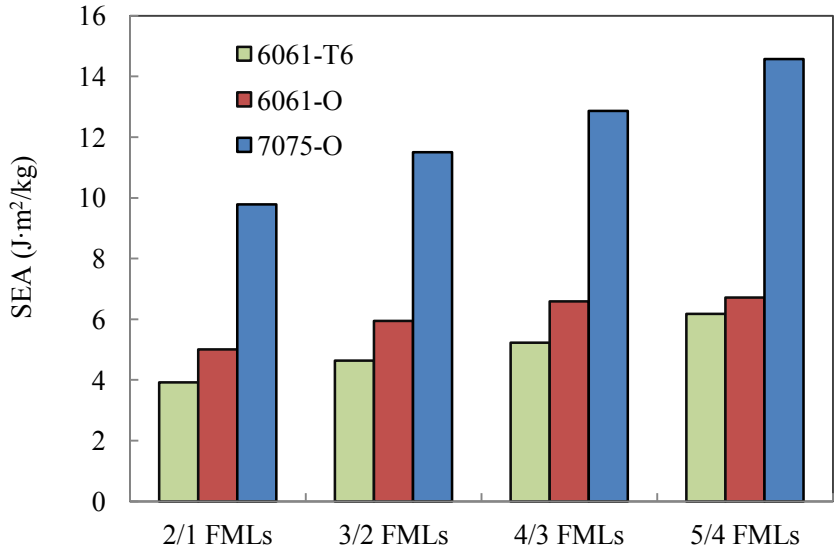

Fig. 4.65 Summary of the specific energy absorption (SEA) values following quasi-static perforation tests.

4.6.5 Low velocity impact tests on FMLs

Prior to conducting low velocity impact test on the FMLs, a series of tests were undertaken on plain CFRP and plain aluminium alloy samples. Figure 4.66 summarizes the quasi-static and impact perforation resistance of these various materials. In all cases, there is a small increase in the energy required to perforate the samples as the strain-rate is increased. For example, the dynamic perforation energy of the GFRP was 17.1% higher than its quasi-static value. The corresponding increases for the 6061-T6, 6061-O and 7075-O alloys are 26%, 14% and 18%. It is interesting to note that these relative increases in perforation energy are of a similar magnitude to the increases in tensile strength observed following the split Hopkinson bar tests in Figure 4.57. Finally, an examination of the perforated samples highlighted similar failure modes in the composite and metal plates at both strain-rates.

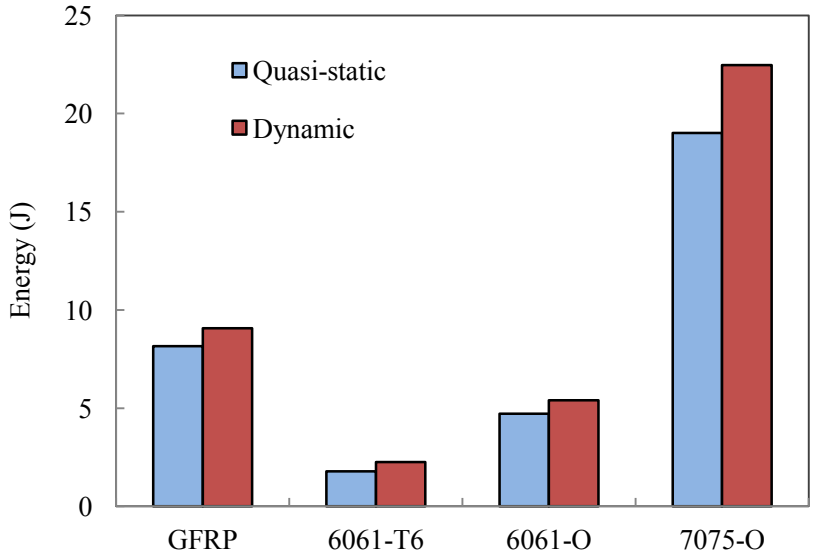

Fig. 4.66 Summary of the energy absorption values following impact perforation tests on the GFRPs and the three aluminium alloys.

Figure 4.67 shows typical load-displacement traces following drop-weight impact tests on the 6061-T6 and 7075-O alloys. Included in the figures are the equivalent traces obtained from the quasi-static perforation tests. An examination of the figure indicates that the loads associated with the dynamic tests are all higher than the quasi-static values. The general shapes of the four dynamic traces are similar to the quasi-static equivalents, although the 5/4 laminates exhibit a saw-toothed appearance under impact conditions. As before, the energy required to perforate the laminates was evaluated by determining the area under the load-displacement traces and the resulting values are shown in Figure 4.68. Here, it is apparent that the 7075-O system offers the greatest perforation resistance, with the thinnest of the four systems out-performing the 6061 laminates by over fifty percent. Once again, for a given thickness, there appears to be little or no difference between the performance of the two 6061 FMLs.

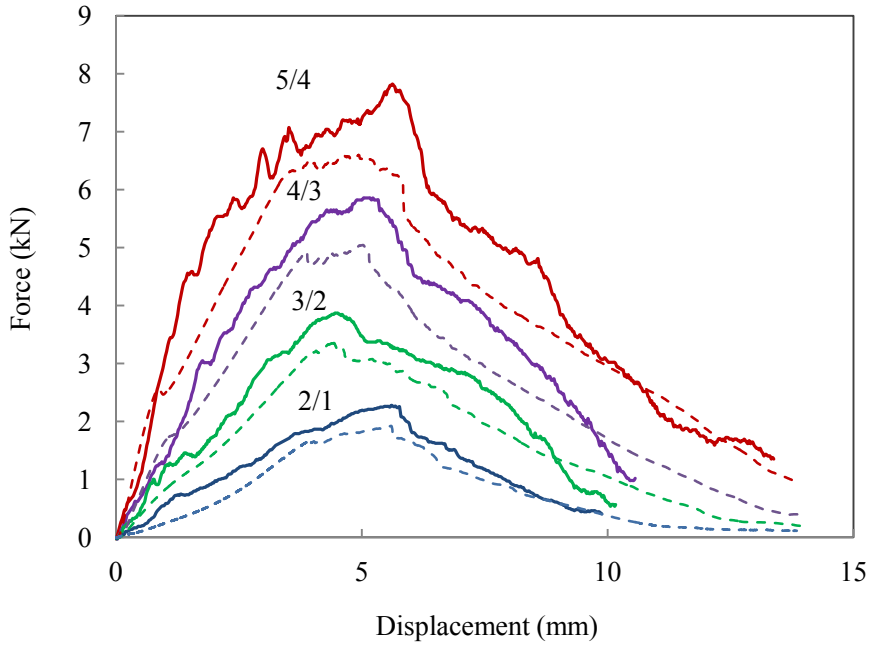

(a). 6061-T6

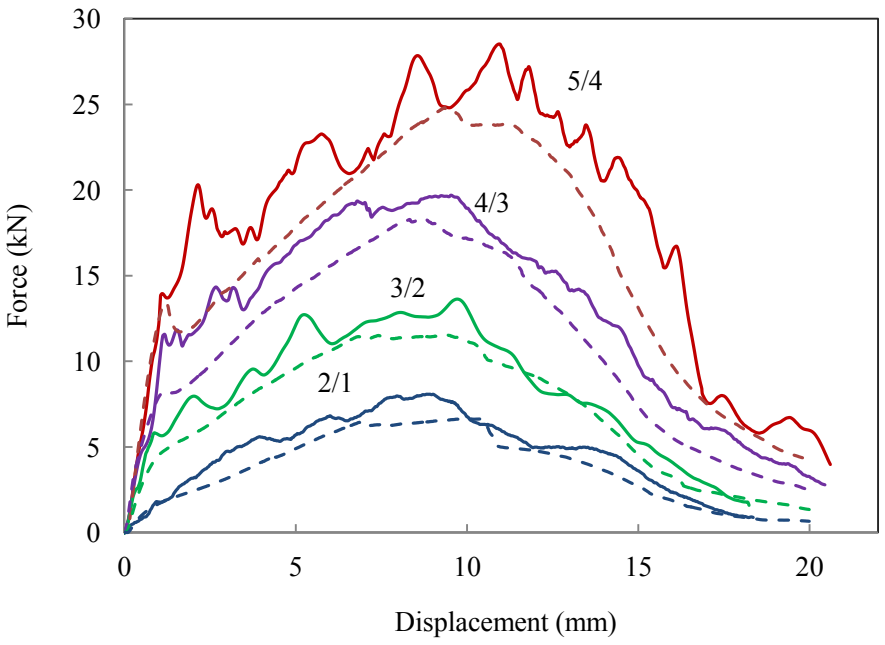

(b). 7075-O

Fig. 4.67 Load-displacement traces following low velocity impact tests on the 6061-T6 and 7075-O FMLs (solid lines). The figure also includes the equivalent quasi-static traces (dashed lines).

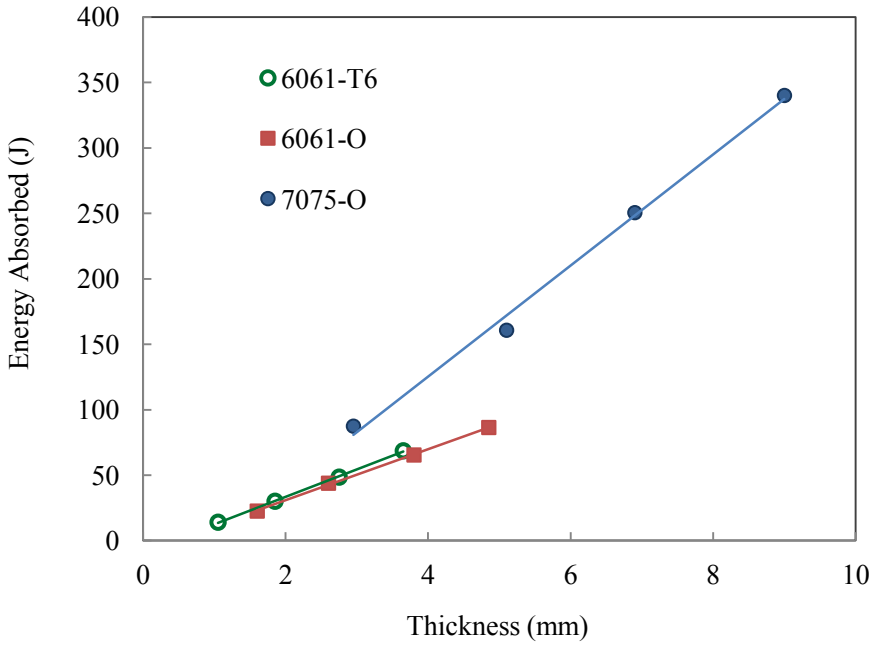

Fig. 4.68 The variation of the energy absorbed during impact perforation tests as a function of plate thickness.

Figure 4.69 shows cross-sections of the dynamically-loaded FMLs, where similar fracture patterns to those observed earlier (see Figure 4.63) are apparent. As before, there is evidence to suggest that the strength of the composite-metal bond is lower in the 7075-O alloy, with there being greater levels of delamination apparent in the cross-sections. Figure 4.70 shows the front and rear surfaces of two configurations based on the 7075-O alloy. Overall, the appearance of the impact-loaded plates is similar to the corresponding quasi-static laminates shown earlier in Figure 4.64.

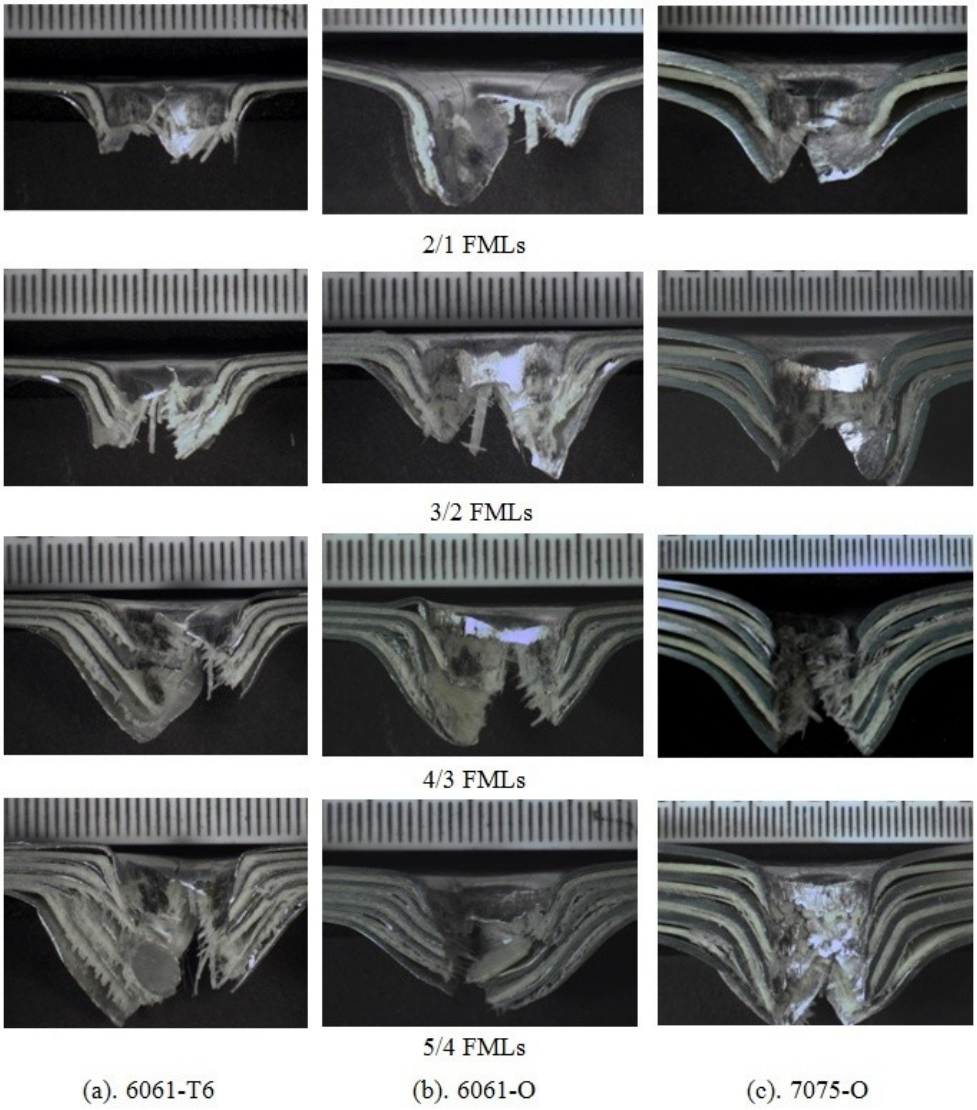

Fig. 4.69 Comparison of cross-sections following impact perforation of FMLs based on the 6061-T6, 6061-O and 7075-O aluminium alloys.

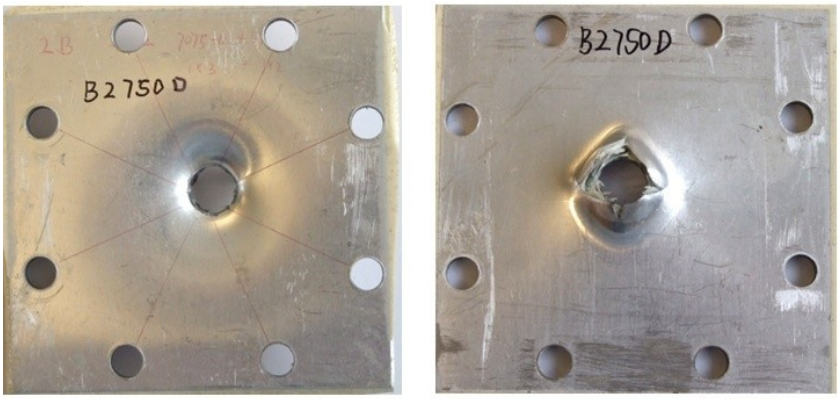

(a) a 3/2 configuration

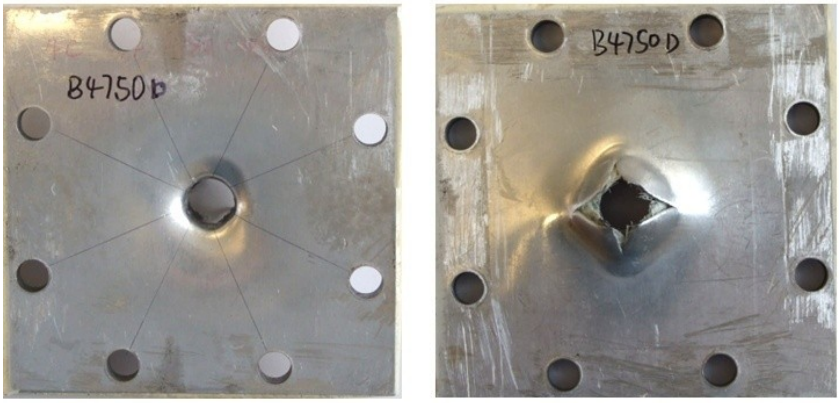

(b) a 5/4 configuration

Fig. 4.70 Photographs of the front and rear surfaces of FMLs based on the 7075-O FML following impact perforation.

The specific energy absorption characteristics of the impact-loaded FMLs are summarised in Figure 4.71, where it is again clear that the 7075-O system offers the most impressive energy-absorbing characteristics, with values that vary between 11.5 and 15.7 Jm^2/kg, depending on the laminate thickness. Once again, it is evident that increasing the thickness of the FML yields a higher value of SEA. For example, the SEA of the 2/1 6061-T6 FML is 5.17 Jm^2/kg whereas that for the 5/4 FML is 7.94 Jm^2/kg.

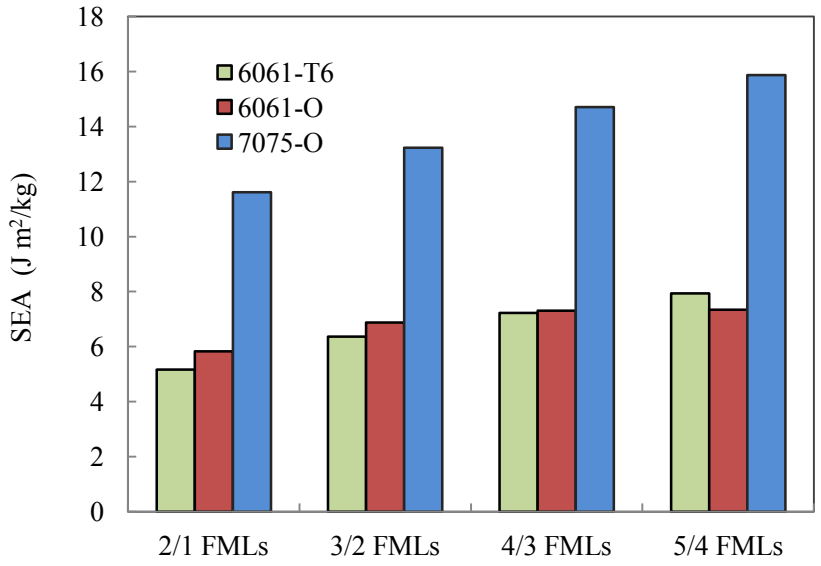

Fig. 4.71 Summary of the specific energy absorption (SEA) values following impact perforation tests.

A comparison of the quasi-static and dynamic values for SEA in Figures 4.65 and 4.71 suggests that slightly higher levels of energy are absorbed under conditions of impact loading. This is highlighted in Figure 4.72, where the dynamic and static values are plotted for all of the configurations investigated here. From the figure, it is evident that the dynamic values of SEA are slightly higher than the static values, reflecting a low level of rate-sensitivity. The evidence suggests that the 6061-T6 system is slightly more rate-sensitive than the 6061-O FMLs. The rate-sensitivity of the FMLs was further investigated by plotting the maximum forces measured dynamically against those measured quasi-statically. These results are shown in Figure 4.73 where, once again, there is evidence of only a small degree or rate-sensitivity in the mechanical response.

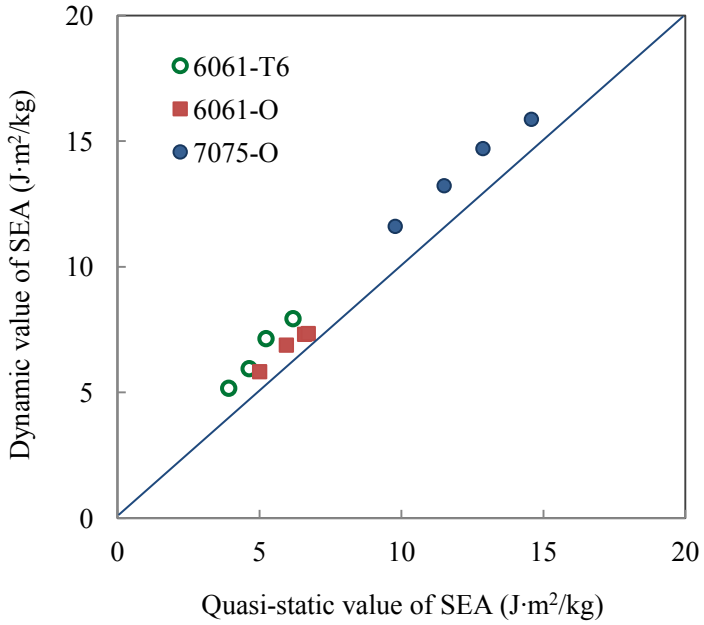

Fig. 4.72 Plot of the dynamic values of SEA against the quasi-static values.

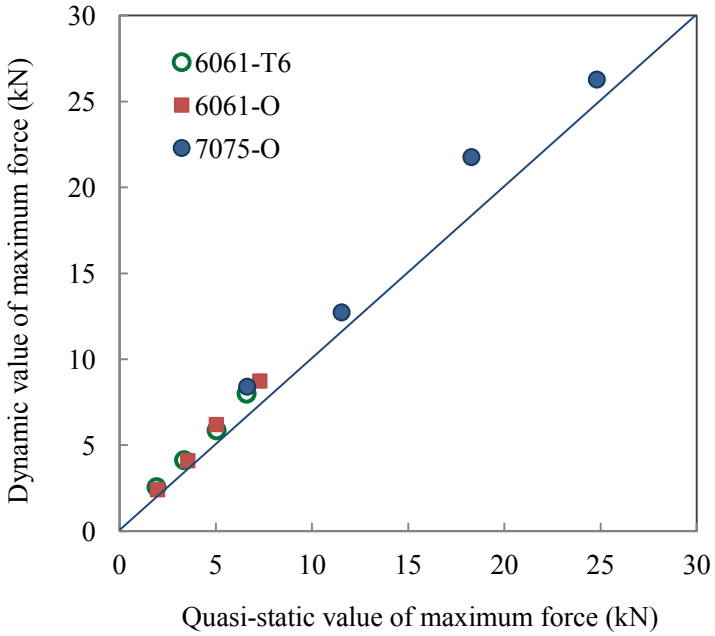

Fig. 4.73 Plot of the dynamic values of maximum force against the quasi-static values.

An insight into the contribution of the aluminium and GFRP constituent layers to the overall perforation resistance of the FMLs was gained by summing the energies absorbed by the plain materials under either quasi-static or, where appropriate, low velocity impact loading. For example, consider the 4/3 6061-O laminate subjected to impact loading. Impact tests on the plain alloy and the three ply GFRP yielded perforation energies of 4.72 and 3.61 Joules respectively. Multiplying the value for the alloy by the number of metal layers, i.e. four and the value for the composite by three,

yields an overall value of 29.73 Joules for the sum of the individual contributions. These values were calculated for all of the laminates, subjected to both static and dynamic loading and the results are plotted against the measured perforation energy of the various FMLs in Figure 4.74. This figure highlights some interesting trends. Firstly, as expected, the energy absorbed by the FMLs is significantly greater than that associated with simply adding the contributions of the various constituent materials. Secondly, all of the data appear to fall on a single line, regardless of the alloy type or laminate thickness. It is also interesting to note that increasing the strain-rate, i.e. passing from quasi-static to impact rates of loading, serves to move the experimental points upwards along the line (the perforation energies of the constituent materials and the FMLs are both rate-sensitive). It is suggested that this graph could be used to obtain estimates for the perforation resistance of thicker FMLs. However, it is not clear how changing the planar dimensions of the target would affect the slope of this trace, and further research is required to assess this.

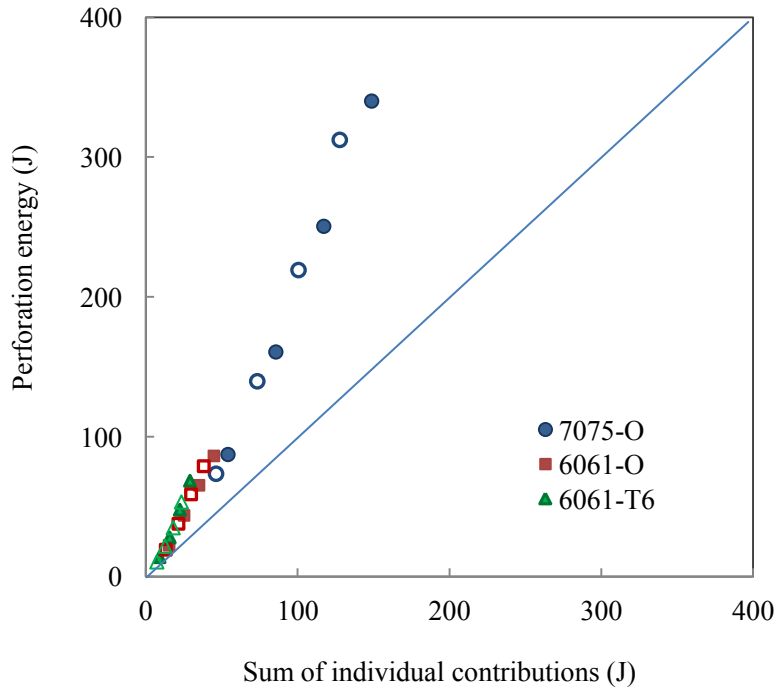

Fig. 4.74 Plot of the values of perforation energy against the aggregated values of the individual constituent materials. (The solid points corresponding to dynamic values and the hollow points/air core to static values)

4.7 Summary

Experimental investigations on PVC foam based sandwiches, composite rod and tube reinforced foams, fibre metal laminates have been undertaken and the results have been summarized in this chapter. Firstly, mechanical properties of the PVC foam, the GFRP, aluminium, the composite rods and the tubes have been presented and characterized. Subsequent, results from perforation and compressive tests on those structures are presented following quasi-static and dynamic tests to evaluate the strength and energy-absorbing capability. Furthermore, the results have been summarized and analyzed to cover perforation resistance, energy absorbing and rate-sensitivity of those hybrid material and structures. Finally, the performance of those structures has been evaluated by SEA chats and summarized as below.

Testing has shown that the perforation resistance of the plain foams and the sandwich panels increases with increasing core density and the linear crosslinked PVC foams offer a higher perforation resistance than the linear PVC foams at low densities, whereas the converse is true at higher densities. It has also been shown that graded foam cores based structures can out-perform their monolithic counterparts which benefits associated with placing the high density foam core in front surface, lowest density foam in the centre of the core and ductile foam at rear surface.

Experimental results have been shown that the energy absorbed by the composite reinforced cores increases linearly with foam density and that it also increases with increasing of composite fraction. The carbon fibre rod reinforced foam panels offer excellent compression strengths and energy-absorbing characteristics to their glass fibre counterparts with SEA ranging from 15-29 kJ/kg at quasi-static rate of strain. In addition, the carbon tube reinforced foam panels offered superior compression strengths and SEA in the range of 45-89 kJ/kg. However, the corresponding SEA of the carbon rod reinforced structures increased by up to sixty percent, whereas the corresponding SEA for the carbon tube reinforced foams decreased to almost seventy percent of the values in passing from quasi-static to dynamic rates of loading.

Tests on FMLs and its individual constituent materials on the glass fibre/epoxy and the various aluminium alloys highlighte a low level of rate-sensitivity over a range of loading rates. The energy

to perforate the FMLs was plotted against that required to perforate the individual constituent materials, where it has been shown that all of the experimental data appear to fall on a straight line, regardless of the thickness of the hybrid material, Such plots could be useful for estimating the perforation resistance of other stacking sequences based on these material systems.

CHAPTER 5 FINITE ELEMENT MODELLING

5.1 Introduction

This chapter introduces numerical modelling theory and finite element models for different composite structures. The finite element models of PVC foam based sandwich structures, composite reinforced foam structures and fibre metal laminates (FMLs) have been developed using a commercial finite element analysis (FEA) package, Abaqus/Explicit. The constitutive models of crushable foam material for PVC foam, orthotropic elastic material and Hashin's failure criteria for glass and carbon fibre reinforced skins are detailed here. 3D rate-dependent failure criteria for a anisotropic composite are employed by using modified Hashin's 3D failure criteria to simulate composite rods and tubes. The aluminium alloys in the FMLs are modelled as an isotropic elasto-plastic material using Johnson-Cook plasticity and the related damage criterion. The FE models will be validated against the experimental data and be further used to undertake parametric studies. The simulation results will be presented in Chapter 6.

5.2 Constitutive model and failure criteria

Finite element models were developed to simulate the response of the composite structures subjected to quasi-static and dynamic loading. The following sections outline the modelling-approaches adopted for the various constituents of composite material used for sandwich structures, composite reinforced foams and FMLs.

5.2.1 Constitutive model of crushable foam material

Each foam was modelled as a crushable foam using hardening curves obtained following compression tests on square blocks. Deshpande and Fleck proposed a phenomenological yield surface for a closed-cell foam (Deshpande and Fleck 2001), given by:

$$\phi \equiv \frac{1}{\left[1+\left(\frac{\alpha}{3}\right)^2\right]}\left[q^2+\alpha^2\sigma_m^2\right]-\sigma_y^2 \le 0 \qquad \text{(Eq. 5.1)}$$

where σ_y is the uniaxial tensile or compressive yield strength of the foam, q is the Von Mises stress, σ_m is the mean stress. The parameter α defines the shape of the yield surface, which is given by:

$$\alpha = \frac{3k}{\sqrt{(3k_t+k)(3-k)}} \qquad \text{(Eq. 5.2)}$$

$$k = \frac{\sigma_c^o}{p_c^o} \qquad \text{(Eq. 5.2 a)}$$

$$k_t = \frac{p_t}{p_c^o} \qquad \text{(Eq. 5.2 b)}$$

where k and k_t are related to the ratios of the initial uniaxial yield stress σ_c^o and the hydrostatic tensile yield stress p_t to the hydrostatic compressive yield stress p_c^o, respectively.

To determine a valid yield surface, It is requested that strength ratios must be in the range of $0 < k < 3$ and $k_t > 0$. The yield surface for the crushable foam in the meridional stress plane is

presented in Figure 5.1.

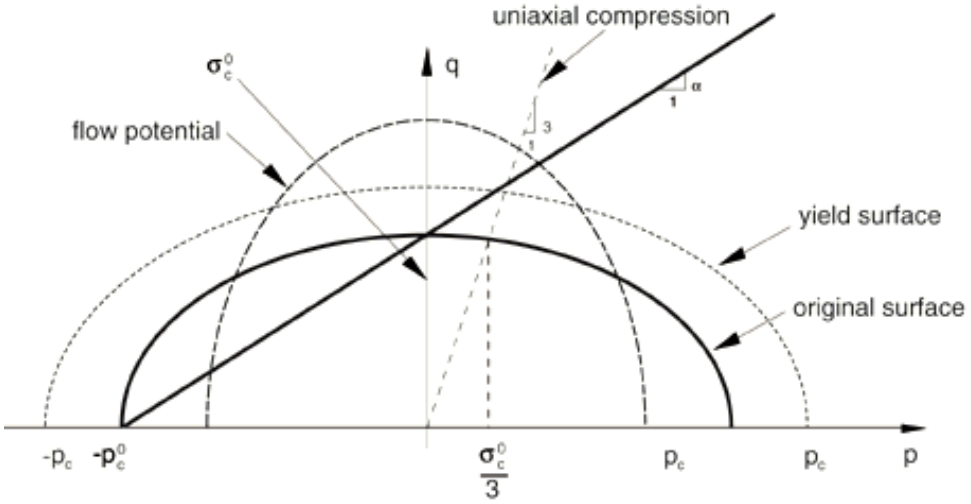

Fig. 5.1 The yield surface and flow potential in the *p–q* stress plane for the crushable foam model with isotropic hardening.

5.2.1.1 Strain hardening

The hardening law defines the value of the yield stress in uniaxial compression as a function of the absolute value of the axial plastic strain. A uniaxial compression test was conducted to define the evolution of the yield surface.

The yield stress p_c in hydrostatic compression provides the evolution of the size of the yield surface and can be experssed as

$$p_c(\varepsilon_{pl}^{vol}) = \frac{\sigma_c(\varepsilon_{pl}^{vol})\left[\sigma_c(\varepsilon_{pl}^{vol})\left(\frac{1}{\alpha^2}+\frac{1}{9}\right)+\frac{p_t}{3}\right]}{p_t+\frac{\sigma_c(\varepsilon_{pl}^{vol})}{3}} \qquad \text{(Eq. 5.3)}$$

where ε_{pl}^{vol} is the plastic volumetric strain for the volumetric hardening model, which is equal to ε_{pl}^{axial}, uniaxial compressive plastic strain. σ_c is the compressive stress under compression test. Therefore, p_c should be deterimed from a uniaxial compression test on a foam. The tabular entries was given in ascending magnitude of ε_{pl}^{axial} and the table started with a zero plastic strain corresponding to the virgin state of the materials.

The yield stress and plastic strain data are calculated as input date to model the characteristics of the PVC foams.

$$\varepsilon_{plas} = \varepsilon_{total} - \varepsilon_{el} \qquad \text{(Eq. 5.4)}$$

where ε_{total} is the total strain and ε_{el} is the elastic strain. The elastic strain was taken as the strain at the yield stress and the volumetric strain was calculated from the deformation of a specimen. The typical crushable strain hardening data for C130 foam are presented in Table 5-1.

Table 5-1 The strain hardening data used to define the hardening characteristics of the C130 crushable foam model.

Yield stress (MPa)	Plastic strain
1.43	0.0
1.62	0.4311
2.02	0.5694
2.44	0.6494
2.88	0.6961
3.35	0.7252
3.90	0.7492
4.94	0.7767
6.95	0.8035
11.86	0.8360

5.2.1.2 Rate dependence of PVC foam

The effect of strain-rate effect has been considered for the PVC foam. The crushable foam materials show an increase in the yield stress as strain rates increase. This increase in yield stress becomes significant when the strain rates are in the range of 10 - 1000 s^{-1} in high-energy dynamic events.

For a rate-dependent material, the equivalent plastic stain-rate follows the uniaxial flow rate definition as:

$$\dot{\varepsilon}_{pl} = h(\bar{\varepsilon}_{pl}, \theta) \qquad \text{(Eq. 5.5)}$$

where h is a strain hardening function, $\bar{\varepsilon}_{pl}$ is the equivalent plastic strain, and θ is the temperature. The rate-dependent hardening curves in terms of the static relation can be expressed as:

$$\bar{\sigma}(\bar{\varepsilon}_{pl}, \dot{\bar{\varepsilon}}_{pl}) = \sigma_y(\bar{\varepsilon}_{pl}) R(\dot{\bar{\varepsilon}}_{pl}) \qquad \text{(Eq. 5.6)}$$

where $\dot{\bar{\varepsilon}}_{pl}$ and R is the equivalent plastic strain-rate and stress ratio ($R = \bar{\sigma}_C / \sigma_C$) respectively.

5.2.1.3 Failure criteria

Damage initiation in the PVC foam was modelled by applying a ductile damage criterion in conjunction with shear damage criterion（ABAQUS theory manual, 2012). Damage development associated with ductile and shear failure is controlled by the fracture energy in terms of the energy required for failure development. A linear softening method was used to specify a development of the damage variable with deformation for elastic-plastic materials. The shear damage criterion assumes that the equivalent plastic strain at the onset of damage is a function of the shear stress ratio and strain rate. The shear stress ratio is defined as $\theta_s = (q + k_s p)/\tau_{\max}$, where k_s is the material parameter, $\tau_{\max}$ is the maximum shear stress. The fracture strains corresponding to the initiation of ductile damage and shear damage and the related strain rate need to be specified.

A tension failure criterion was specified in the lower half of the central region of the panel to model failure of the foam (Abaqus user manual 6.9, 2009). Here, the foam obeys a tensile elasto-plastic relationship that allowes tensile failure. The tensile failure criterion assumes that failure occurs when the pressure stress, p, becomes more tensile than the specified hydrostatic cutoff stress, σ_{cutoff}, i.e.

$$p = \frac{1}{3}|\sigma_{ii}| > \sigma_{cutoff} \qquad \text{(Eq. 5.7)}$$

The criterion assumes that the equivalent plastic strain at the onset of damage is a function of the stress triaxiality and strain rate. The stress triaxiality is defined as $\eta = -p/q$, where p is the pressure stress. In this model, the hydrostatic pressure stress is used as a measure of failure to model either dynamic spall or a pressure cut-off.

During experimental testing, it was noted that the PVC foam panels exhibited large recoverable strains during projectile impact. In order to simulate such large deformation prior to failure, a hyperelastic model was applied to the external region of the panel, i.e. that situated outside the central 40 mm region. The term “strain energy potential” defines the strain energy stored in the material per unit of reference volume (volume in the initial configuration) as a function of the strain at a given point in the hyperelastic material. The Mooney-Rivlin model was selected as a strain energy potential (Abaqus, Theory Manual, 2012), which is

$$U = C_{10}(\overline{I}_1 - 3) + C_{01}(\overline{I}_2 - 3) + \frac{1}{D_1}(J^{el} - 1)^2 \quad \text{(Eq. 5.8)}$$

where C_{10}, C_{01} and D_1 are temperature-dependant material parameters, $\overline{I}_1$ and $\overline{I}_2$ are the first and second deviatoric strain invariants and J^{el} is the elastic volume ratio.

5.2.2 2D Hashin's failure criteria for GFRP and CFRP skins

The composite skins used in sandwich structures were GFRP for plain foam based sandwich panels and CFRP for the graded foam based sandwiches. The constitutive models of the composite laminates, including elastic behaviour, damage initiation and damage evolution are described as below.

Prior to damage initiation, the GFRP and CFRP composite layers were modelled as an orthotropic elastic material. The in-plane longitudinal and transverse moduli of elasticity were assumed to be equal since the GFRP skins were based on a plain weave.

Damage initiation was modelled using Hashin's failure criteria (Hashin, 1973) which assumes four damage initiation mechanisms, namely fibre tension, fibre compression, matrix tension and matrix compression. Using the longitudinal, transverse and shear effective stress tensor components within the plane of the GFRP, the damage initiation criteria can be determined (Fan et al, 2011), and are given as:

Fibre tension:

$$F_f^t = \left(\frac{\hat{\sigma}_{11}}{X_T}\right) + \beta\left(\frac{\hat{\sigma}_{12}}{X_L}\right)^2, \hat{\sigma}_{11} \geq 0 \quad \text{(Eq. 5.9)}$$

Fibre compression:

$$F_f^c = \left(\frac{\hat{\sigma}_{11}}{X_C}\right)^2, \hat{\sigma}_{11} \leq 0 \quad \text{(Eq. 5.10)}$$

Matrix tension:

$$F_m^t = \left(\frac{\hat{\sigma}_{22}}{Y_T}\right)^2 + \beta\left(\frac{\hat{\sigma}_{12}}{S_L}\right)^2, \hat{\sigma}_{22} \geq 0 \quad \text{(Eq. 5.11)}$$

Matrix compression:

$$F_m^c = \left(\frac{\hat{\sigma}_{22}}{2Y_T}\right)^2 + \left[\left(\frac{Y_C}{2S_T}\right)^2 - 1\right]\frac{\hat{\sigma}_{22}}{Y_C} + \left(\frac{\hat{\sigma}_{12}}{S_L}\right)^2, \hat{\sigma}_{22} \le 0 \quad \text{(Eq. 5.12)}$$

where X_T, X_C are the tensile and compressive strengths in the longitudinal direction, Y_T, Y_C are the tensile and compressive strengths in the transverse direction, S_L, S_T are the longitudinal and transverse shear strengths, and β is a coefficient that specifies the contribution of the shear stress to the fibre tensile initiation criterion. Here β was set to zero, i.e. it is assumed that there is no shear stress contribution involved in the initiation of fibre tensile failure.

The material stiffness is given as below prior to damage initiation.

$$\sigma = C_d \varepsilon \quad \text{(Eq. 5.13)}$$

The damage elastic matrix which relates stress and strain relationship controls degradation of the material stiffness, can be expressed as:

$$C_d = \frac{1}{D_h}\begin{bmatrix} (1-d_f)/E_1 & (1-d_f)(1-d_m)v_{21}/E_1 & 0 \\ (1-d_f)(1-d_m)v_{12}/E_2 & (1-d_m)/E_2 & 0 \\ 0 & 0 & (1-d_s)GD_h \end{bmatrix} \quad \text{(Eq. 5.14)}$$

G is the shear modulus and D_h is an overall damage variable which can be expressed as:

$$D_h = 1-(1-d_f)(1-d_m)v_{12}v_{21} \quad \text{(Eq. 5.15)}$$

Here, d_f, d_m, and d_s reflect the current state of fibre, matrix and shear damage respectively.

Damage evolution is modelled by the negative slope of the equivalent stress-displacement relation after damage initiation is achieved. The fracture energies for fibre tension G_{ft}^F, fibre compression G_{fc}^F, matrix tension G_{mt}^F and matrix compression G_{mc}^F failure modes need to be specified to indicate the energy dissipated during damage development. The above criteria can be used with an element removal procedure to remove failed elements from the model.

5.2.3 Modified 3D Hashin's failure criteria

5.2.3.1 Composites rods and tubes using 3D damage model

Composite rod and tubes are anisotropic materials. The composite has different mechanical feature

in longitudinal, through-thickness and revolving directions, depending on fibre fraction in those directions. However, the failure criteria for laminated composites available in ABAQUS can only be applied for the orthogonal coordinate in the panel for shell elements only. These failure criteria fail to consider the third direction through-thickness and strain-rate effects involving 3D solid elements. In order to develop a constitutive model and failure criteria suitable for simulating the composite rod in a cylindrical coordinate system using 3D solid elements, 3D rate-dependent failure criteria for a anisotropic composite was employed here by modifying Hashin's 3D failure criteria (Hashin, 1980; Thuc et.al, 2013), to account for rate effects on the elastic and strength properties. The failure criteria, with the related constitutive model, are then implemented into ABAQUS/Explicit using a VUMAT subroutine provided by Abaqus (Abaqus, Theory Manual, 2012).

5.2.3.2 Modified 3D Hashin's failure criteria

Modified 3D failure criteria (Hashin, 1980; Vo et al. 2013; Sitnikova et al. 2014) may be used to simulate overall response of rolled composite rods in a cylindrical coordinate system (r, θ, z). The failure functions can be expressed as follows:

Fibre tension: $\left(\sigma_{zz} > 0\right)$

$$\text{If} \left(\frac{\sigma_{zz}}{X_{zt}}\right)^2 + \left(\frac{\sigma_{zr}}{S_{zr}}\right)^2 + \left(\frac{\sigma_{z\theta}}{S_{z\theta}}\right)^2 = 1, \text{ then } \; d_{ft} = 1 \qquad \text{(Eq. 5.16)}$$

Fibre compression: $\left(\sigma_{zz} < 0\right)$

$$\text{If} \frac{\left|\sigma_{zz}\right|}{X_{zt}} = 1, d_{fc} = 1, \text{ then } \; d_{fc} = 1 \qquad \text{(Eq. 5.17)}$$

Matrix tension: $\left(\sigma_{rr} + \sigma_{\theta\theta} > 0\right)$

$$\text{If } \frac{\left(\sigma_{rr} + \sigma_{\theta\theta}\right)^2}{X_{rt}^2} + \frac{\sigma_{r\theta}^2 - \sigma_{rr}\sigma_{\theta\theta}}{X_{r\theta}^2} + \frac{\sigma_z^2 + \sigma_{z\theta}^2}{X_{\theta r}^2} = 1 \text{ then } d_{mt} = 1 \qquad \text{(Eq. 5.18)}$$

Matrix compression: $\left(\sigma_{rr} + \sigma_{\theta\theta} < 0\right)$:

$$\text{If} \left[\left(\frac{X_{rc}}{2S_{r\theta}}\right)^2 - 1\right] \frac{\left(\sigma_{rr} + \sigma_{\theta\theta}\right)}{X_{rc}^2} + \frac{\left(\sigma_{rr} + \sigma_{\theta\theta}\right)^2}{4S_{r\theta}^2} + \frac{\sigma_{r\theta}^2 - \sigma_{rr}\sigma_{\theta\theta}}{X_{r\theta}^2} + \frac{\sigma_{zr}^2 + \sigma_{z\theta}^2}{X_{zr}^2} = 1, \text{then } d_{mc} = 1 \qquad \text{(Eq. 5.19)}$$

where X_{zt}, X_{zc}, X_{rt}, X_{rc}, S_{zr}, $S_{z\theta}$ and $S_{r\theta}$ are the various strength components (Hashin and Rotem, 1973) and d_{ft}, d_{fc}, d_{mt} and d_{mc} are the damage variables associated with the four failure modes. The response of the material after damage initiation (which describes the rate of degradation of the material stiffness once the initiation criterion is satisfied) is defined by the following equation:

$$\sigma = C(d) \cdot \varepsilon \qquad \text{(Eq. 5.20)}$$

i.e.

$$\begin{bmatrix} \sigma_{zz} \\ \sigma_{rr} \\ \sigma_{\theta\theta} \\ \sigma_{zr} \\ \sigma_{r\theta} \\ \sigma_{z\theta} \end{bmatrix} = \begin{bmatrix} C_{zz} & C_{zr} & C_{z\theta} & & & \\ C_{rz} & C_{rr} & C_{r\theta} & & & \\ C_{\theta z} & C_{\theta r} & C_{\theta\theta} & & & \\ & & & C_{44} & & \\ & & & & C_{55} & \\ & & & & & C_{66} \end{bmatrix} \begin{bmatrix} \varepsilon_{zz} \\ \varepsilon_{rr} \\ \varepsilon_{\theta\theta} \\ \varepsilon_{zr} \\ \varepsilon_{r\theta} \\ \varepsilon_{z\theta} \end{bmatrix} \qquad \text{(Eq. 5.21)}$$

where the non-zero terms of the above 6 x6 symmetric damaged matrix can be written as:

$$\begin{aligned}
C_{zz} &= (1-d_f)E_z(1-v_{r\theta}v_{\theta r})\Gamma \\
C_{rr} &= (1-d_f)(1-d_m)E_r(1-v_{z\theta}v_{\theta z})\Gamma \\
C_{\theta\theta} &= (1-d_f)(1-d_m)E_\theta(1-v_{zr}v_{rz})\Gamma \\
C_{zr} &= (1-d_f)(1-d_m)E_z(v_{rz}-v_{\theta z}v_{r\theta})\Gamma \\
C_{r\theta} &= (1-d_f)(1-d_m)E_r(v_{\theta r}-v_{zr}v_{\theta z})\Gamma \\
C_{\theta z} &= (1-d_f)(1-d_m)E_z(v_{\theta z}-v_{rz}v_{\theta r})\Gamma \\
C_{44} &= (1-d_f)(1-s_{mt}d_{mt})E_1(1-s_{mc}d_{mc})G_{zr} \\
C_{55} &= (1-d_f)(1-s_{mt}d_{mt})E_1(1-s_{mc}d_{mc})G_{r\theta} \\
C_{66} &= (1-d_f)(1-s_{mt}d_{mt})E_1(1-s_{mc}d_{mc})G_{z\theta}
\end{aligned} \qquad \text{(Eq. 5.22)}$$

where E_z, E_r and E_θ are the Young's modulus in the *z*, *r* and θ directions respectively, G_{ij} is the shear modulus in the *i–j* plane and v_{ij} (*i, j = z, r, θ*) is the Poisson's ratio for transverse strain in the j-direction. The terms s_{mt} and s_{mc} are introduced to control the reduction in shear stiffness resulting from tensile and compressive failure in the matrix respectively. The following values for these

parameters are given in Abaqus: s_{mt} = 0.9 and s_{mc} = 0.5 (Abaqus, Theory Manual, 2012).

The global fibre and matrix damage variables and the constant Γ are given as:

$$d_f = 1-(1-d_{ft})(1-d_{fc})$$

$$d_m = 1-(1-d_{mt})(1-d_{mc}) \qquad \text{(Eq. 5.23)}$$

$$\Gamma = 1/(1-v_{zr}v_{rz}-v_{r\theta}v_{\theta r}-v_{z\theta}v_{\theta z}-2v_{rz}v_{\theta r}v_{r\theta})$$

The Young's moduli, shear moduli, Poisson's ratios and strengths of the composites are given in Table 5-3.

5.2.3.3 Strain-rate effect on material strengths

The influence of strain-rate on the properties of a composite material are frequently modelled using strain-rate dependent functions. Yen (2012) developed the following logarithmic functions to account for strain-rate effects on the strength and modulus of a composite:

$$\{S_{RT}\} = \{S_0\}\left(1+C_1 In\frac{\dot{\bar{\varepsilon}}}{\dot{\bar{\varepsilon}}_0}\right) \qquad \text{(Eq. 5.24)}$$

$$\{E_{RT}\} = \{E_0\}\left(1+C_2 In\frac{\dot{\bar{\varepsilon}}}{\dot{\bar{\varepsilon}}_0}\right)$$

where:

$$\left\{\dot{\bar{\varepsilon}}\right\} = \left\{|\dot{\varepsilon}_z| \quad |\dot{\varepsilon}_r| \quad |\dot{\varepsilon}_z| \quad |\dot{\varepsilon}_r| \quad |\dot{\varepsilon}_{zr}| \quad |\dot{\varepsilon}_{z\theta}| \quad |\dot{\varepsilon}_{r\theta}|\right\}^T$$

$$\{S_{RT}\} = \{X_{zt} \quad X_{rt} \quad X_{zc} \quad X_{rc} \quad S_{zr} \quad S_{z\theta} \quad S_{r\theta}\}^T \qquad \text{(Eq. 5.25)}$$

$$\{E_{RT}\} = \{E_z \quad E_r \quad E_\theta \quad G_{zr} \quad G_{z\theta} \quad G_{r\theta}\}^T$$

The subscript 0 refers to the static value, $\dot{\bar{\varepsilon}}_0 = 1s^{-1}$ is the reference strain-rate, $\dot{\bar{\varepsilon}}$ is the effective strain-rate, C_1 and C_2 are the strain-rate constants, respectively.

5.2.3.4 Implementation of the material model in ABAQUS/Explicit

The user defined VUMAT subroutine was used to implement the material model and the aforementioned failure criteria in ABAQUS/Explicit. Here, during each computational time step, this subroutine is compiled enabling ABAQUS/ Explicit to obtain the necessary information regarding

the state of the material and its mechanical response at each integration point within each element. Hashin's 3D failure criteria given in Equations (5.16) to (5.19) are introduced. The stresses are computed within the VUMAT subroutine using the given strains and material stiffness coefficients. The elastic modulus and strength values are adjusted based on these stresses for strain-rate effects using Equation (5.24). The element status, which is determined by the Hashin failure criteria, is changed from 1 to 0 when an element fails. Associated with this change in element status, the stresses, the stiffness, so at that point are reduced to zero and the element no longer contributes to the model stiffness. The element is removed from the finite element mesh when all of the material status points within an individual element become zero.

5.2.3.5 The 3D damage model of GFRP composite layers in FMLs

Given that a woven glass fibre composite layer is produced by placing fibres in a [0°/90°] pattern, the material behaviour within the plane of the laminate is similar in those two directions according to the material test data. The material tests were based on the composite laminates, instead of individual tests on fibre and resin separately. Therefore, the developed Hashin's 3D failure criteria (Hashin, 1980; Thuc et.al, 2013) can be used to simulate overall response of composite layer accurately in a rectangular coordinate system (x, *y*, z). The failure functions can be expressed as the equation in Section 5.2.3.2. The coordinate direction (x, y, z) was instead of the (r, θ ,*z*) respectively.

5.2.4 Modeling of adhesive layers

The resin layer at the interface between the composite skin, the foam core and the aluminium was modelled using 0.25 mm thick cohesive elements available in Abaqus (Abaqus/Explicit User's Manual, 2012). The initiation and progression of damage were explicitly incorporated in the formulation of the element. The damage initiation criterion and damage evolution were based on the maximum nominal stress and the effective displacement was based on the linear softening law respectively. The damage initiation of the cohesive element is related to the maximum nominal stress criterion, which can be represented as:

$$\max\left\{\frac{t_n}{t_n^0}, \frac{t_s}{t_s^0}, \frac{t_t}{t_t^0}\right\} = 1 \qquad \text{(Eq. 5.26)}$$

where t_n, t_s and t_t are the stress components predicted by the elastic traction-separation behaviour for the current strain without damage and t_n^0, t_s^0 and t_t^0 are the corresponding the critical values of the nominal stress when the deformation is either purely normal to the interface or purely in the first or the second shear directions, respectively. Here, those critical values are set to 10% higher than the tensile and shear strengths of the foam as the bonding strengths cannot be much higher than such strengths to induce the foam failure.

Damage evolution was defined based on the effective displacement with the linear softening law. The damage variable D_{coh} is a function of effective displacement beyond damage initiation. In the case of damage evolution under a constant mode mix, temperature and field variables, the evolution of the damage variable D_{coh} can be reduced to the expression proposed by Camanho and Davila as follows (Camanho and Davila, 2002),

$$D_{coh} = \frac{\delta_m^f(\delta_m^{\max} - \delta_m^0)}{\delta_m^{\max}(\delta_m^f - \delta_m^0)} \qquad \text{(Eq. 5.27)}$$

where δ_m^f is the effective displacement at complete failure, δ_m^0 is relative to the effective displacement at damage initiation, $\delta_m^{\max}$ refers to the maximum value of the effective displacement attained during the loading history. The quantity $\delta_m^f - \delta_m^0$ is a tabular function of the mode mix, temperature and/or field variables.

5.2.5 Modelling aluminium layers

The aluminium alloy was modelled as an elasto-plastic material included a rate-dependent behaviour. Temperature effects on the aluminium alloy were not taken into account due to the ambient condition. The Johnson-Cook material model was used in the form below:

$$\sigma = [A + B(\bar{\varepsilon}_{pl})^n]\left[1 + CIn\left(\frac{\dot{\bar{\varepsilon}}_{pl}}{\dot{\varepsilon}_o}\right)\right] \quad \text{(Eq. 5.28)}$$

where $\bar{\varepsilon}_{pl}$ is the equivalent plastic strain; $\dot{\bar{\varepsilon}}_{pl}$ and $\dot{\varepsilon}_0$ are the equivalent plastic and reference strain rate and A, B, C and n are material parameters. Damage in the Johnson–Cook material model is predicted using the following cumulative damage law:

$$D = \sum\left(\frac{\Delta\bar{\varepsilon}_{pl}}{\bar{\varepsilon}_f^{pl}}\right) \quad \text{(Eq. 5.29)}$$

in which

$$\bar{\varepsilon}_f^{pl} = [D_1 + D_2 \exp(D_3\sigma^*)]\left[1 + D_4 In\left(\frac{\dot{\bar{\varepsilon}}_{pl}}{\dot{\varepsilon}_o}\right)\right] \quad \text{(Eq. 5.30)}$$

where σ^* is the mean stress normalised by the equivalent stress and $\Delta\bar{\varepsilon}_{pl}$ is the increment of equivalent plastic strain during an increment in loading. The parameters D_1, D_2, D_3, and D_4 are constants. Failure is assumed to occur when D = 1. Hence the current failure strain, $\bar{\varepsilon}_f^{pl}$, and thus the accumulation of damage, D, is a function of the mean stress and the strain rate. The constants in the Johnson–Cook model for the three alluminium alloys used in this study are from tests in Chapter 4 and reference in earlier study (Thuc et al, 2013). The Poisson′s ratio and density of the various aluminium alloys were taken as $\nu = 0.3$ and $\rho = 2700$ kg/m^3, respectively.

5.3 Individual models for various composite structures

Finite element models were developed to simulate the response of the foam panels, the foam core sandwich panels and the FMLs subjected to dynamic loading of projectile. The following sections outline the modeling details, including the geometry, the boundary conditions and loading, as well as mesh generation adapted for the various structures.

5.3.1 Detailed model of the foam based sandwiches

The plain foam based sandwiches consisted of PVC foam, GFRP skins and adhesive layers between the foam core and skins. The PVC foam was modelled as a crushable foam material with rate-dependent hardening described in Section 5.2.1. The GFRP skins were modelled as an orthotropic elastic material with 2D Hashin's failure criteria described in Section 5.2.2. The adhesive layers were modeled using damage evolution based on effective displacement described in Section 5.2.4.

5.3.1.1 Boundary, loading conditions and mesh generation

A fully clamped foam panels and foam core sandwich panels subjected to low velocity impact were simulated using ABAQUS/Explicit. Given that the panels were symmetric in nature, a quarter of each panel was modeled with the appropriate boundary conditions applied along the planes of symmetry. Figure 5.2 shows the geometric, boundary and loading conditions for the sandwich panel. Mesh generation is also shown in the same figure. Modelling of the foam panel is carried out by removing the skins and cohesive layers in the sandwich panel. The cylindrical projectile has a mass of 5.56 kg, which is assumed to be rigid in comparison to the sandwich panel. The boundary conditions for projectile are Ux= Uz = URx = URy = URz = 0; Uy ≠0. The peripheral edge is fixed (Ux = Uy = Uz = 0). The quarter edge of projectile and specimen was restrained as symmetric condition, XSYMM or ZSYMM.

The foam was meshed by eight-node reduced integration elements (C3D8R) and the skin by continuum shell elements (SC8R). The time duration for the modelling was set to 0.08 s to allow full perforation. Mesh sensitivity was studied by varying the mesh density within the plane and through the thickness. The mesh was improved until further refinements did not change the prediction

appreciably.

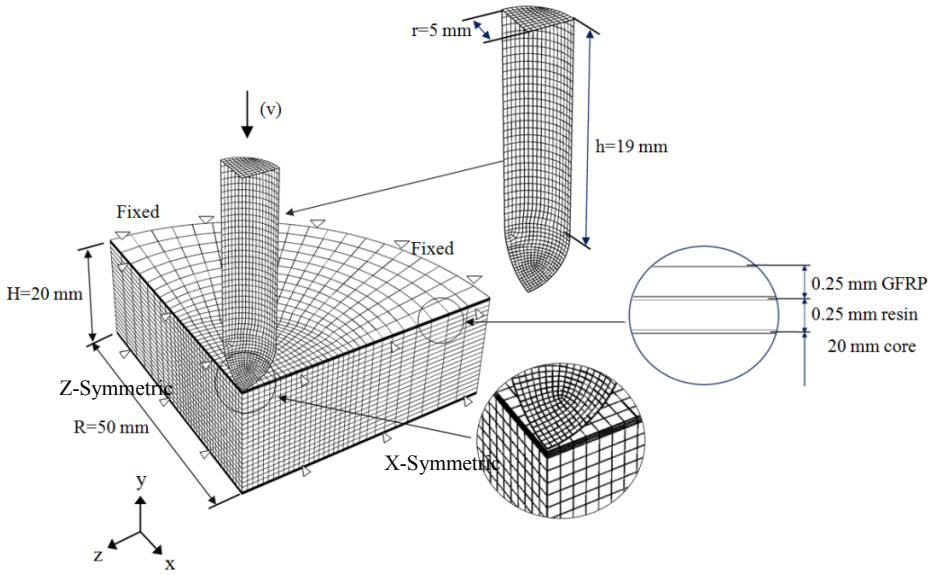

Fig. 5.2 Geometrical, mesh, boundary and loading conditions of the sandwich model.

Material properties of PVC foams were summarized in Chapter 4 and GFRP composite were presented in Table 5-2 and Table 5-3, respectively (Fan et al, 2012).

Table 5-2 Elasticity properties of the GFRP

E_1 (GPa)	E_2 (GPa)	E_3 (GPa)	v_{12}	v_{13}	v_{23}	G_{12} (GPa)	G_{13} (GPa)	G_{23} (GPa)
23	23	5	0.15	0.15	0.15	5	5	5

Table 5-3 Summary of the damage initation data for the GFRP

X^T (MPa)	X^C (MPa)	Y^T (MPa)	Y^C (MPa)	S^T (MPa)	S^T (MPa)	$G_{ft} = G_{mt}(J/m^2)$	$G_{fc} = G_{mc}(J/m^2)$
480	432	480	432	480	480	110000	120000

5.3.1.2 Interaction and contact condition

The general contact interaction was defined between the GFRP skin surfaces and the foam to cope with the case when the cohesive layer is damaged by projectile. In addition the surface-to-surface contact interaction that allows the finite slide was defined between the projectile surface and the node set of the target centre of constituent layers of the sandwich. The total resistance force on the projectile is sum of both the normal and shear contact forces on the above surface-to-surface interaction.

5.3.1.3 Modelling the water support on sandwiches

The water is modeled as a nearly incompressible, viscous Newtonian fluid. The linear U_s - U_p Hugoniot form of the Mie-Grüneisen equation of state is used in the material model. The parameters used to define the material, based on material properties, are listed in Table 5-4.

Table 5-4 Material parameters for water

Parameter	Value
Density (ρ)	998.2 kg/m^3
Bulk modulus (E)	2.246 GPa
Viscosity (η)	0.001003 N s/m^2
Gravity (g)	9.8 m/s^2

Eulerian technique and equation of state material models are used for simulating fluid dynamics in Abaqus/Explicit. The Eulerian element formulation allows the analysis of bodies undergoing severe deformation without the difficulties traditionally associated with mesh distortion. The Eulerian domain is finely meshed with a grid size of 1 mm Eulerian EC3D8R elements. The tank is modeled using traditional Lagrangian shell elements. The contact between the tank and the Eulerian material initially positioned inside of the tank is also modeled using the general contact algorithm. The general contact algorithm in Abaqus/Explicit tracks and enforces contact between the Eulerian material boundary and the Lagrangian elements, enabling effective simulation of the fluid-structure interaction (Abaqus, Theory Manual, 2012).

A gravity load is applied to the entire Eulerian domain of the water instances in the y-direction. Initial geostatic stresses are defined in the water to model the hydrostatic pressure in the tank. The gravity acceleration was added to the model using the Keywords Editor as it cannot be defined directly in Abaqus/CAE.

5.3.2 Modelling the graded foam based sandwiches

Similarly to the plain foam based sandwiches, the graded foam based sandwiches consisted of PVC foam, CFRP skins and adhesive layers between the layered cores and the skins. All of the constituent parts are modeled following the methods presented in Sections 5.2.1, 5.2.2 and 5.2.4.

5.3.2.1 Detailed model of the graded sandwiches

A fully-clamped sandwich panel based on three layered foam cores subjected to low velocity impact was simulated using ABAQUS/Explicit. The geometry as well as the boundary and loading conditions for the sandwich panel are shown in Figure 5.3. Given that the panels were symmetric in nature, a half of each panel was modeled with the appropriate boundary conditions applied along the planes of symmetry. A rigid cylindrical projectile has a mass of 5.56 kg. The initial projectile velocity was set to that based on the perforation energy obtained from experimental tests. The boundary conditions for projectile are the same as those to the single foam sandwich, i.e. Ux= Uz = URx = URy = URz = 0; Uy ≠0. For the peripheral edge of specimen is Fixed (Ux = Uy = Uz = 0). The central cross-section of projectile and specimen was restrained as symmetric condition. The skin and foam were meshed using continuum shell elements (SC8R) and eight nodes reduced integration elements (C3D8R), respectively. A mesh sensitivity analysis was conducted by varying the mesh density within the plane and through the thickness.

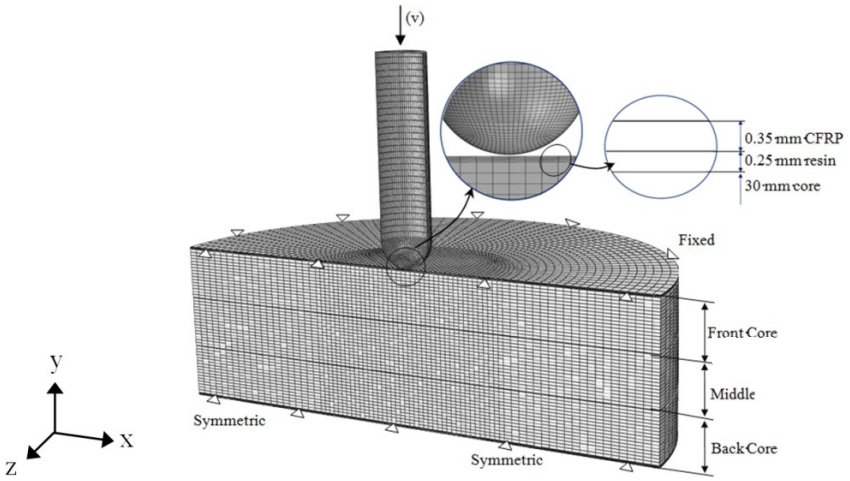

Fig. 5.3 The geometry, mesh, boundary and loading conditions of the sandwich model.

Material properties CFRP composite were presented in Table 5-5 (Ruzaimi, 2013).

Table 5-5 Summary of elasticity properties and the damage initation data for the CFRP

E_1(GPa)	E_2(GPa)	E_3(GPa)	v_{12}	v_{13}	v_{23}	G_{12}(GPa)	G_{13}(GPa)	G_{23} (GPa)
55	55	17	0.07	0.15	0.15	35	17	17
X^T(MPa)	X^C(MPa)	Y^T(MPa)	Y^C(MPa)	S^L (MPa)	S^T (MPa)	$G_{ft} = G_{mt}(J/m^2)$		$G_{fc} = G_{mc}(J/m^2)$
850	600	850	600	600	600	42700		44970

5.3.3 Detailed model of the rod reinforced foam sandwiches

The composite rod reinforced foams consist of PVC foam and the embedded composite rods. The PVC foam was modelled as a crushable foam material with rate-dependent hardening described in Section 5.2.1. The four densities of the cross-link foams, C40, C80, C130 and C200, has been included in the modeling. The composite rods was modeled using user-defined Hashin's 3D failure criteria with rate-dependent behavior for a anisotropic composite material described in Section 5.2.3.

5.3.3.1 Mesh generation, boundary and loading conditions

Figure 5.6 shows the finite element mesh of a PVC foam panel with embedded rods. Here, the PVC core and the rods were meshed using eight-noded solid elements with reduced integration. The foam core size is 50×50×20 mm and the diameters of the rods correspond to those studied experimentally (i.e. 2, 3 and 4 mm). The loading platens above and below the panel were meshed using rigid surface elements. Boundary conditions applied to the top platen were Ux= Uz = URx = URy = URz = 0; Uy ≠0. The bottom platen was fully fixed Fixed (Ux = Uy = Uz = URx = URy = URz = 0). The model has a number of interfaces that need to be considered. These include those between the foam core and platens, those between the composite rod and platen, as well as those between the composite rods and the foam. The platens are allowed to contact the individual nodes of the PVC core. Material properties of PVC foams and composite rods were presented in the Chapter 4, respectively.

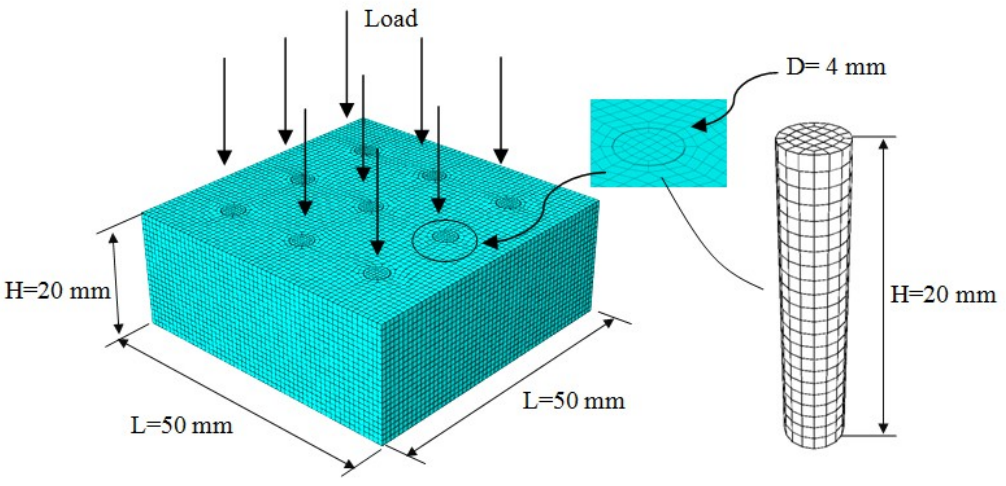

Fig. 5.4 The geometry, mesh, loading conditions of the rod reinforced foam model.

5.3.4 Detailed model of the tube reinforced foam sandwiches

Similar to the rod reinforced foam, the composite tube reinforced foam consists of PVC foam and composites tubes embedded in foam. The composite tubes were again modeled using the user-defined Hashin's 3D failure criteria with rate-dependent behavior.

5.3.4.1 Geometry, mesh generation and loading conditions

The tube reinforced foam panel is consisted of the foam, the composite and the cohesive layers. The PVC foam core and CFRP tubes were meshed using C3D8R elements, which are eight-noded, linear hexahedral elements with reduced integration and hourglass control. The mesh generation geometric, boundary and loading conditions are shown in Figure 5.5. The interfaces between the composite layers were created using eight-node 3D cohesive elements (COH3D8). The core size is 30×30×20 (in mm) and the inner diameters of the tube modelled are 8, 10 and 12.5 mm. The loading platens on both the top and bottom of the panel are meshed using rigid surface elements. The compressive load is applied to the top platen, with an only degree of freedom in the vertical direction. The bottom platen was fully fixed Fixed. A condition of general contact interaction was defined between the two neighboring layers of composites. Surface-based tie constraints were imposed between the composite layer and the cohesive layer to model adhesion between the adjacent layers. The contact interaction property for interaction between the foam and composite layer was also defined. Material properties composite tubes were tested in the Chapter 4.

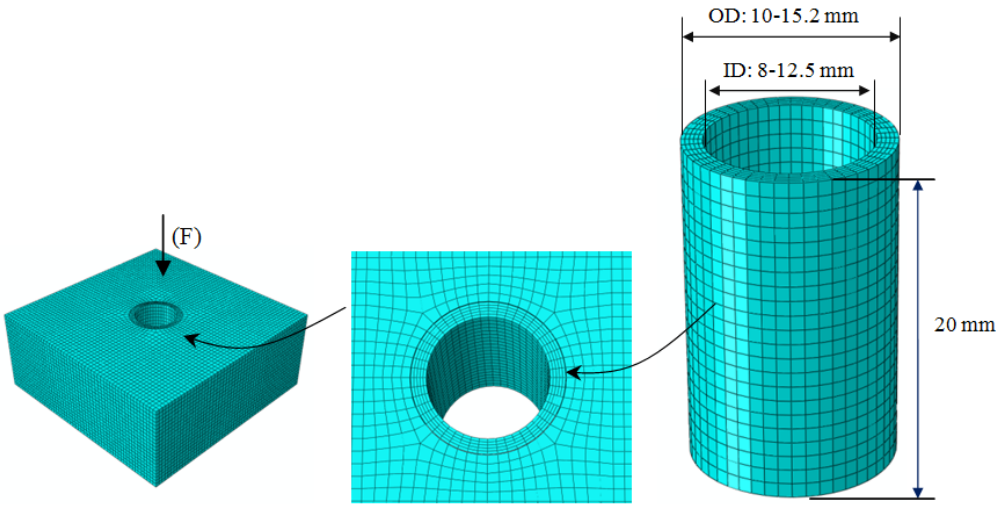

Fig. 5.5 The geometry, mesh and loading conditions of the tubes reinforced foam model.

5.3.5 Modelling the impact response of FMLs

FE modeling of FMLs with stacking sequences of 2/1, 3/2, 4/3 and 5/4 FMLs were developed to simulate the projectile perforation. Fibre metal laminates consisting of aluminium, the composite and the cohesive layers. The GFRP composite layers were modeled using the vectorized user-defined material subroutine (VUMAT) to define Hashin's 3D rate-dependant damage criteria described in Section 5.2.3. The resin layer between aluminium and GFRP layers were simulated using cohesive elements based on nominal stress and energy conjunction defined in terms of traction-separation described in Section 5.2.4. The aluminium alloy layers were modelled as an isotropic elasto-plastic material using Johnson-Cook plasticity and the related damage criteria described in Section 5.2.5.

5.3.5.1 Geometry, mesh, boundary and loading condition

The aluminium and composite layers were again meshed with C3D8R elements, which are eight-noded, linear hexahedral elements with reduced integration and hourglass control. The mesh generation, geometric, boundary and loading conditions are shown in Figure 5.6. The interfaces between the aluminium and composite layer were created using eight-node 3D cohesive elements (COH3D8). The plate size is 75×75 (in mm). The initial velocity applied to the projectile, with an only degree of freedom in the vertical direction. The plate edges are fully fixed. Given that the panels were symmetric in nature, a quart of each panel was modeled with the appropriate boundary conditions applied along the planes of symmetry. A condition of general contact interaction was defined between the two neighboring layers of composites. Surface-based tie constraints were imposed between the composite layer and the cohesive layer to model adhesion between the adjacent layers. The contact interaction property for interaction between the aluminium and composite layer was also defined. Material properties of GFRP used in FMLs are same with GFRP described in Tables 5-2 and 5-3.

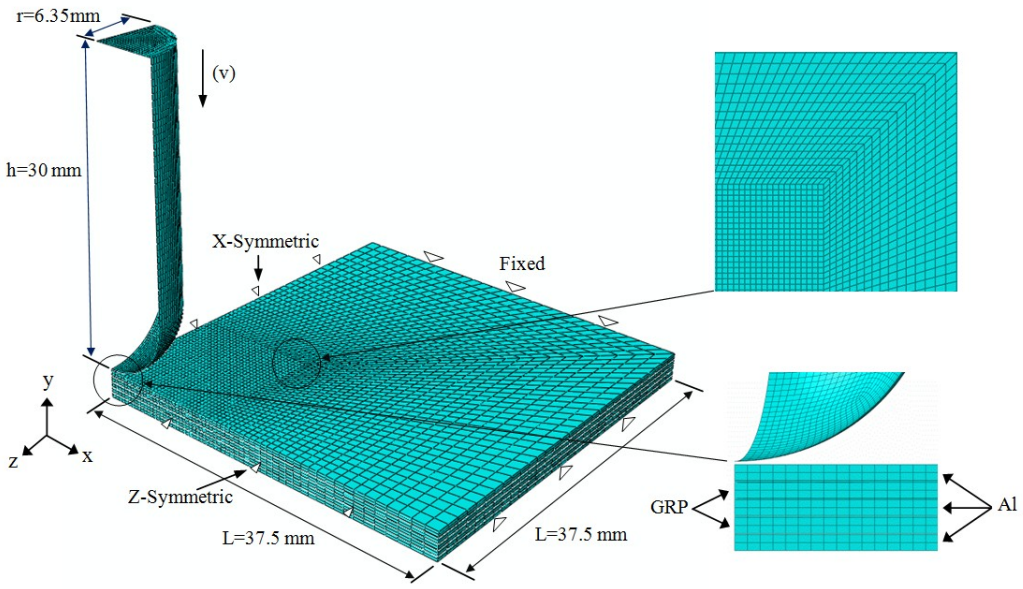

Fig. 5.6 The geometry, mesh, boundary and loading conditions of the model for 3/2 FMLs.

5.3.5.2 Modelling on Erosion of surfaces specified on solid elements

The interaction between elements of each layer is important to the modelling accuracy for a multiple layer FMLs subjected to perforation loading. In order to simulate the real interaction after surface element failure and removal from solid elements, the erosion of surfaces is specified to consider the interaction between newly exposed interior surfaces of the existing solid elements. The exterior and interior faces as eroding contact surface possibly participate in contact shown in Figure 5.7 below.

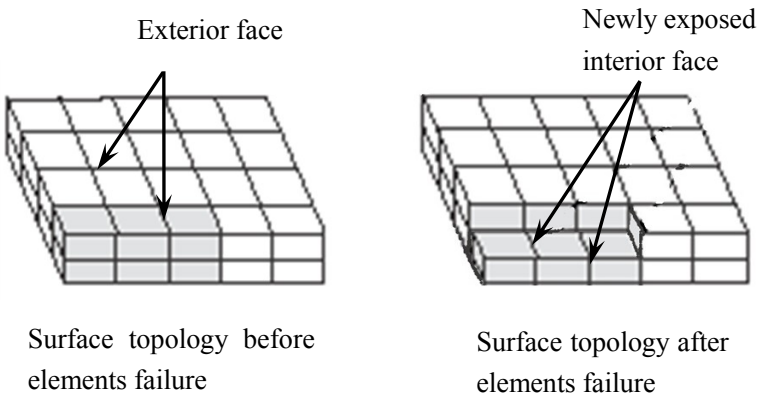

Fig. 5.7 Topology of an eroding contact surface.

For the solid element mesh, each layer consisting more than one element through the layer thickness may fail. Due to each face of the element being potentially be involved in contact, both exterior and interior faces were included in the contact domain that could possibly participate in contact in the FMLs modelling. The general contact algorithm was activated and deactivated as necessary when the elements failed. The general contact algorithm allows the use of element-based surfaces to model surface erosion for analyses. Interior surfaces of both the aluminium and GFRP layers are defined appropriately, the surface topology will evolve to match the exterior of elements that have not failed. The general contact algorithm modifies the list of contact faces and contact edges that are active in the contact domain based on the failure status of the underlying elements. General contact considers a face only if its underlying element has not failed and it is not coincident with a face from an adjacent element that has not failed; thus, exterior faces are initially active, and interior faces are initially inactive. Once an element fails, its faces are removed from the contact domain, and any interior faces that have been exposed are activated. A contact edge is removed when all the elements that contain the edge have failed. New contact edges are not created as elements erode. Based on this algorithm, the active contact domain evolves during the analysis as elements fail.

5.3.5.3 Interaction and contact condition

The general contact interaction was defined between the neighbouring layers of FMLs. In addition, possible interaction between each aluminium layer and the GFRP layers was included as general contact interaction layers to cope with the case of interaction between layers when the layer is damaged during projectile perforation. The interaction between aluminium and GFRP layers to cohesive layers was defined as tie constraints. The surface-to-surface contact interaction was defined to allow the finite slide between the projectile surface and the node set of the target centre on the constituent layers of the FMLs. The total resistance force on the projectile is sum of both the normal and shear contact forces on the above surface-to-surface interaction. Contact exclusions are generated for interactions that are defined with the contact pair algorithm or surface-based tie constraints to avoid redundant enforcement and possibly inconsistent of these interaction constraints. The details for interaction properties are shown in Table 5-6 as below (Fan, 2010).

Table 5-6 The interaction properties specific in this study

Interaction	Contact Algorithms	Mechanical constraint formulation	Friction formulation	Pressure over closure
Projectile-foam	Contact pair	kinematic	Penalty	Linear
Projectile- composite	Contact pair	kinematic	Penalty	Linear
Projectile-AL	Contact pair	kinematic	Penalty	Linear
Platen-foam	Contact pair	kinematic	Penalty	Linear
Platen-composite	Contact pair	kinematic	Penalty	Linear
Composite-foam	General contact	Penalty	Penalty	Linear
Al-GFRP	General contact	Penalty	Penalty	Linear
Al-GFRP	General contact	Penalty	Penalty	Linear
Al-GFRP	General contact	Penalty	Penalty	Linear

The interaction property for both the general contact interaction and contact pair interaction are defined as tangential behavior (friction formulation) and normal behavior (contact pressure – over closure relationship).

5.4 Mesh generation and sensitivity

Mesh sensitivity analysis was carried out by varying the mesh density within the plane and through the thickness. The mesh was improved until further refinements did not change the prediction appreciably. Figure 5.8 shows the variation of the prediction to test data and CPU time with element size for a special specimen. The accuracy of the model can be improved with the increasing of mesh density. However the computation time increased. Therefore, it's recommended to find the balance between element size and CPU computation consumption. The figure shows the difference between FE prediction and test data was less than 15 % if using the elements size less than 1.5 mm. To strike a balance with CPU time, elements size between 0.5 to 1 mm was used in order to get accurate prediction. The elements cell in central area of perforation target on sandwich and FMLs using a fine elements size of 1 mm, wheals the elements size is ratio based size with include size form central to edge of specimen. There were 2 elements through the thickness of composite skins and 20 elements though the 20 mm foam core with a maximum elements size of 1 mm. For the mesh of FMLs, there

was a maximum 0.25 mm thick element though the aluminium and composite layers.

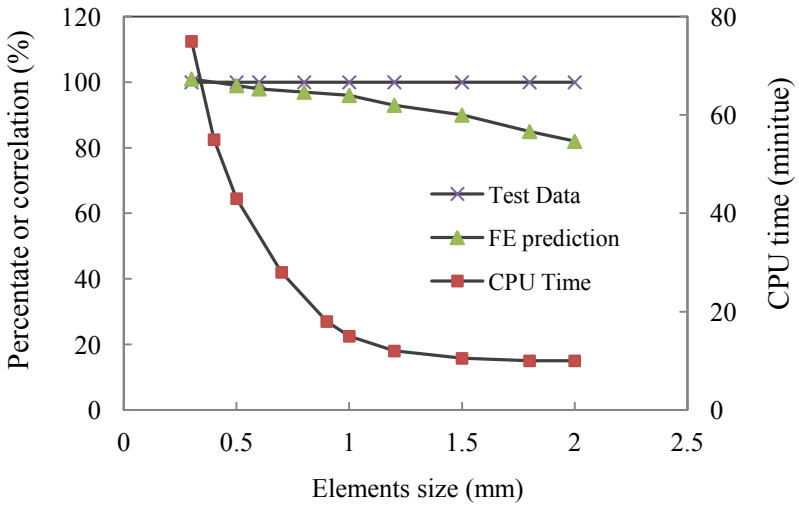

Fig. 5.8 Variation of the prediction to test data and CPU time with element size

5.5 Modelling data output

In the numerical analysis, Abaqus requests are to define variables or variable components as output during a specific analysis step. In the numerical model, stress, strain, reaction force and the displacement, failure of aluminium and Hashin's failure of composite were requested for the whole model. The reaction force and the displacement for the rigid projectile or top platen were recorded in terms of a time history output to be combined as a final load-displacement traces. The output data included history output and field output as below.

History output was generated either from the whole model or specific points in the model. The frequency of data output was dependent on the requested time interval. The individual components of variables can be specified as a history output request. In this modeling, reaction forces for the relevant direction of the model were requested and the displacement was requested as a history output at the specific reference point of the top platen or projectile.

Field output was generated from data that are spatially distributed over the whole model or over a portion of model center. This output presents images of the model at each requested interval. In this FE modeling, the reaction force, the displacement, the stress, the strain and the status as field output were obtained for the entire model. Failure status of the composite materials was requested.

5.6 Summary

This chapter summarises the numerical modelling theory and finite element methods used to simulate the response of the composite structures. Firstly, the constitutive models of the individual components used for composite structures have been presented. The models include crushable foam for the foam core, 2D Hashin's failure criteria for the GFRP and CFRP composite layers, a user defined 3D Hashin's failure criteria for composite rods, tubes and composite layer in FMLs, as well as Johnson-Cook model for the aluminium alloys in FMLs. Cohesive elements for the resin and adhesive layers in the composite structures are also described. Subsequently, the geometry, mesh generation, interaction, boundary and loading conditions for individual FE models have been detailed here, including plain foam based sandwiches, graded foam based sandwiches, rod reinforced foam, tube reinforced foam and fibre metal laminates. Following the detailed models, the mesh sensitivity study and modeling data output are also included in this chapter. The simulation results will be presented in following Chapter 6.

CHAPTER 6 SIMULATION RESULTS AND DISCUSSION

6.1 Introduction

This chapter presents the numerical predictions for the sandwiches, the rod and tube reinforced foam and the FMLs structures using the finite element models developed in Chapter 5. Firstly the load-displacements, failure modes and energy absorptions have been simulated on structures subjected to impact and compressive loading. The finite element models were validated using the experimental data generated in Chapter 4 on a wide range of reinforced systems base on various composite structures.

Subsequently, a series of parametric studies has been carried out using the validated models to predict various composite configurations subject to different load conditions. The influence of impact angle, loading in aqueous environment and pressure difference on sandwiches were investigated. The performance of the graded foam based sandwiches was compared with predictions of plain foam core based counterparts. FE models were used to predict the response of graded cores reinforced by composite rods with different lengths. The simulations of tube reinforced foams and FMLs structures are also presented in this chapter.

6.2 Simulation of the PVC foam based sandwiches

This section presents the results of a numerical study to investigate the perforation resistance of sandwich structures. The FE model for PVC foams using the modeling developed on crushable form material was described in Section 5.2.1 and the composite skins used in sandwich structures were modelled as 2D Hashin's failure criteria, detailed in Section 5.2.2. The mesh generation, boundary and loading conditions are described in Section 5.3.1. The validated FE model was also used to simulate and predict the effect of oblique loading and to study the impact response of sandwich panels on an aqueous support equivalent to water depth of 18 m and sandwich panels subjected to a pressure differential equivalent to flying at an altitude of 10,000 m.

6.2.1 Perforation resistance of the plain PVC foam

Figure 6.1(a) shows a comparison of typical load-displacement traces for both the experimental tests and the FE predictions following impact tests on three of the crosslinked PVC foams. The dash lines included in the figure are the predictions offered by the finite element analyses. An examination of Figure 6.1(a) indicates that the FE model accurately captures the fundamental features apparent in the experimental load-displacement traces. The key features include its slope reflecting the elastic modulus of the foam, a knee following a slope of the traces decreases as the projectile starts to crush the foam and penetrate the top surface of the panel with increasing of load and a final peak before load drops sharply corresponding to a maximum displacement when projectile perforates the foam panel. All the traces show similar increasing trends with increasing of foam density. The FE models exhibit more pronounced oscillatory effects in the initial response of the plates and also tends to over-estimate the initial stiffness for the higher density foams. In spite of these discrepancies, agreement between the numerical and experimental data is good.

Both the experimental and predicted perforation zones for the three foam panels were compared in Figure 6.1(b). Similar distinctive conical-shaped fracture zones have been captured by FE models following impact on those foams with different densities. An examination of those cross-sections between FE and tests indicates that the FE model predicted a cylindrically-shaped shear zone, similar in size to the diameter of the projectile on the lowers density C80 foam (as well as the C60

and C100 foams) whereas a mixed mode of failure, with a cylindrical shear region in the upper half of the panel and a frustrum-shaped zone in the lower portion of the test sample on the the intermediate (130 kg/m^3) and high (200 kg/m^3) density foams.

The distinctive failure modes and failure mechanisms were captured by FE models accurately based on the combined shear and tensile failure criterion to be determined by the tensile and shear fracture properties of the foams. The fracture properties of these foams, subjected to these two modes of loading, have been investigated in a previous study (Hassan and Cantwell 2012) presented in Chapter 4. The resulting values for work of fracture (W_f) of these foams in tension and shear were determined by measured experimental data using the shear rig and the single edge notch bend (SENB) specimen geometry, respectively.

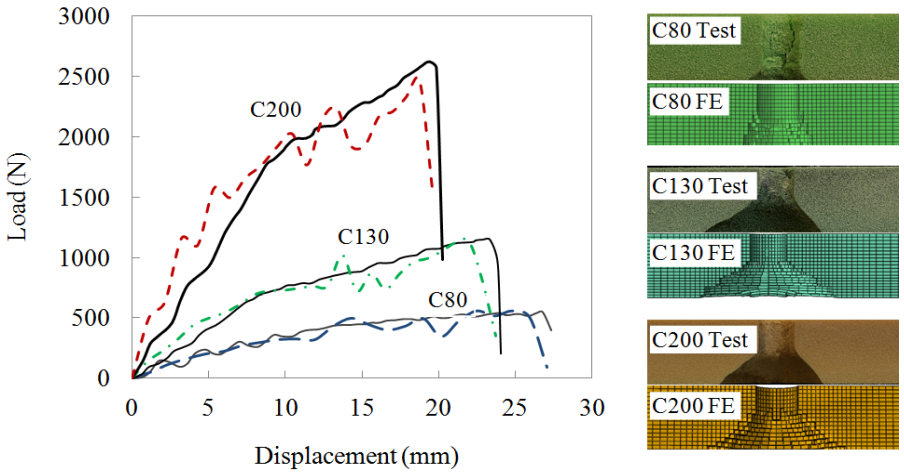

(a) Load-displacement traces (b) cross-sections

Fig. 6.1 Comparison of load-displacement traces and cross-sections of crossed-linked PVC foams. The solid lines correspond to the experimental data and the dashed lines to the predictions.

Figure 6.2(a) presents the load-displacement traces for the two plain PET core materials. In both cases, correlation between the predicted and measured response is good, with the former accurately predicting the initial slope, the maximum load and the maximum displacement. Increasing the density from 100 to 130 kg/m^3 has a significant influence on the impact response with the maximum force and general shape of the load-displacement trace. Figure 6.2(b) shows the comparison of resulting cross-sections for this foam. Again, agreement between the predicted and observed failure modes is excellent, indicating that the FE model accurately predicts the perforation process in these

samples. It is clear that the lowest density foam again exhibits a mixed type of failure with the upper part of the plate failing in the higher energy shear mode and the lower region of the target failing in a tensile mode. Failure in the higher density system PET135 is less distinct, although there is some evidence of a transition region at the mid-plane of the tested sample.

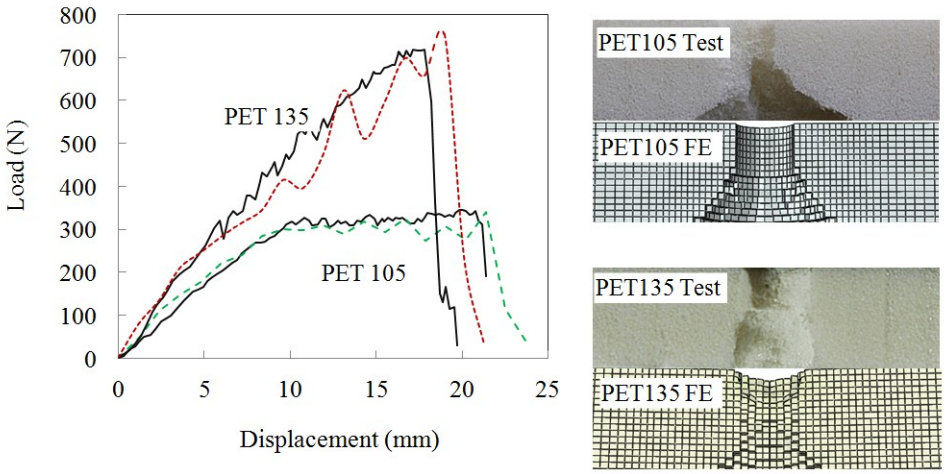

(a) Load-displacement traces (b) cross-sections

Fig. 6.2 Comparison of load-displacement traces and cross-sections of T92 PET PVC foams. The solid lines correspond to the experimental data and the dashed lines to the predictions.

Finally, Figure 6.3 shows the load-displacement traces and cross-sections following impact on the two linear PVC foams. Once again, FE model accurately captured the features of the traces and failure mode. It indicated that increasing the density of the foam serves to increase the initial stiffness of the plate, the maximum load and the maximum measured displacement. The failure mode on both panels exhibits a cylindrically-shaped shear zone with a mixed type of failure failing in the higher energy shear mode.

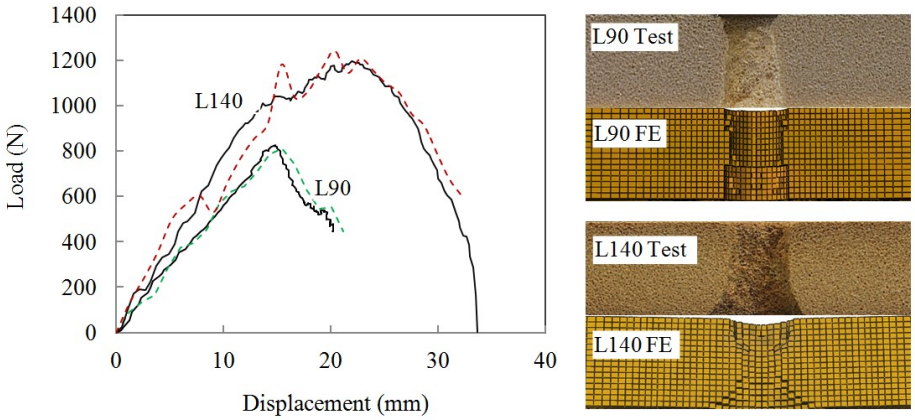

(a) Load-displacement traces (b) cross-sections

Fig. 6.3 Comparison of load-displacement traces and cross-sections of R63 linear PVC foam. The solid lines correspond to the experimental data and the dashed lines to the predictions.

Figure 6.4 presents a comparison of the FE predicted and measured perforation energies of the plain foam materials. The predictions for both the linear PVC and PET foams are extended to include notional materials with densities of 60 and 200 kg/m^3. The properties of these foams were obtained by extrapolating the data from those foams within the same family (Table 4-2 indicates that the majority of mechanical properties vary in a linear manner). An examination of the figure shows that the model predicts the experimental perforation energies with some success in similar trend. It is evident that the linear PVC foams offer a superior perforation resistance to their crosslinked counterparts. It is also clear that the PET foams offer the lowest perforation energies.

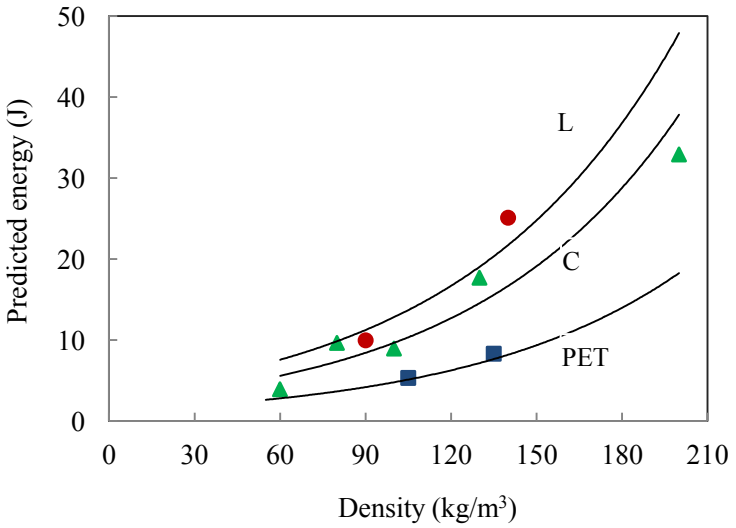

Fig. 6.4 Perforation energy versus density for the linear PVC (circles), crosslinked PVC (triangles) and PET PVC (squares) foam panels.

6.2.2 Perforation resistance of the PVC foam based sandwiches

Figure 6.5(a) presents the experimental and numerical load-displacement traces following low velocity impact on sandwich structures based on the three crossslinked foams presented in Figure 6.1. An examination of the traces indicates that the numerical simulations and the experimental data is reasonable good, with the model capturing most of the features in the experimental data. The FE model predicted a classic load-displacement trace correlated to the measured traces on the lowest density C80 foam, with pronounced peaks associated with fracture of both the upper and lower skins and a relatively smooth plateau resistance resulting from the projectile perforating the foam core. Similar feature to the trace on C200 plain foam, FE model exhibits more pronounced oscillatory effects on the highest density C200 foam sandwiches in the initial response of the plates and also tends to over-estimate the initial stiffness for the higher density foams. The trace for the C130 foam exhibits an initial peak resulting from fracture of the front skin followed by a steadily increasing force up to final perforation.

Figure 6.6(a) shows the measured and predicted load-displacement traces for the sandwiches based on another two low density foams C60 and C100 cross-lined foams. Once again, FE models predicted those trace accurately. Both the traces shows distinctive feature to the lower density C80 foam, with pronounced peak loads associated with perforation of both the upper and lower skins and a smooth plateau resulting from the projectile passing through the sandwiches.

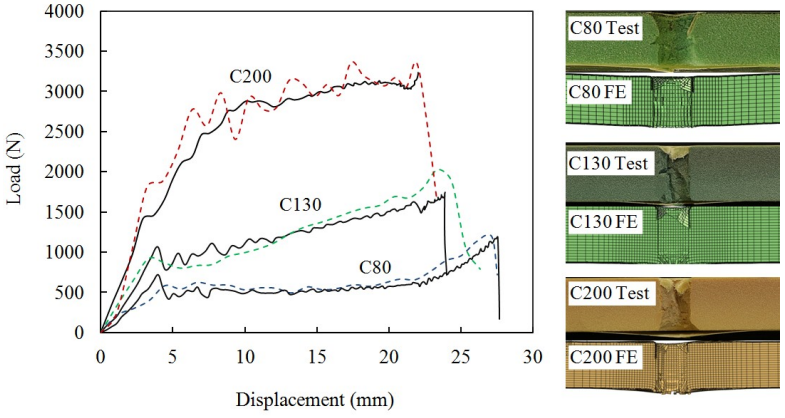

(a) Load-displacement traces (b) cross-sections

Fig. 6.5 Comparison of load-displacement traces and cross-sections of sandwiches made with C200, C130 and C80 foam cores. The solid lines correspond to the experimental data and the dashed lines to the predictions.

Figure 6.5(b) and Figure 6.6(b) presents cross-sections of cross-linked foam core based sandwiches following projectile perforation. All the sandwiches exhibit a similar frustrum-shaped fracture zone, with the projectile shearing a relatively clean hole through the target. In contrast to the failure of plain foam in Figure 6.2(a) suggests that the skins of sandwiches modified the failure of foam cores, with these sandwich structures is absorbing more energy that their plain foam counterparts. The failure mode of FE prediction shows a similar perforation section to the tested specimens.

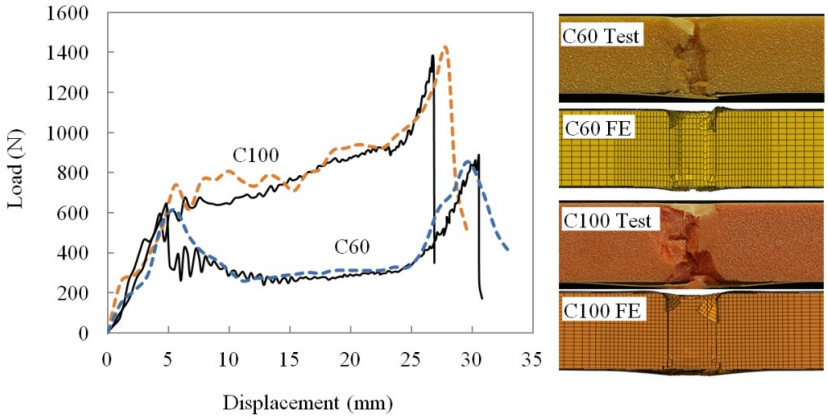

(a) Load-displacement traces (b) cross-sections

Fig. 6.6 Comparison of load-displacement traces and cross-sections of sandwiches made with C100 and C60 foam cores. The solid lines correspond to the experimental data and the dashed lines to the predictions.

Figure 6.7(a) presents the load-displacement traces for the sandwich structures based on the 80 and 140 kg/m^3 linear PVC foams. Both the traces exhibit a well-defined peaks resulting from fracture of the bottom skins as well as a region of constant force in which the projectile passes though the foam core. The linear foam system offers a relatively stable increasing load-displacement curve, although the failure of the top composite skin is difficult to discern. The agreement between FE prediction and test results are good. An examination of those cross-section shows the fracture zone are similar to that observed in the cross-linked foam shown in Figure 6.5(b). It also indicates that the response of the higher density linear PVC foam is once again largely dominated by the fracture behaviour of the core material. Figure 6.8(a) shows the load-displacement traces for the sandwich structures based on the 105 and 130 kg/m^3 PET foams. The FE captured the most of the features and exhibits two well-defined peaks resulting from fracture of the two skins as well as a region of plateau force in which the projectile passes though the foam core. It noted that the lower density PET foam perforated at a lower maximum displacement whereas the lower density linver foam perforated at

more displacement compare to their higher density counterparts. The cross-section of the PET-based system also displays a frustrum-shaped fracture zone similar to that observed in the plain foam, Figure 6.8(b). The model predicted a smaller conical zone to that observed experimentally, incicatting that it has not completely predicted the failure process.

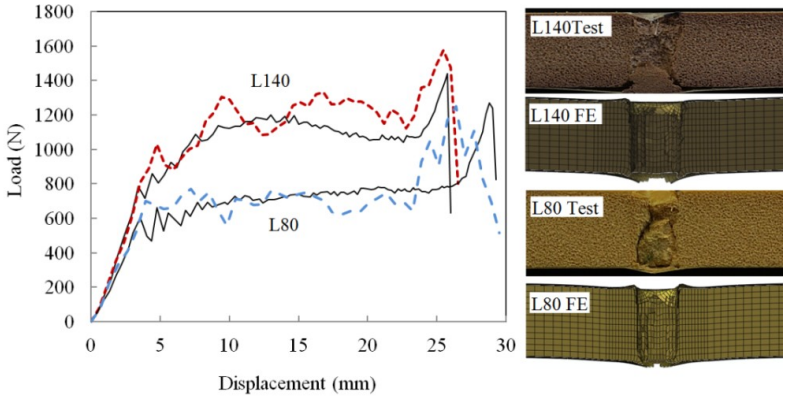

(a) Load-displacement traces (b) cross-sections

Fig. 6.7 Load-displacement traces and cross-sections of sandwiches made with L60 and L140 foam cores. The solid lines correspond to the test data and the dashed lines to the predictions.

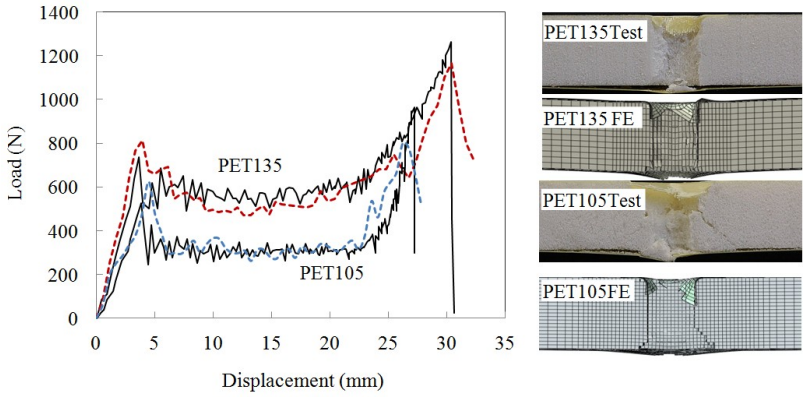

(a) Load-displacement traces (b) cross-sections

Fig. 6.8 Load-displacement traces and cross-sections of sandwiches made with PET135 and PET105 foam cores. The solid lines correspond to the test data and the dashed lines to the FE data.

Figure 6.9 summarised the energies required to perforate the sandwich structures. The points represent the experimental data and the solid line is the numerical prediction. Once again additional structures based on linear PVC and PET foams were modelled by extrapolating the mechanical properties given in Table 4-1. Agreement between the model and the experimental data is generally good. The FE also predicts a trend lines on the three type of foam from lower to higher density. It has been observed that the addition of the composite skins has an important effect on the energy-absorbing capacity of the core in certain cases. This is most pronounced in the highest

density crosslinked PVC foam which exhibited a significant enhancement in impact resistance following the addition of skins. It is interesting to note that a change in failure mode, passing from a mixed tensile-shear in the plain foam to a pure shear mode in the sandwich as shown in the failure modes. As expects, a significant improvement in perforation resistance is the failure mode shifts from tensile failure to pure shear associated with higher fracture energy. The FE predicted trend lines also evident that the perforation resistance of the highest density crosslinked PVC foam is superior to that of its linear counterpart, whereas the converse was true for lower density systems as illustrated in Figure 6.9. Here, the evidence suggests that the shear work of fracture values and perforation resistance exhibit similar trends. Interestingly, the shear fracture properties and perforation energies of the linear and crosslinked foams cross at approximately 115 kg/m^3. The numerical prediction evident that the PET-based sandwich structures offers the lowest perforation resistance in all range of density. Finally, it is clear that the FE predicted trend lines also shows a similar trend to that observed in the experimental data.

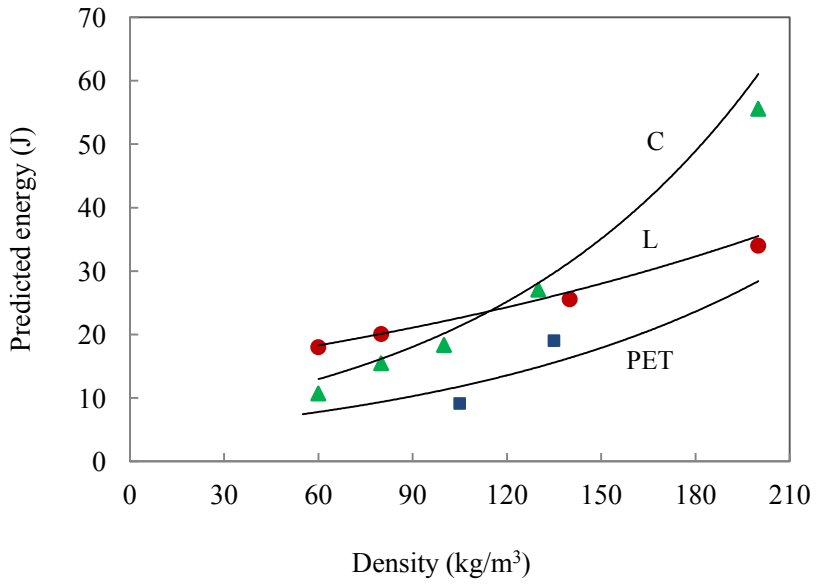

Fig. 6.9 Perforation energy versus density for the linear PVC (circles), crosslinked PVC (triangles) and PET-based (squares) sandwich structures.

6.2.3 The effect of angle of obliquity on the perforation resistance

Normal impacts, such as those reported above, rarely occur in real engineering situations. Instead, components are more frequently loaded at some oblique angle. Such tests are difficult to undertake

experimentally, given the need to guide the projectile, coupled with the presence of a horizontal force component that applies a load to the required guide rails. In this investigation, the process of oblique impact on three types of sandwich structure was modelled using the procedures outlined above.

Figure 6.10(a) shows the predicted load-displacement traces for the C130 and PET105 sandwich panels following oblique impact. With increasing the impact angle, the final peak force shifts to the right, associated with the increase in perforation energy. Figure 6.10(b) also includes the cross-sections resulting from the FE predictions for impact at an angle of 30 degrees. The two crosslinked foams again exhibit a clear cylindrical-shaped perforation zone, similar to that observed under normal impact. The PET foam also displayed a well-defined cylindrical zone, with no evidence of the small conical region predicted during normal impact, Figure 6.10(b).

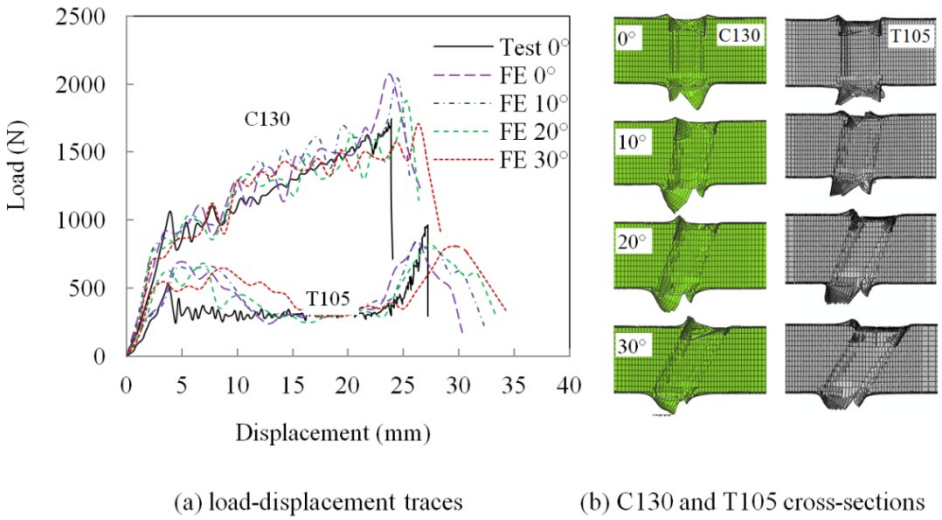

(a) load-displacement traces (b) C130 and T105 cross-sections

Fig. 6.10 Load-displacement traces and cross sections of sandwich panels made with C130 cross-linked PVC and PET105 PVC core subjected to oblique impact at incident angles of 10°, 20° and 30°.

Figure 6.11 shows the variation of perforation with angle of obliquity for sandwich panels based on two crosslinked PVC cores and a PET foam. Here, the impact angle refers to the angle between the axis of the projectile and the normal to the panel. From the figure, it is evident that the perforation energy increases with impact angle, for example, passing from approximately 29 Joules for a normal impact to approximately 35 Joules for thirty degree loading. All three traces exhibit similar trends with the rate of increase in perforation energy increasing with impact angle. Interestingly, the

increase in the perforation energy over this range of impact angles increases with foam toughness. Here, the PET105, C80 and C130 sandwich structures increase by approximately 18%, in passing from normal impact to a thirty degree impact.

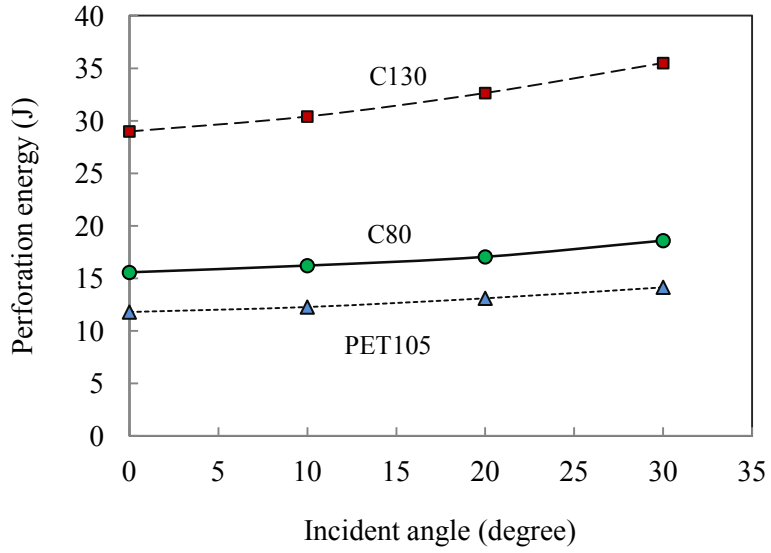

Fig. 6.11 The variation of perforation energy with impact angle for three sandwich structures.

Figure 6.12 shows a sketch of an elliptic oblique cylinder of perforated hole by projectile. A simple geometric analysis shows that the ratio of the surface area of an elliptic oblique cylinder to that of a right cylinder (the projectile creates an elliptical entrance hole on the top surface of the target) is given by:

$$\sqrt{\frac{1}{2}(r^2 + R^2)} \Big/ r \cdot \cos(I)$$

where r, h, R and I are as defined in Figure 6.12. Similarly, the ratio of an elliptic oblique cylinder to that of a right cylinder is given by:

$$\frac{1}{\cos(I)}$$

Given that energy is dissipated in shearing both the composite and foam around the perimeter of the projectile as well as crushing the foam ahead of the impactor, the perforation energy will reflect a combination of both equations. Applying these expressions to the impact conditions at 30 degrees examined here indicates that the surface area increases by 24.8% and the volume by 15.5%. The average increase predicted by the finite element model was 18%, suggesting that the increase in

perforation energy is associated with both the increased area of shear and the increased volume of material crushed under the impactor.

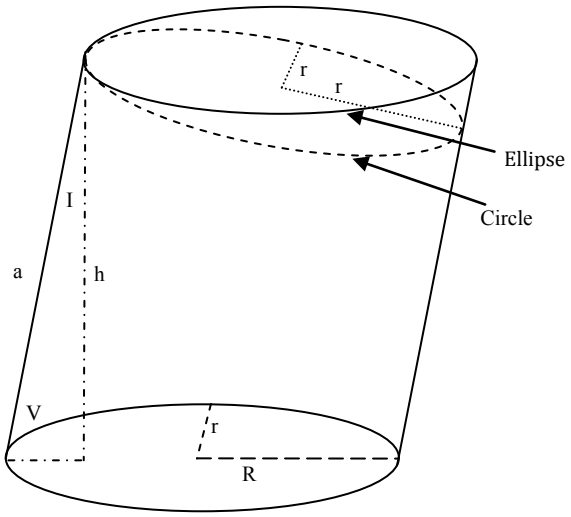

Fig. 6.12 Sketch of an elliptic oblique cylinder.

6.2.4 Impact response of sandwich panel supported on water

The FE model was developed to simulate the impact on sandwich structures in an aqueous environment as a result of sandwich structures are finding increasing use in the design of boats hulls in marine application. Here, the water was meshed as a three-dimensional body in the FE model, with typical properties (shear viscosity, density and wave speed) assigned and details were given in Section 5.3.1.3. In order to simulate the influence of an aqueous environment on the dynamic response of a sandwich structure, the developed FE models was validated to against the test data of sandwich panels supported on a combined circular base filled with water. A series of simulations were undertaken to simulate impact response the sandwich panels supported on a combined circular ring/water base. The model validation based on three types of the tested sandwich structures, these being based on the L140, the PET135 and the C130 foams.

Figure 6.13(a) shows a comparison of the predicted and measured load-displacement traces for the L140 sandwich structure. Included in each figure are the associated FE predictions and the corresponding experimental trace for the previous impact tests (i.e. in the absence of water). An examination of the traces for the linear PVC sandwich structures (L140) indicates that the FE model

accurately captured the basic features. It is clear that the FE simulated the response of panels supported on the water foundation. It exhibits similar traces up to the point at which the projectile approaches the rear surface. Here, the force rises rapidly in the ‘wet’ system before dropping rapidly as the rear surface fractures. It is note that the rear surface peak is much higher in the fully-supported wet panel than in its dry counterpart of the L140 based panels. The predicted and measured load-displacement traces for PET 135 based PVC sandwich structures shown in Figure 6.13(b). The FE prediction shows reasonable agreement with the test results. The traces of the PET135 based sandwiches exhibits similar response with L140 counterpart supported on the water foundation. In contrast with the L140 sandwich structure, it is clear that the lower rear surface peak and lower resistance displacement on the PET135 counterpart. It may be caused by the fracture properties of the different foam core, which strongly influence the perforation resistance of foam core based sandwich. In addition, the wet panel exhibits virtually no out of plane deflection, in contrast to the relatively flexible dry panel. The FE model predicts the experimental data with some success, although the final drop in force is not as abrupt.

The predicted and measured perforation energies for the three wet sandwich structures are compared with their corresponding dry samples in Figure 6.14. From the figure, it is clear that the model accurately predicts the perforation thresholds of all of the sandwich panels. In five out of the six cases, the model slightly overestimates the experimental value, although the differences are not significant. It is interesting to note that the ‘wet’ panels offer a lower resistance to perforation than their dry counterparts. This reduction is largely associated with the inability of the former to deflect out-of-plane. This is demonstrated clearly in Figure 6.13, where the projectile displacement at the instant that the lower skin fails is equal to the initial thickness of the panel (i.e. the flexural response of the target has been largely suppressed).

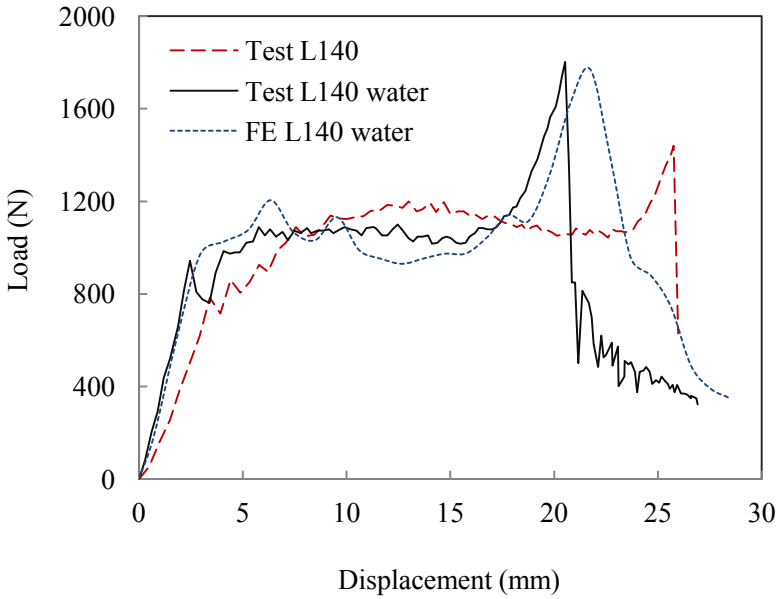

(a) L140 foam based sandwiches

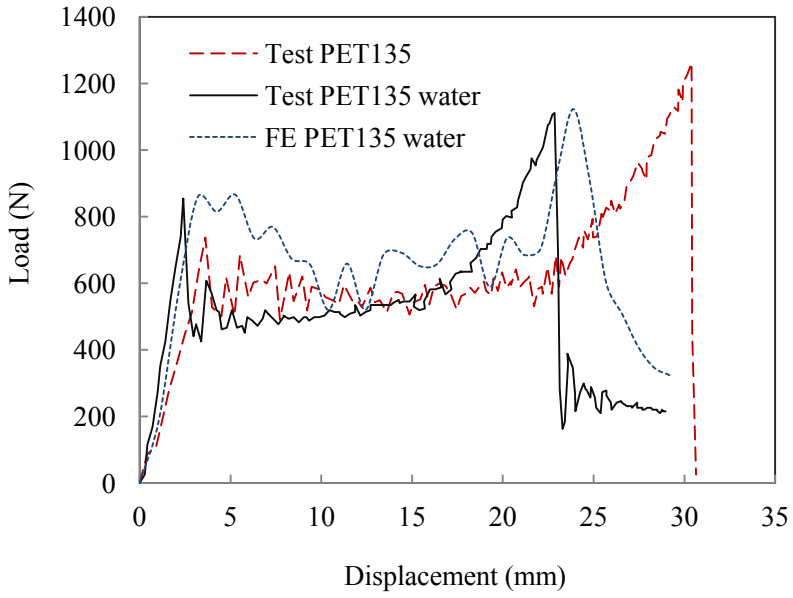

(b) PET135 foam based sandwiches

Fig. 6.13 Comparison of load-displacement traces of sandwiches made withL140 and PET135 foam cores between sandwiches supported on water and without support.

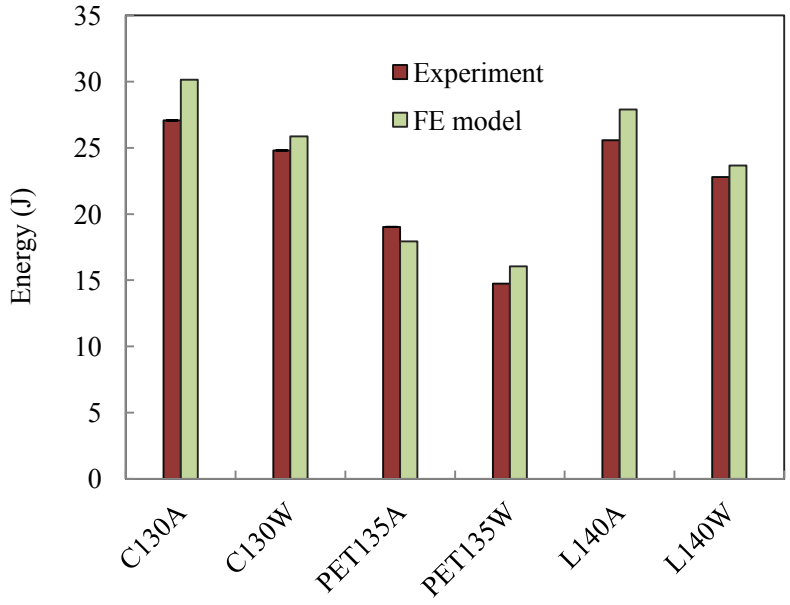

Fig. 6.14 Comparison of energy absorption of sandwiches made with C130, PET135 and L140 foam cores between sandwiches supported on water and without support.

In the final part of this investigation, the FE model was used to predict the response of a sandwich structure, in which the aqueous environment is located on the impact surface, with the distal surface being in contact with air. This can be considered to reflect the case of a boat hull that is in collision with an immersed object. The impact velocity was fixed at 5.6 m/s. Under such a low velocity impact conditions, cavitation is highly unlikely to be an issue. However, the model allows for interaction between the projectile and the water. Clearly, the object striking the hull will be in a pressurised aqueous environment, with the distal surface forming the inner wall of the boat (atmospheric conditions). Such tests would be difficult to replicate in practice and FE modelling therefore represents an ideal technique for investigating this problem. Figure 6.15 presents the load-displacement traces of sandwiches based on PET105 foam cores placed under water to depths of 6, 12 and 18 m (the trace for a panel impacted in air is also included and marked as 0 m). It can be clearly seen that there is an initial displacement associated with the panels immersed under water, due to the prevailing hydrostatic pressure loading. This initial loading also shifts the first peak load to the right. In addition, both the first peak and the second peak loads are reduced with increasing water depth. For example, the first peak load decreases from 650 to 570 N in passing from air to a water depth of 18 m. Similarly, the energy required to perforate the sandwich structures decreases

with increasing depth of immersion, with the perforation energy of the 18 m panel being approximately 10% below that measured in air.

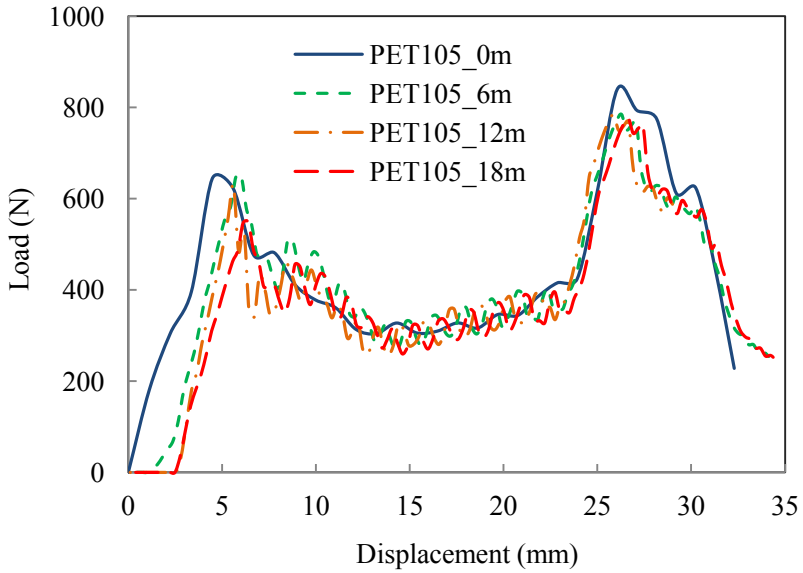

Fig. 6.15 Comparison of load-displacement traces of sandwiches made with PET105 foam cores between sandwiches under water depth of 0, 6, 12 and 18 m.

6.2.5 Impact response of sandwich panels subjected to a pressure difference

Relationship between the pressure and the altitude

In order to simulate the impact response of a sandwich structure subjected to a pressure difference between that of the cabin and that outside an aircraft at an altitude of 10000 meters, the relationship between atmospheric pressure and altitude needs to be employed. Here, the pressure is assumed to decrease in a nonlinear manner from the Earth's surface to the top of the mesosphere. The pressure is affected by weather, temperature and relative humidity. Assuming that the temperature and relative humidity at sea level are 15 ^{o}C and 0 % respectively, the pressure within the troposphere can be calculated using:

$$p = p_0\left(1-\frac{L_T h}{T_0}\right)^{\frac{gM}{RL_T}} \approx p_0 \exp\left(-\frac{gMh}{RT_0}\right) \qquad \text{(Eq. 6.1)}$$

where p_0 = 101325 Pa is the atmospheric pressure at sea level; L_T = 0.0065 K/m is temperature lapse

rate; T_0 = 288.15 K is sea level standard temperature; g = 9.81 m/s^2; M = 0.0290 kg/mol is molar mass of dry air; R = 8.3145 J/(mol.K) is the universal gas constant. The above equation predicts that the atmosphere pressure at 10000 m is equivalent to 25691 Pa.

Impact on sandwich panels subjected to an air-pressure differential

As a result of their superior specific properties, i.e. extremely high strength to weight ratio, energy absorption and good insulation characteristics, sandwich structures are finding increasing use in the design of aircraft structures. In order to investigate the influence of impact in a differential pressure environment on the dynamic response of a sandwich structure, low velocity impact simulations were undertaken on panels subjected to an air-pressure difference between their front and rear faces. Here, the front and the rear faces are under pressures equivalent to atmospheric pressure at sea level and 10000 m, respectively. For comparison, models were also constructed in which both the front and rear surfaces were subjected to sea level atmospheric conditions. Four types of sandwich structure were modelled, these being based on the crosslinked C80 and C130 foams and PET105 and PET135 foams.

Figure 6.16 shows the predicted load-displacement traces for the two crosslinked foam sandwich structures. Included in the figure are the associated FE predictions for the sandwich structures impacted at the sea level (i.e. without an air-pressure differential) and in an air-pressure differential at an attitude of 10000 m, respectively. An examination of the traces for the crosslinked PVC sandwich structures shown in Figure 6.16 indicates that the response of the panel subjected to differential pressure loading is very similar to that modelled under more normal conditions. Similar conclusions can be drawn following an examination of the load-displacement traces for the PET samples in Figure 6.17, where the load-displacement traces for the altitude and sea-level conditions are very similar.

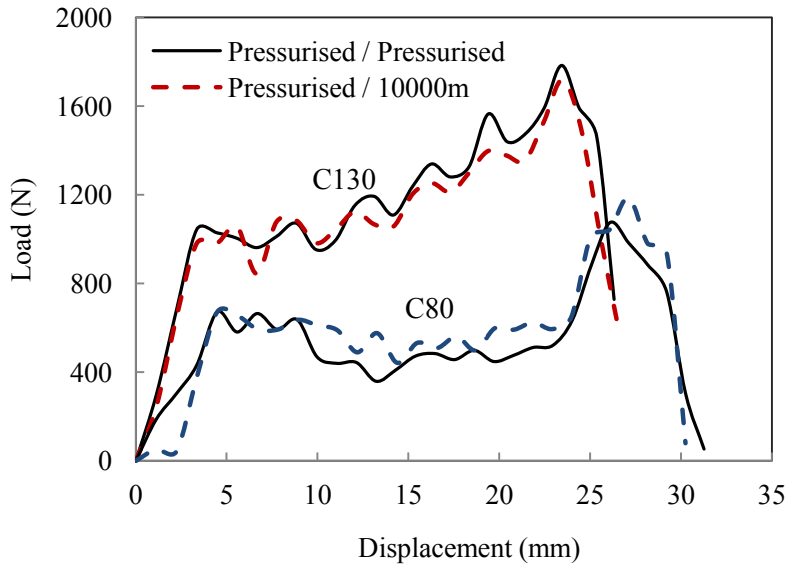

Fig. 6.16 Comparison of the predicted load-displacement traces of cross-linked foam sandwich structures. The solid lines (validated) correspond to sea level conditions and the dashed lines (predicted) correspond to conditions at 10000 m.

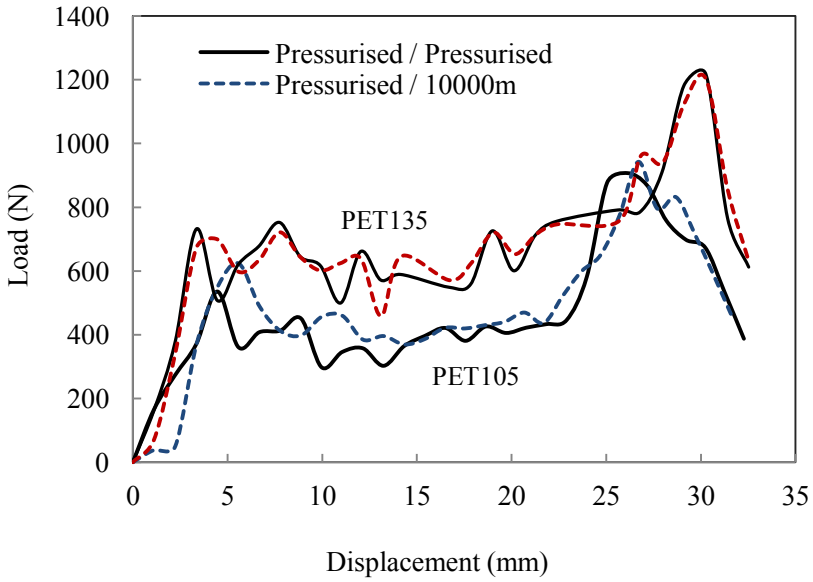

Fig. 6.17 Comparison of the predicted load-displacement traces of PET foam sandwich structures. The solid lines (validated) correspond to sea level conditions and the dashed lines (predicted) correspond to conditions at 10000 m.

A comparison of the predicted perforation energies for the sandwich structures subjected to an air-pressure differential with their corresponding samples without applying such environmental conditions is shown in Figure 6.18. It is interesting to note that the panels subjected to the two different loading conditions offer similar resistances, suggesting that the perforation resistance of a sandwich structure at an altitude of 10,000 metres is similar to that at sea level.

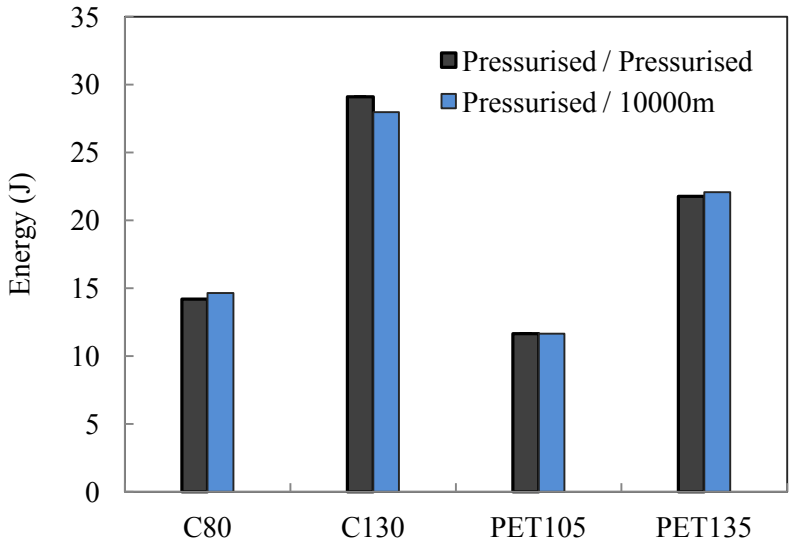

Fig. 6.18. Comparison of the predicted perforation resistances of a range of sandwich structures with no different pressure conditions between the front (impacted) face and the rear (non-impacted) face.

6.3 Simulation of the graded foam based sandwiches

The impact response of the graded sandwich structures is modelled using finite element analysis, detailed in Section 5.3.2 and the predicted load-displacement responses and failure modes are compared with the experimental ones in this section. FE models of the sandwich structures are based on three layer cores fabricated by bonding linear PVC, crosslinked PVC and PEI foams together using the validated models. The predictions between sandwiches with graded foam and their monolithic counterparts with equivalent foam are also compared.

6.3.1 Impact response of the graded foam based sandwiches

Low velocity impact simulations were undertaken on the twelve core configurations. Figure 6.19(a) shows a comparison between the experimental (solid lines) and FE predicted (dashed lines) load-displacement trace for a sandwich panel based on the C100/P80/P60 foam combination. From the comparison of the curves it is clear that the model captures all of the major features of the experimental trace, including the pronounced second peak associated with the crushing of the core against the distal skin. Figure 6.19(b) shows cross-sections of the fully perforated sandwich structures, where the presence of a distinct cylindrically-shaped shear zone is evident in both the test specimen and the model.

Figure 6.19(c) shows the measured and predicted load-displacement traces for the equivalent inverted structure, i.e. the P60/P80/C100 core configuration. The cross-section of the perforated sandwich structures as shown in Figure 6.19(d). An examination of the figure suggests that there are many similarities with its counterpart in Figure 6.19(a). Once again, agreement between the predicted and measured load-displacement curves is generally good, although the model fails to identify the brittle failure mode in the top skin.

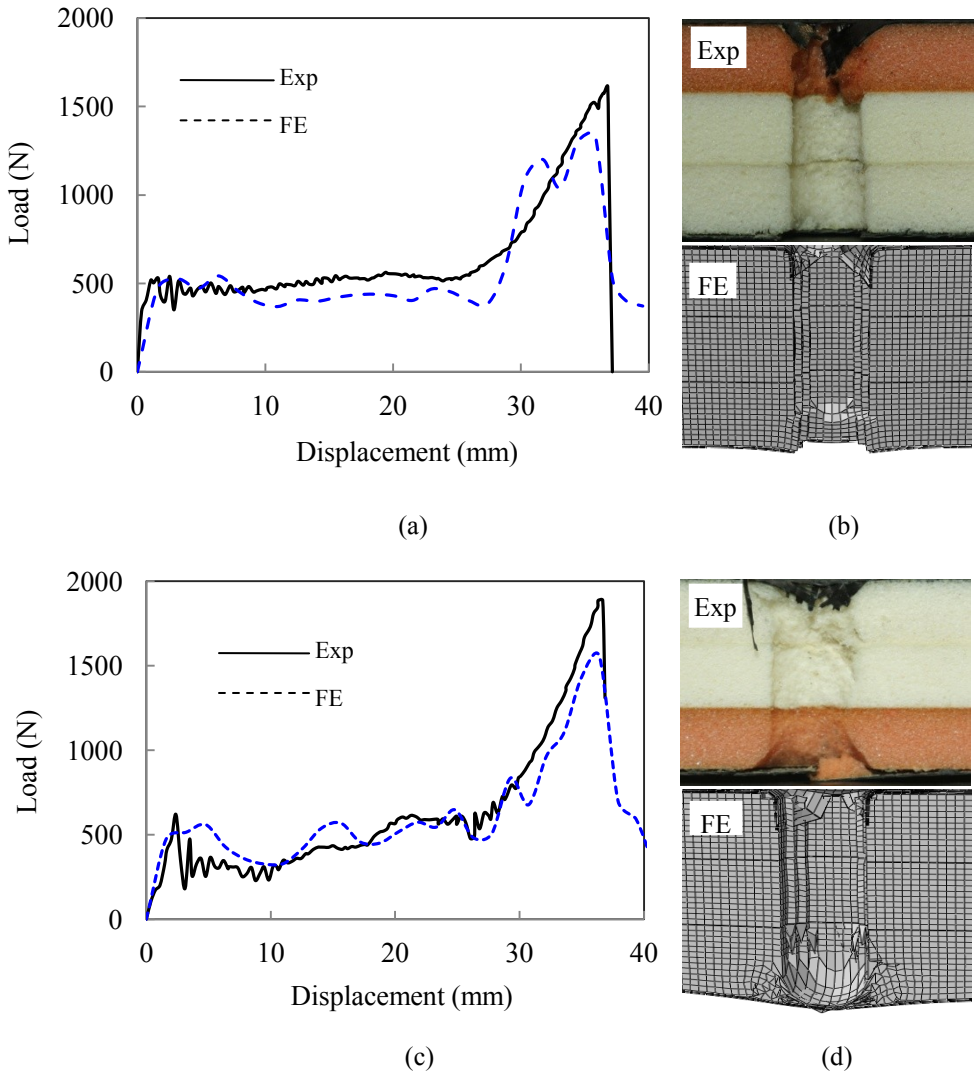

Fig. 6.19 Load-displacement traces and resulting cross-sections for (a, b) the C100/P80/P60 sandwich structure and (c, d) for the P60/P80/C100 sandwich structure.

Figures 6.20(a) and 6.20(c) show the experimental and numerical load-displacement traces for the L80/C60/C200 sandwich structure and the equivalent inverted structure. The experimental trace exhibits a number of distinct regions as the projectile passes through the various components of the sandwich panel. Figure 6.20(b) and 6.20(d), highlight the presence of a crack in the uppermost C200 foam that appears to have influenced the subsequent failure locus in the remainder of the structure. This mixed form of failure has been partly captured by the FE model.

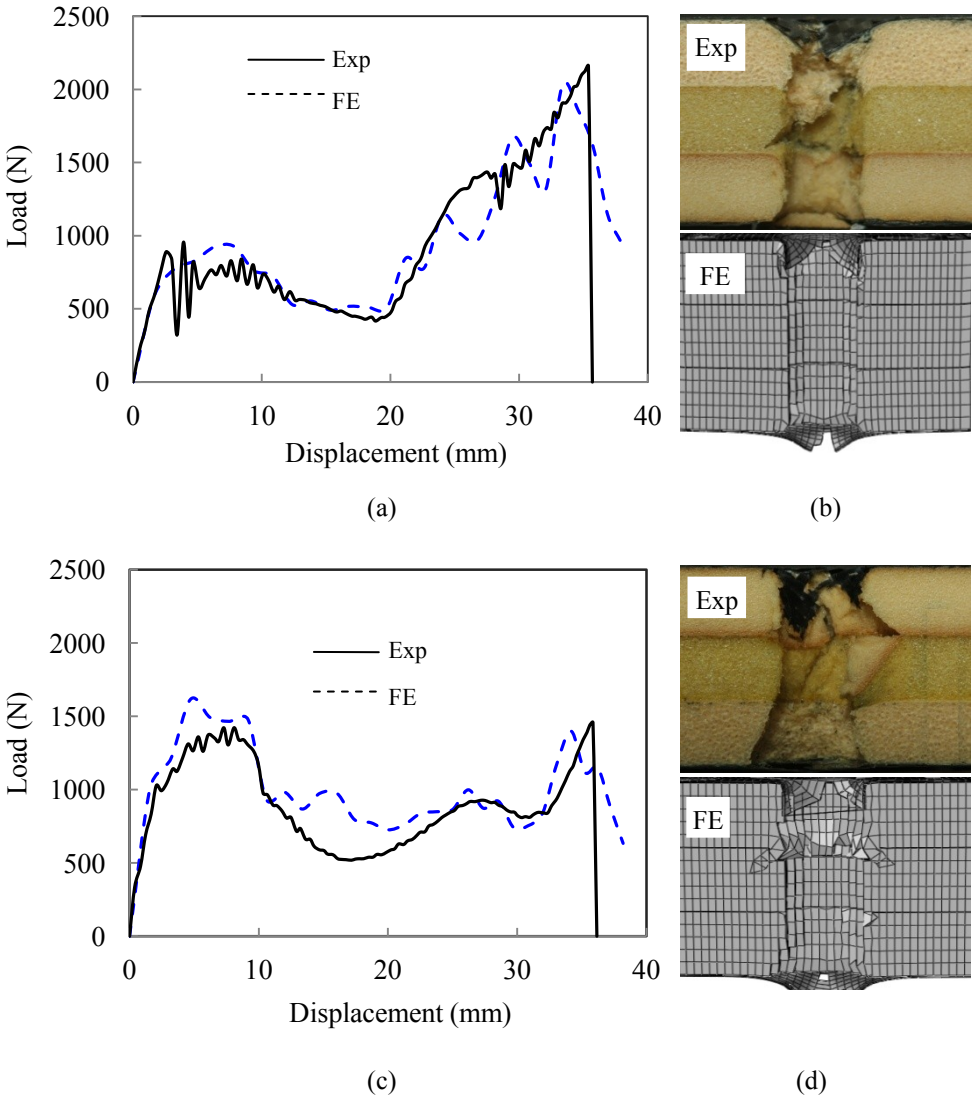

Fig. 6.20 Load-displacement traces and resulting cross-sections for (a, b) the L80/C60/C200 sandwich structure and (c, d) for the C200/C60/L80 sandwich structure.

Figure 6.21(a) shows the force-displacement traces for the L60/P60/L140 sandwich structure. Clearly, there are similarities between this response and that shown in Figure 6.19 (a), with the perforation force increasing in three steps between the peaks associated with fracturing the upper and lower skins. The plateau force resulting from fracturing the tough L140 foam is significantly higher than that required to perforate its lower density L60 counterpart. Finally, the load-displacement response of its inverted counterpart is shown in Figure 6.21(c). Once again, agreement between the experimental data and the model is very good, suggesting that the FE analysis is capable of capturing the fundamental response of these multi-layered structures.

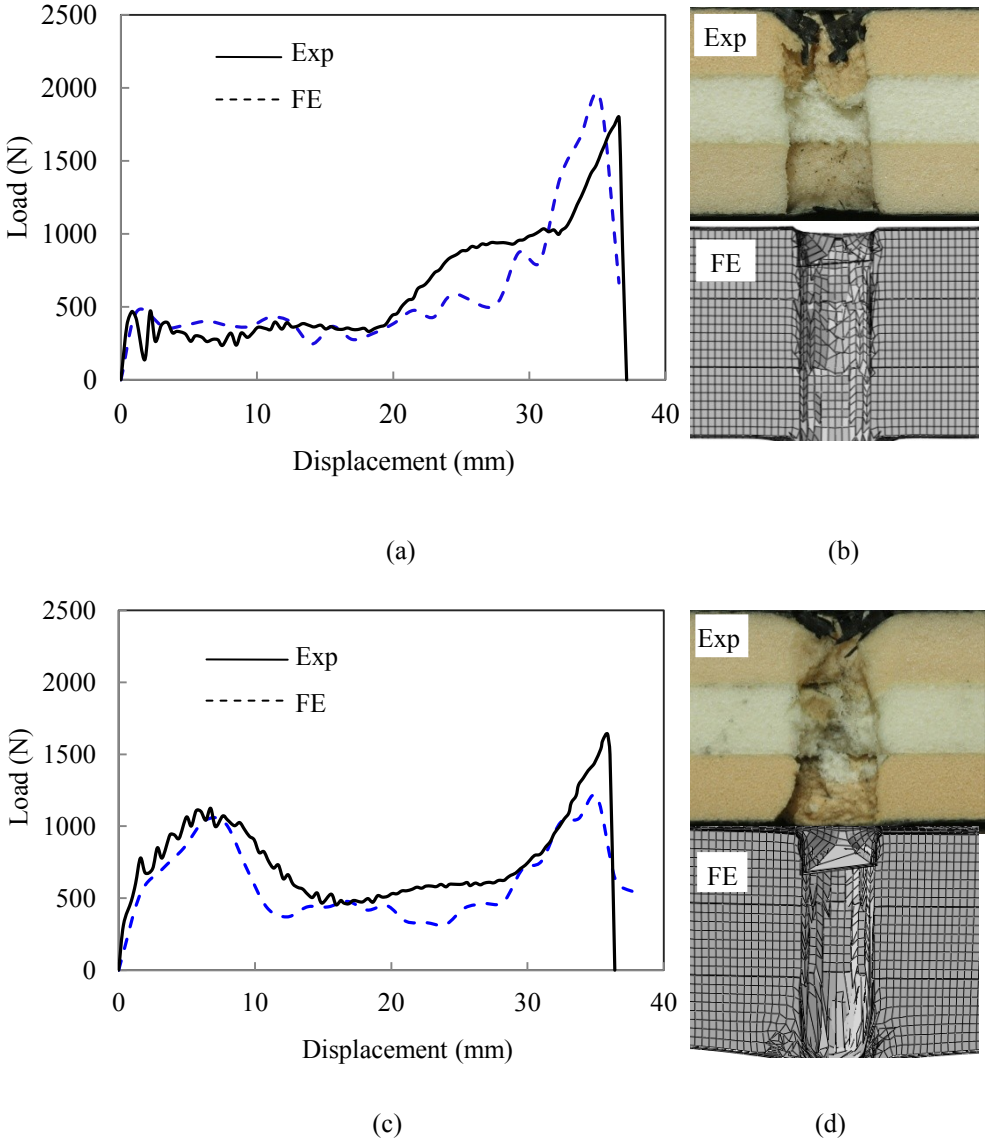

Fig. 6.21 Load-displacement traces and resulting cross-sections for (a, b) the L60/P60/L140 sandwich structure and (c, d) for the L140/P60/L60 sandwich structure.

The energy required to perforate the sandwich structures was calculated by determining the area under the load-displacement traces. Figure 6.22 compares the perforation resistances of the twelve configurations investigated here. From the figure, it is clear that the FE model generally predicts the energy required to perforate the laminates with a high degree of accuracy, with the greatest error being approximately fourteen percent.

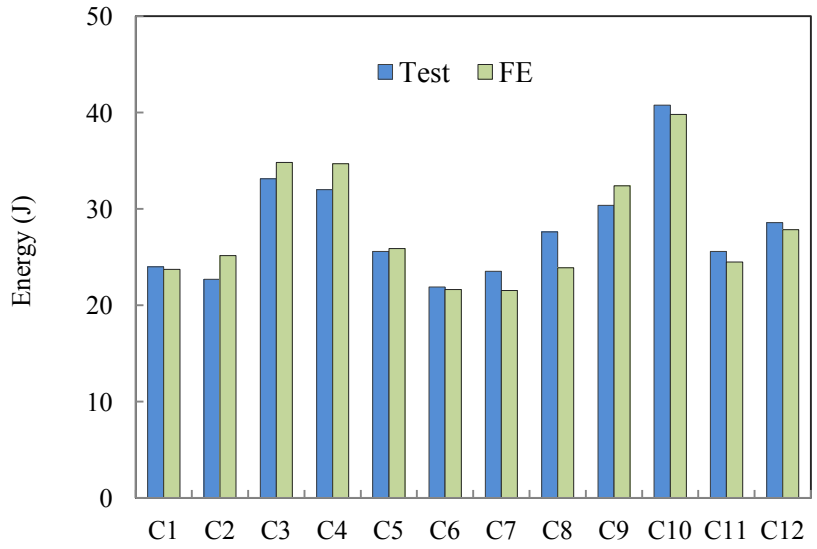

Fig. 6.22 Comparison of the predicated and experimental perforation energies.

In the next stage of this investigation, the perforation resistances of the various graded foam cores were compared with those of similar sandwich structures based on one single type of core, for example a C200/C200/C200 construction. Here, the perforation resistances of these "plain" core materials were predicted using the FE model, since previous work has shown that the perforation resistance of plain sandwich panels can be accurately predicted using this approach (Zhou et al., 2012). The predicted perforation energies of the single density crosslinked PVC sandwiches (with densities ranging from 60 to 200 kg/m^3) are shown in Figure 6.23. The figure indicates that the graded foam core sandwich structures offer a superior perforation resistance to the equivalent monolithic cores.

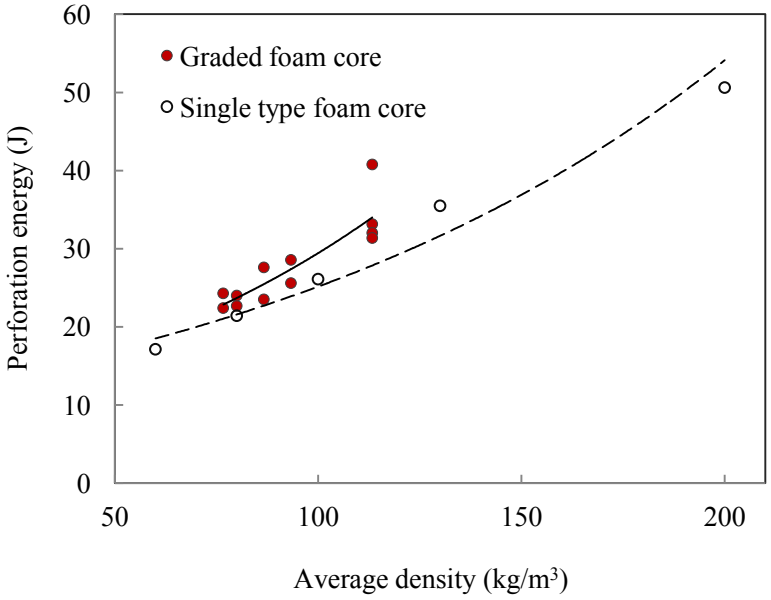

Fig. 6.23 Comparison of perforation energy between sandwich structures based on graded or single type foam cores.

This section investigated numerically the low velocity impact response of sandwich structures based on layered cores. Failure in the majority of the sandwich structures occurred as a results of core shear, with the FE model accurately predicting this mode of failure. The numerical model also predicted the associated load-displacement traces and the corresponding perforation energies with a high degree of accuracy. It has also been shown that graded structures can out-perform their monolithic counterparts in terms of their perforation resistance.

6.4 Simulation of composite rod reinforced foams

This section presents modeling results of the energy-absorbing characteristics of polymer foams reinforced with either carbon or glass fibre reinforced epoxy rods. Here, the reinforced core structures including PVC foam and composite rod were modeled using the finite element models developed in Section 5.2.1 and Section 5.2.3. The mesh generation, boundary and loading conditions are described in Section 5.3.3. Initially, the compression response of 20 mm thick foams containing rods of equal length is modeled and the resulting predictions are compared with experimental data. Subsequently, a series of finite element analyses have been undertaken to investigate the influence of varying foam density, rod diameter, rod length and fibre type on the energy-absorbing characteristics of the reinforced foams.

6.4.1 Simulation of compression tests

The first part of this research investigation focused on characterizing the crushing characteristics of foams reinforced with glass and carbon rods with a length equal to the thickness of the core, i.e. they extended over the entire thickness of the core. These analyses were undertaken in order to ascertain the effect of varying the foam density and rod diameter on the energy-absorbing characteristics of the cores. The finite models were validated by test data, giving confidence to subsequent analyses, in which the lengths of the rods are varied. Figure 6.24 compares the measured and predicted load-displacement traces for three families of reinforced core. Figure 6.24 (a) shows load-displacement traces for four foams reinforced with 2 mm diameter CFRP rods. Increasing the density of the foam serves to increase the initial stiffness as well maximum force recorded during the test. For example, increasing the nominal density of the foam from 40 to 200 kg/m^3 served to increase the maximum recorded force from approximately 7 to 20 kN. Increasing the density of the foam also resulted in a flatter region of stable crushing beyond the peak in the load-displacement trace, due to the greater compression resistance of the core as well as the increased support given to the reinforcing rods. An examination of the figure indicates that the model predicts the trends in the experimental data with reasonable success. In all cases, the finite element model over-predicts the initial peak in the trace although the subsequent level of agreement is good. It is also evident that the

model accurately predicts the onset of final densification, most particularly in the higher density systems. Figure 6.24(b) shows the load-displacement traces for four foams reinforced with 3 mm diameter GFRP rods. As before, increases in the foam density result in an increase in the maximum force sustained by the material and a flattening of the crush region during the middle stages of the test. Once again, there is a good agreement between the experimental data and the numerical prediction for all four materials shown in the figure. It is worth noting that the compression strengths of the foams reinforced with 3 mm diameter GFRP rods were slightly lower than those reinforced with similarly-sized CFRP pins, reflecting the difference in properties reported in Table 4-4. Finally, Figure 6.24(c) shows load-displacement traces following tests on foams reinforced with 4 mm diameter CFRP pins. Here, it is evident that the force in all four samples declines following the initial peak before stabilizing at higher displacements. A comparison of Figures 6.24(a) and 6.24(c) highlights the effect of increasing the rod diameter from 2 to 4 mm. Differences between the two sets of data are most significant in the lower density foam systems. For example, the compression strength of the lowest density foam increases from approximately 7 to 21 kN as the diameter of the reinforcement passes from 2 to 4 mm. Finally, agreement between the predictions and the experimental results is again good, with the model identifying most of the key features in the measured responses.

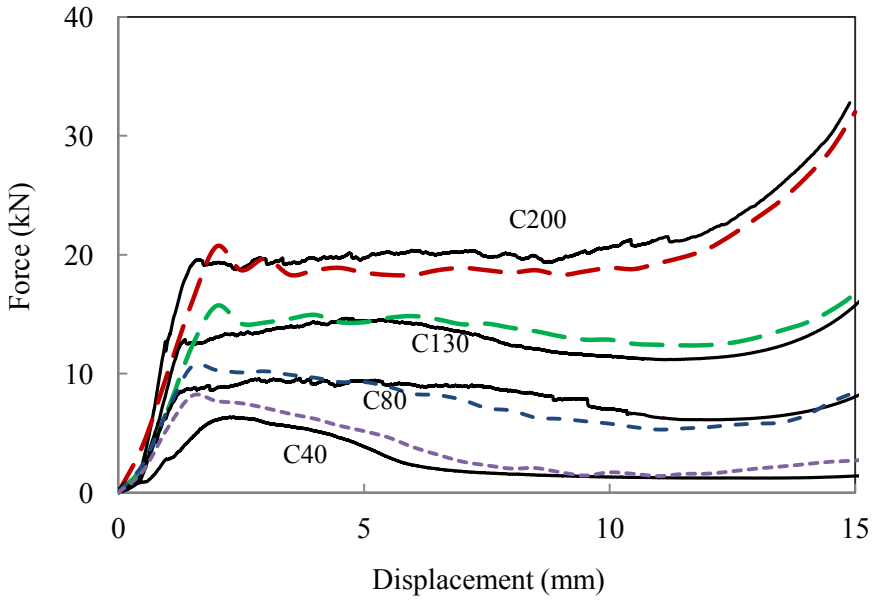

(a) 2 mm diameter CFRP rods

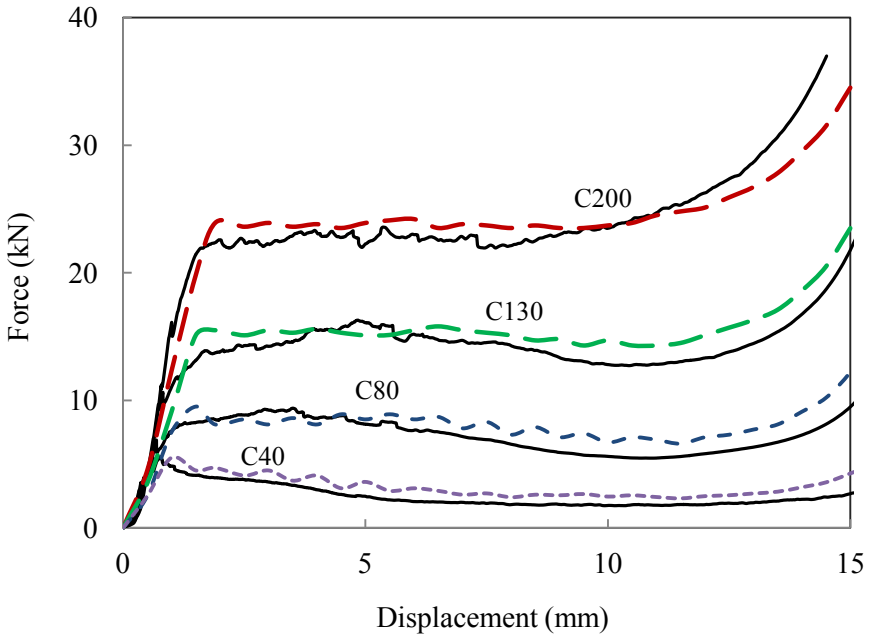

(b) 3 mm diameter GFRP rods

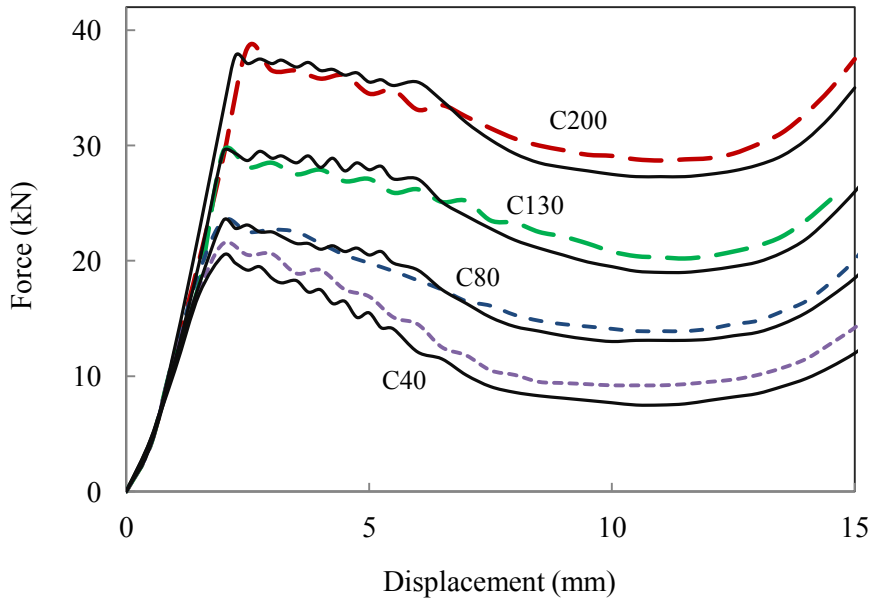

(c) 4 mm diameter CFRP rods

Fig. 6.24 Force-displacement traces PVC foams reinforced by (a) 2 mm diameter CFRP rods (b) 3mm diameter GFRP rods and (c) 4 mm CFRP rods. The solid lines correspond to the experimental curves and the dashed lines to the numerical predictions.

Both the measured and predicted values of energy absorption in the foams were calculated by determining the area under the load-displacement traces and the resulting values for the CFRP-based systems are presented in Figure 6.25. From the figure, it is clear that the absorbed energy increases with both foam density and rod diameter. As expected, reinforcing the foams has the greatest effect in the low density materials, with the incorporation of 4 mm rods serving to increase the level of energy absorption by roughly an order of magnitude relative to the plain foam. It is interesting that there is a significant increase in energy absorption in passing from the 3 to the 4 mm diameter reinforcement, possibly due to a change in failure mode in the vertical pins during crushing. Agreement between the model and the experimental data is good, suggesting that the finite element analysis is capable of predicting the response of these reinforced structures. The specific energy absorption (SEA) values of the reinforced were determined by dividing the energy values in Figure 6.25 by the corresponding mass of the sample and the subsequent variation of SEA with foam density is shown in Figure 6.26. Here, it is evident that for the 2 and 3 mm diameter systems, the SEA increases with increasing foam density. For example, the SEA of the foams based on 2 mm diameter rods increases by approximately fifty percent over the range of densities considered. In contrast, the SEA values of the foams based on the 4 mm diameter rods remains roughly constant as the foam density increases, suggesting that the energy absorption behaviour of these particular foams is effectively dominated by the response of the reinforcing rods, i.e. the foam plays only a secondary role. An examination of the figure indicates that the maximum value of SEA achieved in the carbon-based system is approximately 30 kJ/kg and that such energy-absorption characteristics can be achieved using the lowest density (and least expensive) foam. The foams reinforced with GFRP rods exhibited similar trends to those evident in Figure 6.25, with the energy absorbed by the cores again increasing linearly with foam density. In contrast, for all rod diameters, the associated SEA values for the GFRP structures increased with foam density. For example, the SEA of the foams reinforced with 4 mm diameter rods increased from 21 to 31 kJ/kg over the range of foam densities investigated here.

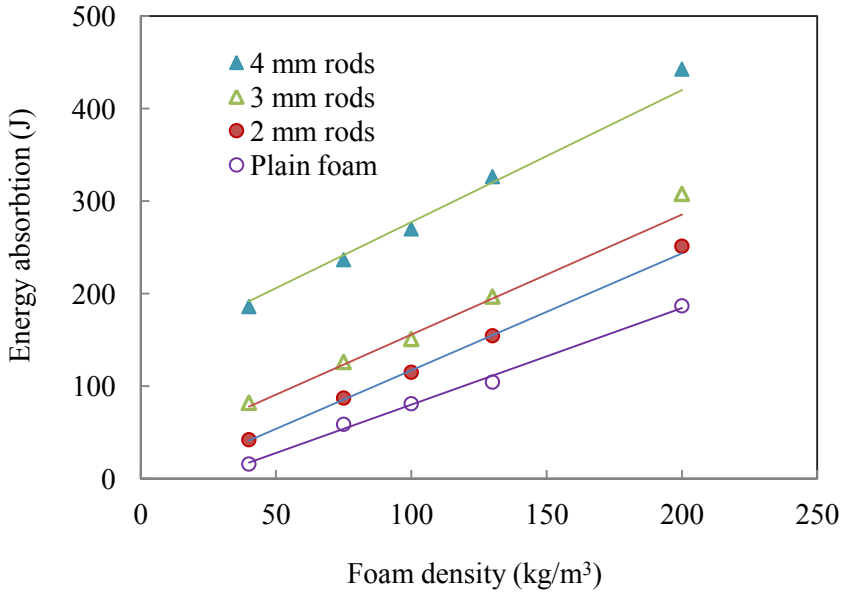

Fig. 6.25 The variation of absorbed energy with foam density and CFRP pin diameter. The points correspond to the experimental data and the solid lines to the numerical predictions.

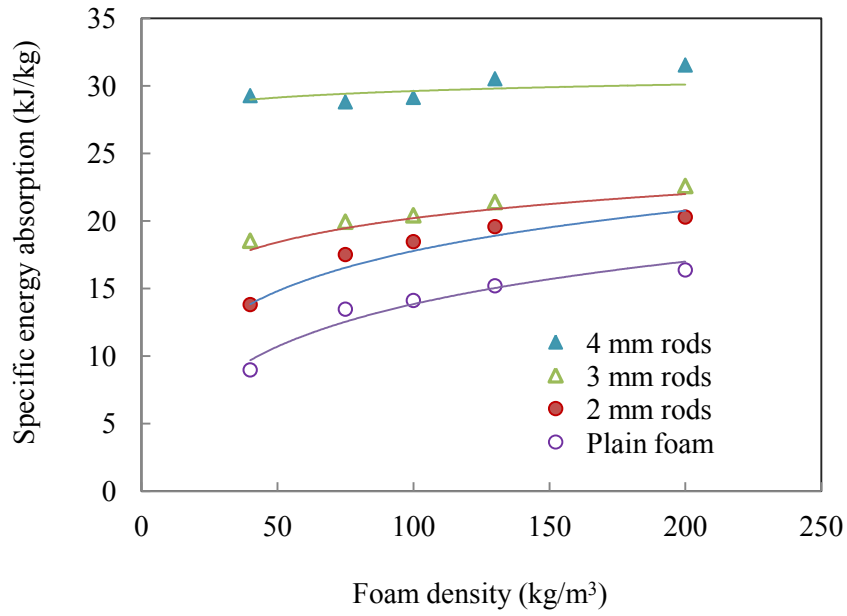

Fig. 6.26 The variation of SEA with foam density and pin diameter. The points correspond to the experimental data and the solid lines to the numerical predictions.

6.4.2 The influence of core thickness

By comparing the numerical data with data from tests on a range of reinforced core structures, it has been demonstrated that the numerical model can be used to predict the crush response of these types of material with a high degree of accuracy. The next part of this study employed the numerical model to investigate the influence of varying the core thickness on the crush characteristics of the reinforced cores. Here, foams with thicknesses of 30 and 40 mm were reinforced with CFRP of equal length. Figure 6.27 shows the resulting force-displacement traces for these two core thicknesses and includes, for comparison, together with the trace corresponding to the 20 mm thick cores analysed in the previous section. An examination of the figure indicates that all traces exhibit similar trends, with the force increasing to a maximum before dropping and stabilizing at an approximately constant force and finally increasing due to densification of the polymer foam. It is clear that the maximum force remains roughly constant with increasing foam thickness suggesting that the rods continue to crush rather than buckle as the core thickness is increased. The traces follow similar paths beyond the maximum force value until the densification threshold, which clearly depends on the initial core thickness.

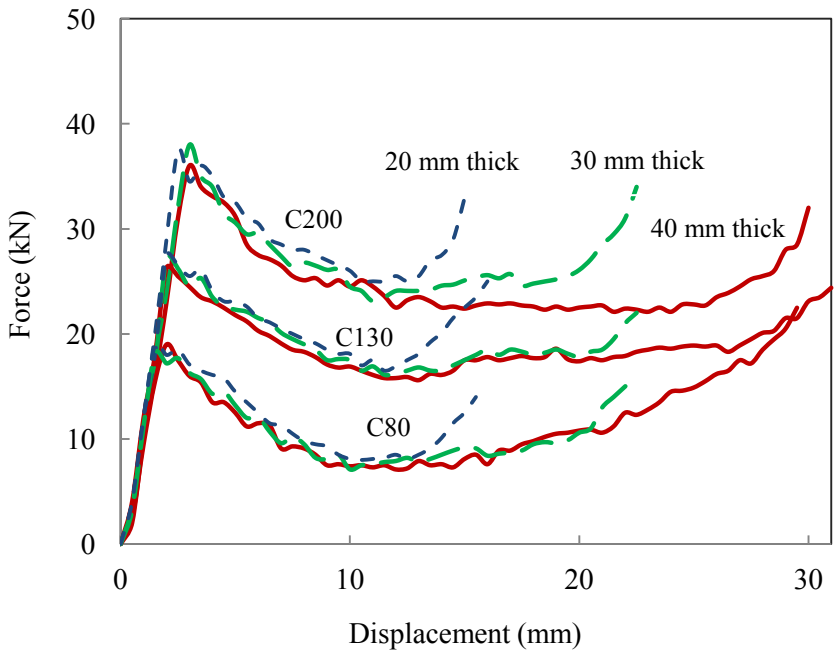

Fig. 6.27 Predicted force-displacement traces for three foam thicknesses and three foam types, reinforced with 4 mm diameter CFRP rods reinforced foam with various densities and thickness.

Figure 6.28 shows the predicted variation of the SEA values with foam density and rod diameter for the 40 mm thick cores. A comparison of the data in this figure with those in Figure 6.29 highlights similar trends with the SEA increasing with foam density for the smaller rods and remaining roughly constant for the largest reinforcements. It is also evident that the predicted SEA decreases with increasing foam thicknesses.

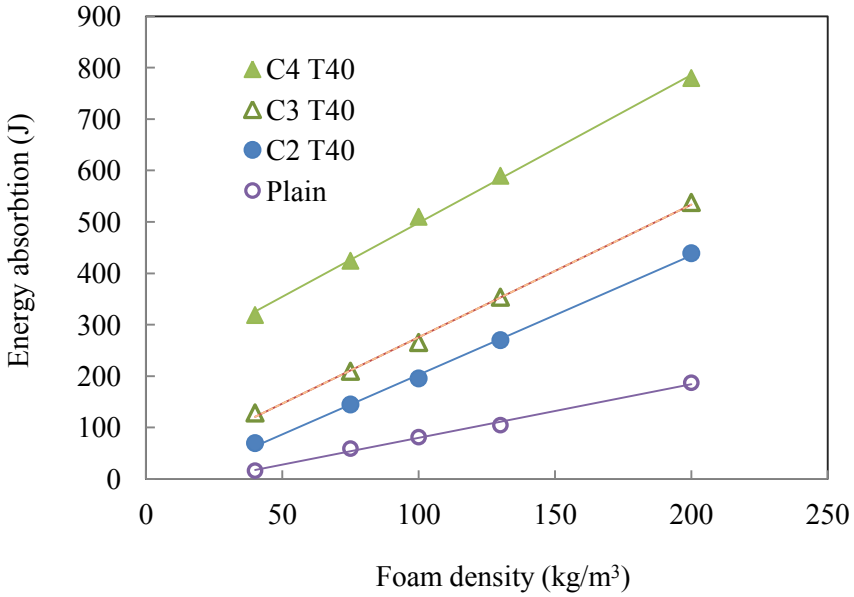

Fig. 6.28 Comparison of energy absorption of 40 mm thick foam reinforced by various diameters of composites.

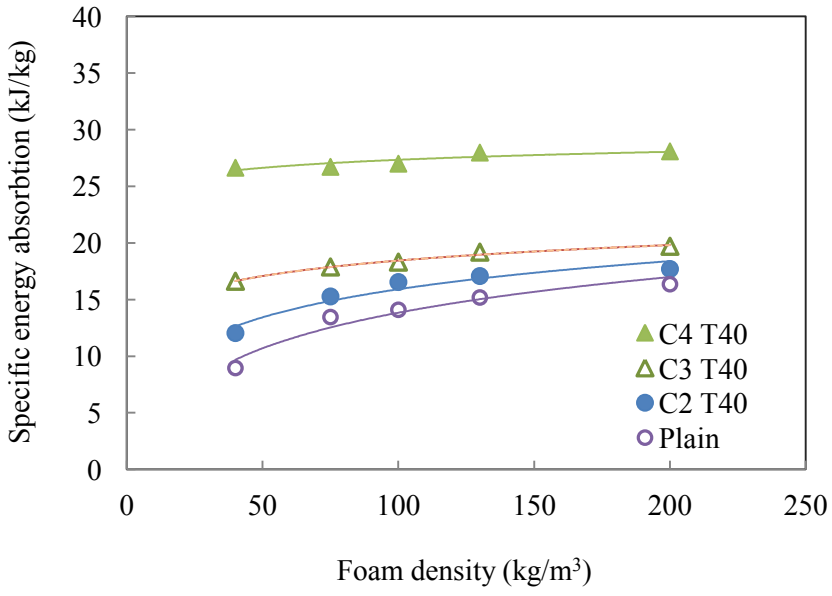

Fig. 6.29 Comparison of specific energy absorption of 40 mm thick foam reinforced by various diameters of composites.

6.4.3 Crushing tests at impact rates of strain

Figure 6.30 presents the load-displacement traces following low velocity compression tests on a 130 kg/m^3 foam reinforced with 2, 3 and 4 mm diameter CFRP rods. The figure also includes the predictions offered by the finite element models of these dynamic tests. All of the experimental traces exhibit a distinct oscillatory response during much of the test. It is clear, however, that the force values tend to stabilize towards a constant value as the test progresses. There is clearly good agreement between the numerical and experimental traces for the four test cases, indicating that the model accurately captures the dynamic compression regime.

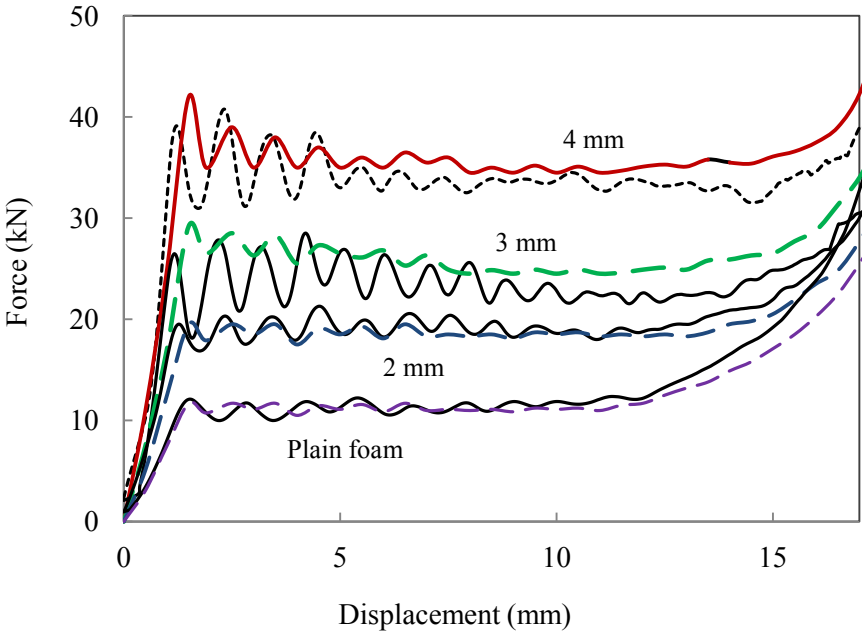

Fig. 6.30 Force-displacement traces for C130 foams reinforced by 2，3 and 4 mm carbon fibre rods subject to impact load. The solid lines correspond to the experimental curves and the dashed lines to the numerical predictions.

Figure 6.31 compares the dynamic and quasi-static specific energy-absorption characteristics of the CFRP and GFRP pins embedded in the 130 kg/m^3 foam as a function of volume fraction of the pins. From Figure 6.31(a), it is clear that the dynamically-loaded CFRP-based structures absorb more energy that their statically-loaded counterparts. For example, the dynamically-loaded structure based on the 4 mm rods (VF = 4.5%) exhibited an SEA that is 63% higher than its quasi-static static equivalent. In contrast, the dynamic values for the GFRP reinforced cores are less sensitive to strain rate, with the dynamic values of SEA for the largest diameter pins (VF = 4.5%) being similar to their

quasi-static values. Figure 6.31(b) shows the energy absorbed under dynamic and quasi-static loading for GFRP.

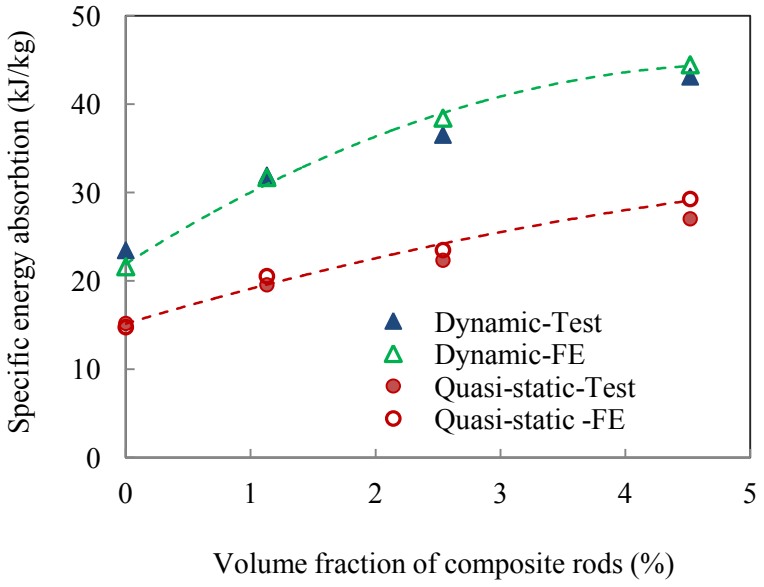

(a) Carbon fibre rods

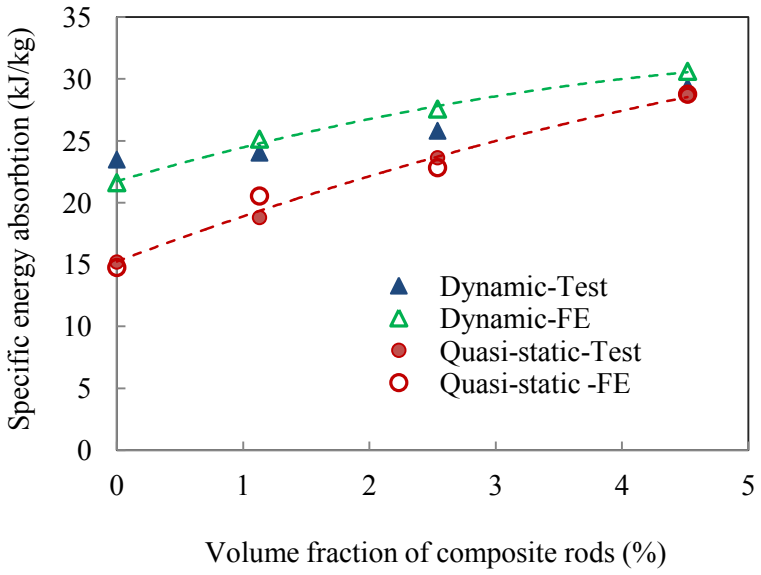

(b) Glass fibre rods

Fig. 6.31 The variation of the energy absorbed under dynamic and quasi-static loading as a function of rod diameter for the 130 kg/m^3 foam. (a) CFRP pins and (b) GFRP pins. The plain foam is shown as a rod diameter of zero. The solid points correspond to the experimental data and the hollow symbols and dashed lines to the numerical predictions.

6.4.4 Simulation of graded rod reinforced foams

Compression tests on graded core structures

The next stage of this research study focused on investigating the energy-absorbing characteristics of graded cores based on rods of different length. The motivation for this study was to investigate the possibility of controlling both the maximum force recorded during the crushing regime, as well as the associated energy-absorbing process. Figure 6.32 shows a finite element mesh for a graded structure containing three lengths of rod, these being 20, 15 and 10 mm. For clarity, the rods have are not fully inserted into the foam. This particular design is referred to as a (432) core, given that it contains four 20 mm long rods, three 15 mm long rods and two 10 mm rods. Clearly, it would be possible to further modify the crush response of the foams by using more than one fibre type within an individual foam and also by using foams based on layers having different densities.

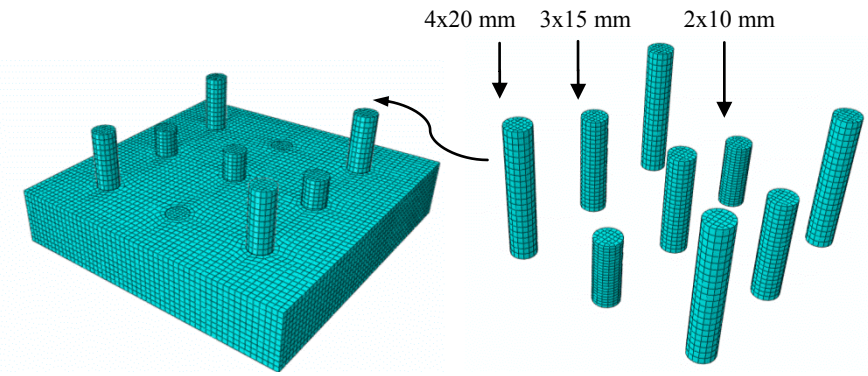

Fig. 6.32 Mode and mesh of PVC foam reinforced by graded carbon rods. (i.e. a 432 is the 4x20 mm long rods, the 3x15 mm intermediate length rods and the 2x10 mm short rods).

Figure 6.33 shows a schematic representation of the three graded core designs that were modelled in this study. Figure 6.33(a) shows a (540) design with four 20 mm rods along the four edges of the block, separated by five shorter 15 mm rods. There are no 10 mm rods, hence the zero in the aforementioned core definition. A (432) core design with just two full length (20 mm) rods and a (441) core with a single 10 mm rod positioned between equal numbers of 15 and 20 mm rods. Figure 6.33(b) shows the arrangement of the graded lengths of composite rods in a (441) structure.

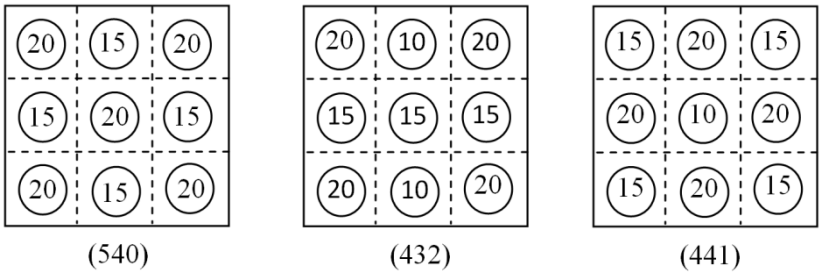

a. Schematic of the three graded structures considered here, (No of 20 mm, No of 15 mm No of 10 mm rods)

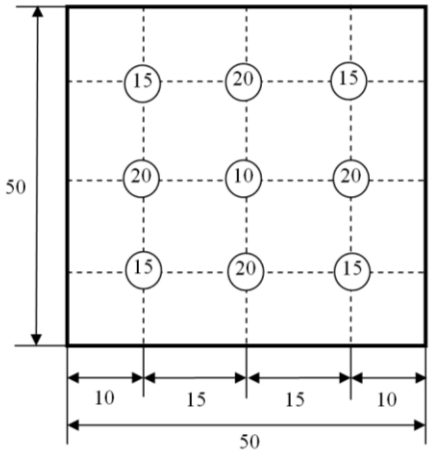

b. Arrangement of graded lengths of composite rods in a (441) structure.

Fig. 6.33 Schematic and arrangement of graded lengths of composite rods

Figure 6.34(a) shows force-displacements predictions for three graded structures based on the (432) and (450) CFRP rod designs. All curves exhibit similar trends with the force increasing in steps as first the longest and then the intermediate and finally the shorter rods are engaged in the compression process. Closer inspection of the C200 (432) sample in Figure 6.34(a), shows that the force initially rises to an initial plateau value of approximately 22 kN as the 20 mm rods and the foam are crushed. This value rises to approximately 28 kN as the 15 mm long rods become involved in the compression process and finally there is a small plateau at 34 kN as the shortest rods begin to be crushed. Figure 6.34(b) shows load-displacement traces for three cores reinforced with a (540) arrangement of 4 mm diameter CFRP rods. Here, the plateau values associated with crushing the 20 and 15 mm reinforcements are slightly higher than those evident in Figure 6.34(a), due to the fact that there is an additional rod of each length in the latter system.

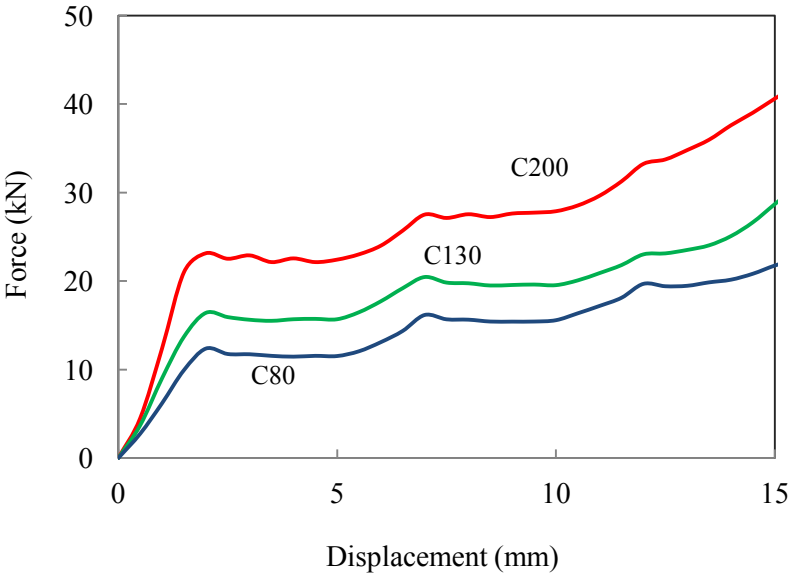

(a) (432) graded structures

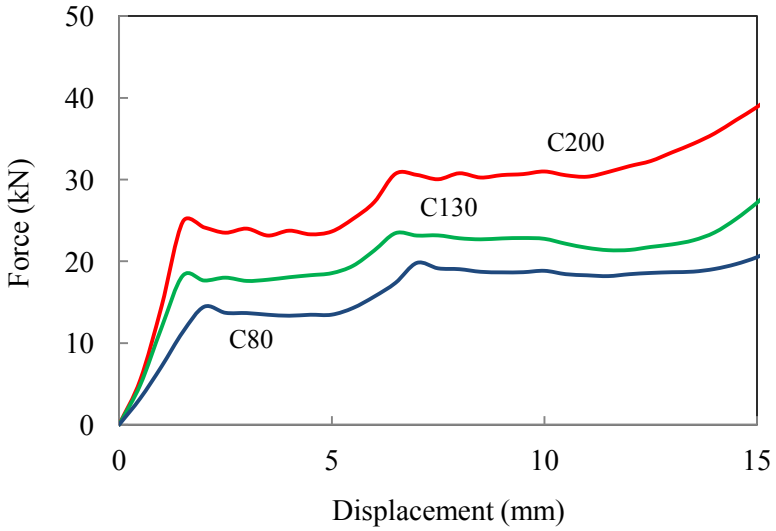

(b) (540) graded rod design.

Fig. 6.34 Comparison of force-displacement traces of foam panels reinforced by 4 mm diameter CFRP rods in (a) a (432) graded structures and (b) a (540) graded rod design.

The finite element model was to investigate how the load is carried by the reinforced foams. Figure 6.35 shows the breakdown of the forces for a 200 kg/m^3 foam based on a (432) configuration. Clearly, the four 20 mm long CFRP rods and the foam carry the initial load, with the latter proving to be the stiffer component. The foam begins to yield at a crosshead displacement of approximately 1.5 mm and the four rods begin to crush at approximately 2 mm. As a consequence of failure in these two constituents materials, the trace for the test sample peaks at a displacement close to 2 mm. The

three 15 mm long rods are engaged at a displacement of 5 mm and this is reflected in the trace for the test specimen. Finally, the shorter, 10 mm pins begin to be loaded at a displacement of 10 mm, resulting in a corresponding rise in the overall trace. This approach can also be used to understanding and ultimately optimise how energy is absorbed in these graded structures.

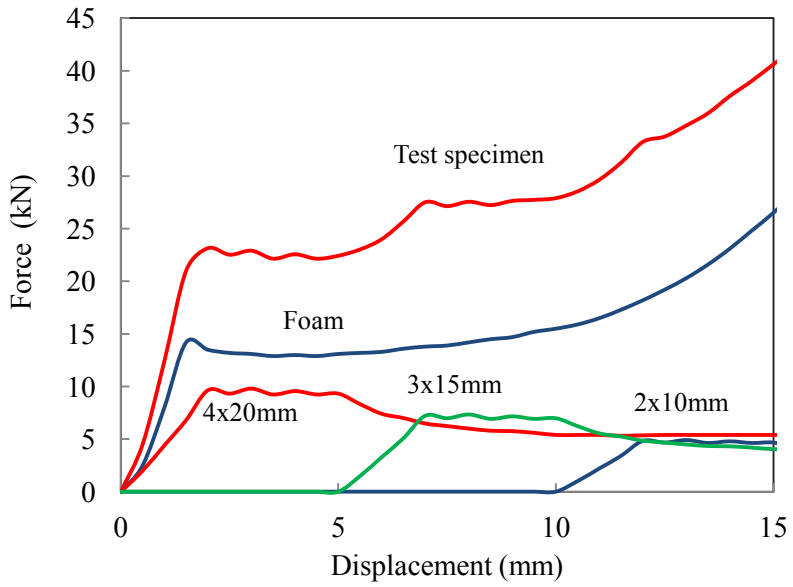

Fig. 6.35 Force-displacement traces of 200 kg/m^3 foam reinforced by graded length rods in a (432) arrangement.

Figure 6.36 shows the breakdown in energy absorption for three foams based on a (432) configuration. An examination of the figure indicates that the energy absorbed by the rods increases withfoam density. For example, the energy absorbed by the four 20 mm long rods increases from 88.8 Joules to 94.6 Joules as the density of the supporting foam in increased from 80 to 200 kg/m^3. Clearly, the energy absorbed by the plain foam increases with density with values passing from 44.2 to 211 Joules over the range considered here. The values for the three lengths of CFRP rod and the polymer foam can be summed to give the overall values for this design of structures to yield overall values of energy absorption for the reinforced cores (solid triangles) between 205 and 372 Joules. These values are clearly lower than those associated with the conventional systems based on foams containing nine 20 mm long rods (open tiangles) highlighlighting the compromise between energy-absorption and the previously-discussed controlled force-displacement history.

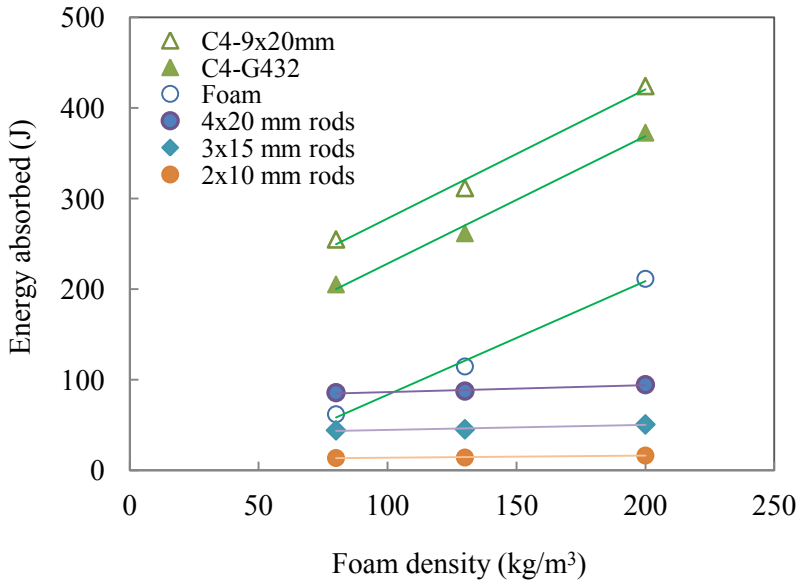

Fig. 6.36 Breakdown of energy absorption in a 200 kg/m^3 foam reinforced by CFRP rods in a (432) arrangement.

Figure 6.37 shows the predicted variation of energy absorption values of foam reinforced by graded length rods with foam density and different arrangements. A comparison of the data in this figure highlights similar trends with the SEA increasing with foam density and the energy absorption for three foams based on a (54) configuration shows the advantage performance over the the configuration (441) and (432).

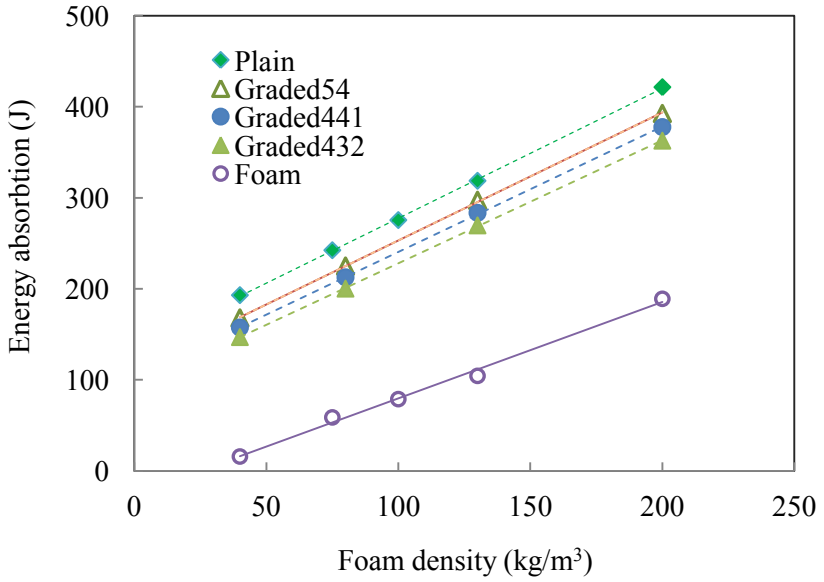

Fig. 6.37 Comparison of energy absorption of foam reinforced by graded length rods between different arrangements

Figure 6.38 indicates that the predicted SEA are similar with increasing foam density. It is an evident the graded length rods reinforced have similar performance form lower density to high density foam. The foam reinforced with graded rods has a continue increasing plateau resistance foam shown in Figure 6.34, highlights the advantage performance in both resistance foam and energy absorbing.

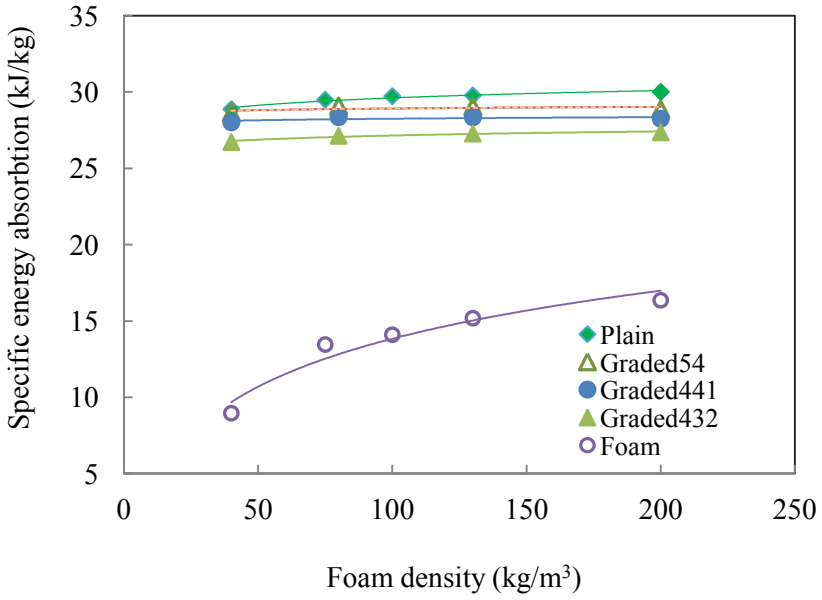

Fig. 6.38 Comparison of specific energy absorption of foam reinforced by graded length rods between different arrangements.

The simulation on foams reinforced with graded composite rods in this section, demonstrated that the finite element models are capable of accurately predicting the crushing response of the foams under both quasi-static and dynamic loading conditions. It has been shown that increasing the rod diameter resulted in an increase in the measured values of SEA. Similarly, increasing the density of the foam yielded an increase in SEA, although the relative increase in energy absorption tended to decrease at higher densities. Increasing the strain-rate during the compression test serves to increase the energy-absorbing capability of the reinforced cores, primarily due to rate effects in the PVC foam. Finally, it has been shown that it is possible to control the crushing force by using rods of different length. Here, the finite element model can be used to design structures exhibiting particular crushing characteristics and energy-absorbing properties.

6.5 Simulation of composite tube reinforced foams

The finite element (FE) models were developed to predict the compressive response and energy-absorbing capability of composite tube reinforced PVC foams. A vectorized user material subroutine (VUMAT) was employed to define Hashin's 3D damage criteria for the composite tube to model the corresponding deformation and failure mechanisms, which is detailed in Section 5.2.3. The FE model for PVC foam was described in foregoing Section 5.2.1. The mesh generation, boundary and loading conditions are described in Section 5.3.4. The models developed here were used to predict the load–displacement traces and failure modes in the tube reinforced foam structures, which were validated against the corresponding experimental results.

6.5.1 Simulation of compression tests on individual tube

The modeling for tube reinforced foam panels was developed similar to the rod reinforced foam. Prior to model the foam panel with embedded tubes, the individual tubes were simulated and compared with the experimental results. Figure 6.39 shows comparison of load-displacement traces obtained from FE prediction and the corresponding experimental results of the 8, 10 and 12.5 mm tubes individually. Reasonably good correlation has been obtained in terms of the initial stiffness, the first peak load, plateau load and damage evolution. It clearly shows that the predicted load from FE modeling, similar to the testing, is in a reducing trend after the first peak load during the compression process.

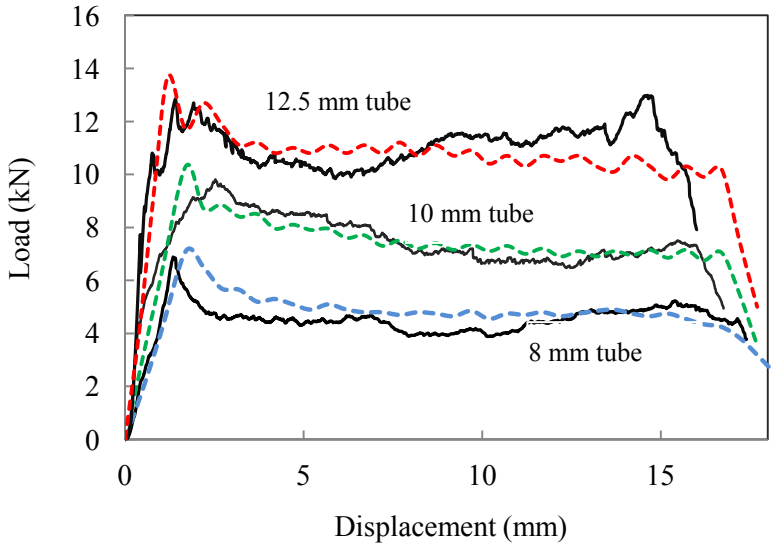

Fig. 6.39 Load-displacement traces of individual carbon tube in diameter of 8, 10 and 12.5 mm under

compression load. (The solid lines correspond to test data and dashed lines to predictions.)

Figure 6.40 shows the comparison of progressive deformation and failure modes for the 10 mm CFRP tube obtained from testing and FE modelling. The basic features of the extensive splaying, fibre fracture and matrix cracking for the crushed tube were captured. Both modeling and testing indicate a progressive collapse of the tube. However, the simulated failure mode shows less extensive splaying of fibre, which may be caused by the automatic removed of the failed elements. The more accurate material data for the resin and fibre in the circum direction can be used to improve the simulation of the failure modes.

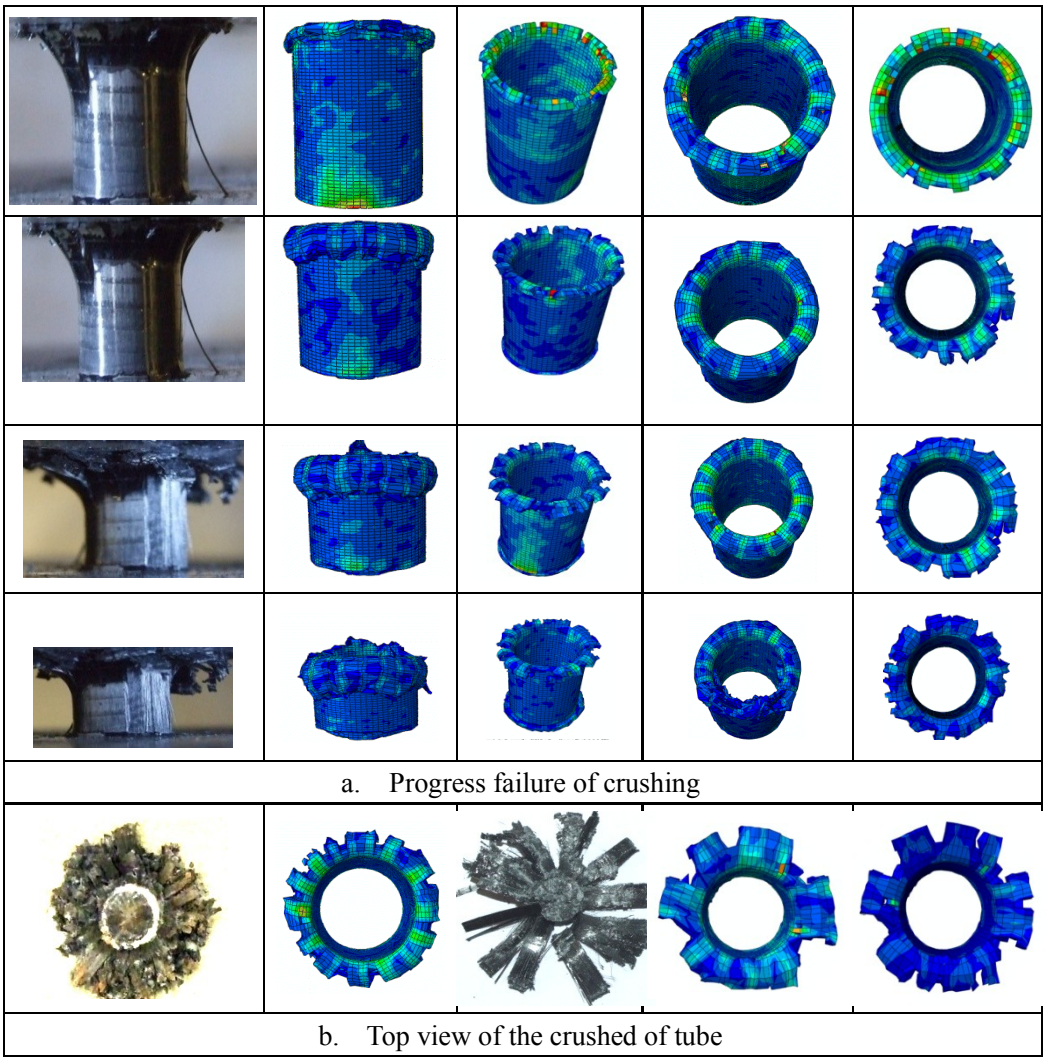

a. Progress failure of crushing

b. Top view of the crushed of tube

Fig. 6.40 Comparison of progress deformation and failure for 10 mm CFRP tubes between test FE modeling.

6.5.2 Simulation of compression test on tube reinforced foam panel

PVC foam panels with densities of 40, 80 and 130 kg/m^3 were embedded with CFRP tubes in three diameters, i.e. 8, 10 and 12.5 mm. Figure 6.41 shows load-displacement traces obtained from numerical modeling and the corresponding experimental results of the tubes embedded in 130 kg/m^3 PVC foam panel. The test results of a plain PVC foam panel without any tube are also shown in the figure to highlight the enhancement of carbon tube. Again, agreements between the experimental results and the finite element simulations are very good, with features well captured in the initial stiffness, the peak load, the damage evolution and the densification. Clearly, the load resistance increased significantly to a average plateau load from 11.3 to 22.7 kN for the 8, 10 and 12.5 mm tube reinforced foam panels respectively. It is noted that the plateau load of 12.5 mm tube reinforced foam panel is 8 times of the plain foam panel without embedded tube.

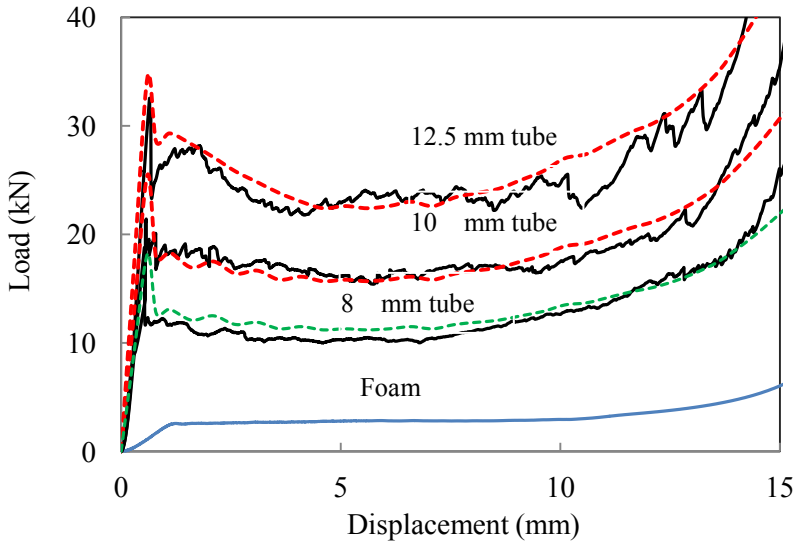

Fig. 6.41 Comparison of load-displacement traces of C130 foam embedded in carbon tube in diameter of 8, 10 and 12.5 mm. (The solid lines correspond to test data and dashed lines to predictions.)

Figure 6.42 shows a comparison of the cross-sections of deformation and failure modes for C80 foam core panel with embedded CFRP tubes obtained from test and FE modelling. The core structure was deformed by 75% from its original configuration. The basic features of the foam crushing failure and the tube failure were captured. The failure modes of FE show less crushing debris due to the failed elements being removed automatic by the element control. The failed tubes

are displayed is the crushing states, which indicate a progressive collapse of tube embedded in the PVC foam. The failure also indicates that the strong constraint from the foam forces the CFRP tube to have crushing failure along their longitudinal axis, which explains the enhancement of the foam in terms of its energy absorption. However, the failed elements in the modeling may cause element penetration with each other, which underestimates resistance of the tube under compressive load.

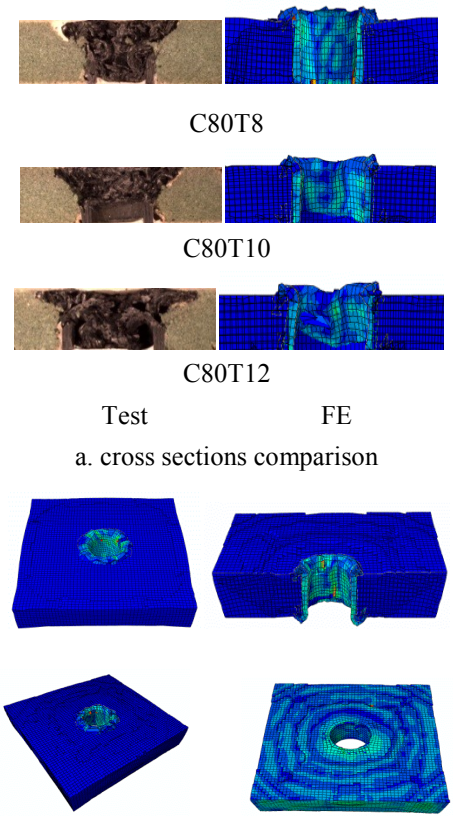

a. cross sections comparison

b. FE simulation

Fig. 6.42 Comparison of cross-sections and deformation/ failure modes of crushed tube reinforced foam panels.

The comparison of the load-displacement traces of the individual tube, predicted force of tube embedded in foam, and whole panel with a density of 130 kg/m^3 and embedded CF tube in diameters of 12.5 mm are exhibited in Figure 6.43. The dashed line corresponds to the FE predictions whilst the solid line to the experimental results. The test results of plain foam also included. An examination of the response of tube shows that the trend of the individual tube without foam constraint in a downward during the later stage of compression crushing, whilst the tube embedded shows a densification at the final stage. The load-displacement curves of the tube embedded is evident that the tube contributes over 80% of the carrying capactity load and energy

absorption of foam panel and the tube embedded tube over perform more than twice of individual tube without foam support in the case of 12.5 mm tube embedded in C130 foam. This evidence clearly supports the suggestion embedded tube in foam panel can modify the failure process and greatly enhance the crush performance of the tubes.

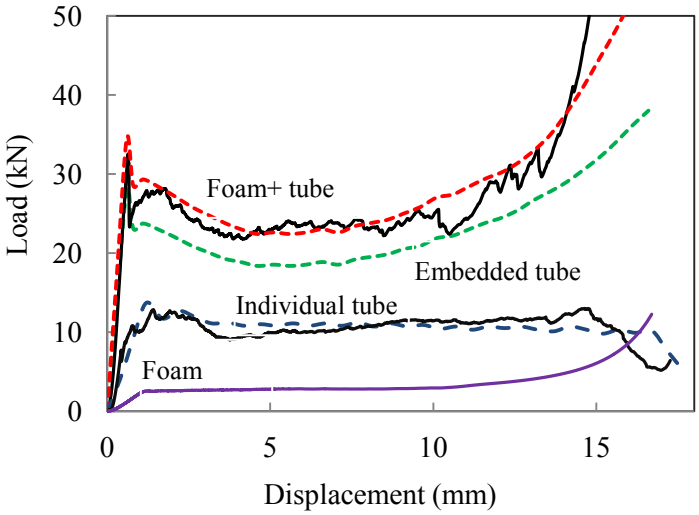

Fig. 6.43 Comparison of load-displacement traces between individual carbon tube in diameter 12.5 mm and tube embedded in C130 foam under compression load.

6.5.3 Energy absorption prediction

Figure 6.44 shows the comprehensive comparison of energy absorptions obtained from experimental tests and FE predictions for individual and embedded carbon tube in diameters of 8, 10 and 12.5 mm in foam panel with density form 40 to 130 kg/mm^3. The points is experimental data and the dash line is the numerical prediction. In general, correlation is quite good between test data and FE predication for the individual tube on the energy bar chart with a difference less than 5 %, whereas the difference on the tube reinforced foam is slight higher. The FE predictions for the 40 kg/m^3 foam panels are slightly lower than those of experimental measurements, whilst such the predictions for the higher density panels are slightly higher. The possible reason is that due to the weak constraint offered by the foam with a lower density, in the modeling such crushing causes element penetration with each other, which underestimates resistance of the tube to the compressive load. In the case of tube in higher density foam, the strong constraint from the foam forces the CFRP tubes to have a crushing failure along their longitudinal axis, which offer a continuous load resistance without buckling

failure leading to a total crush. The FE simulation assumes an ideal case in comparison to the real state of experiment test.

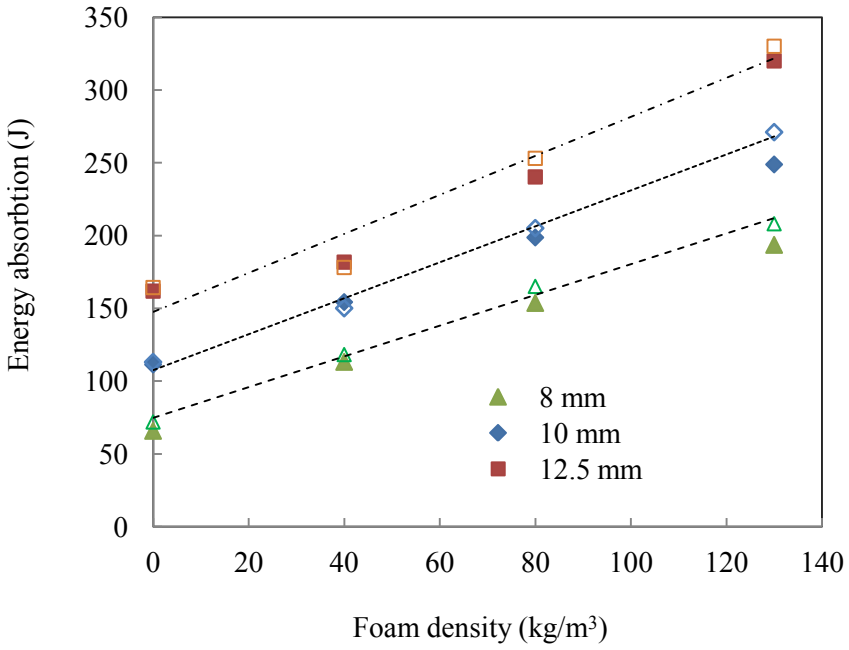

Fig. 6.44 Comparison of energy absorption charts for individual tube in diameter of 8, 10, 12.5 mm and tube reinforced foam density from 0 to 130 kg/mm^3. (The hollow points are FE prediction and the solid points are experimental data).

This section present the FE simulation of load-displacement traces on PVC foam panels with embedded carbon fibre tubes, which are compared with the corresponding test results. Good agreement was obtained in terms of the load–displacement traces, the deformation and failure modes. This evidence clearly supports the suggestion that embedded tube in foam panel can modify the failure process and greatly enhance the crushing performance of the tubes.

6.6 Simulation of FMLs subjected to impact loading

The finite element models have been developed to predict the structural behaviour of fibre metal laminates subject to perforation loading. The material constitutive model and failure criteria for composite layers, resin layers and aluminium layers are described in Section 5.2.3, Section 5.2.4 and Section 5.2.5 respectively. The mesh generation, boundary and loading conditions are described in

Section 5.3.5. Modeling results were compared with the experimental results, in terms of load-displacement relationships, energy absorption, deformation and failure modes. The perforation loading on individual layers has been modeling firstly to validation the FE modeling. The perforation prediction on FMLs has also been compared with the experimental data.

6.6.1 Simulation of the aluminuium and composite layer

Prior to modelling the response of FMLs structures, modelling on plain aluminium alloy and GFRP layers was carried out to validate the model. Figure 6.45 shows a comparison between the experimental and the numerical load-displacement traces for the individual layers of the 7075-O and 6061-O aluminium alloys. Both the initial stiffness and peak load were captured by FE modes accurately. The traces for subsequent perforation behavior show a similar trend with experimental results. The peak loads from the numerical predictions for two different aluminium layers were 910 and 3205 Newton, respectively. The FE predications are only 12.3 % and 10.9 % higher than the corresponding experimental tests. The predicted perforation energies were 5.8 and 23.9 J, which are only 7.1 % higher and 6.7 % higher than the corresponding experimental results.

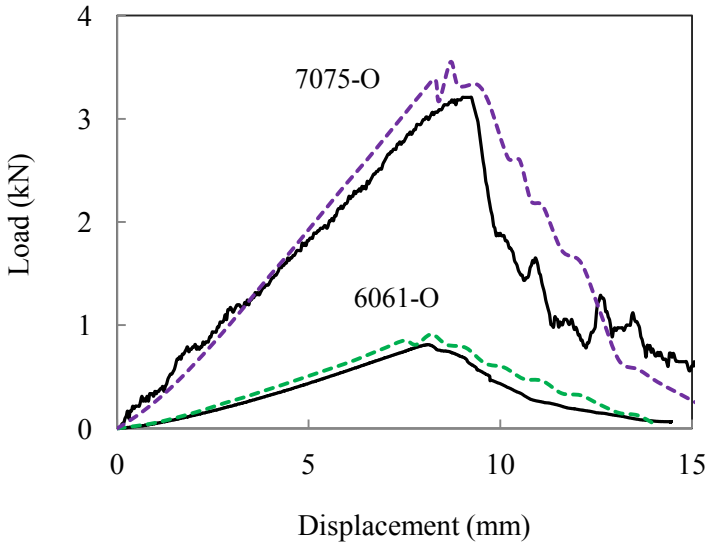

Fig. 6.45 Load-displacement traces of individual aluminium layers following perforation test. (The solid line corresponding to tests and dash line to FE modeling results)

Figure 6.46 shows the comparison of failure mode between the experimental and the numerical prediction. The typical features of a ductile alloy were simulated by FE models. The FE prediction

captured deformation and fracture zone accurately as the experimental specimen did. The predicted model also shows a circular fragment from central of specimen similar to the perforated sample.

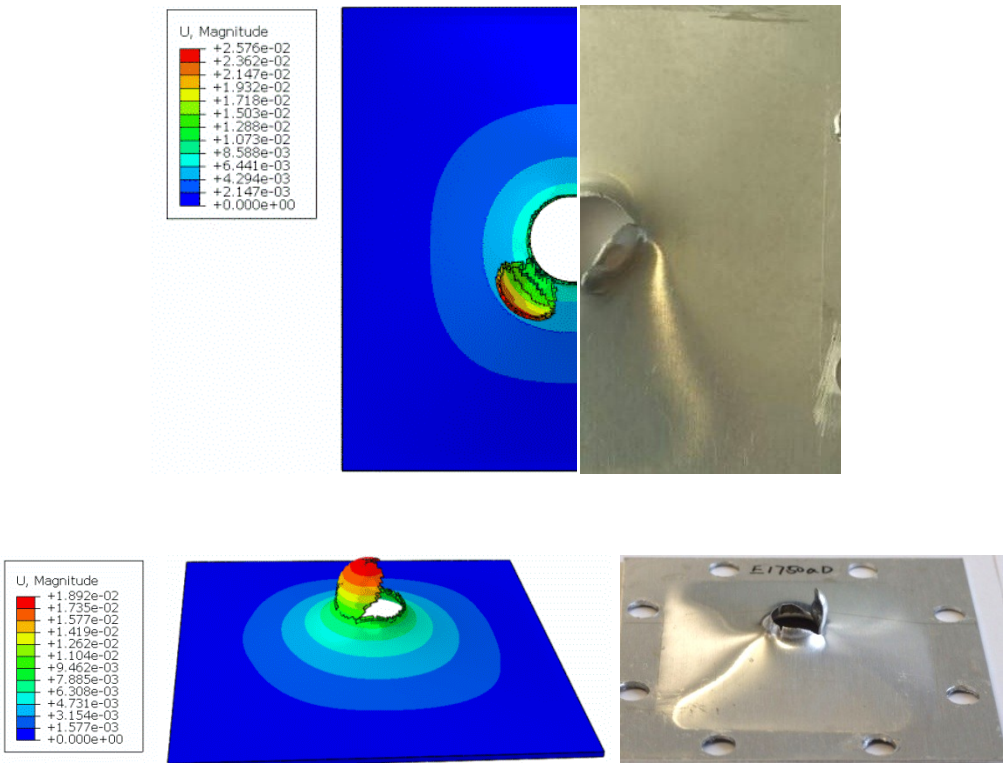

(a) Comparison of experimental and FE

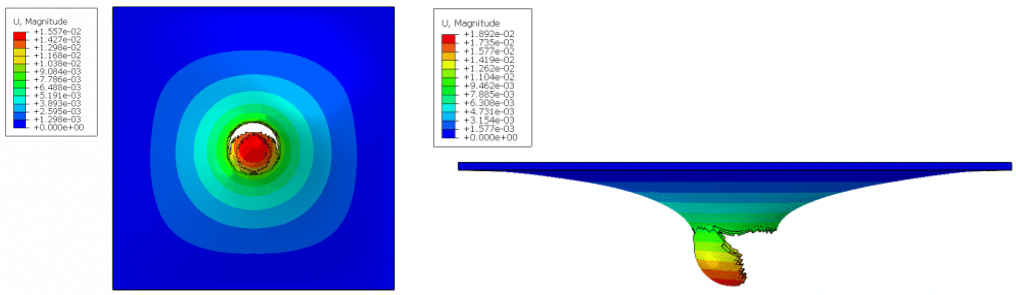

(b) FE prediction

Fig. 6.46 Comparison of cross-sections following impact perforation of 7075-O aluminium alloys.

Figure 6.47 presents the comparison between the experimental and the numerical load-displacement traces for the 3-ply and 5-ply composite layers subjected to a low velocity impact. The FE model captured the basic feature for stiffness, the displacement at the peak load and peak load for both the

composite layers. The load-displacement traces show that the initial agreement in the first 1 mm displacement. The peak loads from the numerical predictions for these layers were 1015 and 1692 N, respectively, with a difference between the FE prediction and tested data is within 12 %. The predicted perforation energies base on the traces were 3.35 and 5.51 J respectively, with a difference less than 10 % to the corresponding experimental results.

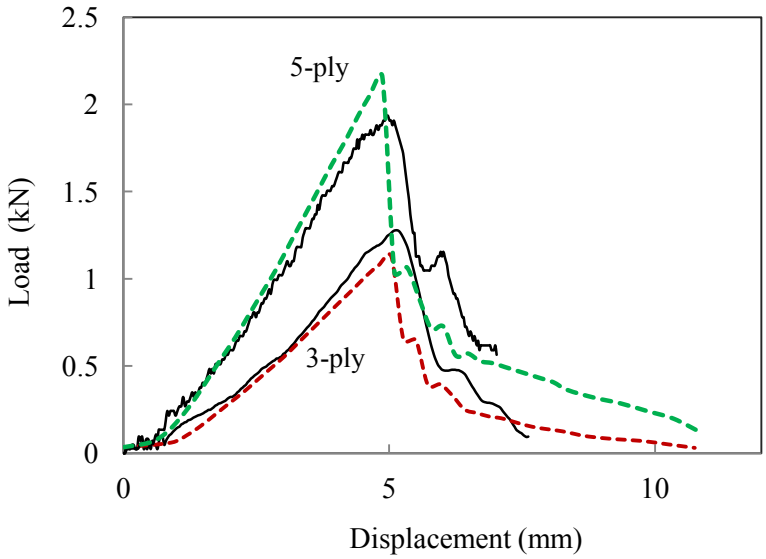

Fig. 6.47 Load-displacement traces of perforation test on individual glass fibre layers. (The solid line corresponding to tests and dash line to FE modeling results)

Figure 6.48 shows the comparison of cross-sections following impact perforation on the composite layers. Clearly, the FE model captured the failure mode in terms of deformation, size of perforation zone and fracture shape. In general, the numerical models produced a reasonably good prediction on the stiffness and displacement, peak load and fractured shape for GFRP laminates.

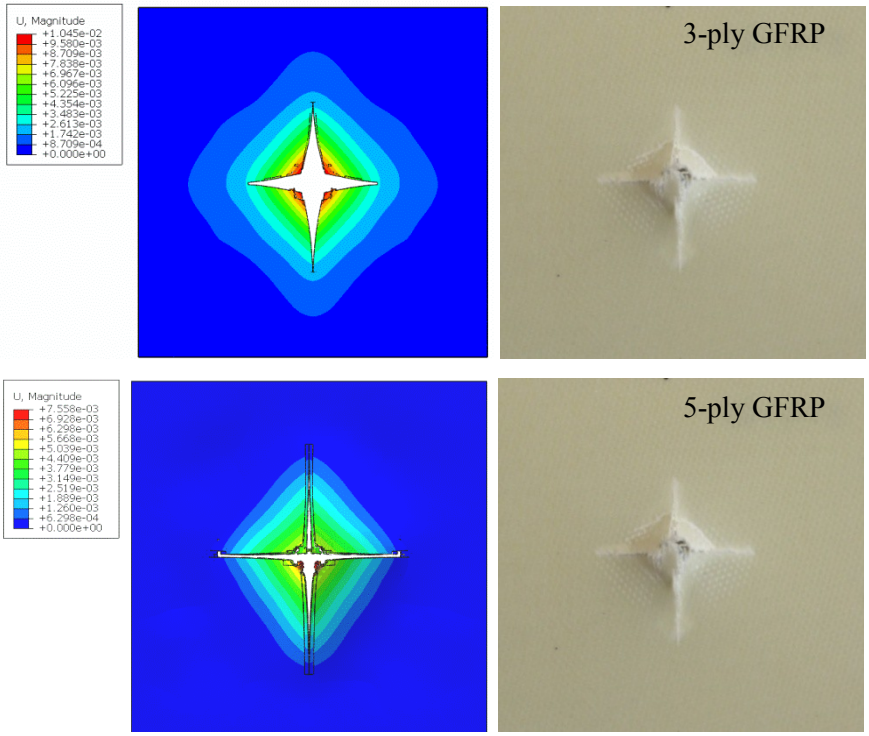

Fig. 6.48 Comparison of cross-sections following impact perforation of composite layer.

6.6.2 Simulation of FMLs

Finite element models for 6061-T6, 6061-O and 7075-O alloys based FMLs were developed to simulate the perforation response on a series of multilayer configurations ranging from a simple 2/1 lay-up to a 5/4 stacking sequence. Figure 6.49 show the predicted and the related experimental load-displacement traces of 2/1, 3/2, 4/3 and 5/4 FML plates made with 6061-T6 and 3-ply composite layers subjected to low velocity impact. The load-displacement traces show a linear up stiffness up to the fist peak load. The predicted traces exhibit pronounced oscillatory effects for the 4/3 and 5/4 FMLs in perforation and also tend to slightly over-estimate the peak load for the thick FMLs. The predicted peak loads for the 6061-T6 based 2/1 to 5/4 FML plates were 2.2, 3.7, 5.5 and 7.8 kN, respectively. The differences are within 12 % to the experimental results. The predicted initial stiffness and the displacement at the peak load for the targets were in good agreement with the corresponding experimental results.

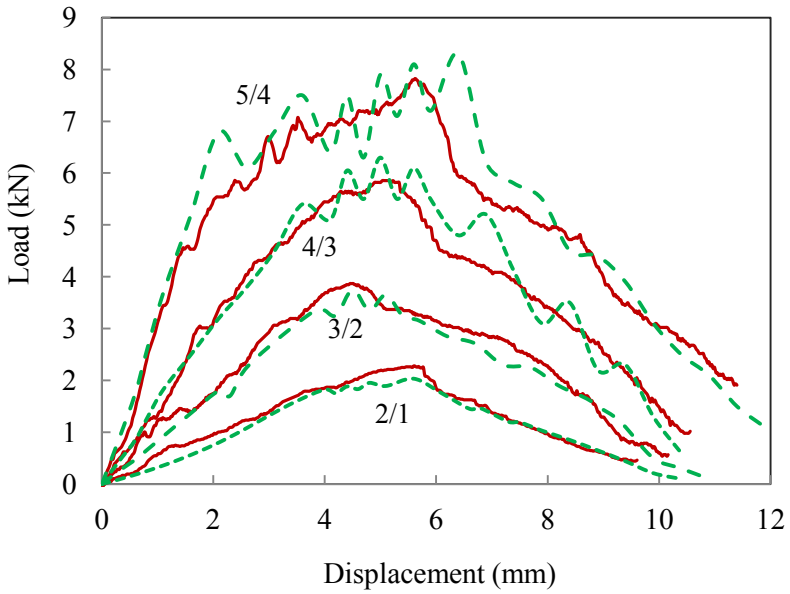

Fig. 6.49 Comparison of load-displacement traces of 2/1, 3/2, 4/3 and 5/4 6061-T6 based fibre metal laminates between FE and experimental tests. (The solid line corresponding to tests and dash line to FE modeling results)

Figure 6.50 shows the 1 mm thick 7075-O aluminium alloy and 5-ply GFRP based FMLs. The load-displacement traces of the FMLs show an initial linear stiffness, followed by gradually increasing resistance resulting from progressive fracture of the layers until the on-set of final perforation. Both the FE prediction and experimental traces exhibit a saw-toothed appearance under impact conditions. The modeling results captured the basic features of the initial stiffness, peak load and displacement in a good agreement with the corresponding experimental results. Similar to the traces on 6061-T6 based FMLs, the FE models exhibit more pronounced oscillatory effects on the four traces. In comparison to the 6061-T6 based FMLs, the displacement in relation to the peak load and the final perforation are more or less doubled. It indicates a larger deformation and more energy absorption. The predicted peak loads for the 7075-O based FMLs plates were increased from 6.6 and 30.5 kN from 2/1 to 5/4 FMLs. The differences between the predictions and experiment data are reasonable within 13 %. The corresponding perforation energies were from 84.4 to 345.5 Joules. From a comparison of the experimental and predicted curves, it is clear that the model captures all of the major features of the experimental trace, including the initial stiffness, peak load, displacement at the peak load and post perforation process.

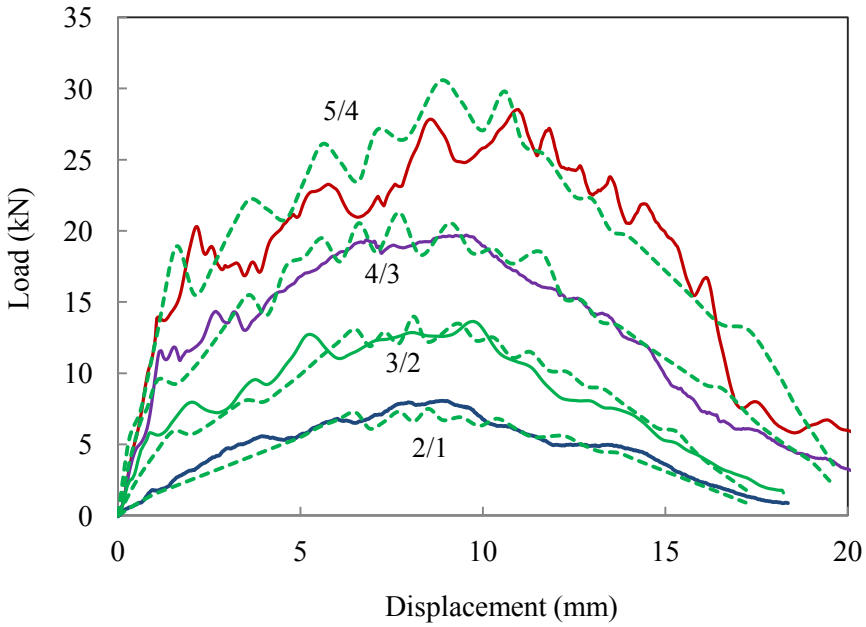

Fig. 6.50 Comparison of load-displacement traces of 2/1, 3/2, 4/3 and 5/4 7075-O based fibre metal laminates between FE and experimental tests. (The solid line corresponding to tests and dash line to FE modeling results)

Figure 6.51 shows the comparison of the simulated and experimental failure modes of 3/2 FMLs made of the three types of aluminium subjected to perforation impact. The basic features of the experimental failure modes for all the FMLs plates were well simulated, in terms of interlaminar damage, delamination, the cross cracks at the rear face and the local deformation mode at the target centre. Since the difference between the FML plates was the thickness of aluminium and the number of composite plies in the composite layer, the experimental failure modes for these three FMLs plates were similar. The delamination effect is more obvious in the thick 7075-O based FMLs than in the 6061 based FMLs. The delamination between the composite and the aluminium was accurately simulated.

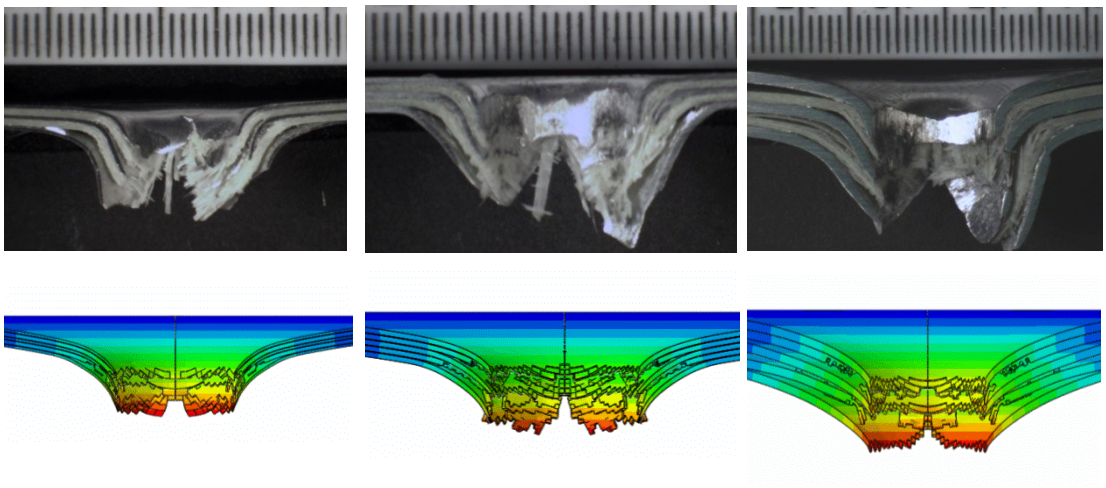

(a). 6061-T6 (b). 6061-O (c). 7075-O

Fig. 6.51. Comparison of cross-sections following impact perforation of 2/3 FMLs based on the 6061-T6, 6061-O and 7075-O aluminium alloys.

6.6.3 Prediction of energy absorption

Figure 6.52 show the comparison between the perforation energy and the corresponding test results in a chart form. The points are experimental data and the dash line is the numerical prediction. Clearly, very good correlation was obtained, i.e. the finite element models developed are well validated against the test results.

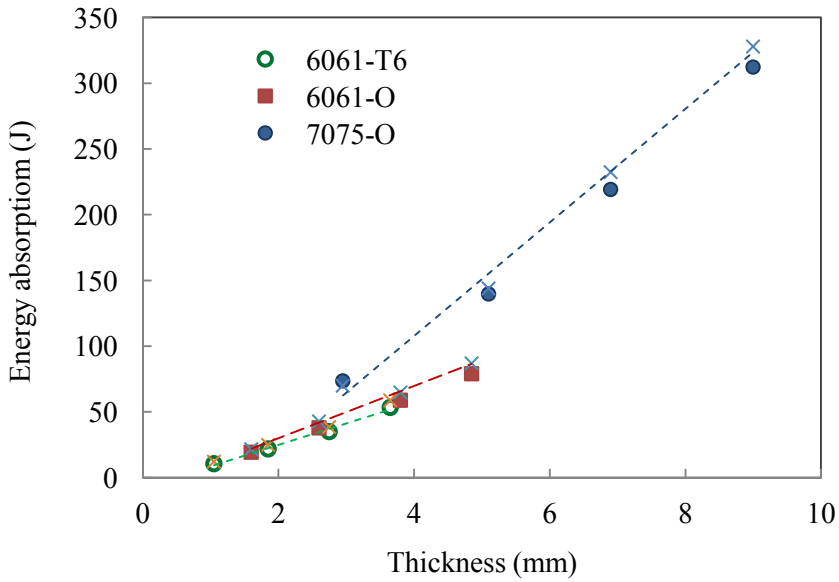

Fig. 6.52 Comparison of energy absorption of 2/1, 3/2, 4/3 and 5/4 fibre metal laminates between FE and experimental tests. (The points are experimental data and the cross points and dash lines are the prediction.)

Finite element models have been developed to simulate the perforation behaviour of fibre metal laminates with various stacking sequences and three different aluminium alloys subjected to impact loading. Good correlation has been obtained between the numerical simulations and the experimental results, in terms of load-displacement traces, peak load, failure mode and perforation energy. Reasonable agreement is evident shown in deformation mode and failure mode. The evidence suggests that the impact resistance and energy absorption increased with the increasing of laminates thickness and area density. It also suggests that the 7075-O alloy based FMLs offers the best impact resistance and energy absorptions. The validated finite element models, which cover the configurations of 2/1, 3/2, 4/3 and 5/4 laminates made with different layers included 3-ply and 5-ply composite and various thinckness of aluminiums are ready to be used for further parametric studies of FMLs subjected to different loading conditions.

6.7 Summary

Numerical investigations on PVC foam based sandwiches, composite rod and tube reinforced foams, fibre metal laminates have been undertaken using the FE models described in Chapter 5. The response of the composite structures was predicted using the finite element analysis package Abaqus/Explicit. The FE models have been validated by the experimental results presented in Chapter 4, with good correction.

The FE predictions have been summarized and analysed to show the response of these structures under various loading conditions. The models for the sandwich and FML structures are capable of predicting the perforation resistance and absorbed energies. The sandwich structures subjected to oblique impact and impact in an aqueous environment and at a pressure difference have also been predicted.

The modeling results for the rod and tube reinforced structures has shown reasonably good simulations on the compressive response of those structures, with reliable predictions of their compressive strength and energy absorption. The performance of those structures with various configurations have been analysed and studied to identify an optimized configuration of each structure. The developed FE modes are ready to be used to conduct further parametric designs and studies.

CHAPTER 7 CONCLUSIONS AND RECOMMENDATIONS FOR FUTURE WORK

7.1 General summary

The objectives of the research are to undertake a detailed investigation of complex hybrid material systems include low velocity impact response of PVC foam based sandwiches structures, the response of quasi-static and dynamic compression of composite rods and tube reinforced foam structures, and quasi-static and dynamic response of FMLs subject to projectile perforation. A series of experimental tests carried out include tensile, compression, three-point bending, shear, projectile impact, drop-weight impact and Split Hopkinson Pressure Bar tests, to characterize the mechanical properties of the foam, composite material and aluminium used in the structures.

The Finite Element Method has been used to model the response of the novel hybrid composite structures tested. A vectorized user material subroutine (VUMAT) was employed to define Hashin's 3D damage criteria for composite layers to model the corresponding deformation and failure mechanisms. Using validated FE models, parametric studies were further carried out to investigate the response of different configurations of composite structures subject to various loading conditions.

7.1.1 Sandwich structures

- The low velocity perforation resistance of a range of plain foams and their associated sandwich structures has been characterised by determining the energy required to perforate the panels. Investigations have shown that the perforation resistance of the plain foams and the sandwich panels is strongly dependent on the properties and failure mechanisms of the foam core. The energy absorption chart of the plain foams suggests that the higher density crosslinked foams have out-performed their linear counterparts and the PET foams offer the lowest perforation energy, with values approximately one half of those offered by the crosslinked foams. However, the energy charts of plain foam based sandwiches suggest that the linear crosslinked PVC foams offer a higher perforation resistance than the linear PVC foams at densities lower than 110 kg/m^3, whereas the converse is true at higher densities.
- The perforation resistances of the sandwich structures follow the trends in the shear fracture

properties of the foams, suggesting that the shear properties and mode of failure is important in determining the perforation resistance of thin-skinned sandwich structures.

- Finite element analyses simulating oblique impact on a number of the sandwich structures subjected to an air-pressure differential have indicated that the energy required for target perforation increased with the angle of obliquity. This reflects the increase in surface area of material failing in shear as well as the increased maximum displacement, associated with a larger volume of foam that is crushed during impact failure.
- Investigation on impact response of a sandwich structure in an aqueous environment was carried out to be considered to reflect the case of a boat hull that is in collision with an immersed object. It has also been shown that sandwich structures impacted in a marine environment offer a lower perforation resistance than those tested in air. The energy required to perforate the sandwich structures decreases approximately 10% with increasing depth of immersion up to 18 m.
- Finite element simulations also indicated that sandwich structures impacted in an environment with an air-pressure difference on their front face (atmospheric pressure at 10000 m) and the rear face (cabin pressure) offer a similar perforation resistance to those tested under normal atmospheric conditions.
- Low velocity impact on graded foam based sandwiches structures with various cores arrangements has been tested and simulated. It has been shown that graded structures can out-perform their monolithic counterparts in terms of their perforation resistance and energy absorption.
- Experimental testing on graded foam based sandwiches structures has shown that placing the higher density foam uppermost in the laminate leads to an enhanced impact performance relative to sandwich panels in which the higher density foam is in contact with the distal surface. Secondary benefit associated with placing the lowest density foam in the centre of the core layer has been observed. Third effects associated with positioning a ductile foam on the distal surface have also been noted.

7.1.2 Composite reinforced foam structures

- The crushing characteristics of composite rod reinforced PVC foam panels for potential use of lightweight energy-absorbing sandwich structures have been undertaken. The energy-absorbing

capability of the reinforced foams has been evaluated though a serious quasi-static and dynamic compression tests on a range of crosslinked PVC foam panels with densities ranging from 40 to 200 kg/m^3, reinforced with composite rods with diameters of 2, 3 and 4 mm.

- Experimental tests have been shown that both the compression strength as well as the energy-absorbing capability of the reinforced foam panels is significantly higher than their plain foam counterparts. Both the compression strength of the reinforced foams, as well as the energy absorbed during crush have been shown to obey a simple rule of mixtures.
- The carbon fibre rod reinforced foam panels have offered superior compression strengths and energy-absorbing characteristics to their glass fibre counterparts at quasi-static rates of strain. An examination of the failed samples has indicated that the carbon rods have been reduced to debris, whilst the glass pins have been crushed to an even fine powder.
- Tests at impact rates of strain again have highlighted the superior characteristics of the carbon-based systems. Here, the specific energy absorbing capacity of the carbon fibre structures increases by up to sixty percent, in passing from quasi-static to dynamic rates of loading. In contrast, the corresponding dynamic enhancement factor for the glass-based foams decreases to almost zero as the rod diameter was increased.
- A series of finite element analyses have been undertaken using the developed Hashin's 3D damage criteria to investigate the influence of varying foam density, rod diameter, rod length and fibre type on the crushing and energy-absorbing characteristics of the rods reinforced foams. The measured values of energy absorption are normalized by the density of the structure to yield values for specific energy absorption to evaluated performance of various structures.
- The modelling predictions are shown in a good agreement with experimental tests that increasing the fibre content results in an increase in the measured values of SEA. Similarly, increasing the density of the foam yields an increase in SEA, although the relative increase in energy absorption tends to decrease at higher densities. Increasing the strain-rate during the compression test serves to increase the energy-absorbing capability of the reinforced cores, primarily due to rate effects in the PVC foam.
- The study on rods reinforced foam structures has shown that it is possible to control the crushing force by using rods of different length. Here, the finite element model can be used to design structures exhibiting particular crushing characteristics and energy-absorbing properties.

- The crushing characteristics of composite tube reinforced PVC foam panels for potential use of lightweight energy-absorbing sandwich structures have been undertaken. The energy-absorbing capability of the reinforced foams has been evaluated though a serious quasi-static and dynamic compression tests on a range of crosslinked PVC foam panels with densities ranging from 40 to 200 kg/m^3, reinforced with composite tubes with inner diameters of 8, 10 and 12.5 mm.
- The investigation on tube reinforced foam panels has shown that tubes reinforced foam similar to the rod reinforced foam, increasing the density of the foam yields an increase in SEA and increasing the tube diameter from 8 to 12.5 mm results in an increase in the measured values of SEA. The carbon tube reinforced foams out perform to the glass tube reinforced foams.
- The tube reinforced foams have shown superior performance to the rod reinforced foam, with SEA values form 61.5 – 85.1 kJ/kg over the rods system of 31.2 - 45 kJ/kg at quasi-static loading. However, on the contrary, at dynamic loading increasing the strain-rate during the compression test serves to decrease the energy-absorbing capability of tube reinforced foams, due to the different failure mechanisms of tube at high stain-rate crushing. The rod reinforced foam indicates an advantage at dynamic loading although the SEA values are lower than the tube reinforced foam.
- The compressive crushing of the tube reinforced foam panels has been simulated by the finite element models with implementing a user-defined constitutive model and strain-rate dependent failure criteria. The simulation supports suggestion that the embedded tube in a foam panel can modify the failure process and greatly enhance the crushing performance of the tube. The FE model developed can be used to predict the response of the composite reinforced foams for structural design analysis and optimization.

7.1.3 Fibre metal laminates

- Experimental tests have been carried out to characterise the material properties of aluminium (6061-T6, 6161-O, 7075-O) and GFRP at both quasi-static and dynamic loading using universal test machine and SHPB. The SHPB results have also shown that both the yield strength and the dynamic Young's modulus of the aluminium alloys are rate-dependent. There are increases in yield strength and the dynamic Young's modulus with increasing strain-rate.

- Rate effects on the perforation resistance of fibre metal laminates based on combinations of three different aluminium alloys and a glass fibre reinforced epoxy resin have been investigated. Tests on the plain composite and plain aluminium alloy samples have highlighted a low level of rate-sensitivity (between 10 and 15%) in passing from quasi-static to impact rates of strain.
- The failure modes are similar under both testing conditions. The failure modes observed in FML samples perforated at quasi-static and impact rates of loading are also very similar, taking the form of plastic deformation in the metal layers, fibre fracture in the composite layers and limited delamination in certain samples.
- The investigations have shown again that the differences are typically less than fifteen percent over the range of loading conditions in both the peak load and the perforation energy. This evidence suggests that FMLs based on the glass fibre/epoxy and the various aluminium alloys are not particularly rate sensitive over the range of rates considered here.
- The energy to perforate the FMLs is plotted against that required to perforate the individual constituent materials, where it has been shown that all of the experimental data appear to fall on a straight line, regardless of the thickness of the hybrid material, its constituent materials or the applied strain rate. Such plots could be useful for estimating the perforation resistance of other stacking sequences based on these material systems.
- The FE models have been validated to predict the perforation resistance and energy-absorbing capability of FMLs. User-defined constitutive models and strain-rate dependent Hashin's 3D damage criteria have been implemented into finite element models using a vectorized user material subroutine (VUMAT) for the composite layers to predict behaviour of FMLs accurately. The validated finite element models, which cover different stacking sequences, are ready to be used for further parametric studies of FMLs with various configurations subjected to different loading conditions.

7.2 Recommendations for Future Work

Sandwich structures and FMLs will be likely subjected to high velocity impact at most of situations in aerospace and automotive application. Based on the investigations above the following recommendations are suggested as future work.

- To carry out experimental investigations on sandwich structures and FMLs subjected to high velocity impact and blast loading.
- It would be valuable to undertake Hopkinson bar tests on PVC foam under high strain rate compression loading in order to obtain the accurate data for the corresponding peak stress, plateau stress and dynamic Young's modulus. The experimental material data will be used to improve the accuracy of the modelling so as to simulate the PVC foam based sandwiches under high velocity impact and blast loading.
- It would be interesting to carry out the further parametric studies on sandwich structures and FMLs using the developed numerical modelling to simulate the different loading conditions for projectile with various diameter and shapes.
- To investigate the perforation resistance and performance of graded foam based sandwiches with various configurations of number of the layers, stacking sequences of the hybrid structures of more foam types.
- To investigate the crushing resistance and performance of rod and tube reinforced foam panels with various skins thickness of GFRP and CFRP. It is to investigate the performance of foam panels reinforced by composites with various configurations such as combination of rod and tube, hybrid structure of composite layer types, rod or tube diameters, array arrangement and proportion or volume fraction.
- To develop analytical models to predict the response of sandwich structures and FMLs under impact loading and the response of composite reinforced foam panels subjected to compressive crushing. To develop an empirical equation base on experimental and numerical data to predict the energy absorption and the peak load of the composite structures with extended configurations.

REFERENCES

ABAQUS, Theory Manual. Version 6.11. Pawtucket: Hibbitt, Karlsson & Sorensen, Inc., 2012

ABAQUS/Explicit, User's Manual. Version 6.11. Pawtucket: Hibbitt, Karlsson & Sorensen, Inc., 2012

Airoldi A, Bettini P, Zazzarini M, Scarpa F, Failure and energy absorption of plastic and composite chiral honeycombs, Structures Under Shock and Impact XII. WIT Press. 2013;101–114.

Alderliesten R, On the development of hybrid material concepts for aircraft structures. Recent Patents Engineering 2009; (3):25-38.

Aktay L, Johnson AF, and Kroplin B-H, Numerical modelling of honeycomb crush behaviour, Engineering Fracture Mechanics, 2008; (75): 2616–2630.

Alia RA, Cantwell WJ, Langdon GS, Yuen SCK, Nurick GN, The energy-absorbing characteristics of composite tube-reinforced foam structures. Composites: Part B, 61:127–135.

Alipour MM and Shariyat M, An elasticity-equilibrium-based zigzag theory for axisymmetric bending and stress analysis of the functionally graded circular sandwich plates, using a Maclaurin-type series solution. European Journal of Mechanics, 2012; (34): 78-101.

Altenaiji M., Guan Z.W., Cantwell W.J., Zhao Y., Schleyer G.K., Characterisation of aluminium matrix syntactic foams under drop weight impact, Materials and Design 2014; 59 : 296–302.

Avila AF, Failure mode investigation of sandwich beams with functionally graded core, Composite Structures, 2014; (81), 323–330.

Asundi A, Choi Alta YN. Fiber metal laminates: an advanced material for future aircraft. J Mater Process Technol, 1997; (63):384–394.

BS ISO 844: 1998, Cellular plastic – compression test for rigid materials-specification.

BS ISO 13586:2000, Plastics - Determination of fracture toughness (GIC and KIC) – linear elastic fracture mechanics (LEFM) approach.

Ball A, On the bifurcation of cone cracks in glass plates, Philosophical Magazine, 1996; (73) 1093.

Beard SJ and Chang FK, Design of braided composites for energy absorption, Journal of Thermoplastic Composite Materials, 2002; (15):3–12.

Beumler T, Pellenkoft F, Tillich A, Wohlers W, Smart C, Airbus costumer benefit from fiber metal laminates. Airbus Deutschland GmbH, 2006; Ref. no: L53pr0605135-Issue 1. p.1-C18.

Buitrago BL, Santiuste C, Sánchez-Sáez S, Barbero E, Navarro C, Modelling of composite sandwich structures with honeycomb core subjected to high-velocity impact, Composite Structures, 2010;(92),

2090-2096.

Botelho EC, Rezende MC, Pardini LC. Hygrothermal effects evaluation using the Iosipescu shear test for glare laminates, J Braz Soc Mech Sci Eng, 2008; 30(3):213.

Botelho EC, Silva RA, Pardini LC, Rezende MC. A review on the development and properties of continuous fiber/epoxy/aluminum hybrid composites for aircraft structures. Mater Res 2006; 9(3):247-256.

Camanho P.P and. Dávila and C.G., Mixed-Mode Decohesion Finite Elements for the Simulation of Delamination in Composite Materials, NASA/TM-2002-211737.

Cantwell WJ, Kiratisaevee H, Hazizan M.A., Impact loading of light weight structures, International Journal of Impact Engineering, 2008;(35)1:61-63.

Cartie D and Fleck N, The effect of pin reinforcement upon the through-thckness compressive strength of foam-cored sandwich panels, Composites Science and Technology; 2003; (16):2401-2409.

Caprino G, Spataro G, Del LS. Low-velocity impact behaviour of fibre glass aluminium laminates. Composite: Part A, 2004; (35):605–616.

Carrillo JG, and Cantwell WJ, Scaling effects in the low velocity impact response of fibre-metal laminates, Journal of Reinforced Plastics and Composites, 2008 (27):893-907.

Chai GB and Zhu S, A review of low-velocity impact on sandwich structures, Proc. Inst. Mech. Eng., Part L: Journal of Materials Design and Applications, 2011; (225): 207-230.

Chai GB, Manikandan P, Low velocity impact response of fibre-metal laminates: A review, Composite Structures, 2014: (107):363-381.

Chen S, Chen K, Peng G, Jia L, Dong P. Effect of heat treatment on strength, exfoliation corrosion and electrochemical behavior of 7085 aluminum alloy, Materials & Design, 2012;(35):93-98.

Childress JJ, Freitas G, Z-Direction pinning of composite laminates for increased survivability, In: Proceedings of the AIAA aerospace design conference, Irvine, California, February 1992; 92–109.

Cowper GR, Symonds PS, Strain hardening and strain rate effect in the impact loading of cantilever beams, Brown University, Division of Applied Mathematics, Report No. 28, 1957.

Cui L, Kiernan S and Gilchrist MD, Designing the energy absorption capacity of functionally graded foam materials, Materials Science and Engineering A, 2009; (507): 215–225.

Deshpande, VS and Fleck NA, Multi-axial yield behavior of polymer foams, Acta Materialia. 2001; (49)10: 1859–1866.

Dolbeer RA, Wright SE, Weller J, Begier MJ, Wildlife strikes to civil aircraft in the United States

1990-2013. FAA National Wildlife Strike Database, Serial Report Number 20, July, 2014.

Eager (1991), Whither advanced materials. Adv. Mater. Processes, ASM International, June 1991, 25–29

EADS Deutschland GmbH, Corporate Research Centre Report, The research requirements of the transport sectors to facilitate an increased usage of composite materials. Part I: The composite material research requirements of the aerospace industry. Report prepared June 2004

Etemadi E, Khatibi Afaghi A. and Takaffoli M. (2009), 3D finite element simulation of sandwich panels with a functionally graded core subjected to low velocity impact, Composite Structures, 2009; (89): 28–34.

Elke Hombergsmeier. Development of advanced laminates for aircraft structures. Proceedings of 25th International Congress of the Aeronautical Sciences. September 2006, Hamburg, Germany.

Fan J Investigation of the behaviour of fibre metal laminates subjected to low velocity impact. PhD thesis. University of Liverpool; 2010.

Fan J, Guan ZW and Cantwell WJ (2011), Numerical modelling of perforation failure in fibre metal laminates subjected to low velocity impact loading, Composite Structures, 2011; (93): 2430–2436.

Farley GL. Effect of specimen geometry on the energy absorption capability of composite materials. Journal of Composite Materials, 1986; (20):390-400.

Farley GL and Jones RM, Crushing characteristics of composite tubes with "Near-Elliptical" cross sections, Journal of Composite Materials, 1992; (26):1741-1751.

Flesher ND, Crash Energy Absorption of Braided Composite Tubes PhD. Thesis, Stanford University; 2006.

Fleischer HJ, Design and explosive testing of a blast resistant luggage container, Structures Under Shock and Impact IV, 1996; 51-59.

Franz T, Nurick GN and Perry MJ, Experimental investigation into the response of chopped-strand mat glassfibre laminates to blast loading. International Journal of Impact Engineering, 2002; (27): 639-667.

Gardner N, Wang E and Shukla A, Performance of functionally graded sandwich composite beams under shock wave loading, Composite Structures, 2012; (94): 1755–1770.

Guan ZW, Aktas A, Potluri P, Cantwell WJ, Langdon G, Nurick GN, The blast resistance of stitched sandwich panels, International Journal of Impact Engineering, 2014;(65): 137-145.

Composite materials handbook, Volume 3 polymer matrix composites materials usage, design, and analysis,17 June 2002

Hashin Z and Rotem A A fatigue failure criterion for fiber reinforced materials. Journal of Composite Materials 1973; (7): 448-464.

Hashin Z. Failure criteria for unidirectional fiber composites, Journal of Applied Mechanics, 1980;(47):329–334.

Hassan MZ, Cantwell WJ, The influence of core properties on the perforation resistance of sandwich structures – An experimental study. Composites: Part B: Engineering, 2012; (43): 3231–3238.

Hassan MZ, Cantwell WJ, Strain rate effects in the mechanical properties of polymer foams. International Journal of Polymers and Technologies, 2011; (3)1:27-34.

Hanssen AG, Girard Y, Olovsson L, Berstad T, Langseth, A numerical model for bird strike of aluminium foam-based sandwich panels. International Journal of Impact Engineering, 2006; 32(7): 1127-1144.

Heimbs S, Computational methods for bird strike simulations: a review. Computers & Structures, 2011; (89) 23-24: 2093-2112.

Heimbs S, Van DB, Duplessis Kergomard Y, Dau F, Malherbe B, Rubber impact on 3D textile composites. Applied Composite Materials, 2012; (19) 3-4: 275-295.

Heimbs S, Lang H, Havar T, Rim release analysis: impact of aircraft wheel flange fragment on wing flap mechanism. In: Structures Under Shock and Impact XII, N. Jones, C.A. Brebbia, WIT Press, 2012.

Heimbs S, Energy absorption in aircraft structures. In: Presented at the first international workshop on hydraulic equipment and support systems for mining IWHEM2012. Huludao, China; 2012.

Hosur MV, Mohammed AA, Jeelani S, Processing of nanoclay filled sandwich composites and their response to impact loading, Journal of Reinforced Plastics and Composites, 2008; 27(8):797-818.

Hohe J, Hardenacke V, Fascio V, Girard Y, Baumeister J, Stöbener K, Weise J, Lehmhus D, Pattofatto S, Zeng H, Zhao H, Calbucci V, Rustichelli F and Fiori F, Numerical and experimental design of graded cellular sandwich cores for multi-functional aerospace applications, Materials and Design, 2012; (39): 20–32.

Icardi U and Ferrero L, Optimisation of sandwich panels with functionally graded core and faces, Composites Science and Technology, 2009; (69): 575–585.

Jacob GC, Fellers JF, Simunovic S, Starbuck JM, Energy absorption in polymer composites for automotive crashworthiness. Journal of Composite Materials, 2002; (36): 813-849.

Jacob GC, Fellers JF, Simunovic S, and Starbuck JM, Energy absorption in polymer composites for automotive crashworthiness. Journal of Composite Material, 2002(36):813-850.

Kaw A, Mechanics of composite material, second edition. CRC Press, Taylor & Francis Group, 2006. ISBN: 10: 0-8493-1343-0

Kalyanam S, Beaudoin AJ, Dodds JRH, Barlat F. Delamination cracking in advanced aluminium-lithium alloys-experimental and computational studies, Engineering Fracture Mechanics, 2009; (76)14: 2174-2191.

Kermanidis T, Labeas G, Sunaric M, Ubels L, Development and validation of a novel bird strike resistant composite leading edge structure, Applied Composite Materials, 2005; (12)6: 327-353.

Lascoup B, Aboura Z, Khellil K, Benzeggagh M, Impact response of three-dimensional stitched sandwich composite, Composite Structure, 2010; (92): 347–353.

Leijten JB, Bergsma HEN., Beukers OK, Experimental study of the low-velocity impact behaviour of primary sandwich structures in aircraft, Composites Part A:Applied Science and Manufacturing, 2009;(40)2:164-175.

Lee DD, Evaluation of lightweight material concepts for aircraft turbine engine rotor failure protection, Federal Aviation Administration Report No. DOT/FAA/AR-96/110, July 1997.

Lee LJ, Huang KY and. Fann YJ, Dynamic Responses of Composite Sandwich Plate Impacted by a Rigid Ball. Journal of Composite Materials 1993;(27), 1238.

Lee WS, Lai CH, Chiou ST, Numerical study on perforation behaviour of 6061-T6 aluminium matrix composite. J Mater Process Technol, 2001; (117): 125–131

Lendze T, Wojtyra R, Guillaumat L, Biateau C, Imielińska K, Low velocity impact damage in glass/polyester composite sandwich panels, Advances in Materials Science, 2006;(6):26-34.

Lin C and Hoo Fatt MS, Perforation of sandwich panels with honeycomb cores by hemispherical nose projectiles. Journal of Sandwich Structures and Materials, 2005; (7)2: 133-172.

Mahfuz H, Kamath MV, Jeelani S and Vaidya UK, Low-velocity impact response of cross-ply laminated sandwich composites with hollow and foam-filled Z-pin reinforced core. Journal of Compos Technology and Research. 1999; (21)2: 1-14.

Mallick PK, Fiber-reinforced composites, Materials Manufacturing and Design. Third edition, CRC Press, Taylor & Francis Group LLC, 2007.

Mamalis AG, Manolakos DE, Ioannidis MB, Papapostolou DP, The static and dynamic axial collapse of CFRP square tubes: finite element modeling. Composite Structures, 2006; (74):213–225.

Marasco AL, Cartie DDR, Partridge IK, Rezai A, Mechanical properties balance in novel Z-pinned sandwich panels: out-of-plane properties. Composites Part A, 2006; (37): 295–302.

McGregor C, Vaziri R, Xiao X, Finite element modelling of the progressive crushing of braided composite tubes under axial impact. International Journal of Impact Engineering, 2010; (37): 662–672.

McGregora C, VazirI R, Xiao, Finite element modelling of the progressive crushing of braided composite tubes under axial impact. International Journal of Impact Engineering, 2010; (37) 6:

662–672.

McGregor C.J., Vaziri R., Poursartip A., Xiao X, Simulation of progressive damage development in braided composite tubes under axial compression. Composites Part A: Applied Science and Manufacturing, 2007; (38), 2247–2259.

Meguid SA, Mao RH, Ng TY (2008) FE analysis of geometry effects of an artificial bird striking an aeroengine fan blade. International Journal of Impact Engineering 2008; (35):487–498.

Mines RAW, Worrall C.M, Gibson AG, Low velocity perforation behaviour of polymer composite sandwich panels. International Journal of Impact Engineering 1998; (21): 855-879.

Mouritz AP, Review of z-pinned composite laminates. Composites Part A: Applied Science and Manufacturing, 2007; (38)12: 2383–2397.

Mouritz AP (2007), Compression properties of z-pinned composite laminates. Composite Science Technology 2007; 67(15–16): 3110-3120.

Mouritz AP, Ballistic impact and explosive blast resistance of stitched composites Composites Part B, 2001; 32: 431-439.

Morris K, The history of PVC: The chemical and industrial production of polyvinyl chloride, Maclaren University of Minnesota,1969.

Nandan R, DebRoy T, Bhadeshia HKDH. Recent advances in friction stir welding-process, weldment structure and properties. Progress Materials Science, 2008; (53): 980-1023.

Nettles A and Hodge A, Impact testing of glass/phenolic honeycomb panels with graphite/epoxy facesheets. 35th International SAMPE Symposium, Anaheim, CA; 1990.

Ochelski S, Bogusz P, Kiczko A. Static and axial crush performance of unfilled and foamed-filled composite tubes. Bulletin of the Polish Academy of Sciences Technical Sciences, 2012; (60):31-35.

Olmi F and Nascimento, KD (1999), Small debris impact simulation using MSC/DYTRAN, 1999 MSC Worldwide Aerospace Conference Proceedings, 1999; (1).

Palazotto A.N., Herup EJ and Gummadi LNB. (2000) Finite element analysis of low-velocity impact on composite sandwich plates, Composite Structures 2000; (49), 209-227.

Park JH, Ha SK, Kang KW, Kim CW, Kim HS, Impact damage resistance of sandwich structure subjected to low velocity impact. Journal of Materials Processing Technology, 2008; (201)1–3:425-430.

Payeganeh GH, Ghasemi FA, Malekzadeh K, Dynamic response of fibre-metal laminates (FMLs) subjected to low-velocity impact. Thin-Walled Structure, 2010; (48):62–70.

Perez JL, Benitez LH, Oliver M, Climent, H.: Survey of aircraft structural dynamics nonlinear problems and some recent solutions.,The Aeronautical Journal, 2011;(115): 653-668.

Pinho ST, Camanho PP, Moura MF, (2004), Numerical simulation of the crushing process of composite materials International Journal of Crashworthiness, 2004: (9):263–276.

Potluri P, Kusak E, Reddy TY, Novel stitch-bonded sandwich composite structures. Composite Structure 2003; 59(2): 251-259.

Red Chris, Estimated market for aerospace composite structures, 2014. (Available from CFC www.compositesworld.com)

Rouse M, Ambur DM, Bodine J and Dopker B, Evaluation of a composite sandwich fuselage side panel with damage and subjected to internal pressure. NASA Technical Memorandum 110309.

Ramadan M, Azzam A, Mohamed AE, Hashim A, Low velocity impact properties of foam sandwich composites: a brief review. International Journal of Engineering Science and Innovative Technology, 2014 (3)2, ISSN: 2319-5967.

Rahmani O., Malekzadeh K., Mohammad S. and Khalili R. (2010), Analytical solution for free vibration of sandwich structures with a functionally graded syntactic foam core, Materials Science Forum, 2010; (636-637): 1143-1149.

Raju KS, Tomblin JS. Energy absorption characteristics of stitched composite sandwich panels. J Composite Material, 1999; (33) 8: 712–728.

Reyes G, Cantwell WJ, The mechanical properties of fibre-metal laminates based on glass fibre reinforced polypropylene. Compos Science Technology 2000; (60):1085–1094.

Reyes VG and Cantwell, WJ, The high velocity impact response of composite and FML-reinforced sandwich structures. Composites Science and Technology, 2004; (64): 35-54.

Rejab MRM, Cantwell WJ, The mechanical behaviour of corrugated-core sandwich panels. Composites Part B: Engineering, 2013; (47):267-277.

Rejab MRM, Ushijima K, Cantwell WJ, The shear response of lightweight corrugated core structures, Journal of Composite Materials,2013; (0): 1-14.

Saucray JM, Structural vulnerability problematic overview for future smart fixed wing counter rotating open rotor aircraft. Workshop on Dynamic Failure of Composite and Sandwich Structures, Toulouse, 2011.

Sburlati R, An axisymmetric elastic analysis for circular sandwich panels with functionally graded cores, Composites: Part B: Engineering, 2012; (43): 1039–1044.

Schmuesser DW, Wickliffe LE, Impact energy absorption of continuous fibre composite tubes. Journal Engineering Material Technology, 1987;(109):72–77.

Schubel PM, Luo JJ, Daniel IM, Low velocity impact behavior of composite sandwich panels, Composites Part A: Applied Science and Manufacturing, 2005(36) 10:1389-1396.

Schubel PM, Luo JJ, Daniel I.M, Impact and post impact behavior of composite sandwich panels, Composites Part A: Applied Science and Manufacturing, 2007(38)3: 1051-1057.

Seo H, Hundley J, Hahn HT, and Yang J-M, Numerical simulation of glass fiber-reinforced aluminium laminates with diverse impact damage, AIAA Journal, 2010; (48):676-687.

Smith M., Guan Z, Cantwell WJ, Finite element modelling of the compressive response of lattice structures manufactured using the selective laser melting technique, International Journal of Mechanical Sciences, 2013(67):28–41.

Shockey DA, Giovanola, JH, Simons, JW, Erlich DC, Klopp RW and Skaggs SR Advanced armor technology: application potential for engine fragment barriers for commercial aircraft, Federal Aviation Administration Report No. DOT/FAA/AR-97/53, September 1997.

Sitnikova E, Guan ZW, Schleyer GK, Cantwell WJ, Modelling of perforation failure in fibre metal laminates subjected to high impulsive blast loading, International Journal of Solids and Structures. 2014; (51): 3135-3146.

Silcock MD, Hall W and Fox BL, Finite element modeling of composite tubular crash structures with an explicit code, 6th Annual SPE Automotive Composites Conference, 2006; 669–682.

Soutis C, Carbon fiber reinforced plastics in aircraft applications, Materials Science and Engineering A, 2005; (412):171.

Straznicky PV, Laliberte JF, Poon C, Fahr A. Applications of fiber-metal laminates. Polymer Composite 2000; (21):558–67.

Tamer S, Egemen A, Mustafa OB, Onur C, A review: Fibre metal laminates, background, bonding types and applied test methods, Materials and Design, 2011; (32): 3671–3685.

Tarlochan F, Ramesh S, Harpreet S. Advanced composite sandwich structure design for energy absorption applications: blast protection and crashworthiness. Composite B: Engineering, 2012; (43):2198–208.

Tarlochan F, Ramesh S. Composite sandwich structures with nested inserts for energy absorption application. Composite Structure 2012; (94):904–916.

Tao XF, Zhao YY. Compressive behavior of Al matrix syntactic foams toughened with Al particles. Scripta Materialia, 2009; (61):461- 464.

Tan KT, Yoshimura A, Watanabe N, Iwahori Y and Ishikawa T. Effect of stitch density and stitch thread thickness on damage progression and failure characteristics of stitched composites under out-of-plane loading. Compos Science Technology, 2013;(74): 194-204.

Thornton, PH and Edwards PJ, Energy Absorption in Composite Tubes, Journal of Composite Materials 1982(16): 521–545.

Thornton PH, Energy absorption in composite structures. Journal of Composite Materials, 1979;

(26):247-262.

Thornton PH, Energy Absorption in Composite Structures, Journal of Composite. Materials, 1979; (13): 247-262.

Tolga Dursun and Costas Soutis, Review Recent developments in advanced aircraft aluminium alloys, Materials and Design, 2014; (56): 862–871

Vaidya UK, Nelson S, Sinn B, Mathew B, Processing and high strain rate impact response of multi-functional sandwich composites. Composite Structure, 2001; (52):429–440.

Villanueva GR and Cantwell WJ. The high velocity impact response of composite and FML-reinforced sandwich structures. Composites Science and Technology, 2004; (64): 35-54.

Vlot A, Impact properties of fiber metal laminates. Composites Engineering 1993; (3):911-927.

Vlot A and Fredell RS, Impact damage resistance and damage tolerance of fibre metal laminates. In: Proceedings of the 9th international conference on composite materials Spain, 1993; (6): 51–58.

Vlot A , Impact loading on fibre metal laminates. Int J Impact Eng; 1996; (18):291–307.

Vlot A, Kroon E, and LaRocca G, Impact resistance of fiber metal laminates. Key Engineering Materials 1998; (141-143):235-276.

Vlot A, Vogelesang LB, Vries T (1999). Towards application of fibre metal laminates in large aircraft. Aircraft Engineering Aerospace Technology, 1999; (71):558–570.

Vo TP, Guan ZW, Cantwell WJ, Schleyer GK, Low-impulse blast behaviour of fibre–metal laminates. Composite Structures, 2002; (94)3:954–965.

Vo TP, Guan ZW, Cantwell WJ, Schleyer GK. Modelling of the low-impulse blast behaviour of fibre–metal laminates based on different aluminium alloys, Composites: Part B, 2013;(44): 141–151.

Vogelesang LB, Vlot A. (2000), Development of fibre metal laminates for advanced aerospace structures. Journal of Mater Process Technology, 2000; (103):1-5.

Wang E, Gardner N, Shukla A, The blast resistance of sandwich composites with stepwise graded cores, International Journal of Solids and Structures, 2009; (46) 18-19:3492-3502.

Wang E, Gardner N, Shukla A, The blast resistance of sandwich composites with stepwise graded cores, International Journal of Solids and Structures, 2009; (46): 3492–3502.

Warren AS, Developments and challenges for aluminium- A Boeing perspective. Mater Forum, 2004; (28):24–31.

Wen HM, Reddy TY, Reid SR and Soden PD, Indentation, penetration and perforation of composite laminates and sandwich panels under quasi-static and projectile loading, Key Engineering Materials, 1998;(501):141-143.

Wilshaw TR (1971), The Hertzian fracture test, Journal of Physics D: Applied Physics, 1971; (4)

1567.

Wu G, Yang J-M., and Hahn HT, The impact properties and damage tolerance of bi-directionally reinforced fiber metal laminates, Journal of Materials Science, 2007; (42):948-957.

Xiao X, Botkin M, Johnson NL.(2009), Axial crush simulation of braided carbon tubes using Mat58 in LS-DYNA, Thin-Walled Structures, 2009(47): 740–749.

Xia F, Wu XQ, Study on impact properties of through-thickness stitched foam sandwich composites. Composite Structure, 2010; (92)2: 412-421.

Xia F and Wu X, Work on low-velocity impact properties of foam sandwich composites with various face sheets, Journal of Reinforced Plastics and Composites, 2010; (29)7: 1045-1054.

Xia F and Wu X, Work on impact properties of foam sandwich composites with different structure, Journal of Sandwich Structures and Materials, 2010; (12): 47-62.

Xiong J, Vaziri A, Ma L, Papadopoulos J, Wu. Compression and impact testing of two-layer composite pyramidal-core sandwich panels. Composite Structure, 2012; (94):793–801.

Yang M and Qiao P, Higher-order impact modeling of sandwich structures with flexible core, International Journal of Solids and Structures 2005; (42): 5460–5490.

Yen CF, Ballistic impact modeling of composite materials. In: Proceedings of the 7th international LS-DYNA users conference, 2002; (6):15–23.

Zangani D, Ambrosetti S, Franitza P, Illing-Guenther H, Koenig RP, Development of a novel concept of explosion-resistant cargo container for narrow-body aircrafts. ICAS 2010, 27th International Congress of the Aeronautical Sciences, Nice, 2010.

Zhang X, Hounslow L, Grassi M, Improvement to low-velocity impact and compression after impact performance of z-fibre pinning. In: Proceedings of the 13th international conference on composite materials, San Diego; July 2003.

Zhou J, Hassan MZ, Guan ZW. and Cantwell WJ (2012), The low velocity impact response of foam-based sandwich panels; Composites Science and Technology, 2012; (72): 1781-1790.

Zhou J, Guan ZW, Cantwell WJ, Liao Y (2014), The Energy-Absorbing behaviour of foam cores reinforced with composite rods,Composite structure, 2014; (114):346-356.

Zhou G. and Hill M, Investigation of parameters governing the damage and energy absorption characteristics of honeycomb sandwich panels, Journal of Sandwich Structures and Materials, 2007;(9): 309–342.

Zhu F, Lu G, Ruan D, Wang Z, Plastic Deformation, Failure and Energy Absorption of Sandwich Structures with Metallic Cellular Cores International Journal of Protective Structures, 2011; (4): 507-541.

Zuhri MYM, Guan ZW, Cantwell WJ, The mechanical properties of natural fibre based honeycomb core materials. Composites: Part B 2014; (58) 1–9.

Zupan M, Chen C and Fleck NA (2003). The plastic collapse and energy absorption capacity of egg-box panels. International Journal of Mechanical Sciences, 2003; (45): 851–871.

Web: http://aluminium.matter.org.uk

Web: http://www.bmw.com

Web: www.compositesworld.com

Web: http://www.diabgroup.com

Web: www.en.wikipedia.org/wiki/Northrop_Grumman_B-2_Spirit

Web: www.f35.com/global/participation/united-states

Web: http://www.hexcel.com

Web: https://www.sunseeker.com